

**QUANTITATIVE MEASUREMENTS OF RHENIUM-188**  
**FOR RADIONUCLIDE THERAPIES**

by

Pedro Luis Esquinas Fernández

B.Sc. Physics, Universidad de Granada, 2012

A THESIS SUBMITTED IN PARTIAL FULFILLMENT OF  
THE REQUIREMENTS FOR THE DEGREE OF

DOCTOR OF PHILOSOPHY

in

THE FACULTY OF GRADUATE AND POSTDOCTORAL STUDIES  
(Physics)

THE UNIVERSITY OF BRITISH COLUMBIA  
(Vancouver)

June 2017

© Pedro Luis Esquinas Fernández, 2017

## Abstract

Over the last three decades, Rhenium-188 ( $^{188}\text{Re}$ ) applications in Nuclear Medicine therapies have gathered a lot of interest thanks to the favorable physical and chemical characteristics of this isotope. In order to optimize  $^{188}\text{Re}$  therapies, the accurate knowledge of the activity distribution within the patient body is required. To this end, the nuclear medicine images must yield accurate quantitative measurements. However, the decay of  $^{188}\text{Re}$  results in a large variety of emissions such as  $\beta$ -particles,  $\gamma$ -particles and Bremsstrahlung, making quantitative measurements of  $^{188}\text{Re}$  activity a very difficult task. The objective of this thesis was to develop a series of methods which would allow us to perform accurate measurements of  $^{188}\text{Re}$  activities in the nuclear medicine department.

To address the thesis' objective, four major studies were carried out: 1) to ensure that measurements of patients administered activities are accurate, a practical method to determine dose-calibrator dial settings using a thyroid-probe was developed; 2) to assess the influence of  $^{188}\text{Re}$  multiple emissions on quantitative imaging, a series of Monte-Carlo simulations of  $^{188}\text{Re}$  single photon emission computed tomography (SPECT) were performed; 3) to assess the image quality and image quantification accuracy of a pre-clinical SPECT camera based on multi-pinhole collimators, a series of experiments using phantoms filled with  $^{188}\text{Re}$  were performed and; 4) to investigate the accuracy of quantitative  $^{188}\text{Re}$  SPECT using a clinical system as well as the accuracy of image-based dosimetry calculations in the context of  $^{188}\text{Re}$  radioembolization, a series of phantom experiments and Monte-Carlo simulations were performed.

The proposed thyroid-probe method enabled us to determine dose-calibrator settings for  $^{188}\text{Re}$  which resulted in measurements of activity within 5% of the sample's true value. The analysis of Monte-Carlo simulations indicated that Bremsstrahlung photons emitted from  $^{188}\text{Re}$

do not really affect image-quantification. The results from phantom experiments showed that accurate quantification of  $^{188}\text{Re}$  activities is possible in pre-clinical and clinical SPECT when images are reconstructed with iterative algorithms and corrections for attenuation, scatter using the triple-energy window method, resolution loss and dead-time. Due to the sub-optimal segmentation methods, dosimetry calculations based on  $^{188}\text{Re}$  images underestimated the true dose by 15-20%, on average.

## **Lay Summary**

Rhenium-188 ( $^{188}\text{Re}$ ) is a promising isotope for applications in Nuclear Medicine therapies. In order to optimize therapies using  $^{188}\text{Re}$ , it is essential to accurately measure the amount of this isotope's activity administered to patients, as well as the distribution of activity within the patient's body. In particular, the knowledge of the  $^{188}\text{Re}$  activity distribution in patients allow us to determine the amount of radiation dose delivered during treatment. The goal of this thesis is to develop quantitative methods to accurately measure  $^{188}\text{Re}$  activities in patient studies. These methods, which are now being implemented in some clinics, will ensure that 1) the  $^{188}\text{Re}$  activities administered into patients are safe and 2) the outcomes from clinical and pre-clinical studies using  $^{188}\text{Re}$  are reliable. Most importantly, these methods will help us to improve our understanding of the effects of radiation dose delivered during  $^{188}\text{Re}$  treatments and the effectiveness of these therapies.

## Preface

The material presented in Chapter 2 has been published as a journal article: Pedro L. Esquinas, Jesse Tanguay, Marjorie Gonzalez, Milan Vuckovic, Cristina Rodríguez-Rodríguez, Urs O. Häfeli and Anna Celler, “Accuracy, reproducibility, and uncertainty analysis of thyroid-probe-based activity measurements for determination of dose calibrator settings”, *Medical Physics*, 43 (2): 6309-6321 in December 2016. I wrote most of the manuscript with contributions from Dr. Jesse Tanguay, Dr. Anna Celler and Dr. Urs O. Häfeli. Dr. Marjorie Gonzalez and Dr. Cristina Rodríguez-Rodríguez assisted me with the thyroid-probe and dose-calibrator experiments. Dr. Milan Vuckovic performed the High-Purity  $\gamma$ -ray spectroscopy experiments. The preliminary results from this project were also presented at the Society of Nuclear Medicine and Medical Imaging (SNMMI) conference in June 2015, Baltimore, US.

The work presented in Chapter 3 was published as part of a journal article: Carlos F. Uribe, Pedro L. Esquinas, Marjorie Gonzalez and Anna Celler, “Characteristics of Bremsstrahlung emissions of  $^{177}\text{Lu}$ ,  $^{188}\text{Re}$  and  $^{90}\text{Y}$  for SPECT/CT quantification in radionuclide therapy”, *Physica Medica* 32:691-700 in May 2016. I performed the Monte-Carlo simulations of  $^{188}\text{Re}$  SPECT/CT imaging, assisted in the experiments and contributed writing part of the manuscript. Dr. Carlos F. Uribe performed the Monte-Carlo simulations of  $^{177}\text{Lu}$  and  $^{90}\text{Y}$ , as well as the experiments and he wrote the majority of the manuscript. Dr. Marjorie Gonzalez assisted with experiments and Dr. Anna Celler provided guidance and revised the manuscript. The preliminary results from this study were presented at the IEEE NSS/Medical Imaging Conference (MIC) in October 2013, Seoul, South Korea.

The study presented in Chapter 4 was published as a journal article: Pedro L. Esquinas, Cristina Rodríguez-Rodríguez, José Carlos de la Vega, Mehrdad Bokharaei, Katayoun Saatchi,

Maryam Shirmohammad, Urs O. Häfeli, Vesna Sossi and Anna Celler, “ $^{188}\text{Re}$  image performance assessment using small animal multi-pinhole SPECT/PET/CT system”, *Physica Medica* 33:26-37 in January 2017. Dr. Cristina Rodríguez-Rodríguez and I performed most of the phantom experiments and I wrote the majority of the manuscript with help from Dr. Cristina Rodríguez-Rodríguez. José Carlos de la Vega, Dr. Mehrdad Bokharaei and Dr. Katayoun Saatchi produced the  $^{188}\text{Re}$  microspheres that were used in the animal experiment. Maryam Shirmohammad assisted with the experiments. Dr. Urs O. Häfeli, Dr. Vesna Sossi and Dr. Anna Celler provided guidance and contributed to the revision of the manuscript. The preliminary results of this study were presented at the IEEE NSS/MIC conference in October 2014, Seattle, US. The animal study was carried out in accordance with the Animal Care Committee of The University of British Columbia under the approved protocol “VECTor/CT Biodistribution and Imaging Studies”, certificate number A12-0172.

The project presented in Chapter 5 has been submitted for publication as a journal article: Pedro L. Esquinas, Carlos F. Uribe, Marjorie Gonzalez, Cristina Rodríguez-Rodríguez, Urs O. Häfeli and Anna Celler, “Accuracy of activity quantification and image-based dosimetry calculations for Rhenium-188 SPECT/CT”. I have written the majority of the manuscript with assistance from Dr. Anna Celler. I received assistance from Dr. Carlos F. Uribe, Dr. Marjorie Gonzalez and Dr. Cristina Rodríguez-Rodríguez during the phantom experiments and manuscript review. Dr. Anna Celler and Dr. Urs O. Häfeli provided guidance during the design of experiments and also reviewed the manuscript. The preliminary findings from this study were presented at the European Association of Nuclear Medicine conference in October 2016, Barcelona, Spain.

The material presented in Chapter 6 is part of an ongoing collaboration with the Nuclear Medicine department at Kovai Center Medical Hospital (Coimbatore, India). The preliminary results from this study have been submitted for publication in a Special Issue on  $^{188}\text{Re}$ , for the International Journal of Nuclear Medicine and Research: Anna Celler and Pedro L. Esquinas, “Personalized dosimetry for  $^{188}\text{Re}$  radionuclide therapies based on post-treatment SPECT/CT scans”. Dr. Anna Celler has written most of the manuscript with my help, and I have analysed the data presented in the study. The Ethics Committee of Kovai Center Medical Hospital approved the patient scans. A written informed consent was obtained from all the patients before taking part in the study.

## Table of Contents

<b>Abstract.....</b>	<b>ii</b>
<b>Lay Summary .....</b>	<b>iv</b>
<b>Preface.....</b>	<b>v</b>
<b>Table of Contents .....</b>	<b>viii</b>
<b>List of Tables .....</b>	<b>xv</b>
<b>List of Figures.....</b>	<b>xviii</b>
<b>List of Abbreviations .....</b>	<b>xxvi</b>
<b>Acknowledgements .....</b>	<b>xxix</b>
<b>Dedication .....</b>	<b>xxxi</b>
<b>Chapter 1: Introduction .....</b>	<b>1</b>
1.1    Fundamentals of Nuclear Medicine: Diagnostic and Therapy .....	1
1.2    Quantitative SPECT Imaging .....	6
1.2.1    Requirements for Quantitative SPECT .....	6
1.2.2    The Image Reconstruction Algorithm .....	8
1.2.3    Attenuation and Scatter Corrections .....	11
1.2.4    Collimator-Detector-Response Compensation .....	12
1.2.5    Detector Dead-time Correction.....	12
1.2.6    System Calibration.....	14
1.3    Fundamentals of Image-Based Dosimetry in Nuclear Medicine .....	15
1.3.1    The Absorbed Dose Equation for Radionuclide Therapies .....	15
1.3.2    Determination of the Time-Integrated Activity .....	16
1.3.2.1    The Conjugate View Method.....	17

1.3.2.2	The Hybrid Planar/SPECT Method and the Purely SPECT Method.....	19
1.3.3	Determination of S-Value.....	20
1.4	Rhenium-188.....	23
1.4.1	Characteristics of $^{188}\text{Re}$ Decay.....	24
1.4.2	Production of $^{188}\text{Re}$ : the $^{188}\text{W}/^{188}\text{Re}$ Generator.....	27
1.4.3	Applications of $^{188}\text{Re}$ in Nuclear Medicine .....	28
1.5	Statement of the Problem, Aim and Thesis Outline .....	30
1.5.1	Aim of the Thesis.....	32
1.5.2	Thesis Outline.....	33
<b>Chapter 2: Accuracy and Uncertainty Analysis of a Thyroid-Probe Based Method to</b>		
<b>Determine Dose-Calibrator Settings .....</b>		<b>35</b>
2.1	Introduction.....	35
2.2	Materials and Methods.....	38
2.2.1	Determination of Dose Calibrator Settings Using the Thyroid Probe .....	39
2.2.1.1	Thyroid-probe Efficiency Curve.....	39
2.2.1.2	Sample Activity Determination Using the Thyroid-probe.....	45
2.2.1.3	Geometry Correction Factors.....	47
2.2.1.4	Determination of the Dose Calibrator Dial Settings .....	48
2.2.2	Uncertainty of Dose Calibrator Settings Determined with the Thyroid Probe.....	49
2.2.3	Determination of Accuracy of Thyroid-probe Activity Measurements.....	50
2.3	Results.....	51
2.3.1	Determination of Dose Calibrator Settings Using a Thyroid-Probe.....	51
2.3.1.1	Thyroid-Probe Efficiency Curve.....	51

2.3.1.2	Dose Calibrator Dial Settings for $^{188}\text{Re}$ .....	52
2.3.1.3	Geometry Correction Factors.....	55
2.3.2	Factors Affecting Uncertainty of Dose Calibrator Settings Determined with the Thyroid-Probe.....	56
2.3.2.1	Uncertainties of Thyroid-Probe Efficiency Curve.....	56
2.3.2.2	Uncertainties of Thyroid-Probe Activity Measurements.....	57
2.3.2.3	Uncertainties of Dose Calibrator Settings.....	59
2.3.3	Accuracy of Thyroid-Probe Activity Measurements.....	60
2.3.4	Limitations and Practical Considerations in the Nuclear Medicine Department.....	63
2.4	Conclusions.....	63
<b>Chapter 3: Characteristics of <math>\gamma</math>-emissions and Bremsstrahlung production by <math>^{188}\text{Re}</math> for SPECT/CT Quantification in Radionuclide Therapies .....</b>		<b>65</b>
3.1	Introduction.....	65
3.2	Materials and Methods.....	66
3.2.1	Simulation of Spectra Detected by SPECT Camera.....	66
3.2.1.1	Camera Modeling.....	66
3.2.1.2	Phantom Simulations .....	68
3.2.2	Phantom Experiments .....	70
3.3	Results.....	72
3.4	Discussion.....	75
3.4.1	Comparison of Simulations and Phantom Experiments .....	75
3.4.2	Quantitative Analysis of $^{188}\text{Re}$ Bremsstrahlung Simulations.....	76
3.4.3	Spectra Analysis and Optimization of Acquisition Parameters .....	77

3.5	Conclusions.....	78
<b>Chapter 4: <sup>188</sup>Re Image Performance Evaluation of a Pre-Clinical Multi-Pinhole</b>		
<b>SPECT/PET/CT system.....80</b>		
4.1	Introduction.....	80
4.2	Materials and Methods.....	81
4.2.1	The VECTor/CT System.....	81
4.2.1.1	VECTor/CT.....	81
4.2.1.2	Image Reconstruction and System Calibration.....	83
4.2.2	Phantom Experiments.....	84
4.2.2.1	Image Quality.....	86
4.2.2.2	Image Quantification .....	87
4.2.2.2.1	Mouse-size Phantom Experiments.....	87
4.2.2.2.2	Multi-source Phantom Experiments.....	88
4.2.2.3	Data Processing for Image Quantification.....	89
4.2.3	Ex-vivo Study .....	90
4.2.4	Understanding <sup>188</sup> Re and VECTor/CT.....	91
4.2.4.1	Analysis of the Measured Energy Spectra.....	91
4.2.4.2	Monte-Carlo Simulations.....	91
4.3	Results.....	93
4.3.1	Phantom Experiments.....	93
4.3.1.1	Image Quality.....	93
4.3.1.2	Image Quantification .....	95
4.3.2	Understanding <sup>188</sup> Re and VECTor/CT.....	98

4.3.2.1	Experimental Energy Spectra .....	98
4.3.2.2	Monte-Carlo Simulations.....	100
4.3.2.2.1	Validation of Monte-Carlo Simulations.....	100
4.3.2.2.2	Analysis of $^{188}\text{Re}$ Emissions and Scatter Volumes .....	100
4.3.3	Ex-vivo Study .....	101
4.4	Discussion.....	103
4.5	Conclusions.....	110
<b>Chapter 5: Accuracy of Activity Quantification and Image-Based Dosimetry Calculations</b>		
<b>for <math>^{188}\text{Re}</math> SPECT/CT .....</b>		
<b>112</b>		<b>112</b>
5.1	Introduction.....	112
5.2	Materials and Methods.....	114
5.2.1	$^{188}\text{Re}$ Phantom Experiments.....	115
5.2.1.1	Quantification Experiments .....	115
5.2.1.2	Dead-time Experiments .....	119
5.2.2	Monte-Carlo Simulations for $^{188}\text{Re}$ SPECT.....	122
5.2.3	Image Reconstruction, Data Processing and Camera Calibration .....	123
5.2.4	Image-Based Dosimetry Calculations.....	125
5.2.4.1	OLINDA S-Values Method .....	126
5.2.4.2	Point Dose Kernel (PDK) Method.....	126
5.2.4.3	Monte-Carlo Simulations for $^{188}\text{Re}$ Dosimetry Calculations.....	127
5.3	Results.....	127
5.3.1	Measurements of Camera Dead-time Factors.....	127
5.3.2	$^{188}\text{Re}$ Quantification .....	128

5.3.3	Image-Based Dosimetry.....	132
5.4	Discussion.....	134
5.4.1	Accuracy of $^{188}\text{Re}$ SPECT Image Quantification .....	134
5.4.2	Accuracy of $^{188}\text{Re}$ SPECT Image-Based Dosimetry .....	140
5.5	Conclusions.....	143
<b>Chapter 6: Image-Based Dosimetry of Patients Undergoing <math>^{188}\text{Re}</math>-Lipiodol Trans-arterial Radioembolization .....</b>		<b>145</b>
6.1	Introduction.....	145
6.2	Materials and Methods.....	149
6.2.1	Preparation of $^{188}\text{Re}$ -Lipiodol .....	149
6.2.2	Patient Selection Criteria .....	149
6.2.3	Treatment Planning and Imaging Protocol .....	150
6.2.4	Image Reconstruction, Camera Calibration and Activity quantification.....	151
6.2.5	Dosimetry Protocols.....	152
6.2.5.1	Hybrid Planar/SPECT – OLINDA.....	153
6.2.5.2	Hybrid Planar/SPECT – Voxel S-Value.....	155
6.2.5.3	Purely SPECT – Voxel S-Value .....	156
6.3	Results.....	157
6.4	Discussion.....	164
6.5	Conclusions.....	166
<b>Chapter 7: Conclusions and Future Work.....</b>		<b>168</b>
7.1	Conclusions.....	168
7.2	Future Work.....	171

7.2.1	Comparison of $^{188}\text{Re}$ -SSS/Lipiodol and $^{188}\text{Re}$ -HDD/Lipiodol in Vivo Dosimetry of Patients Undergoing Trans-Arterial Radioembolization .....	171
7.2.2	Performance Evaluation of an Iterative Dual-threshold Segmentation Method for $^{188}\text{Re}$ Imaging: Phantom and Simulation Study.....	172
<b>Bibliography .....</b>		<b>174</b>
<b>Appendices.....</b>		<b>194</b>
Appendix A - Supplementary Material for Chapter 3 .....		194
A.1	Geometry Correction Factors.....	194
A.2	Uncertainties of Dose Calibrator Settings Determined with the Thyroid Probe ....	196
A.3	Calculation of the Source Geometry Correction Factor using Monte-Carlo .....	199
Appendix B - Supplementary Material for Chapter 5.....		203
B.1	VECTor/CT Calibration Experiments .....	203
B.2	Calculation of Image Contrast and Contrast-to-noise Ratio.....	203
B.3	Monte-Carlo Model of VECTor/CT .....	204

## List of Tables

Table 1.1 Characteristics of most commonly used isotopes in diagnostic nuclear medicine [2–6]	2
Table 1.2 Characteristics of most commonly used isotopes in radionuclide therapy [11–15]	5
Table 1.3 Energy and yields from most abundant $^{188}\text{Re}$ emissions [14]	26
Table 2.1 Manufacturer specifications, source geometry, activity, photopeak energy and photon yield for isotopes used in thyroid-probe efficiency calibration experiment. The quantities in brackets represent the expanded uncertainties ( $k = 2$ ) at 95% confidence level. Nuclear data was obtained from the Nuclear Data Sheets [96,97].	41
Table 2.2 Energy window settings for isotopes used in thyroid-probe efficiency calibration experiment. The values in brackets indicate the window boundaries.	44
Table 2.3 Manufacturer specifications, source geometry, activity, photopeak energy and photon yield for isotopes used to evaluate accuracy of thyroid-probe activity estimates. The quantities in brackets represent the expanded uncertainties ( $k = 2$ ) at 95% confidence level. Nuclear data was obtained from the Decay Data Evaluation Project [98] and the Nuclear Data Sheets [11,14,99].	46
Table 2.4 Energy window settings for isotopes used to evaluate the accuracy of thyroid-probe activity estimates. The values in brackets indicate the window boundaries.	47
Table 2.5 Comparison between $^{188}\text{Re}$ dose calibrator settings determined empirically by different methods and recommended by the manufacturer. All reported uncertainties are expanded uncertainties ( $k = 2$ ) at 95% confidence level.	53
Table 2.6 Top: expanded uncertainty components ( $k = 2$ , at 95% confidence level) of the TP-based $^{188}\text{Re}$ activity. Bottom: resulting uncertainties of $^{188}\text{Re}$ activity, $^{188}\text{Re}$ DC dial settings and $^{188}\text{Re}$ DC activity readings using the TP-based dial settings.	60

Table 2.7 Comparison between activity measured with HPGe and activity measured with the thyroid-probe for $^{99m}\text{Tc}$ , $^{188}\text{Re}$ , $^{131}\text{I}$ and $^{57}\text{Co}$ . All the reported uncertainties are expanded ( $k = 2$ ) at 95% confidence interval. ....	63
Table 3.1 Characteristics of the SymbiaT LEHR, MELP and HE collimators. Data obtained from manufacturer datasheets [115]. Note: the LEHR, MELP and HE collimator specifications were determined using $^{99m}\text{Tc}$ , $^{67}\text{Ga}$ and $^{131}\text{I}$ sources, respectively. ....	67
Table 3.2 Relative contributions of primary, scatter and BRS photons to the $^{188}\text{Re}$ image acquired using 20% wide energy window set on the 155 keV photopeak. Contributions to the entire image and the <i>source ROI</i> were estimated.....	75
Table 4.1 Characteristics of UHRC and HE-UHRC geometry. All dimensions are in mm.....	82
Table 4.2 Energy window settings used for reconstruction of $^{188}\text{Re}$ and $^{99m}\text{Tc}$ data. All the quantities are in keV. ....	83
Table 4.3 Summary of phantom experiments performed to evaluate image quality and image quantification of $^{188}\text{Re}$ with the VECTor camera. ....	85
Table 4.4 Activities, source-to-background ratio and acquisition times for the mouse-size phantom experiments. ....	88
Table 4.5 Summary of slope values obtained from linear fits to the multi-source phantom quantification experiment data.....	96
Table 4.6 Distributions of the $^{188}\text{Re}$ -labeled microspheres at 60 min after tail vein injection into the C57BL/6 mouse. ....	103
Table 5.1 Energy window settings (narrow and wide) for the $^{188}\text{Re}$ quantification and the dead-time phantom experiments. Extra windows A and B were used to measure the count-rate in the entire energy spectrum. ....	117

Table 5.2 Details of $^{188}\text{Re}$ phantom quantification experiment. ....	118
Table 5.3 Phantom activities, estimated dead-time correction factors and percentage errors of total phantom activity quantification. Note: Phantom A, Hot-Water has relatively low activity as it was scanned three half-lives later after Air and Water measurements..	132
Table 6.1 Administered $^{188}\text{Re}$ -Lipiodol activities, tumor volumes and imaging protocols of the four patients investigated in this study. The tumor volumes (reported by the physicians) were determined from diagnostic contrast enhanced CT images. ....	151
Table 6.2 Effective half-lives of tumor and organs at risk determined with the hybrid planar/SPECT method (H) and the purely SPECT method (P). ....	160
Table 6.3 Tumor and organs at risk doses per injected activity. The doses were determined with the Hybrid OLINDA, the Hybrid Voxel S and the Purely SPECT Voxel S methods. All quantities are expressed in mGy/MBq. Data are average $\pm$ SD over the four patients. The quantities in parenthesis represent the range of values. ....	162
Table 6.4 Radiation doses absorbed by tumor, normal liver and lungs calculated with the hybrid - OLINDA (H-O), the hybrid - Voxel S (H-VS) and the purely SPECT - Voxel S (P-VS) methods. All the quantities are in Gy. ....	163

## List of Figures

- Figure 1.1 Diagram of photon attenuation (A) and photon scattering (B) in SPECT. The dashed lines represent the photon paths. Photons 1 and 3 are properly collimated and detected by the SPECT crystal. Photons labelled as 2 are considered “attenuated” because these can no longer be detected. Photon 4 is scattered within the patient and subsequently detected, providing wrong information about the source location. .... 7
- Figure 1.2 Collimator-detector response (CDR) of a small radioactive source at two different distances. The detected source profile at a close distance shows a narrower distribution than the profile at far distance. .... 8
- Figure 1.3 Flow diagram of the MLEM iterative image reconstruction algorithm. The algorithm starts with an initial image estimate that is forward projected to obtain estimated projections. The projections are compared to the measured projections and a projection error is computed. The projection error is backprojected to create an error image that is used to update the initial image estimate. The procedure is repeated until convergence is reached. .... 9
- Figure 1.4 Illustration of dead-time calibration curve (A) and dead-time correction factor tabulated curve (B)..... 13
- Figure 1.5 Whole body planar images (anterior view) of a patient that received an intra-hepatic injection of 1.9 GBq of  $^{188}\text{Re}$ -Lipiodol for the treatment of liver cancer. The images were acquired 3 hours, 24 hours and 48 hours post-administration of  $^{188}\text{Re}$ -Lipiodol.  $I_{\text{max}}$  represents the maximum pixel intensity of each planar image..... 18
- Figure 1.6 Example of tumor time activity curve (from the patient data of Figure 1.5) determined with the hybrid planar/SPECT method. The activity measurements were fit to a mono-

exponential function from $t = 3$ hours (time of first scan) to infinity. The activity	
between 0 h and $t = 3$ h was assumed to grow linearly. ....	19
Figure 1.7 Voxel S-Values for isotopes commonly used in radionuclide therapy. The voxel size	
is 4.8 mm, typical of SPECT reconstructed images.....	23
Figure 1.8 Decay scheme of $^{188}\text{Re}$ [14]. Only the three most intense $\beta$ -decay branches, and the	
three most intense $\gamma$ -emissions (blue arrows) are shown. ....	25
Figure 1.9 Energy spectrum of $\beta$ -emissions by $^{188}\text{Re}$ [60]. ....	26
Figure 1.10 Schematic view of a typical $^{188}\text{W}/^{188}\text{Re}$ generator. ....	27
Figure 1.11 Diagram of $^{188}\text{W}$ production. The quantity $\sigma$ represents the reaction cross-section (in	
barns).....	28
Figure 2.1 Diagram showing the steps and measurements involved in the thyroid probe-based	
method to determine dose calibrator settings.....	38
Figure 2.2 Thyroid-probe experimental setup. ....	39
Figure 2.3 Energy spectrum of $^{99\text{m}}\text{Tc}$ acquired with the thyroid-probe. Dashed lines show the	
boundaries of the lower window, photopeak and upper window. The shaded area	
represents the scatter estimate using the triple energy window method. ....	43
Figure 2.4 Energy spectra of $^{152}\text{Eu}$ and $^{22}\text{Na}$ measured with the thyroid-probe and used for the	
efficiency calibration experiment. The photon yields are shown in parenthesis. ....	51
Figure 2.5 Thyroid-probe efficiency curve (solid line) as a function of energy determined by	
fitting the 2-parameter linear function in $\log(\epsilon)$ . Dashed lines represent the derived	
uncertainty from the fit. Error bars represent experimental uncertainties. All	
uncertainties are expanded uncertainties ( $k = 2$ ) at 95% confidence level. ....	53

Figure 2.6 Atomlab 100plus relative response for three source geometries (10-mL plastic syringe, 20-mL plastic syringe and 25-mL glass vial) filled with increasing volumes of $^{188}\text{Re}$ solution. ....	55
Figure 2.7 Comparison of the analytical and the Monte-Carlo vial-to-reference geometry correction factors. ....	56
Figure 2.8 Energy spectra of $^{99\text{m}}\text{Tc}$ , $^{188}\text{Re}$ , $^{131}\text{I}$ and $^{57}\text{Co}$ measured with the thyroid-probe and used to evaluate accuracy of activity estimates. ....	62
Figure 3.1 Geometry of SPECT camera model implemented in GATE. (A) lateral view, (B) 3-D surface rendered view and, (C) magnified frontal view showing the collimator holes. Note: the lateral shielding volume surrounding the camera head is not shown in these views. ....	66
Figure 3.2 Photon yields of Bremsstrahlung (TBY), $\gamma$ -particles (NBYradioactive) and X-rays (NBYX-ray) generated by the $^{188}\text{Re}$ decay source inside the simulated Jaszczak phantom (INSIDE), and the corresponding yields of photons that escaped the phantom (OUTSIDE). ....	72
Figure 3.3 Energy spectra of (A: INSIDE) total photons produced inside the Jaszczak phantom after $^{188}\text{Re}$ decay and (B: OUTSIDE) total photons that escaped the phantom. The contribution from BRS photons is also shown in both cases. ....	73
Figure 3.4 Comparison between experimental and simulated $^{188}\text{Re}$ energy spectra for LEHR, ME and HE collimator. ....	73
Figure 3.5 Analysis of different components of the simulated $^{188}\text{Re}$ energy spectra acquired with LEHR, ME and HE collimators. ....	74

Figure 3.6 Profiles obtained from $^{188}\text{Re}$ planar images using a 20% width window set around the 155 keV photopeak. ....	74
Figure 4.1 (a) The VECTor/CT camera system (printed with permission of MILabs) (b) Cross-sectional diagram of the collimator geometry with the Field of View (FOV) and the Central Field of View (CFOV). ....	82
Figure 4.2 Geometry of (a) the two micro- <i>Jaszczak</i> phantoms, (b) the two line-source phantoms and (c) the multi-source phantom. Due to the arrangement of the small sources in the multi-source phantom, two syringes were needed in order to scan a total of 6 sources. All reported volumes (in mL) refer to the filling volumes. All dimensions are in mm. ....	87
Figure 4.3 Transaxial slices from the SPECT images of the micro- <i>Jaszczak</i> resolution phantoms filled with $^{188}\text{Re}$ and $^{99\text{m}}\text{Tc}$ . The phantom rod diameters are shown in mm. The sector with the smallest distinguishable rods are highlighted with a red dashed triangle. Note: the largest rods (1.7 mm) of Phantom a-1 were not effectively filled with $^{99\text{m}}\text{Tc}$ . ....	94
Figure 4.4 Contrast and contrast-to-noise ratio as a function of rod diameter and level of counts for $^{188}\text{Re}$ (a, c) and $^{99\text{m}}\text{Tc}$ (b, d), scanned using HE-UHRC and UHRC. ....	95
Figure 4.5 Quantification accuracy of $^{99\text{m}}\text{Tc}$ -UHRC, $^{99\text{m}}\text{Tc}$ -HE-UHRC, $^{188}\text{Re}$ -UHRC and $^{188}\text{Re}$ -HE-UHRC line source phantom experiments for VOI A (a) and VOI B (b). The dashed horizontal line shows the 10% error level. ....	96
Figure 4.6 Quantification accuracy of $^{99\text{m}}\text{Tc}$ -UHRC (a), $^{99\text{m}}\text{Tc}$ -HE-UHRC (b), $^{188}\text{Re}$ -UHRC (c) and, $^{188}\text{Re}$ -HE-UHRC (d) multi-source phantoms as a function of activity concentration. A line of best fit is plot for sources in water and in the presence of 0.85 MBq/mL to 1 MBq/MI background activity. ....	97

Figure 4.7 Energy spectra from  $^{99m}\text{Tc}$ -UHRC,  $^{99m}\text{Tc}$ -HE-UHRC,  $^{188}\text{Re}$ -UHRC and  $^{188}\text{Re}$ -HE-UHRC acquisitions of a line-source in a (cold) water phantom obtained at three different bed positions corresponding to different count-rate levels. For each isotope and collimator, the count-rates in the energy spectra were divided by the phantom activity..... 98

Figure 4.8 Comparison of experimental and simulated energy spectra of the  $^{188}\text{Re}$  point source scanned with UHRC. The energy spectra were normalized to the sum of counts in the energy interval from 100 keV to 700 keV. .... 99

Figure 4.9 Monte-Carlo simulations of spectra components for the  $^{188}\text{Re}$ -UHRC acquisition of a point source (placed inside a cylindrical water phantom) at the center of CFOV (a), and 4 cm off-center (b). Sub-figure (c) shows the simulated spectra of scattered photons categorized by the location of their last interaction. .... 101

Figure 4.10 Coronal slices of the fused SPECT/CT mouse scans showing the biodistribution of  $^{188}\text{Re}$  microspheres (1 hour after injection). Images were acquired using UHRC and HE-UHRC. The dashed lines indicate regions of uptake in the lungs and liver..... 102

Figure 4.11 Activity concentration profiles drawn parallel to the main axis of phantom for the  $^{99m}\text{Tc}$  UHRC/HE-UHRC and  $^{188}\text{Re}$  UHRC/HE-UHRC SPECT images of the line source in air (a-d). Coronal slices of the fused SPECT/CT images of the line-source air phantoms (e-h). The color-map of SPECT images was re-scaled to 0.1 of the maximum value in each SPECT image to better visualize the background signal.... 106

Figure 5.1 Photographs, axial and coronal CT slices of the thorax phantom (from the experiment with phantom filled with air) with the two configurations of spheres and bottles (A

and B) used in the quantification experiments. The spheres and bottles are labeled as S1-S6 and B1-B4, respectively. ....	115
Figure 5.2 A-B) Phantom calibration curves used to determine dead-time correction factors (DTCF) for HE and ME collimators. C-D) DTCF as a function of the observed total count-rate for HE and ME collimators. Fit parameters of HE dead-time: $\tau_P = 3.4 \times 10^{-5}$ s; $\tau_{NP} = 3.7 \times 10^{-14}$ s. Fit parameters of ME dead-time: $5.4 \times 10^{-5}$ s; $\tau_{NP} = 5.3 \times 10^{-6}$ s. ....	121
Figure 5.3 Diagrams showing the two image-based dosimetry approaches that were investigated in this study (OLINDA S-Value and point-dose kernel) and compared to the reference dose obtained from the Monte Carlo-based calculation. For OLINDA and point dose kernel, the volumes of interests were segmented using two methods: a fixed 40% threshold and CT-based boundaries. ....	125
Figure 5.4 Recovery curves (RC) of air, water and hot-water phantoms scanned with high-energy and medium-energy collimators and reconstructed the narrow (solid-line) and wide (dashed line) scatter window settings. Note: data with wide scatter windows settings were available for phantom configuration A only. ....	130
Figure 5.5 Box-plots summarizing the quantification errors of the total activity measured in the SPECT images of the phantoms with and without dead-time corrections. The dashed lines show the $\pm 10\%$ error limits. ....	131
Figure 5.6 Percent errors of the average absorbed dose-rates calculated using: OLINDA S-Values with 40% threshold segmentation (OL-A), OLINDA S-Values with CT-based segmentation (OL-B), point dose kernel with 40% threshold segmentation (PDK-A) and point dose kernel with CT-based segmentation (PDK-B).....	133

Figure 5.7 Comparison of simulated true scatter, simulated TEW-narrow scatter estimate and simulated TEW-wide scatter estimate from a  $^{188}\text{Re}$  point-source and a 2.0 cm diameter sphere filled with  $^{188}\text{Re}$  in air and water and scanned using HE collimator. Row 1: simulated energy spectra obtained from counts within a 5.0 cm diameter circular ROI around the source center. The wide (W) and narrow (N) scatter window settings are indicated with vertical dashed lines. Row 2-4: Simulated projection images. Row 5: profiles along the simulated projection images. .... 137

Figure 5.8 Comparison of simulated true scatter, simulated TEW-narrow scatter estimate and simulated TEW-wide scatter estimate from a  $^{188}\text{Re}$  point-source and a 2.0 cm diameter sphere filled with  $^{188}\text{Re}$  in air and water and scanned using ME collimator. Row 1: simulated energy spectra obtained from counts within a 5.0 cm diameter circular ROI around the source center. The wide (W) and narrow (N) scatter window settings are indicated with vertical dashed lines. Row 2-4: Simulated projection images. Row 5: profiles along the simulated projection images. .... 138

Figure 5.9 (A,D) Monte-Carlo dose-maps showing the 20-mL sphere and the 111-mL sphere in hot water; (B,E) Dose-profiles along the 20-mL sphere and the 111-mL sphere for three cases: Monte-Carlo dose-map, dose-map obtained from images reconstructed with (“PDK-A RR”) and without resolution recovery + filtered with a 5-mm Gaussian kernel (“PDK-A no RR + Gaussian”); (C,F) Dose volume histograms calculated for the 20-mL and 111-mL spheres derived from images with and without resolution recovery. The cumulated dose was calculated from the dose-rate map, assuming the physical decay of  $^{188}\text{Re}$  only. .... 143

Figure 6.1 Anterior whole-body view of Patient 01 showing the manually drawn organ's ROIs.	
Note: The thyroid and the urinary bladder were not visible on SPECT/CT.....	155
Figure 6.2 Planar images of <sup>188</sup> Re-Lipiodol biodistribution in the four patients investigated in this study. The images shown were acquired 3 hours post-administration of the radiopharmaceutical. For comparison purposes, the counts in each image were normalized by the corresponding injected activity. ....	157
Figure 6.3 CT (top-row) and fused SPECT/CT (bottom-row) coronal slices showing the <sup>188</sup> Re-Lipiodol biodistribution within the liver and the segmented tumor boundaries of the four patients investigated in this study.....	159
Figure 6.4 Comparison of tumor time-activity curves for all the patients (A) and organ-time activity curves for Patient 03 (B). The time-activity curves were determined from purely SPECT data and were normalized by the injected activity. With this normalization, the area under these curves represents the residence time.....	161
Figure 6.5 Dose volume histograms (DVH) of tumor and normal liver volumes of the patients investigated in this study. For the sake of comparison, the dose-range on each DVH is set to [0Gy, 50Gy].....	164
Figure A.1 Diagram of vial source and disk source used for geometry correction factor estimation.....	195
Figure A.2 Comparison between experimental and Monte-Carlo simulations of the thyroid probe efficiency.....	202

## List of Abbreviations

<b>3-D</b>	3-dimensional
<b>AADR</b>	Average absorbed dose rate
<b>BRS</b>	Bremsstrahlung
<b>CCT</b>	Contrast-enhanced CT
<b>CDR</b>	Collimator-detector response
<b>CF</b>	Calibration factor
<b>CFOV</b>	Central field of view
<b>CNR</b>	Contrast-to-noise ratio
<b>DC</b>	Dose calibrator
<b>DTCF</b>	Dead-time correction factor
<b>DVH</b>	Dose-volume histogram
<b>EGS</b>	Electron-gamma shower
<b>ENDSF</b>	Evaluated nuclear structure data file
<b>FOV</b>	Field of view
<b>FWHM</b>	Full width half maximum
<b>GATE</b>	Geant4 applications for tomography emission
<b>HCC</b>	Hepatocellular carcinoma
<b>HDD</b>	Hexadecyl-4,-7-diaza-1,-10-decaedithiol
<b>HE</b>	High energy
<b>HEDP</b>	Hydroxyethylidenediphosphate
<b>HE-UHRC</b>	High energy – ultra-high resolution (mouse-size) collimator

<b>HPGe</b>	High-purity Germanium
<b>HSA</b>	Human Serum Albumin
<b>IAEA</b>	International Atomic Energy Agency
<b>KMCH</b>	Kovai Medical Center Hospital
<b>LEHR</b>	Low energy high resolution
<b>MC</b>	Monte-Carlo
<b>MCA</b>	Multi-channel analyzer
<b>MCNP</b>	Monte-Carlo N-Particle
<b>MELP</b>	Medium energy low penetration
<b>MIRD</b>	Medical Internal Radiation Dose
<b>MLEM</b>	Maximum likelihood expectation maximization
<b>NM</b>	Nuclear medicine
<b>OSEM</b>	Ordered subset expectation maximization
<b>PCR</b>	Polymerase chain reaction
<b>PDK</b>	Point dose kernel
<b>PET</b>	Positron emissions tomography
<b>POSEM</b>	Pixel-based ordered subset expectation maximization
<b>RC</b>	Recovery coefficient
<b>ROI</b>	Region of interest
<b>RR</b>	Resolution recovery
<b>SPECT</b>	Single photon emission computed tomography
<b>TEW</b>	Triple energy window

<b>TIAC</b>	Time-integrated activity curve
<b>TP</b>	Thyroid probe
<b>UHRC</b>	Ultra-high resolution (rat-size) collimator
<b>VOI</b>	Volume of interest

## Acknowledgements

It has been almost 5 years since I entered this lab, and so much has happened. I have gone through so many experiments, training, presentations, writing and, finally, I reached the top of this mountain called PhD and placed my flag. This flag not only has my name (with a “Dr.” in front!), but also the names of so many people who have been guiding, teaching, supporting and being at my side during this adventure. I would like to use this part of my thesis dissertation to say Thank you to each one of you. I hope you don’t mind I use your first name, I prefer to make this more personal.

Thank you Anna for your constant guidance, advice, help and support all these years. Most importantly, thank you for believing in me. My success is your success.

Thank you Vesna, Urs and Francois (my PhD Committee) for your feedback and positive comments that definitely helped directing my project towards the right direction. Thank you all (including Anna!) for reading my thesis, you are one of the few privileged people in the world that read it before its official release to the public.

Thank you the Medical Imaging Research Group members: Xinchu, Laurel, Hillgan and Wei and the former members Jesse, Carlos and Sonoko. From co-workers you became colleagues, from colleagues you became friends, and from friends you became my second family.

Thank you Cristina, Marjorie and Carlos (again!). You have been the three major pillars of my experiments with Rhenium-188 (the best radionuclide in the world!). Cristina, I have learned a lot of Chemistry from you during our long experiments at CCM. Marjorie, Thank you so much for staying with us every time we used the clinical camera, and most importantly, for

always being willing to let us perform experiments at VGH. Carlos, you and I had a romance with Monte-Carlo and that will always keep us together.

Thank you to all my colleagues, classmates and collaborators that through many interactions you have become my friends. I would like to write each one of your names but then my thesis would have too many pages (I am very popular) and UBC would never approve it (they are a bit picky with the formatting...). I am sure you know who you are. Thank you.

Thank you to all my friends who have been part of my non-academic life in Vancouver. Although I tend to be doing academic stuff all the time, my time as a PhD student would have been so difficult if I didn't have you to make me happy and balance my work. Especially, Thank you to my roommates Wenly, Madina, Rienaldy and Andres as we have shared so many good moments.

Thank you to my family in Spain. Thank you to my parents for their support and trust in all my choices since I was a little kid. I know it has been difficult to be that far away. Thank you for the effort. I miss you. Thank you to my sister Leti for always taking care of me and now, for bringing (with Juan!) to the world my niece Leti Jr (I think we all agree that my niece is the cutest baby in the south of Spain!). I love you all.

Thank you to the best and most accurate alarm (always waking me up at 6.00 AM) in this universe. I believe she has an internal atomic clock. I am talking about my dog Nebula. Nebula (a.k.a. "the cosmic dog"), you have brought so much energy and happiness to my life. I can't live without you.

And finally, the last Thank you goes to the most important person in my life: Rie. Thank you for staying at my side. For accepting me regardless of my mood or my stress levels. We have learn so much from each other and that has been beautiful. This PhD is 50% yours. Te quiero.

## Dedication

To Manuel Félix Herrera Gómez (1987-2013),  
who is now flying through the Universe

## Chapter 1: Introduction

### 1.1 Fundamentals of Nuclear Medicine: Diagnostic and Therapy

Nuclear Medicine (NM) is the branch of medicine that uses unsealed radioactive compounds (radiopharmaceuticals) for diagnosis and/or treatment of diseases. Currently, the majority NM procedures performed in clinics are intended for diagnosis purposes. However, the number of therapeutic NM procedures (also known as radionuclide therapies) is on the rise [1].

In a typical diagnostic study, a pharmaceutical labelled with a  $\gamma$ -emitting or positron-emitting radionuclide is injected into the body of the patient. Thanks to its biological and molecular properties, the radiopharmaceutical is able to target the diseased site (e.g., tumor cells) and its  $\gamma$ -emissions (or secondary annihilation photons, for the case of positron emitters) can be detected using single photon emission computed tomography (SPECT) or positron emission tomography (PET) scanners. These NM cameras collect the information about the origin and intensity of the radiopharmaceutical emissions at different angular views around the patient (referred to as projections). Such information is subsequently processed (a step known as image reconstruction, see Section 1.2.2) and a 3-dimensional (3-D) image of the radiopharmaceutical distribution within the patient's body is obtained and used for diagnostic purposes. Table 1.1 shows the characteristics of some of the diagnostic radionuclides most commonly used in NM.

**Table 1.1 Characteristics of most commonly used isotopes in diagnostic nuclear medicine [2–6]**

<b>Isotope</b>	<b>Half-life [h]</b>	<b>Decay mode</b>	<b>Main photon energy [keV]</b>	<b>Intensity of photon emission [%]</b>	<b>Radiopharmaceutical</b>	<b>Applications</b>
$^{99m}\text{Tc}$	6.01	IT <sup>†</sup>	140	89	$^{99m}\text{Tc}$ -PHOSPHONATE, $^{99m}\text{Tc}$ -MIBI, $^{99m}\text{Tc}$ -HYNIC	Diagnosis of bone tumors, diagnosis of heart-conditions (myocardial perfusion), diagnosis of neuroendocrine tumors
$^{18}\text{F}$	1.83	$\beta^+$	511	193	$^{18}\text{F}$ -FLUORO-DEOXY GLUCOSE (FDG)	Diagnostic and staging of cancer
$^{67}\text{Ga}$	78.28	EC <sup>††</sup>	93, 185	39, 21	$^{67}\text{Ga}$ -CITRATE/TRANSFERRIN	Diagnosis of tumor, especially lymphomas
$^{68}\text{Ga}$	1.13	$\beta^+$	511	178	$^{68}\text{Ga}$ -DOTA	Diagnosis of neuroendocrine tumors
$^{111}\text{In}$	67.2	EC	171, 245	91, 94	$^{111}\text{In}$ -IBRITUMOMAB	Radioimmunotherapy (pre-therapy imaging)

<sup>†</sup>IT = isomeric transition decay; <sup>††</sup>EC = electron capture decay

Alternatively, radionuclide therapies are promising procedures for the treatment of unlocalized tumors (e.g., metastases) where surgical tumor resection or traditional external beam radiotherapy is not a suitable treatment option. In these therapies, radiopharmaceuticals are labelled with  $\beta^-$  or  $\alpha$ -emitting isotopes and are injected into the body of the patient. The pharmaceutical is then able to target the tumor cells and the interaction of  $\beta^-$  or  $\alpha$  particles with the targeted tissue results in the local deposition of energy and potentially the destruction of these tumor cells. Thanks to the short interaction range of charge particles in tissue [7], most of the particle's energy is deposited within the tumor site, minimizing the energy absorbed (and therefore, the toxicity) by the surrounding normal tissue. The physical characteristics and applications of some of the isotopes most commonly used in radionuclide therapies are presented in Table 1.2. The choice of the optimal isotope depends on the target tumor characteristics. For instance, high-energy  $\beta$ -emitting isotopes such as  $^{90}\text{Y}$  are suitable for treating bulky tumors thanks to their higher particle penetration range whereas  $\alpha$ -emitters like  $^{223}\text{Ra}$  are optimum for the treatment of small tumor metastases.

Patient-specific radionuclide therapies consist of two major steps. First, the patient undergoes a diagnostic NM procedure to determine the extent of disease, predict the likelihood of response to a given radiopharmaceutical and to assess the amount of activity to be injected. In order to better predict the therapeutic dose, the diagnostic pharmaceutical must be identical (or very similar) to the therapeutic one to ensure that the same pharmacokinetics and tumor uptake will take place during both diagnosis and treatment. In the second step, the optimum amount of therapeutic radiopharmaceutical is delivered. As shown in Table 1.2, some of the commonly used isotopes in radionuclide therapies also emit photons with energies suitable for SPECT imaging which allows us to image the bio-distribution of the therapeutic tracer and to calculate

the radiation dose delivered to targets (i.e., tumor) and organs at risks [8]. The combination of diagnosis and therapy using the same pharmaceutical in personalized nuclear medicine is termed ‘theranostics’. Some examples of ‘theranostics’ agents are  $^{99m}\text{Tc}$ - $^{188}\text{Re}$  microspheres for treatment of hepatocellular carcinoma [9] and  $^{111}\text{In}$ - $^{90}\text{Y}$  IBRITUMOMAB for radioimmunotherapy [10].

In order to ensure that the pharmacokinetic information obtained during the diagnostic step of the theranostic procedure is accurate, as well as to guarantee accuracy of dosimetry calculations based on post-therapy SPECT, the NM images must represent the true radioisotope’s concentration (in MBq/mL) within the patient body. In other words, the images of the tracer biodistribution must be quantitatively accurate. However, accurate quantitative SPECT imaging is challenging due to multiple image-degrading effects such as photon attenuation, photon scatter, resolution loss and dead-time. The remaining sections of this chapter describe the principles of quantitative imaging and image-based dosimetry calculations (Sections 1.2 and 1.3, respectively). Additionally, the main characteristics of  $^{188}\text{Re}$ , a promising isotope in NM which is the focus of this thesis, are described in Section 1.4. Finally, the aim and outline of this thesis are introduced in Section 1.5.

**Table 1.2 Characteristics of most commonly used isotopes in radionuclide therapy [11–15]**

<b>Isotope</b>	<b>Half-life [d]</b>	<b>Decay mode</b>	<b>Maximum particle energy<sup>†</sup> [keV]</b>	<b>Maximum range in tissue [mm]</b>	<b>Main photon energy [keV]</b>	<b>Intensity of photon emission [%]</b>	<b>Radiopharmaceutical</b>	<b>Applications</b>
<sup>131</sup> I	8.02	$\beta^-$	971	2.3	364	82	<sup>131</sup> I-MIBG; NaI-131; Bexxar	Neuroendocrine tumors, thyroid cancer, radioimmunotherapy
<sup>177</sup> Lu	6.73	$\beta^-$	498	1.8	113, 208	6, 11	<sup>177</sup> Lu-DOTATATE; <sup>177</sup> Lu-DOTATOC	Neuroendocrine tumors
<sup>90</sup> Y	2.67	$\beta^-$	2280	11.3	N/A		Zevalin; <sup>90</sup> Y-microspheres	Radioimmunotherapy, radioembolization of liver cancer,
<sup>188</sup> Re	0.71	$\beta^-$	2120	10.4	155	16	<sup>188</sup> Re – HEDP; <sup>188</sup> Re – microspheres	Palliation of painful bone metastases, radioembolization of liver cancer
<sup>223</sup> Ra	11.43	$\alpha$	5716	<0.1	84, 269	25, 14	<sup>223</sup> Ra-dichloride	Metastatic prostate cancer

<sup>†</sup>For  $\alpha$ -decay, the energy spectrum of emitted  $\alpha$ -particles is discrete. For <sup>223</sup>Ra, this cell represents the energy of the most abundant  $\alpha$ -particle by this isotope

## 1.2 Quantitative SPECT Imaging

### 1.2.1 Requirements for Quantitative SPECT

Thanks to the introduction of hybrid SPECT/CT systems, the advances in iterative image reconstruction algorithms and the availability of accurate correction methods for image-degrading effects, SPECT is considered a quantitative imaging modality [16]. The main requirements for a quantitative SPECT image reconstruction algorithm are:

- 1) the algorithm must behave in a linear fashion as a function of the activity present in the scanner field of view (FOV);
- 2) the algorithm must compensate for the attenuation of photons within the patient's body as well as remove the scattered photons from the data (Figure 1.1 A and B);
- 3) the algorithm must include corrections for the losses of detected photons due to detector dead-time. Dead-time is defined as the time required by the system to process a detected event. During this time, the SPECT system is not able to record another event.
- 4) Additionally, the reconstructed data (typically in units of counts per voxel) must be calibrated to obtain an image with units of activity (MBq) or activity concentration (MBq/mL) per voxel.

The requirements mentioned above are sufficient to obtain reconstructed images in which the total activity measured in the entire FOV corresponds to the injected activity (within uncertainty) [17,18]. However, there is an additional source of image degradation: the collimator-detector response (CDR). The CDR is the principal cause of the poor spatial resolution of SPECT images. The loss of resolution due to CDR consists of a combination of four effects: intrinsic detector resolution, collimator resolution, septal penetration and septal scatter [19]. Figure 1.2 illustrates the CDR response of a point-source at two different distances

from the collimator. The effect of CDR might affect quantification accuracy of structures within the SPECT image because the activity distribution spills out of the physical boundaries of the object of interest. This effect, also known as partial volume effect (PVE), is more severe for small objects where the object's size is comparable to (or less than) three times the SPECT system resolution [20].

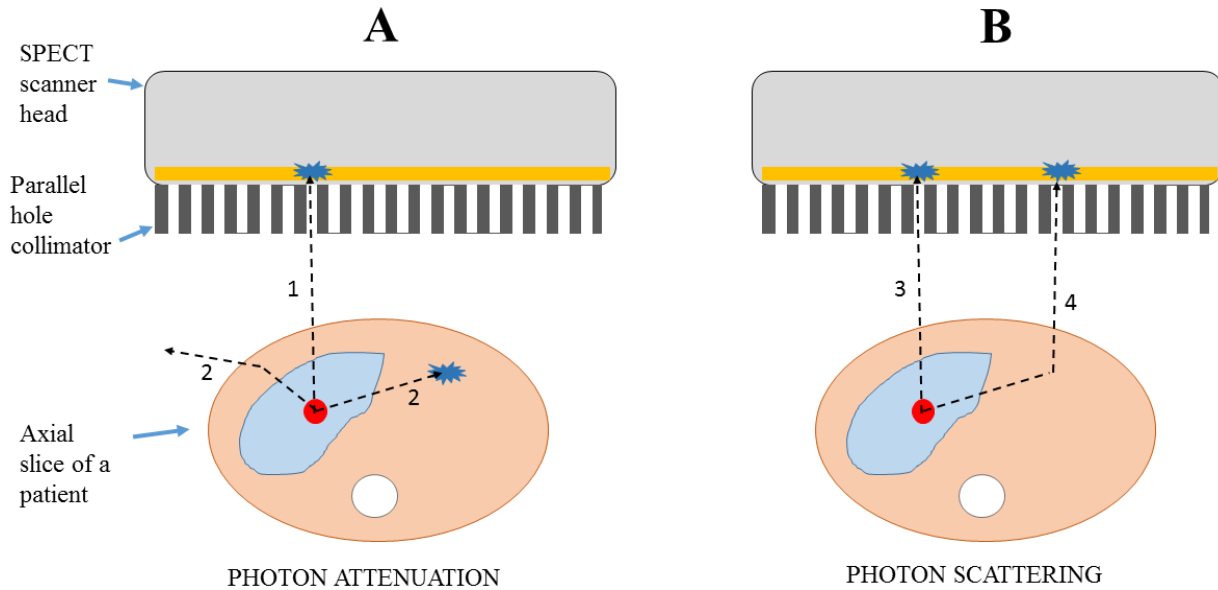


**Figure 1.1 Diagram of photon attenuation (A) and photon scattering (B) in SPECT. The dashed lines represent the photon paths. Photons 1 and 3 are properly collimated and detected by the SPECT crystal. Photons labelled as 2 are considered “attenuated” because these can no longer be detected. Photon 4 is scattered within the patient and subsequently detected, providing wrong information about the source location.**

Since image-based dosimetry calculations require the knowledge of the activity distribution in structures such as organs and tumors (Section 1.3), a compensation for CDR should be included in the reconstruction algorithm to optimize quantification accuracy of SPECT imaging and subsequent image-based dosimetry calculations.

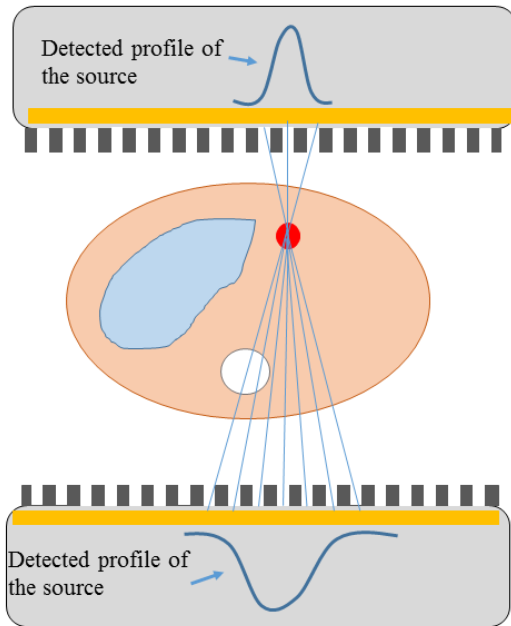


**Figure 1.2 Collimator-detector response (CDR) of a small radioactive source at two different distances. The detected source profile at a close distance shows a narrower distribution than the profile at far distance.**

### **1.2.2 The Image Reconstruction Algorithm**

In order to obtain a 3-D image representing the activity distribution within the patient's body using SPECT, a series of projection images are acquired at different angular views. These measured projections are processed following an analytical or iterative algorithm (i.e., image reconstruction) to obtain the 3-D image. Details of image reconstruction methods can be found elsewhere [21,22].

The standard reconstruction algorithm used for quantitative SPECT is the iterative ordered-subset maximum likelihood expectation maximization (OSEM) algorithm [23], which is an accelerated version of the maximum likelihood expectation maximization method (MLEM) [24]. The main principle of the MLEM algorithm is to determine the 3-D activity distribution that is most likely to produce the measured projections. This iterative method is derived from Poisson statistics and offers the possibility to model the physical characteristic of the acquisition process

in the reconstruction and therefore to compensate for the image-degrading effects listed in Section 1.2.1.

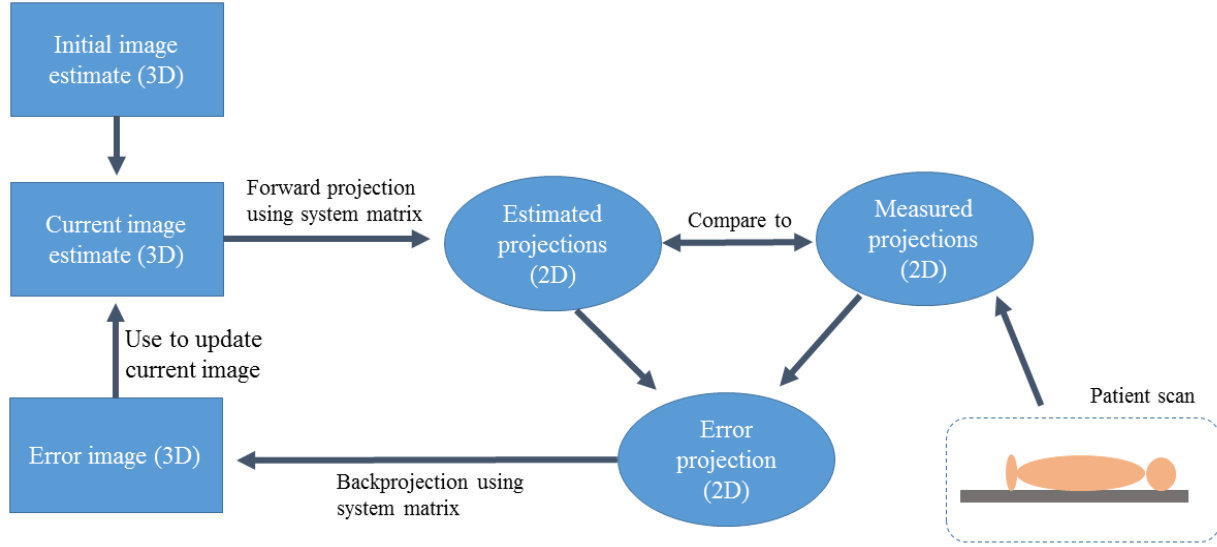


**Figure 1.3** Flow diagram of the MLEM iterative image reconstruction algorithm. The algorithm starts with an initial image estimate that is forward projected to obtain estimated projections. The projections are compared to the measured projections and a projection error is computed. The projection error is backprojected to create an error image that is used to update the initial image estimate. The procedure is repeated until convergence is reached.

Figure 1.3 shows a diagram of the general structure of the MLEM iterative reconstruction algorithm. The new estimate of the 3-D image ( $X_j^{new}$ ) is obtained from the old image estimate ( $X_j^{old}$ ) using the following iterative equation:

$$X_j^{new} = \frac{X_j^{old}}{\sum_{i=1}^N C_{ij}} \sum_{i=1}^N C_{ij} \frac{g_i}{\sum_{k=1}^M C_{ik} X_k^{old}}, \quad (1.1)$$

where  $g_i$  represents the measured projection pixel  $i$  and  $N$  represents the total number of projection pixels. The quantity  $C_{ij}$  corresponds to the element  $ij$  of the system matrix. The system matrix represents the probability that photon which is emitted from the image voxel  $j$ , is

detected in the projection pixel  $i$ . The quantity  $M$  corresponds to the total number of voxels in the image  $X_k^{old}$ .

The behavior of the MLEM equation is described as follows:

- a) an initial estimate of the 3-D activity distribution is generated. The initial estimate can be as simple as a uniform image;
- b) the current estimate ( $X_j^{old}$ ) of the 3-D image is forward projected to generate a set of projection estimates  $\sum_{k=1}^M C_{ik} X_k^{old}$ ;
- c) the ratio between each measured projection  $g_i$  and each estimated projection  $\sum_{k=1}^M C_{ik} X_k^{old}$  is calculated. These ratios represent the projection error estimates;
- d) the generated projection error estimates are backprojected into the image space to create an error image ( $\sum_{i=1}^N C_{ij} \frac{g_i}{\sum_{k=1}^M C_{ik} X_k^{old}}$ );
- e) the error image is normalized and multiplied by the old image estimate to obtain a new image estimate  $X_j^{new}$ ;
- f) the process starts again with the new image estimate and repeats (steps b to e) until a stopping condition is met (e.g., the total number of iterations is reached).

The OSEM method accelerates the reconstruction by taking only a subset of the total acquired projections to update the image estimate. For example, if the patient's scan was acquired using a total of 24 projections and the image is reconstructed using OSEM with 4 subsets and 1 iteration, then the image would be estimated using the following subsets of projections at each sub-iteration: {1,5,9,13,17,21} for sub-iteration 1; {2,6,10,14,18,22} for sub-iteration 2; {3,7,11,15,19,23} for sub-iteration 3; and {4,8,12,16,20,24} for sub-iteration 4. In this example, the OSEM would update the image four times in one iteration.

### 1.2.3 Attenuation and Scatter Corrections

Several clinically available reconstruction algorithms include CT-based attenuation corrections and window-based scatter corrections. The CT-based attenuation makes use of a linear-attenuation coefficient map that is derived from a low-dose CT image of the patient's body. The attenuation map is implemented into the system matrix during the forward/back-projection steps (Section 1.2.2) of the reconstruction algorithm to model the effects of attenuation in the projection estimates.

Currently, there are multiple methods available in the clinical SPECT reconstruction software to correct for scatter. One approach is to use energy window-based methods such as the dual-energy window [25] or the triple-energy window (TEW) [26] methods. In the TEW method, the counts measured in two scatter windows set up around the photopeak window are used to estimate the spatial distribution of scattered photons at each measured projection. The projection images of the estimated scattered photons are subsequently included as an additional term in the denominator of the OSEM reconstruction algorithm (at the forward projection step) of Equation 1.1. Although the TEW method only approximates the spatial distribution of scatter [27], its simplicity, fast implementation and relatively good quantification accuracy [28,29] makes it attractive for clinical use. Alternatively, scatter can be estimated using analytical methods [30,31] or by means of Monte-Carlo simulations of the projection images of scattered photons to be implemented during the forward projection step of the reconstruction process [32]. Monte-Carlo or analytical methods yield better accuracy of scatter estimates than window-based methods but significantly increase the computation time, making them rather impractical for clinical use. Nevertheless, the introduction of fast Monte-Carlo techniques [33], parallel

computing and/or GPU-computing [34,35] might allow to bring these computationally expensive methods into routine clinical practice.

#### 1.2.4 Collimator-Detector-Response Compensation

The compensation for the loss of resolution due to CDR response is often performed by modelling the distance-dependent spatial resolution into the system matrix of the iterative reconstruction [36,37]. In this method, the spatial blurring of the collimator is modelled by a distance-dependent Gaussian function. The standard deviation of such function ( $\sigma_{sys}(d)$ ), which represents the system resolution at distance  $d$ , can be determined using the following expression:

$$\sigma_{sys}(d) = \sqrt{\sigma_i^2 + \sigma_{coll}^2(d)}, \quad (1.2)$$

where  $\sigma_i$  represents the intrinsic detector resolution and  $\sigma_{coll}(d)$  represents the distance-dependent collimator resolution. The main problem of implementing CDR response into the system matrix of the OSEM algorithm is that it substantially increases the computation time. Additionally, the CDR-compensation method described in Equation 1.2 does not include modelling of the septal penetration or septal scatter which can be substantial for isotopes emitting medium or high-energy photons such as  $^{111}\text{In}$ ,  $^{131}\text{I}$  or  $^{67}\text{Ga}$  [19].

#### 1.2.5 Detector Dead-time Correction

In nuclear medicine, traditional diagnostic scans do not have to consider detector dead-time because the amounts of injected activities are low. However, nuclear medicine images of patients who underwent radionuclide therapies often suffer from detector dead-time due to very high administered activities, which result in very high flux of photons striking the detector. If the images of patients acquired after therapy are intended for dosimetry calculations, the photon

losses due to camera dead-time must be accounted for to guarantee accurate determination of activity distribution.

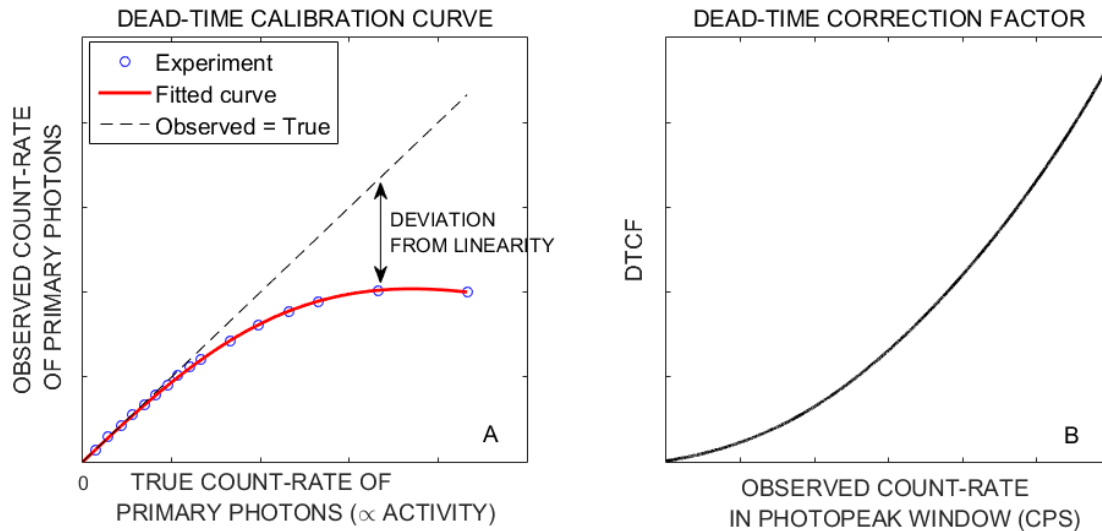


**Figure 1.4 Illustration of dead-time calibration curve (A) and dead-time correction factor tabulated curve (B).**

Since quantitative SPECT images are created using primary photons only (i.e., collimated photopeak photons that did not scatter within the patient or the camera), the dead-time correction factors (DTCFs) must represent the dead-time losses of these photons only. There are two main methods to determine DTCFs. In the first approach, the DTCFs can be determined from experimental phantom calibration curves. Essentially, these curves represent the measured (referred to as observed) count-rate of primary photons as a function of increasing activity in the phantom. The shape of the curve should be a straight line. However, it deviates from linearity for high-activities (i.e., high observed count-rates) where the detector experiences dead-time (Figure 1.4 A). The deviation of the observed primary-photon count-rate from linearity is used to estimate the DTCF which can be tabulated against the observed photopeak count-rate (Figure 1.4 B) [38] or the total detected count-rate in the entire energy spectra. The main drawback of this

method is that the DTCTF obtained from these calibration curves might be inaccurate in cases where the scattering conditions in the patient are too different from the conditions in calibration scans. In the second approach, a marker (point-source) of well-known activity is placed within the scanner FOV and its primary photon count-rate is measured with and without the patient. The DTCTF is determined from the ratio of counts in a small region of interest (ROI) drawn around the marker from the patient + marker scan (where dead-time is present) and the marker alone [39].

### 1.2.6 System Calibration

The system calibration factor, which converts the counts in the reconstructed image into the units of activity (or activity concentration), can be determined by acquiring a planar image of a point-source of the isotope of interest with well-known activity. During the acquisition, the energy window settings must be identical to those selected during the typical SPECT scans. The system calibration factor can be determined with the following equation:

$$k = \frac{C}{t \times A} \quad (1.3)$$

where  $C$  represents the counts in the photopeak window,  $t$  represents the acquisition time of the planar scan and  $A$  represents the activity of the isotope. The point-source method relies on the assumption that scatter and attenuation within the point-source are minimal, so the measured counts in the photopeak window represent primary photons only. If the isotope's emissions include high-energy photons (above the measured photopeak), the previous assumption may not hold true due to the presence of down-scattered high-energy photons in the photopeak window. In such case, the TEW method can be applied to remove the counts due to down-scattered photons in the photopeak window. The point-source calibration method is expected to yield

accurate estimates of the reconstructed activity if all the image-degrading factors are properly compensated for during the reconstruction.

Alternatively, the calibration factor can be determined from a tomographic acquisition of a large phantom that models the conditions of a typical patient scan. This method is recommended in cases where the reconstruction algorithm is not fully quantitative. In such case, the system calibration factor ( $cps \rightarrow MBq$ ) is derived from an image that suffers from the same quantification inaccuracies as the patient images.

### 1.3 Fundamentals of Image-Based Dosimetry in Nuclear Medicine

#### 1.3.1 The Absorbed Dose Equation for Radionuclide Therapies

In radionuclide therapies, the radiation dose absorbed by a given target tissue can be determined using quantitative post-treatment SPECT imaging. The equation that governs 3D image-based internal dosimetry is described in the Committee on Medical Internal Radiation Dose (MIRD) pamphlets [8,40,41]:

$$D(r_T, T_D) = \sum_{r_S} \tilde{A}(r_S, T_D) S(r_T \leftarrow r_S). \quad (1.4)$$

The quantity  $D(r_T, T_D)$  represents the mean radiation absorbed dose (i.e., energy deposited per unit mass) to a target tissue  $r_T$  over a dose-integration period  $T_D$ , in the presence of activity distributed uniformly within a source tissue  $r_S$ . The quantity  $\tilde{A}(r_S, T_D)$  represents the time-integrated activity (total number of nuclear decays) in the source  $r_S$  over the time period  $T_D$  and  $S(r_T \leftarrow r_S)$  is the absorbed dose in  $r_T$  per nuclear decay in  $r_S$  (also known as S-value). The following sections describe the fundamentals of time-integrated activity determination and the calculations of S-values.

### 1.3.2 Determination of the Time-Integrated Activity

The time-integrated activity  $\tilde{A}(r_S, T_D)$  is defined as the total number of decays in a given source region  $r_S$  over a period of time  $T_D$ . Therefore, calculating  $\tilde{A}(r_S, T_D)$  requires the accurate knowledge of the source's activity as a function of time, between the time interval  $[0, T_D]$ , where  $T_D$  is usually infinity. In practice, this is achieved by:

- obtaining a series of NM images (planar or SPECT) of the activity distribution at different time points;
- delineating the source region of interest (image segmentation) at each time point;
- calculating the activity within the segmented source region at each time point to create the so-called time-activity curve and;
- integrating the time-activity curve (i.e., calculating the area under the curve). The time-integration can be performed numerically or, in some cases, it might be calculated analytically if the measured activity values are fit to a function. The choice of the fitting function depends on the temporal distribution and the number of sampling activity points. Additionally, it depends on the details of the pharmacokinetic modeling that describes the uptake-washout of activity in the source region [42].

The general procedure described above clearly illustrates the need for accurate quantitative imaging in order to obtain an accurate estimate of the time-integrated activity, and therefore, absorbed dose (Equation 1.4). There are three possible imaging protocols that can be used to determine the time-activity curve for each source region: the conjugate view (planar) method, the hybrid planar/SPECT method and the purely SPECT method.

### 1.3.2.1 The Conjugate View Method

Traditionally, the time-integrated activity was determined by taking a series of conjugate views (anterior-posterior) using planar NM acquisitions in order to measure the activity in source organs after administration of the radiopharmaceutical. The mathematical formulation of the conjugate view method is described in the MIRD pamphlet No. 16 [43]. Based on this method, the source activity  $A_S$  can be estimated using the following equation:

$$A_S = \sqrt{\frac{I_A I_P}{e^{-\mu_e x}} \frac{f_S}{k}}, \quad (1.5)$$

where  $I_A$  and  $I_P$  represent the count-rate in the source region at the anterior and posterior views, respectively. The quantity  $e^{-\mu_e x}$  represents the effective photon transmission factor across the patient thickness  $x$  through the source region. The effective transmission factor may be determined directly by measuring the ratio of the count rates  $I/I_0$ , obtained using a planar scan of a calibrated flood source without ( $I_0$ ) and with the patient in place ( $I$ ). If the flood source does not contain the isotope of interest, a scaling factor is applied to the ratio  $I/I_0$  to account for the differences in photon attenuation between the flood source and the isotope of interest. The factor  $k$  represents the camera calibration factor (Equation 6.2) and  $f_S$  is a factor used to correct for photon attenuation within the source region. Equation 6.2 assumes that the source organ is embedded within tissue containing no radioactivity. Further improvements can be made to equation 6.2 to account for more complex situations in which one or more source organs overlap with each-other or when source organs are in the presence of background activity [43].

Figure 1.5 shows the planar images (anterior view) at three time points (3 hours, 24 hours and 48 hours post administration) of a patient that received an injection of  $^{188}\text{Re}$  – Lipiodol, a radiopharmaceutical used for treatment of liver cancer [44]. Details about time-integrated

activity curve (TIAC) calculations, organ segmentation and curve fitting for this and other patients receiving  $^{188}\text{Re}$  – Lipiodol therapy are described in Chapter 6.

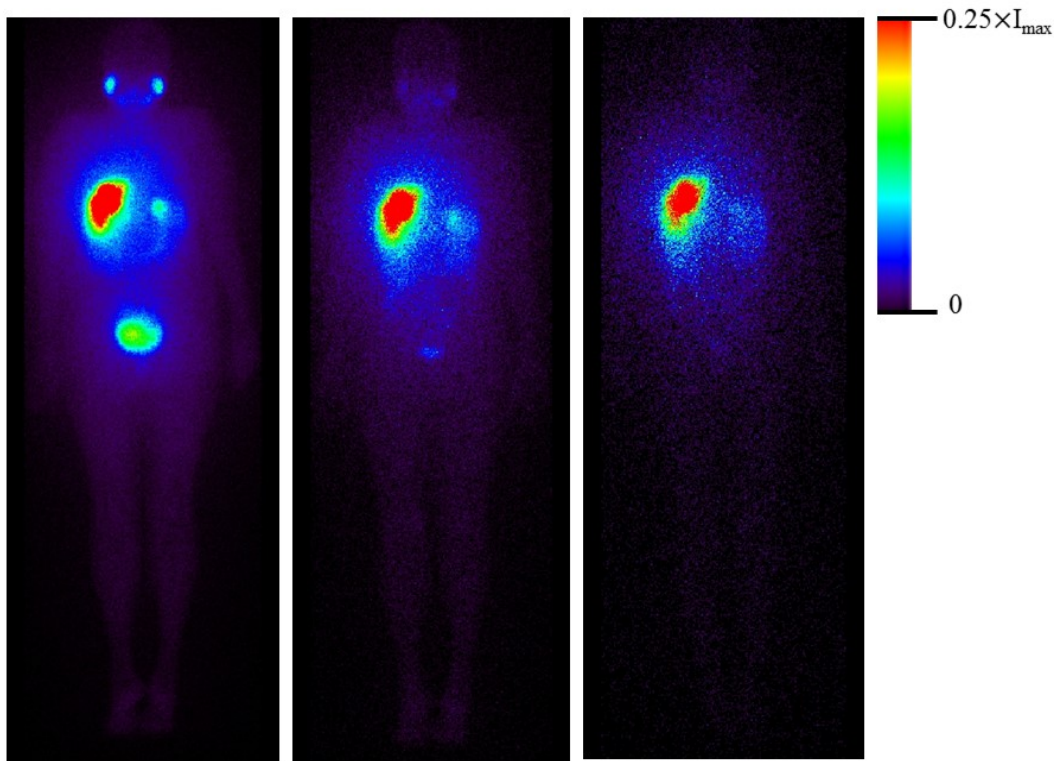


**Figure 1.5** Whole body planar images (anterior view) of a patient that received an intra-hepatic injection of 1.9 GBq of  $^{188}\text{Re}$ -Lipiodol for the treatment of liver cancer. The images were acquired 3 hours, 24 hours and 48 hours post-administration of  $^{188}\text{Re}$ -Lipiodol.  $I_{\max}$  represents the maximum pixel intensity of each planar image.

In general, the main limitations of the conjugate view method are its inability to perform proper quantification, to resolve the source depth and its lack of reliability to estimate the activity in overlapping tissues. Therefore, a hybrid planar/SPECT or purely SPECT approach is recommended for image-based dosimetry calculations [8]. The conjugate-view method has one more limitation. Due to the lack of 3-D spatial information of activity distribution of planar

images, the conjugate method only allows to estimate the TIACs at the organ level as opposed to SPECT-based methods. Therefore, dose calculations based on the conjugate view method are limited to mean dose absorbed to target organs. There is mounting evidence that the mean absorbed dose over the target organ is not necessarily a predictor of deterministic effects such as tumor control or normal-organ toxicity [45].

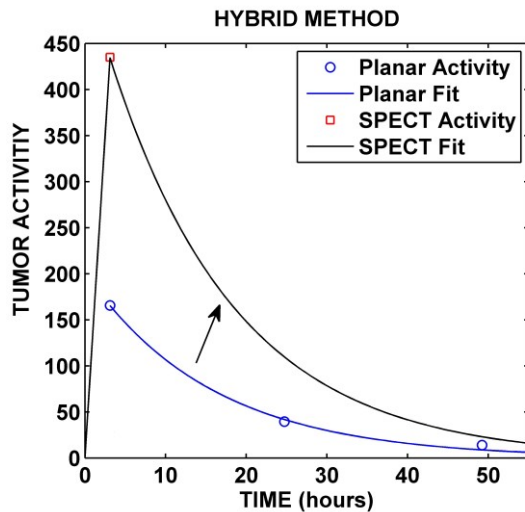


**Figure 1.6** Example of tumor time activity curve (from the patient data of Figure 1.5) determined with the hybrid planar/SPECT method. The activity measurements were fit to a mono-exponential function from  $t = 3$  hours (time of first scan) to infinity. The activity between 0 h and  $t = 3$  h was assumed to grow linearly.

### 1.3.2.2 The Hybrid Planar/SPECT Method and the Purely SPECT Method

The hybrid method requires a series of planar images (conjugate views) of the patient's activity distribution and at least one SPECT scan. The planar acquisitions are used to determine the functional form (i.e., the shape) of the time-activity curve for each source region. Subsequently, each source's absolute activity is determined from the quantitative SPECT image of the patient and the time-activity curve is re-normalized so that the time-activity curve passes through the SPECT based activity measurement. Figure 1.6 shows the time-activity curve determined with the hybrid method for the same patient shown in Figure 1.5.

Finally, the time-activity curve of each source region can be accurately determined by acquiring a series of quantitative SPECT scans. This technique is known as the volumetric or purely SPECT method.

Both the hybrid and the purely SPECT methods are expected to yield better accuracy of TIACs and therefore, dose absorbed by target organs [46] if the SPECT image reconstruction is quantitative, as discussed in Section 1.2. Additionally, thanks to the 3D spatial information of activity distribution provided by SPECT, the hybrid and volumetric methods offer the possibility to calculate TIAC at organ, sub-organ or voxel level. However, voxel-level dosimetry requires exact co-registration of SPECT images from different time points to generate accurate voxel time-activity curves. The option to perform voxel-level dosimetry allows us to generate dose-volume histograms (DVH) and calculate other dosimetric parameters such as maximum, minimum and median dose for a given region of interest. These dosimetric parameters have been shown to be better predictors than average organ dose for deterministic effects such as tumor control, normal-organ toxicity and patient survival [8,38].

### **1.3.3 Determination of S-Value**

The second step in internal dosimetry calculation is to combine the TIAC ( $\tilde{A}(r_S, T_D)$ ) in the source region with the S-Value  $S(r_T \leftarrow r_S)$  to determine the absorbed dose to a given target region. The S-Value represents the fraction of absorbed dose in the target region per one decay of the isotope present in the source region. Therefore, determination of the S-factor requires the knowledge of the physics of the isotope's decay (energy, abundance and type of particles emitted) and the information about the specific anatomy of the source and target. There are different methods to determine the S-Value depending on the type of dosimetry calculations to

be performed (organ, sub-organ or voxel level). The following paragraphs summarize these methods.

For organ dosimetry, isotope-specific S-Values are determined using standard computational phantoms that model the average human anatomy [40,47]. The pre-calculated S-values are available through different commercial or research software packages such as the Organ Level Internal Dose Assessment (OLINDA) [47] and IDAC [48]. The main limitation of pre-calculated S-values based on the “average” human phantom data is that the anatomy of the patient may differ significantly from the “average” phantom.

For sub-organ dosimetry, the voxel S-Value method [49], the point dose kernel (PDK) method and the Monte-Carlo method are available. The voxel S-Value method combines the 3-D activity distribution at the voxel level with pre-calculated lookup tables (i.e., voxel S-Value tables) to determine the corresponding 3-D dose distribution. The look-up tables contain information about the absorbed dose fraction in an array of target voxels due a single source voxel. It is important to note that the look-up tables are isotope-, tissue- and voxel size – specific. As opposed to pre-calculated organ-level S-Values, voxel S-Values allow us to generate high-order dosimetric parameters (DVHs, maximum and minimum dose, etc.) for a region of interest. Furthermore, they generate 3-D dose distributions fast. However, the application of voxel S-Value method is not valid for regions of known tissue density inhomogeneity. For example, the air-tissue interface in the chest region or the bone-tissue interfaces near skeletal regions. In these cases, the use of voxel-S method may lead to large errors in estimated doses [50]. Figure 1.7 shows the profile of the absorbed dose rate per unit activity (mGy/MBq/s) as a function of distance in a voxelized soft-tissue phantom (i.e., voxel S-Values) for  $^{188}\text{Re}$ ,  $^{131}\text{I}$ ,  $^{177}\text{Lu}$  and  $^{90}\text{Y}$  [51].

The PDK method is similar to the voxel-S value method with the only difference that in the PDK method the source activity is defined as a point-source at the center of the voxel whereas the voxel-S method assumes the source activity is distributed uniformly within the voxel.

The most accurate method to determine doses based on quantitative SPECT imaging is the Monte Carlo method. In this method, the reconstructed SPECT images provide information about the activity distribution of the radiopharmaceutical within the patient's body. The Monte Carlo code transports the emitted particles through a computerized version of the patient's anatomy that can be generated from a CT image of the patient. This method allows to perform fully patient-specific dosimetry as it takes into account the true anatomy and source-target region geometries. The main drawback of the Monte Carlo method is its complexity and the computation time. Some examples of Monte Carlo programs used for dosimetry applications are Monte-Carlo N-Particle (MCNP) [52], Geant4 applications for tomographic emission (GATE) [53,54] and the electron-gamma shower code (EGS) [55].

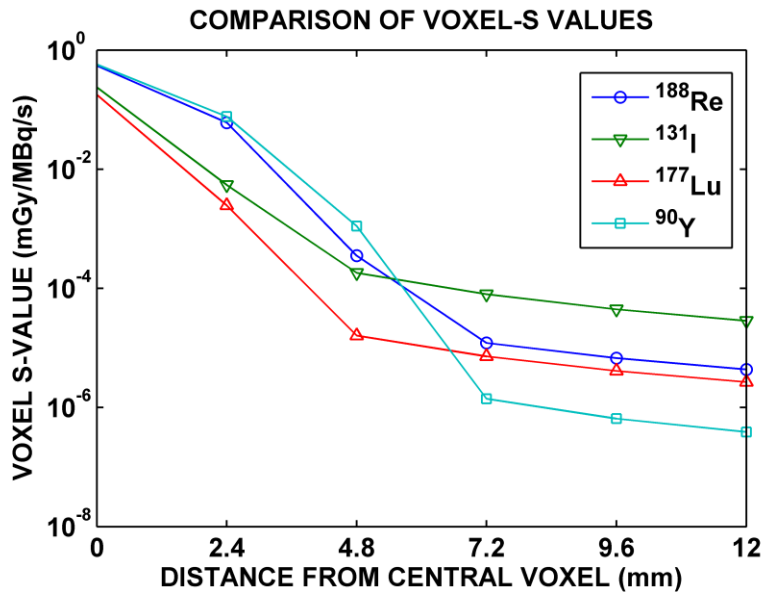


Figure 1.7 Voxel S-Values for isotopes commonly used in radionuclide therapy. The voxel size is 4.8 mm, typical of SPECT reconstructed images.

#### 1.4 Rhenium-188

Table 1.2 presented some of the most common isotopes used for radionuclide therapies. Among these isotopes, there is Rhenium-188 (<sup>188</sup>Re). The interest in the use of <sup>188</sup>Re in radionuclide therapies has grown over the last decades thanks to its favorable physical and chemical characteristics. Firstly, Re<sup>188</sup> decays by emission of high-energy beta particles ( $E_{max} = 2.1$  MeV) which are suitable to deliver high radiation dose to targeted tumor cells. Secondly, the decay of <sup>188</sup>Re is accompanied by emissions of 155-keV photons which can be imaged using SPECT, allowing to perform image-based dosimetry calculations for <sup>188</sup>Re therapies [56,57]. Additionally, the chemistry of <sup>188</sup>Re is similar to that of its *congener* <sup>99m</sup>Tc, making the pair <sup>188</sup>Re-<sup>99m</sup>Tc an ideal candidate for theranostic applications. Lastly, <sup>188</sup>Re can be cost-effectively obtained from a <sup>188</sup>W/<sup>188</sup>Re generator which, due to the parent's half-life of 69 days, has a useful shelf-life of several months [58,59]. For the remainder of this chapter, the main characteristics of

production and decay of  $^{188}\text{Re}$ , as well as its main clinical applications, are described.

Additionally, the challenges of performing quantitative measurements of  $^{188}\text{Re}$  activities in nuclear medicine, which led to the main motivation of this doctoral dissertation, are discussed.

#### 1.4.1 Characteristics of $^{188}\text{Re}$ Decay

Rhenium-188 decays by  $\beta^-$  (half-life,  $T_{1/2} = 17$  h) to  $^{188}\text{Os}$  (Figure 1.8). The  $\beta^-$  decay is the emission  $\beta$ -particles (electrons) with a continuous energy spectrum, accompanied by emissions of electron-antineutrinos which share with electrons the energy and momentum of the decay. For  $^{188}\text{Re}$ , there are two main  $\beta$ -decay branches with maximum  $\beta$ -energies of 2120 keV (70%) and 1965 keV (26.3%) (Figure 1.8). There are additional  $\beta$ -decay branches with lower probabilities (<5%). The net  $\beta$ -emission energy spectrum of  $^{188}\text{Re}$  is shown in Figure 1.9. This energy spectrum represents the number of  $\beta$ -particles emitted per decay of  $^{188}\text{Re}$  as a function of the electron's energy. The average energy of the emitted  $\beta$ -particles from  $^{188}\text{Re}$  is 764 keV.

In addition to  $\beta$ -particles,  $^{188}\text{Re}$  decay is accompanied by emissions of  $\gamma$ -particles, conversion electrons, X-Rays and Auger Electrons (Table 1.3). Gamma-particles are photons emitted from de-excitation of the daughter nucleus  $^{188}\text{Os}$ . The most abundant emission (15.6%), which has the energy of 155 keV, is of great interest for radionuclide therapies because it allows to image  $^{188}\text{Re}$  with SPECT systems and therefore, to perform image-based dosimetry.

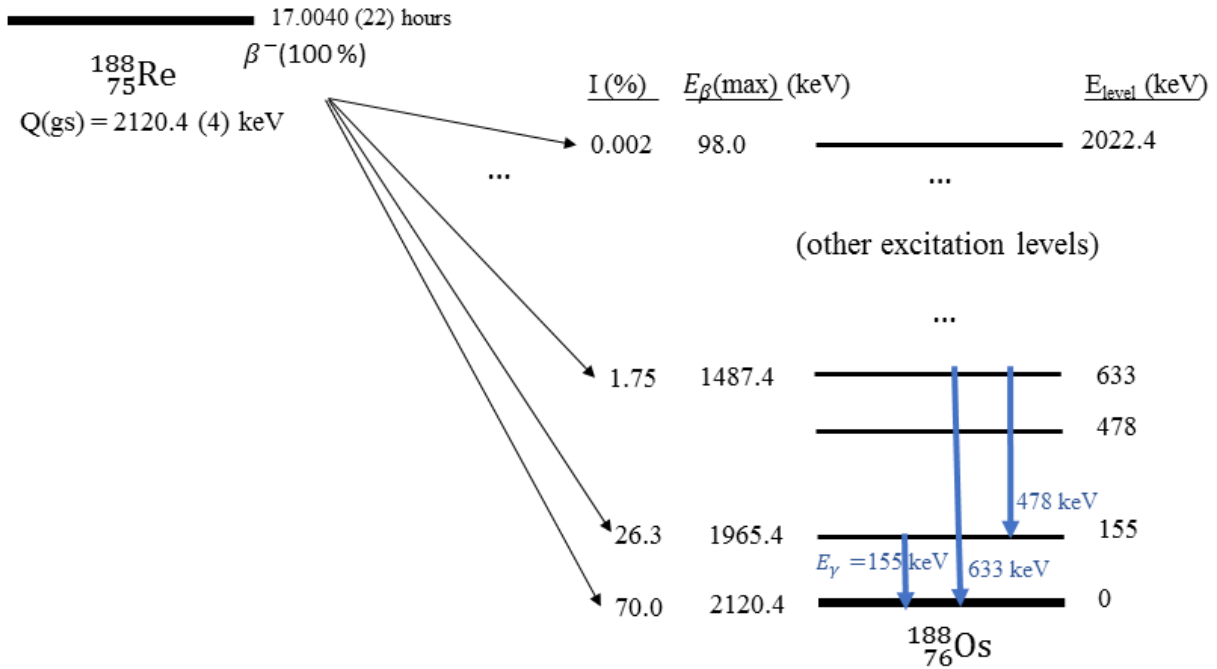
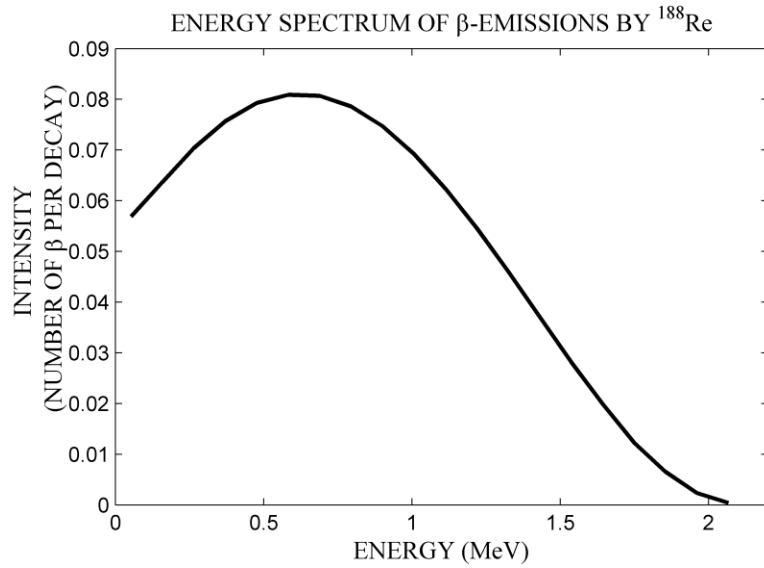


Figure 1.8 Decay scheme of  $^{188}\text{Re}$  [14]. Only the three most intense  $\beta$ -decay branches, and the three most intense  $\gamma$ -emissions (blue arrows) are shown.

The conversion electrons are the result of the internal conversion process. In this process, the de-excitation energy of the daughter nucleus  $^{188}\text{Os}$  is used to eject an atomic electron instead of emitting a  $\gamma$ -particle. The ejected electron leaves a vacancy in the electronic shells that is subsequently filled by another atomic electron from a higher energy level. As a result of this transition, a characteristic X-rays and/or Auger electrons are emitted. As opposed to  $\beta$ -particles, the energy spectra of conversion electrons and Auger electrons are discrete (Table 1.3).



**Figure 1.9** Energy spectrum of  $\beta$ -emissions by  $^{188}\text{Re}$  [60].

**Table 1.3** Energy and yields from most abundant  $^{188}\text{Re}$  emissions [14]

Type	Energy [keV]	Yield [%]
$\beta_1^-$	$E_{\max} = 1965.4$	26.3
$\beta_2^-$	$E_{\max} = 2120.4$	70.0
X-ray ( $k\alpha$ )	61-63	3.8
X-ray ( $k\beta$ )	71-73	1
$\gamma$ -photons	155	15.6
	478	1.1
	633	1.4
	829	0.4
Conversion Electrons	82	5.0
	142	5.9
Auger Electrons	7	7.0

### 1.4.2 Production of $^{188}\text{Re}$ : the $^{188}\text{W}/^{188}\text{Re}$ Generator

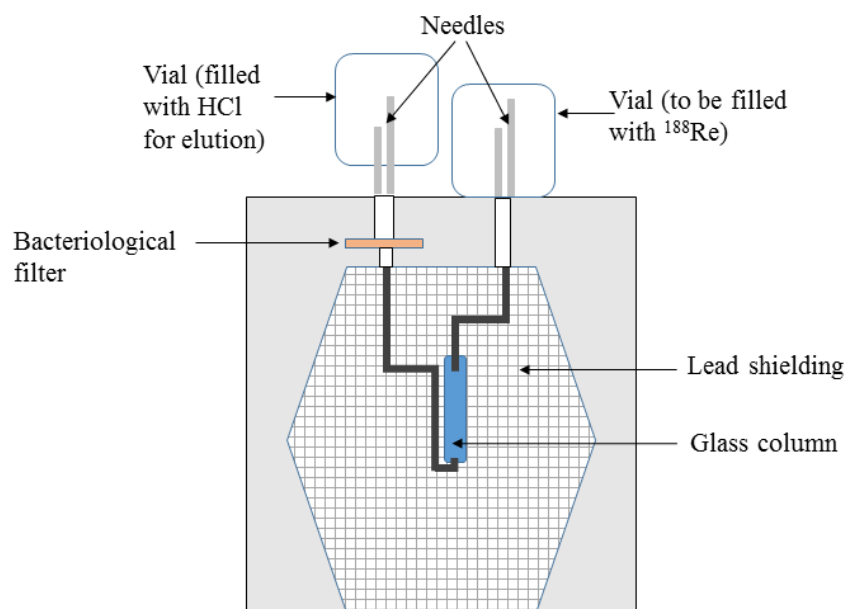


**Figure 1.10** Schematic view of a typical  $^{188}\text{W}/^{188}\text{Re}$  generator.

One of the benefits that  $^{188}\text{Re}$  brings into radionuclide therapies is the availability of Tungsten-188 ( $^{188}\text{W}$ )/ $^{188}\text{Re}$  generators which can supply  $^{188}\text{Re}$  activity on-demand in the nuclear medicine department. A radionuclide generator is essentially an in-house isotope production unit in which a long-lived parent nucleus ( $^{188}\text{W}$ , half-life 69 days) is decaying into a short-lived daughter ( $^{188}\text{Re}$ , half-life 17 hours). Thanks to the difference in half-lives between the parent and the daughter, the daughter isotope can be repeatedly removed from the generator. Figure 1.10 shows a schematic view of a common alumina-based  $^{188}\text{W}/^{188}\text{Re}$  generator. In these generators, the parent nucleus is absorbed on the glass column material while the daughter  $^{188}\text{Re}$  is selectively eluted from the generator with a sterile solution (saline). The end product is high activity concentration of liquid  $^{188}\text{Re}$  solution, with a low  $^{188}\text{W}$  breakthrough.

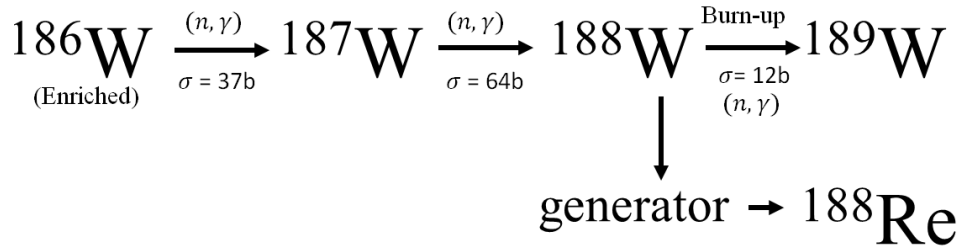


**Figure 1.11 Diagram of  $^{188}\text{W}$  production. The quantity  $\sigma$  represents the reaction cross-section (in barns).**

As  $^{188}\text{Re}$  is obtained mainly through the decay of  $^{188}\text{W}$  in the generator, its availability is directly related to the availability and/or production of  $^{188}\text{W}$ . The parent  $^{188}\text{W}$  is produced by double neutron capture by  $^{186}\text{W}$  in a nuclear reactor, as shown in the reaction diagram of Figure 1.11. The double neutron capture is a very inefficient process because it depends on the product of the two individual neutron-capture cross-sections. Since these cross-sections have relatively low values ( $\sim 10^{-24} \text{ cm}^2$ ), the product of the cross-sections is even smaller and therefore, the  $^{188}\text{W}$  production yield is low. Additionally, a fraction of the produced  $^{188}\text{W}$  is lost due to neutron burn-up (a radiative neutron capture by  $^{188}\text{W}$  that produces  $^{189}\text{W}$  plus the emission of a  $\gamma$ -particle). As a consequence, very high neutron flux reactors are needed to produce  $^{188}\text{W}$  with high-specific activities to be used as a generator [61]. The use of enriched  $^{186}\text{W}$  targets (instead of natural W) to produce  $^{188}\text{W}$  is also important to increase the production yield and to minimize the production of other radioactive isotopes of W. According to the recent report by the International Atomic Energy Agency (IAEA) [62], only the following reactors have capabilities to produce  $^{188}\text{W}$  having adequate specific activities for used in generators: SM Reactor, RIAR, Dmitrovgrad, Russian Federation; ORNL HFIR, USA and BR2 Reactor, Belgium.

### 1.4.3 Applications of $^{188}\text{Re}$ in Nuclear Medicine

Thanks to its favorable physical and chemical characteristics,  $^{188}\text{Re}$  is an isotope with a wide range of applications in nuclear medicine therapies. The most common therapies using

$^{188}\text{Re}$  focus on the treatment of liver cancer with intra-hepatic radioembolization [63] and the palliation of bone pain in patients suffering from prostate cancer using  $^{188}\text{Re}$ -1,1-hydroxyethylidenediphosphonate ( $^{188}\text{Re}$ -HEDP) [64,65]. Additionally, other less common applications of  $^{188}\text{Re}$  include the treatment of rheumatoid arthritis with  $^{188}\text{Re}$ -colloids [66],  $^{188}\text{Re}$ -labelled monoclonal antibodies for radioimmunotherapy [67] and the use of liquid  $^{188}\text{Re}$  in endovascular brachytherapy for the treatment of in-stent stenosis [68,69]. The major findings from  $^{188}\text{Re}$  clinical studies on radioembolization therapies and  $^{188}\text{Re}$ -HEDP bone pain palliation are summarized in the following paragraphs.

Radioembolization is a clinical procedure that combines embolization and internal radiation therapy to treat liver cancer. This procedure exploits the fact that tumors in the liver receive most of their blood supply from the hepatic artery, whereas normal liver tissue receives most of its blood supply from the portal vein. During radioembolization,  $^{188}\text{Re}$ -labeled particles such as Lipiodol [63], Human-Serum Albumin (HSA) [70,71] or polymer-based microspheres [9] are administered through the hepatic artery, lodge in hepatic end-arterioles and deliver radiation to the surrounding tumor cells. There are multiple papers reporting the efficacy of  $^{188}\text{Re}$  radioembolization. In a large study (185 patients) supported by the IAEA which used  $^{188}\text{Re}$ -Lipiodol [44,72,73], 25% of the treated patients showed partial response (defined as at least 50% reduction in tumor size). Similarly, a small study (10 patients) reported partial response in 20% of the patients treated with  $^{188}\text{Re}$ -HSA radioembolization [70].

$^{188}\text{Re}$ -HEDP is an effective radiopharmaceutical for the palliative treatment of bone metastases. Lange *et al.* [65] reported an overall 69% pain response in patients receiving this therapy, a similar response to that of external beam radiotherapy. Similar findings were reported

by Chen et al [64], where most of the patients experienced an improvement in the quality of life without induction of serious bone marrow reduction.

In addition to all the clinical applications, a substantial amount of research is currently performed at the pre-clinical level mostly directed at development and labeling pharmaceuticals with  $^{188}\text{Re}$ . Most of this work is focused on pre-clinical studies for liver cancer therapies. In a recent publication, Verger et al. [74] introduced starch-based micro-particles that can be labeled with both  $^{68}\text{Ga}$  and  $^{188}\text{Re}$  for applications in radioembolization. Similarly, Häfeli et al. [75] developed polymer-based microspheres that can be loaded with  $^{99\text{m}}\text{Tc}$  or  $^{188}\text{Re}$  [9]. Both  $^{68}\text{Ga}$ - $^{188}\text{Re}$  and  $^{99\text{m}}\text{Tc}$ - $^{188}\text{Re}$  microspheres are promising agents for new generation of liver radioembolization. In parallel with clinical studies, pre-clinical research of  $^{188}\text{Re}$  tracers also includes Radioimmunotherapy studies [76] and bone palliation studies [77].

### **1.5 Statement of the Problem, Aim and Thesis Outline**

Optimization of  $^{188}\text{Re}$  therapies requires the accurate knowledge of the administered activity and the activity distribution within the patient's body. Unfortunately, the decay of  $^{188}\text{Re}$  is very complex, resulting in a large variety of emissions such as  $\beta$ -particles,  $\gamma$ -particles, or X-rays from which only the 155 keV photons are useful for imaging and measurements of activity. In addition, the interaction of  $\beta$ -particles with the surrounding tissue produces Bremsstrahlung (BRS) radiation which introduces further undesired emissions. In such scenario, isolating the 155 keV signal from the rest of emissions to perform quantitative measurements of  $^{188}\text{Re}$  becomes a very challenging task.

Addressing this challenge involves understanding the physics of  $^{188}\text{Re}$  emissions and its interactions with a variety of nuclear medicine equipment. First, to ensure that patients receive the appropriate prescribed treatment dose, the  $^{188}\text{Re}$  activity must be accurately measured using

dose calibrators (DC). The problem with dose calibrators is that the DC reading might be highly sensitive to the sample's geometry, especially for  $\beta$ -emitting isotopes [78]. Many authors recommend to determine the correct dose-calibrator dial settings experimentally, for each isotope and geometry used routinely in the department [79]. However, the recommended methods require the use of equipment that is not readily available in the nuclear medicine department. Since the amount of activity eluted from the  $^{188}\text{W}/^{188}\text{Re}$  generator may be different each time, it is crucial to verify that dose-calibrator readings for  $^{188}\text{Re}$  are accurate as patient injected dose solely depends on this single measurement.

Second, the characteristics of  $^{188}\text{Re}$  emissions, and in particular, the production of Bremsstrahlung by  $^{188}\text{Re}$ , must be investigated to understand their influence on the activity measurements with SPECT.

Third, the introduction of new  $^{188}\text{Re}$ -labeled pharmaceuticals and therapies into clinical practice relies on pre-clinical studies that often use small animal SPECT systems. The aim of such studies is to determine the radiotracers' pharmacokinetics, targeting ability and potential toxicity in different organs. To accurately quantify tracer uptake, these imaging systems are required to provide users with high resolution, quantitative and statistically robust images. To this date, the performance of pre-clinical quantitative  $^{188}\text{Re}$  SPECT has not been evaluated. This task is essential to guarantee that the outcome from these pre-clinical studies is reliable.

Lastly, in order to assess the effectiveness of  $^{188}\text{Re}$  therapies, the knowledge of the radiation dose delivered to targets and organs at risk is required. Such knowledge can be used, for instant, to determine the maximum dose that is tolerated by organs at risk, or to estimate the minimum dose required to control the tumor. As described in Section 1.3, dosimetry can be performed using quantitative  $^{188}\text{Re}$  SPECT images. The accuracy of quantitative  $^{188}\text{Re}$  images

will be influenced by the choice of the collimator, the image acquisition parameters and the accuracy of the corrections for image-degrading factors implemented in the reconstruction algorithm (Section 1.2). Several studies extensively investigated quantitative capabilities of SPECT for imaging radionuclide therapy isotopes such as  $^{131}\text{I}$  [42],  $^{177}\text{Lu}$  [80] and  $^{90}\text{Y}$  [10]. At this time, however, no systematic studies of quantitative  $^{188}\text{Re}$  SPECT have been reported.

### **1.5.1 Aim of the Thesis**

The aim of this thesis was to establish a practical method for quantitative measurements of  $^{188}\text{Re}$  activity distribution in patient studies. To address this goal, four objectives, which focused on each of the challenges described above, were proposed:

- 1) To develop a practical method to determine (or verify) DC settings that ensures accurate measurements of patient's injected activities.
- 2) To investigate the characteristics of  $\gamma$ -emissions and Bremsstrahlung production in tissue by  $^{188}\text{Re}$  and understand their influence on quantitative SPECT imaging.
- 3) To evaluate the  $^{188}\text{Re}$  image performance of a state-of-the-art pre-clinical SPECT/CT multi-pinhole system.
- 4) To investigate the quantification accuracy of  $^{188}\text{Re}$  SPECT imaging for clinically relevant situations and reconstruction methods. In addition, to determine the accuracy of image-based dosimetry calculations for  $^{188}\text{Re}$  therapies.

Additionally, the quantitative method developed in this thesis was applied to perform patient-specific dosimetry of patients undergoing  $^{188}\text{Re}$ -Lipiodol trans-arterial radioembolization therapy.

## 1.5.2 Thesis Outline

This thesis is structured as follows. In Chapter 1, the topics related to quantitative SPECT imaging and dosimetry calculations for radionuclide therapies are described. These topics serve as a background foundation to introduce the isotope  $^{188}\text{Re}$  and its main applications in nuclear medicine. The chapter ends summarizing the challenges related to quantitative measurements of  $^{188}\text{Re}$  in nuclear medicine, which leads to the four thesis subprojects.

In Chapter 2, a practical method to determine the DC settings using a thyroid-probe is described. The accuracy and uncertainty analysis of this method is evaluated and reported. The method was applied to determine  $^{188}\text{Re}$  dial settings for two commercial dose calibrators.

Chapter 3 summarizes the results of a simulation study that investigates the characteristics of  $^{188}\text{Re}$  emissions, with special emphasis on Bremsstrahlung production in tissue.

In Chapter 4, the methods and results from a series of phantom experiments aimed to evaluate the performance of VECtor/CT (a state-of-the-art pre-clinical multi-pinhole SPECT/CT system) for  $^{188}\text{Re}$  are reported. The image performance was evaluated in terms of the spatial resolution, the contrast, the contrast-to-noise ratio and the accuracy of activity quantification. In parallel, a series Monte-Carlo simulations of this pre-clinical system were performed to understand the challenges of multi-pinhole imaging of  $^{188}\text{Re}$ . The results of these simulations are also presented in this chapter.

Chapter 5 focuses on  $^{188}\text{Re}$  imaging using clinical SPECT camera. The accuracy of standard clinical reconstruction methods applied to  $^{188}\text{Re}$  is investigated by performing a series of phantom experiments. The phantom experiments were combined with Monte-Carlo simulations of a clinical SPECT system to investigate the limitations of the TEW scatter

compensation method. Based on the most quantitative  $^{188}\text{Re}$  images obtained using clinical reconstruction protocols, the accuracy of dosimetry calculations was investigated.

In Chapter 6, the methods and findings described in Chapter 2, 3 and 5 are applied to perform patient-specific dosimetry for patients receiving  $^{188}\text{Re}$ -Lipiodol radioembolization. The average tumor and organs at risk doses were calculated for a total of 4 patients. Additionally, the pharmacokinetics of  $^{188}\text{Re}$ -Lipiodol in tumor and healthy tissue is determined and compared to other published studies. The patients in this study were treated at Kovai Medical Centre Hospital (KMCH) (Coimbatore, India). The project is a collaboration between the Medical Imaging Research Group (Vancouver, Canada) and Nuclear Medicine department at KMCH, led by Dr. Ajit Shinto.

Finally, Chapter 7 summarizes the main conclusions of this thesis and discuss possible lines of future work that could help to improve the quality of  $^{188}\text{Re}$  therapies.

The structure of Chapters 2 to 6 follows the traditional journal article scheme with self-contained introduction, methods, results, discussion and conclusions.

## **Chapter 2: Accuracy and Uncertainty Analysis of a Thyroid-Probe Based Method to Determine Dose-Calibrator Settings**

### **2.1 Introduction**

In nuclear medicine departments, the activity of radiotracers is measured using dose calibrators (DC). A dose calibrator (also known as re-entrant ionization chamber) consists of a pressurized gas detector which measures the ionization current generated by radiation (emitted by the radiotracer) crossing its sensitive volume. The intensity of the generated current is proportional to the total energy deposited by radiation in the gas chamber. In order to obtain an activity reading, the current is converted into units of activity by applying an appropriate calibration factor (also referred to as DC dial-setting). Dial-settings must be specified for each isotope and source geometry and are applied or varied with either a dial or a numeric keypad placed on the DC. Instrument manufacturers supply DC dial-settings for most isotopes commonly used in nuclear medicine measured in standard source geometries.

However, DC readings for some isotopes, especially those which emit  $\beta$ -particles and/or low energy photons may be highly sensitive to source geometry [78,81–83]. Since  $\beta$ -emitting isotopes are gaining importance in Nuclear Medicine for radionuclide therapies (for example  $^{188}\text{Re}$ ,  $^{90}\text{Y}$  or  $^{177}\text{Lu}$ ), having the correct dial settings to determine activity is critical for ensuring that patients receive their prescribed treatments and are not underdosed or overdosed. Based on multiple studies investigating the geometry dependence of the dose calibrator response to  $\beta$ -emitting isotopes [78,84–87], it has been recommended to empirically determine dose calibrator settings for less common isotopes and non-standard geometries that may be used in clinical procedures [79].

Methods to experimentally determine or verify dose-calibrator settings require independent measurements (or prior knowledge) of the activity of a sample of the isotope of interest. There are two main approaches to measure sample activity: liquid scintillation counting and  $\gamma$ -ray spectroscopy techniques. The former method was applied to determine DC settings to a variety of standard and non-standard isotopes used in nuclear medicine including  $^{117m}\text{Sn}$  [88],  $^{188}\text{Re}$  [89],  $^{62}\text{Cu}$  [90], and  $^{223}\text{Ra}$  [91]. On the other hand, using the  $\gamma$ -ray spectroscopy approach, Cannata *et al.* [92] determined  $^{99m}\text{Tc}$  DC settings with a  $4\pi\gamma$ -sodium iodide (NaI) detector. Similarly, Marengo *et al.* [93] and Beattie *et al.* [94] used High Purity Germanium detectors (HPGe) to calibrate their DC for  $^{188}\text{Re}$  and two  $\beta^+$ -emitting isotopes ( $^{89}\text{Zr}$  and  $^{124}\text{I}$ ). These methods, however, require the use of sophisticated equipment that is not easily accessible in average nuclear medicine departments.

A practical approach to determine DC settings is to make use of the equipment that is already available in the NM departments. Gamma camera, well-counter and thyroid-probe are such widely available NM instruments capable to perform  $\gamma$ -ray spectroscopy measurements. Our decision to use the thyroid-probe (TP) was justified by the following reasons: TP has relatively high counting sensitivity, its configuration and collimation allow for reproducible measurements of sources of different sizes (contrary to well-counter), it offers a fast and flexible user interface to analyze the data, and finally, it is less frequently used for patient studies (thus, more available) than gamma camera.

Using the TP (or any other  $\gamma$ -ray spectrometer) to determine DC settings for the isotope of interest involves performing three measurements (Figure 2.1). First, the energy-dependent efficiency of the thyroid-probe (i.e., NaI detector) must be established using standard sources with well-known activities. This step is crucial, as the accuracy of the TP-based activity

measurements depends on the accuracy of its efficiency determination. At the second stage, the gamma radiation emitted by the sample of the investigated isotope is measured with the TP. Now, this sample activity can be determined using  $\gamma$ -ray spectroscopy methods, given that the information about the TP efficiency, isotope photon yield and half-life are known. If necessary, background, source-geometry and dead-time corrections should be applied during the efficiency and the activity determination steps. Finally, in the third step, the TP based activity is used to determine the DC settings by direct calibration or using the calibration curve method [89]. The details of the latter approach will be discussed in Section 2.2.1.4; it is used in cases when the true sample activity cannot be determined prior to the DC measurement. Each of these steps introduces errors that propagate and impact the accuracy of the DC settings determination. Identification of sources of these errors and estimation of their values is essential if one wants to optimize the accuracy of determination of the TP-based dose calibrator settings, and maximize accuracy of future activity measurements.

In this work, we discuss this methodology and identify and analyze the sources of errors associated with each step of the measurement process. In order to illustrate the performance of the TP method, and to compare its results with the published data [89], we applied it to determine DC dial settings for accurate measurement of  $^{188}\text{Re}$  activity.

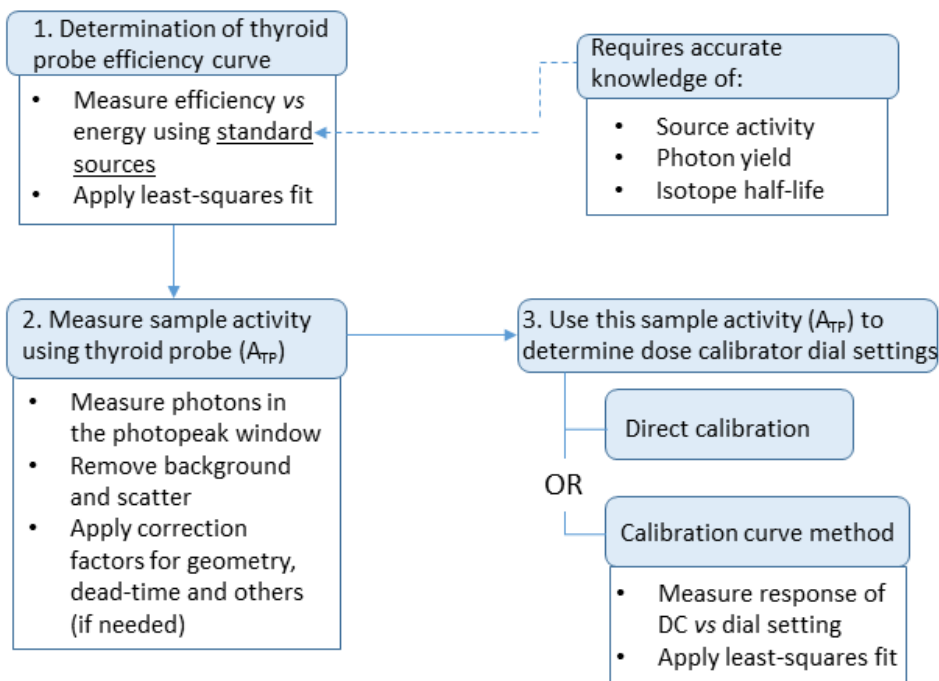


**Figure 2.1** Diagram showing the steps and measurements involved in the thyroid probe-based method to determine dose calibrator settings.

## 2.2 Materials and Methods

The thyroid probe used in this study was an Atomlab 950 Thyroid Uptake System (Biodex Medical Systems, USA). This system contains a 5.08 cm x 5.08 cm (diameter x height) NaI crystal coupled to a multi-channel analyzer (MCA) with 1024 channels which enables acquisition of the energy spectrum of  $\gamma$ -emission. The MCA is connected to a personal computer for system operation, data acquisition and analysis. A lead collimator placed at the front of the system accepts only photons coming within the probe acceptance angle, thus limiting background counts. In our experiments, a custom designed Styrofoam box was used to support radioactive sources. Source positions were determined using a custom-made distance template,

as shown in Figure 2.2. All sources were placed at the same distance from the detector ( $d = 20.5$  cm) which resulted in the total acceptance angle equal to  $14^\circ$ .

Following manufacturer recommendation, before every experiment, a daily energy calibration test of the probe was performed using a  $^{137}\text{Cs}$  source. In addition, a blank scan was acquired each day to measure the ambient background radiation. In all our experiments, the multi-channel analyzer was set to cover the energy range from 0 keV to 763.5 keV, which resulted in a 1024 channel spectrum with the energy bin size of 0.746 keV. For analysis, the acquired spectra were saved in ASCII format and processed using MATLAB (Mathworks, US).

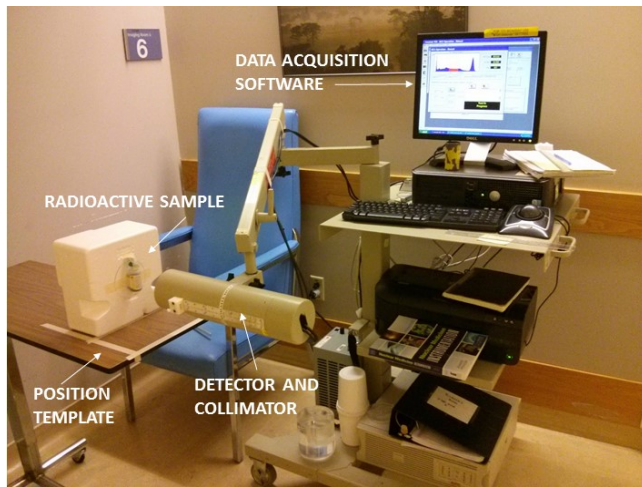


**Figure 2.2** Thyroid-probe experimental setup.

## **2.2.1 Determination of Dose Calibrator Settings Using the Thyroid Probe**

Figure 2.1 summarizes the steps needed to determine DC settings based on TP measurements of activity. The following sections describe these steps in detail.

### **2.2.1.1 Thyroid-probe Efficiency Curve**

Prior to measuring sample activity, the energy-dependent efficiency of the TP must be determined. This should be done using standard sources with well-known activities. We let  $\epsilon(E)$  represent this efficiency, defined as:

$$\epsilon(E) = \frac{N_{\text{photopeak}}(E)}{N_{\text{emitted}}(E)} \kappa(E) DT(\dot{N}) f \quad (2.1)$$

where  $E$  represents the energy of the photopeak photons,  $N_{\text{photopeak}}(E)$  is the number of detected photopeak photons,  $N_{\text{emitted}}(E)$  is the number of these photons emitted from the radioactive source and the factors  $\kappa(E)$  and  $DT(\dot{N})$  represent correction factors for source-geometry (if sources with different geometries are used for calibration) and dead-time losses (due to high detector count-rate,  $\dot{N}$ ), respectively. The variable  $f$  represents any other factors that may affect efficiency determination such as the coincidence sum peaks from cascade emissions (in particular, when using standard sources with multiple  $\gamma$ -emissions). A detailed analysis on the factors that may affect  $\gamma$ -ray spectroscopy measurements for NaI detectors can be found in the American National Standard Institute (ANSI) report N42.12-1994 [95]. Based on Equation 2.1, the TP efficiency will depend on a number of factors, including the characteristics of the NaI crystal, the geometry of the source and the source-to-detector distance.

The TP efficiency was measured using two NIST-traceable calibration sources:  $^{152}\text{Eu}$  and  $^{22}\text{Na}$  (Table 2.1). The geometry of  $^{152}\text{Eu}$  (a point source encapsulated in solid 0.6 cm thick acrylic disk and placed parallel to the detector front plane) was used as the reference geometry. Since the  $^{22}\text{Na}$  activity was encapsulated in a thinner (0.3 cm) solid acrylic disk, a correction factor (disk-to-reference) had to be applied to account for its geometry. The geometry correction factor was estimated using an analytical expression that accounts for the differences in photon attenuation between the  $^{152}\text{Eu}$  and the  $^{22}\text{Na}$  disks geometries (Section 2.2.1.3). The measured count-rates of  $^{152}\text{Eu}$  and  $^{22}\text{Na}$  sources were 0.5 kcounts/s and 0.7 kcounts/s, respectively, well below the TP maximum count rate of 100 kcounts/s reported by the manufacturer. Therefore, the

dead-time losses were assumed to be negligible (i.e.,  $DT$  factor was equal to 1). For higher count rates, however, it is essential to measure dead-time of the system so that the factor  $DT$  can be estimated. The TP dead-time can be measured by various methods such as the “decaying-source method” [96] or the “two-source method” [95]. Although coincidence sum peaks may be important for  $^{152}\text{Eu}$ , this factor was assumed to be negligible because of the large source-to-detector distance (20.5 cm) and the small acceptance angle ( $14^\circ$ ) which minimized the chance of detecting coincident emissions falling within the same solid angle. The validity of these assumptions was later confirmed by the accuracy of activity estimates obtained with the TP method (Section 2.3.3) and the agreement between the measured and simulated TP efficiency (Appendix A).

**Table 2.1** Manufacturer specifications, source geometry, activity, photopeak energy and photon yield for isotopes used in thyroid-probe efficiency calibration experiment. The quantities in brackets represent the expanded uncertainties ( $k = 2$ ) at 95% confidence level. Nuclear data was obtained from the Nuclear Data Sheets [97,98].

<b>Isotope</b>	<b>Manufacturer</b>	<b>Geometry (material; dimensions)</b>	<b>Activity [MBq]</b>	<b>Emission Energy [keV]</b>	<b>Photon Yield</b>
$^{152}\text{Eu}$	Isotope Products Labs, USA	Solid acrylic disk; d = 2.5 cm, h = 0.6 cm	0.065(2)	121.7817(6)	0.2853(32)
				244.6974(16)	0.0755(8)
				344.2785(24)	0.2659(40)
$^{22}\text{Na}$	Isotope Products Labs, USA	Solid acrylic disk; d = 2.5 cm, h = 0.3 cm	0.072(2)	511.0	1.8076(8)

The energy spectra of the calibration sources were measured 5 times. After each measurement, the source was intentionally removed and re-positioned again at the Styrofoam box so that the variability in photopeak counts due to source positioning could be evaluated. In particular, the energy spectra of  $^{152}\text{Eu}$  and  $^{22}\text{Na}$  were measured each time for 68 and 20 minutes, respectively, which resulted in more than 10000 counts in their respective photopeaks. For each energy spectrum, the following analysis was performed:

- The counts acquired from the daily blank scan (ambient radiation) were removed from the measured energy spectra. The ambient count-rate was approximately 1.5% of the  $^{152}\text{Eu}$  and  $^{22}\text{Na}$  source count-rates.
- A wide energy window was selected around the photopeak to count the number of detected photons ( $N_{detected}$ ). They included both photopeak and scattered photons with energies that fell within the photopeak window.
- Two additional windows were positioned on both sides of the photopeak and counts were recorded ( $N_L$  and  $N_U$ ). The upper and lower windows were selected as indicated in Figure 2.3. Details of the energy window settings for the efficiency calibration isotopes can be found in Table 2.2.
- The total number of photopeak photons,  $N_{photopeak}$ , was calculated by subtracting the scatter component ( $N_{SC}$ ), from the total number of detected photons:

$$N_{photopeak} = N_{detected} - N_{SC} \quad (2.2)$$

where the scatter component, estimated using the triple energy window method [26], is equal to:

$$N_{SC} = \frac{1}{2} \left( \frac{N_U}{W_U} + \frac{N_L}{W_L} \right) \times W_{detected}, \quad (2.3)$$

where  $N_U$  and  $N_L$  represent the number of photons detected in the upper and lower windows, respectively, and  $W_{detected}$ ,  $W_U$  and  $W_L$  represent the width of the corresponding windows.

- A geometry correction factor was applied to the TP efficiency value measured at 511 keV ( $^{22}\text{Na}$ ).

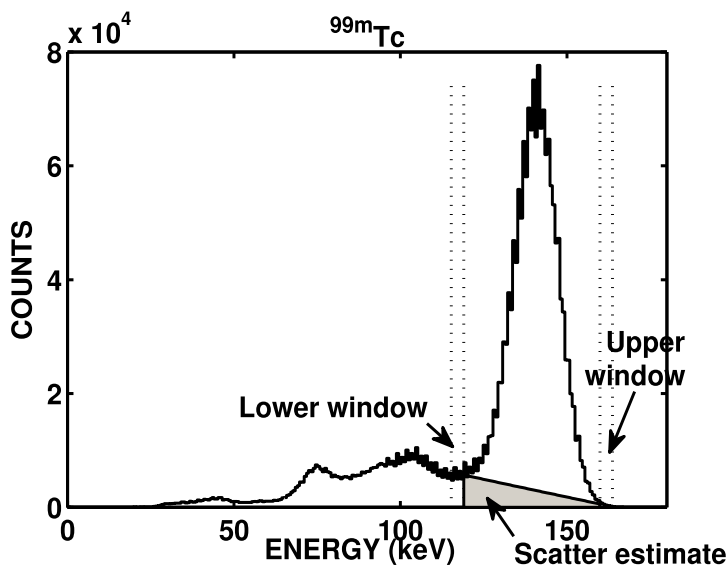


Figure 2.3 Energy spectrum of  $^{99m}\text{Tc}$  acquired with the thyroid-probe. Dashed lines show the boundaries of the lower window, photopeak and upper window. The shaded area represents the scatter estimate using the triple energy window method.

For each photopeak  $E$ , the number of emitted photons  $N_{emitted}(E)$  was calculated as the product of the time-integrated activity (i.e., the total number of decays occurring during acquisition time  $T$ ) and the photon yield corresponding to the analyzed photopeak  $E$  (i.e., the number of photons with energy  $E$  emitted per decay; see Table 2.1):

$$\begin{aligned}
N_{emitted}(E) &= \int_0^T A_0 Y(E) \exp\left(-\frac{\ln 2}{T_{1/2}} t\right) dt = A_0 Y(E) T_{1/2} \left[ 1 - \exp\left(-\frac{\ln 2}{T_{1/2}} T\right) \right] \\
&= A_0 Y(E) DF\left(T_{1/2}, T\right)
\end{aligned} \tag{2.4}$$

where  $T$  represents the acquisition time,  $T_{1/2}$  represents the isotope half-life,  $A_0$  represents the activity of the source at time of measurement and  $Y(E)$  represents the photon yield for the photopeak of energy  $E$ . The factor  $DF(T_{1/2}, T)$  represents the solution to the time-integral of the exponential function.

**Table 2.2 Energy window settings for isotopes used in thyroid-probe efficiency calibration experiment. The values in brackets indicate the window boundaries.**

Isotope	Energy [keV]	$W_{photo}$ [keV]	$W_U$ [keV]	$W_L$ [keV]
$^{152}\text{Eu}$	122	(105,141)	(141,152)	(96,105)
	245	(219,282)	(282,296)	(190,219)
	344	(313,395)	(395,401)	(299,313)
$^{22}\text{Na}$	511	(460,562)	(562,572)	(450,460)

In order to characterize the efficiency of the thyroid-probe as a function of energy, the following 2-parameter function was fit to the experimental data using a weighted least-squares fitting method:

$$\log(\epsilon'(E)) = a + bE. \tag{2.5}$$

The weighting factors for the least-square fit were defined as:

$$w_{\epsilon}(E) = \frac{\epsilon(E)}{\Delta\epsilon(E)} \quad (2.6)$$

where  $\Delta\epsilon(E)$  represents the efficiency uncertainty. Uncertainty analysis is described in the Appendix A.2.

### 2.2.1.2 Sample Activity Determination Using the Thyroid-probe

Once the efficiency of the thyroid probe is obtained, the unknown activities of additional samples can be determined using the following equation:

$$A = \frac{N_{\text{photopeak}}(E)}{\epsilon'(E)DF(T_{1/2}, T)Y(E)} \kappa(E)DT(\dot{N})f \quad (2.7)$$

where  $\epsilon'(E)$  represents the fitted efficiency at energy  $E$ ,  $\kappa(E)$  represents the geometry factor that corrects for differences between geometry of the calibration source (reference) and that of the measured sample,  $DT(\dot{N})$  represents the dead-time correction factor and  $f$  represents additional correction factors, as discussed in section 2.2.1.1.

The method was applied for  $^{99m}\text{Tc}$ ,  $^{188}\text{Re}$ ,  $^{131}\text{I}$  and  $^{57}\text{Co}$  sources (Table 2.3). In the cases of  $^{99m}\text{Tc}$ ,  $^{188}\text{Re}$  and  $^{131}\text{I}$ , the activities were diluted in 20 mL of water and dispensed into 25 ml glass vials. A geometry correction factor (vial-to-reference) was applied when estimating the activities of these samples. The  $^{57}\text{Co}$  source was confined at the bottom part of a plastic tube ( $r = 0.6$  cm,  $h = 7.5$  cm) therefore a geometry correction factor (tube-to-reference) was also applied in this case. Since the measured count-rate of all investigated isotopes was lower than 5 kcounts/s, the count losses due to dead-time were assumed to be negligible. The ambient count-rate was 0.1%, 5%, 4% and 33% of the  $^{99m}\text{Tc}$ ,  $^{188}\text{Re}$ ,  $^{123}\text{I}$  and  $^{57}\text{Co}$  sources count-rates, respectively. While a single 140 keV photopeak was used to measure  $^{99m}\text{Tc}$  activity, for  $^{188}\text{Re}$  and  $^{131}\text{I}$ , three photopeaks were identified in each spectrum and activities of these radionuclides were determined independently

using each of these peaks. Estimating the activity of the  $^{57}\text{Co}$  source was challenging due to the overlap between its two photopeaks: 122 keV and 136 keV. For this reason, the  $^{57}\text{Co}$  activity was estimated using two different methods: 1) using a standard photopeak window set around 122 keV and; 2) using a wider window covering both the 122 keV and the 136 keV photopeaks and using the sum of the corresponding photon yields. The energy window settings for each of these isotopes are shown in Table 2.4.

**Table 2.3 Manufacturer specifications, source geometry, activity, photopeak energy and photon yield for isotopes used to evaluate accuracy of thyroid-probe activity estimates. The quantities in brackets represent the expanded uncertainties ( $k = 2$ ) at 95% confidence level. Nuclear data was obtained from the Decay Data Evaluation Project [99] and the Nuclear Data Sheets [11,14,100].**

<b>Isotope</b>	<b>Manufacturer</b>	<b>Geometry (material; dimensions)</b>	<b>Emission Energy [keV]</b>	<b>Photon Yield</b>
$^{99\text{m}}\text{Tc}$	$^{99}\text{Mo}/^{99\text{m}}\text{Tc}$ generator. Lantheus Medical Imaging (USA)	20 mL water; 25 mL glass vial	140.511(2)	0.885(4)
$^{188}\text{Re}$	$^{188}\text{W}/^{188}\text{Re}$ generator. ITG (Germany)	20 mL water; 25 mL glass vial	155.041(8)	0.1561(36)
			477.992(50)	0.01081(20)
			632.983(42)	0.01374(26)
$^{131}\text{I}$	Jubilant DraxImage (Canada)	20 mL water; 25 mL glass vial	284.305(10)	0.612(12)
			364.489(10)	0.815(8)
			636.989(8)	0.0716(20)
$^{57}\text{Co}$	Reflex Industries (USA)	12x75 mm plastic tube	122.06065(24)	0.8560(34)
			136.47356(58)	0.1068(16)

**Table 2.4 Energy window settings for isotopes used to evaluate the accuracy of thyroid-probe activity estimates. The values in brackets indicate the window boundaries**

Isotope	Energy [keV]	$W_{photo}$ [keV]	$W_U$ [keV]	$W_L$ [keV]
$^{99m}\text{Tc}$	140	(119,160)	(160,164)	(115,119)
$^{188}\text{Re}$	155	(135,177)	(177,182)	(129,135)
	478	(428,523)	(523,540)	(417,427)
	633	(574,684)	(684,706)	(551,574)
$^{131}\text{I}$	284	(237,312)	(312,325)	(232,237)
	364	(325,409)	(409,428)	(317,325)
	637	(578,681)	(681,685)	(570,578)
$^{57}\text{Co}$	122	(99,141)	(141,145)	(96,99)
$^{57}\text{Co}$	122+136	(99,150)	(150,157)	(96,99)

### 2.2.1.3 Geometry Correction Factors

Three types of geometry correction factors were calculated to account for differences between the source and reference geometry used for calibration of the TP: 1) a vial-to-reference geometry correction factor  $\kappa_{VR}(E)$  for each photopeak energy  $E$  of  $^{99m}\text{Tc}$ ,  $^{188}\text{Re}$  and  $^{131}\text{I}$  isotopes; 2) a disk-to-reference geometry correction factor  $\kappa_{DR}(E)$  for the 511 keV  $^{22}\text{Na}$  photopeak and; 3) a tube-to-reference geometry correction factor  $\kappa_{TR}(E)$  for the 122 keV and 136 keV  $^{57}\text{Co}$  photopeaks.

In general, each source-to-reference geometry correction factor was estimated as the ratio of the average photon transmission factor in the 0.6 cm thick solid acrylic disk (reference geometry) to the average photon transmission factor in the geometry of interest. Details of the

specific source-geometry correction factor calculations used in our study can be found in the Appendix A.1.

In order to validate the analytical geometry correction factor model, Monte-Carlo simulations of the TP system and the vial and reference source geometries were performed. The details of the Monte-Carlo simulations can be found in the Appendix A.3. The accuracy of the analytical geometry factor was evaluated by the percent difference between the analytical ( $\kappa(E)$ ) and the Monte-Carlo geometry factor ( $\kappa_{MC}(E)$ ):

$$\%_{geo}(E) = \frac{\kappa(E) - \kappa_{MC}(E)}{\kappa_{MC}(E)} \times 100. \quad (2.8)$$

#### 2.2.1.4 Determination of the Dose Calibrator Dial Settings

After measuring the sample activity using the thyroid probe, the dose calibrator dial settings can be determined. There are two possible scenarios:

- a) **Direct calibration.** This method can be applied to the samples for which activity was determined using thyroid-probe prior to the DC measurements. In this case, the sample is placed inside the dose-calibrator and the dial-setting is adjusted until the DC activity reading ( $A_{DC}$ ) agrees with the activity determined by the thyroid-probe ( $A_{TP}$ ).
- b) **Calibration curve method.** This method, introduced by Zimmerman *et al.* [89], is very useful in cases when the sample activity is too high for the thyroid-probe (i.e., high dead-time losses) or when the isotope half-life is very short. The method is a four-step procedure. First, the sample is placed inside the DC and the dial-settings (DS) are uniformly changed over a wide range of values. At each dial-setting, the apparent activity ( $A_{app}$ ) of the sample (i.e., the DC reading) is recorded. Second, a polynomial fit of degree 1 is applied to the measured data ( $A_{app}$  vs DS) resulting in a function

$A'_{app}(DS) = c \times DS + d$  that describes the response of the DC to the change in dial-setting. Third, the sample is left to decay until its activity is low enough ( $< 1$  MBq) to prevent dead-time losses in the TP detector. Then, the sample activity is measured with the TP ( $A_{TP}$ ) and it is decay corrected to the time of DC measurements. The correct dial-setting is determined from the calibration curve [ $A'_{app}(DS)$ ] as the DS value that yields an activity reading equal to the activity measured with the TP (i.e.,  $A_{TP}$ ).

In our work, the calibration curve method was applied to determine  $^{188}\text{Re}$  DC settings for two commercial dose calibrators: Atomlab 100plus (Biodex Medical Systems, USA) and Capintec CRC55-tR (Capintec, USA). The empirically determined  $^{188}\text{Re}$  DC dial settings were compared with the manufacturer recommendations and with experimental settings reported in the literature [89]. Although Zimmerman findings were obtained using a different Capintec model (CRC-15R), the  $^{188}\text{Re}$  DC settings for both CRC-15R and CRC-55tR are the same (as reported by the manufacturer [101,102]).

### 2.2.2 Uncertainty of Dose Calibrator Settings Determined with the Thyroid Probe

As discussed in Section 2.2.1, the method to determine DC settings for a new isotope (or a new sample geometry) using TP consists of the following three steps: 1) efficiency calibration of TP, 2) determination of activity of the new isotope sample using TP and, 3) determination of the DC dial settings for the new isotope. Based on equations 2.1 to 2.8, the uncertainty of the TP-based DC dial settings ( $\Delta DS$ ) is affected by the following factors:

- Uncertainty of the TP-efficiency  $\Delta\epsilon$ , which was calculated by applying the standard error propagation formula [103] through Equation 2.1. This uncertainty depends mainly on the uncertainty of the photopeak counts  $\Delta N_{photopeak}$ , the uncertainty of the number of

emitted photons  $\Delta N_{emitted}$  (which is dominated by the standard-source activity uncertainty  $\Delta A_0$  and the uncertainty of the photon yield  $\Delta Y$ ) and the uncertainties associated to geometry ( $\Delta \kappa$ ) and dead-time correction factors ( $\Delta DT$ ), when applicable. The uncertainty of the fitted efficiency ( $\Delta \epsilon'(E)$ ) was determined by the uncertainty of the measured efficiency propagated through Equation 2.5.

- Uncertainty of sample activity determination using the TP ( $\Delta A$ ), which was calculated by applying the error propagation formula to equation 2.7. The main factors affecting the uncertainty of the TP-based activity are the uncertainty of the photopeak counts  $\Delta N_{photopeak}$  and the uncertainty of the fitted efficiency curve  $\Delta \epsilon'(E)$ . Additionally, uncertainty of the sample's geometry correction factor was also determined.

A detailed mathematical description of uncertainty calculations can be found in the Appendix A.2.

### 2.2.3 Determination of Accuracy of Thyroid-probe Activity Measurements

In order to evaluate the accuracy of activity determination using TP-based gamma spectroscopy method, the true activity of a sample must be known to be compared with that determined using the TP. Thus, for each investigated isotope ( $^{99m}\text{Tc}$ ,  $^{188}\text{Re}$ ,  $^{131}\text{I}$  and  $^{57}\text{Co}$ ) this information had to be independently acquired. In the case of  $^{57}\text{Co}$ , which is a NIST-traceable source, the true activity was provided by the calibration report. The activities of other isotopes were measured using a High Purity Germanium detector (HPGe) (Canberra, USA) available at the BCCA Cyclotron Laboratory. The efficiency of the HPGe detector was independently determined using a NIST-traceable multi-nuclide source (Eckert & Ziegler Isotopes products, USA) having the same geometry as the  $^{99m}\text{Tc}$ ,  $^{188}\text{Re}$  and  $^{131}\text{I}$  sources. In all cases, the activities

were in the range of 37 - 74 kBq (1 - 2  $\mu$ Ci) which resulted in the HPGe dead-time losses below 6%.

The accuracy of the activity determined with the TP ( $A_{TP}$ ) was quantified in terms of the percent difference with respect to the true activity ( $A_{TRUE}$ ):

$$\%_{diff} = \frac{(A_{TP} - A_{TRUE})}{A_{TRUE}} \times 100 \quad (2.9)$$

where  $A_{TRUE}$  represents the activity determined with HPGe for  $^{99m}\text{Tc}$ ,  $^{188}\text{Re}$  and  $^{131}\text{I}$ ; and the activity provided by the calibration report for  $^{57}\text{Co}$ .

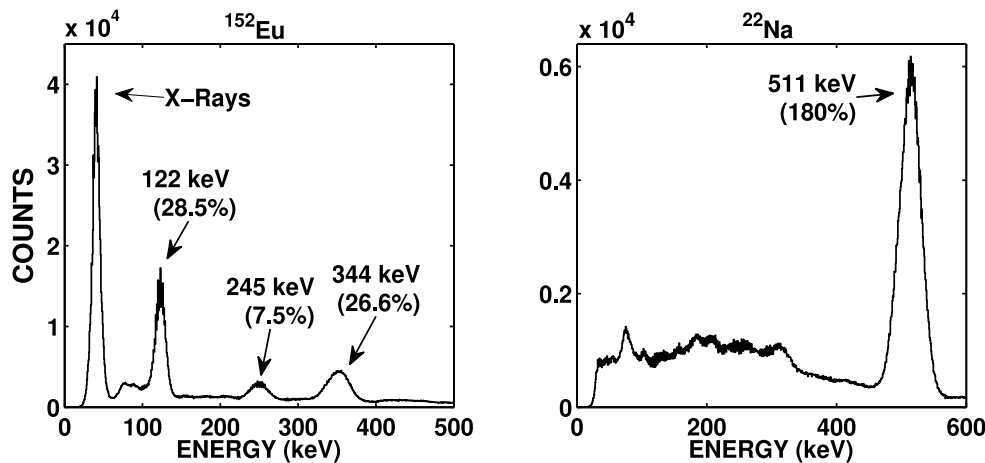


Figure 2.4 Energy spectra of  $^{152}\text{Eu}$  and  $^{22}\text{Na}$  measured with the thyroid-probe and used for the efficiency calibration experiment. The photon yields are shown in parenthesis.

## 2.3 Results

### 2.3.1 Determination of Dose Calibrator Settings Using a Thyroid-Probe

#### 2.3.1.1 Thyroid-Probe Efficiency Curve

The energy spectra of  $^{152}\text{Eu}$  and  $^{22}\text{Na}$  measured using the TP are shown in Figure 2.4. The low energy (30 – 45 keV) peak observed in  $^{152}\text{Eu}$  corresponds to the X-ray emissions from its respective daughter nuclei [98] (for  $^{22}\text{Na}$ , the X-rays have very low energies and are not displayed [97]). The measured values of the TP efficiencies are shown in Figure 2.5. Note that

the measured efficiency at 511 keV ( $^{22}\text{Na}$ ) was re-scaled using the disk-to-reference geometry factor. The TP efficiency curve derived from these measurements is also shown in Figure 2.5. While there are many functions that could be used to model the detector efficiency, a simple 2-parameter model (Equation 2.5) was used as there was a limited number of efficiency points, it was a simple model and provided an adequate fit to the experimental data (p-value < 0.01 and the  $R^2 = 0.9850$ ). This is likely because the NaI-efficiency decreases smoothly with energy for energies greater than 120 keV [104]. If additional data points were measured at energies below 120 keV, a function with more than two parameters might be necessary to accurately describe the efficiency of the thyroid-probe.

The parameters of the fit obtained in our study are specific to the reference source geometry, a combination of the TP lead collimator and source-to-detector distance of 20.5 cm and the intrinsic efficiency of this particular NaI detector. It is important to note that the efficiency curve determined in this study cannot be directly applied to a different thyroid-probe, even when all the experimental conditions are identical, as the intrinsic efficiency may vary between detectors.

### **2.3.1.2 Dose Calibrator Dial Settings for $^{188}\text{Re}$**

The  $^{188}\text{Re}$  activity was extracted from a  $^{188}\text{W}/^{188}\text{Re}$  generator (iTG – Isotopen Technologien München, Germany), diluted into 20 mL water and dispensed into a 25-mL glass vial. Since the sample activity was too high to be measured using the TP prior to DC measurements, the “calibration curve method” (Section 2.2.1.4) was applied. The response of both dose calibrators in the measured dial setting range was well modelled by the linear function  $A'_{app} = c \times DS + d$ , with  $R^2 = 1$  and  $R^2 = 0.9987$  for Atomlab 100plus and Capintec CRC-55tR, respectively.

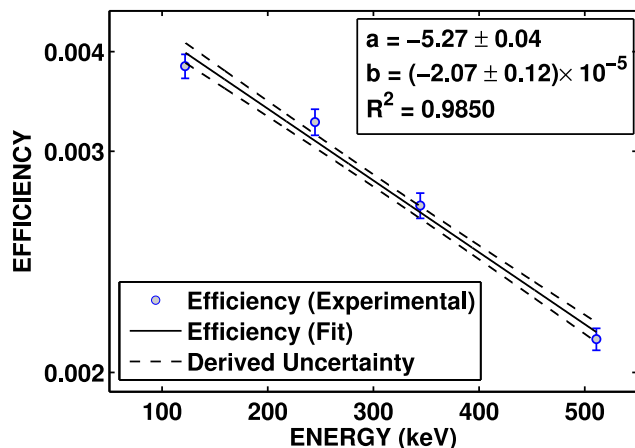


Figure 2.5 Thyroid-probe efficiency curve (solid line) as a function of energy determined by fitting the 2-parameter linear function in  $\log(\epsilon)$ . Dashed lines represent the derived uncertainty from the fit. Error bars represent experimental uncertainties. All uncertainties are expanded uncertainties ( $k = 2$ ) at 95% confidence level.

Table 2.5 Comparison between  $^{188}\text{Re}$  dose calibrator settings determined empirically by different methods and recommended by the manufacturer. All reported uncertainties are expanded uncertainties ( $k = 2$ ) at 95% confidence level.

	Atomlab 100plus Setting #	Geometry	Capintec CRC-55tR Setting # (x10)	Geometry
<b>Manufacturer</b>	86.6	Plastic syringe, vial or thin wall glass ampoule	496	5 mL ampoule
<b>Thyroid Probe</b>	$76.5 \pm 4.8$	20 mL solution dispensed into 25 mL glass vial	$646 \pm 43$	20 mL solution dispensed into 25 mL glass vial
<b>Zimmerman[89]</b>		N/A	$631 \pm 4$	5 mL ampoule
			$621 \pm 3$	5 mL SoloPak vial

Rhenium-188 dose calibrator settings determined with the thyroid-probe are shown in Table 2.5. These results are compared to the manufacturer recommended settings and to other recommended settings found in the literature [89]. For both dose calibrators, the manufacturer-recommended values disagree with those determined in our experiments.

For Atomlab 100plus, using the manufacturer-recommended settings would over-estimate the  $^{188}\text{Re}$  activity by approximately 10% relative to the TP-based settings. It is important to note that the manufacturer recommends to use these settings when measuring  $^{188}\text{Re}$  in a rather broad variety of geometries (a plastic syringe, vial or thin wall glass ampoule) which are all different than our calibration geometry (a 25-mL glass vial). In order to clarify if the difference between TP-based and manufacturer settings are caused by variations in response due to source geometry, the Atomlab 100plus activity readings were additionally determined for three different containers: a 10-mL plastic syringe, a 20-mL plastic syringe and the 25-mL glass vial used for calibration (Figure 2.6). The difference in DC response for a plastic syringe and the 25-mL glass vial was less than 4%. These results, in addition to the independent measurement of  $^{188}\text{Re}$  sample activity using HPGe, suggest that using TP-based dial settings would result in more accurate activity readings than when using manufacturer-recommended settings for the Atomlab 100plus. Figure 2.6 also shows that, for filling volumes larger than 5-mL, the Atomlab 100plus dose calibrator response remains nearly constant for the 20-mL syringe and the 25-mL glass vial. Similar findings were reported for a 3-mL vial filled with increasing volumes of  $^{186}\text{Re}$  [84] and

for a 10-mL plastic syringe filled with  $^{90}\text{Y}$  [85].

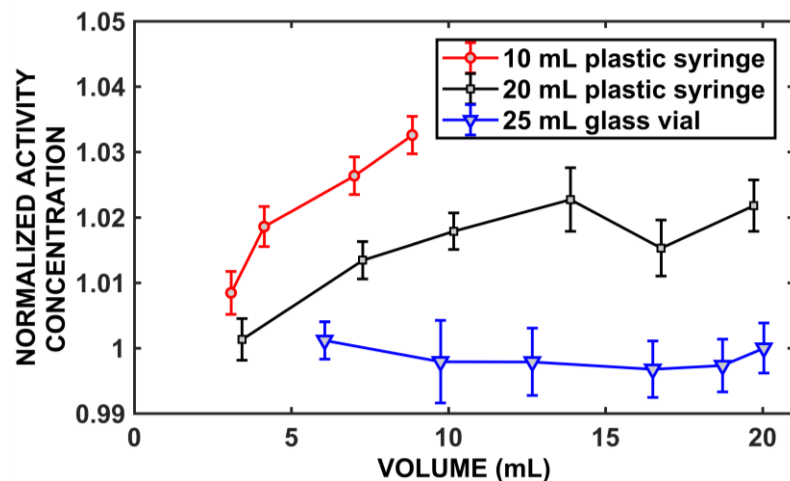


Figure 2.6 Atomlab 100plus relative response for three source geometries (10-mL plastic syringe, 20-mL plastic syringe and 25-mL glass vial) filled with increasing volumes of  $^{188}\text{Re}$  solution.

For Capintec CRC-55tR, the manufacturer recommended  $^{188}\text{Re}$  dial setting is  $496 \times 10$  [101]. This setting, which is also recommended for CRC-15R models [102], was reported to over-estimate  $^{188}\text{Re}$  activity by 30% [89]. The TP-based  $^{188}\text{Re}$  settings for CRC-55tR confirms the results of Zimmerman [89] and illustrate the importance of experimental determination of DC settings, in particular for non-conventional isotopes.

### 2.3.1.3 Geometry Correction Factors

Figure 2.7 shows a comparison between the vial-to-reference ( $\kappa_{VR}$ ) geometry correction factors and those obtained with Monte-Carlo simulations for  $^{99\text{m}}\text{Tc}$ ,  $^{188}\text{Re}$  and  $^{131}\text{I}$  photopeaks. The analytical model (described in Appendix A.1) underestimates the Monte-Carlo factors by 2.4%, on average. Differences in the calculated factors are likely due to the approximations used in the analytical method which only consider uniform photon attenuation, while the Monte-Carlo simulation accounts for attenuation, scatter and also the changes in the energy spectrum of photons reaching the detector. Despite these differences in modelling, the analytical method still

provides a good approximation of the geometry correction factors and it is necessary to improve the accuracy of TP-based activity estimates when sources with different geometries are used. The application of the vial-to-reference geometry factor is especially important for low energy photons, for which the loss of counts in the photopeak were approximately 10% to 14% due to larger photon attenuation within the vial source as compared to the reference disk geometry.

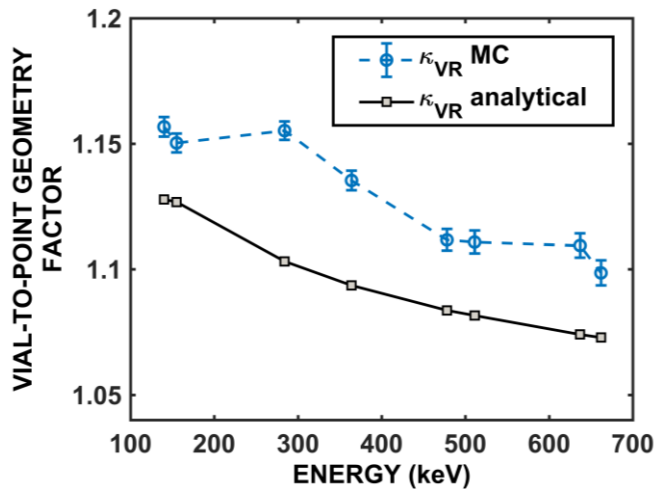


Figure 2.7 Comparison of the analytical and the Monte-Carlo vial-to-reference geometry correction factors.

### 2.3.2 Factors Affecting Uncertainty of Dose Calibrator Settings Determined with the Thyroid-Probe

In the following sections, all the reported uncertainties represent expanded uncertainties. The expanded uncertainties were calculated by multiplying the standard uncertainties (Section 2.2.2 and Appendix A.2) by a coverage factor  $k = 2$ , which resulted in the uncertainty interval having a 95% confidence interval.

#### 2.3.2.1 Uncertainties of Thyroid-Probe Efficiency Curve

The uncertainties of the TP efficiency values, which are represented by the error bars in Figure 2.5, ranged from 3.2% to 4.4% (relative uncertainty). These error bars were calculated by combining the contributions from the individual uncertainties discussed in Section 2.2.2. The

most significant contribution was the uncertainty of the number of emitted photopeak photons ( $\Delta N_{emitted}$ ), which accounted for 2.9% at most. This uncertainty is determined by the uncertainty of the isotope half-life, the uncertainty of the photon yield (reported on nuclear data tables) and the uncertainty of the standard source activity (provided by the manufacturer). These individual contributions cannot be minimized and set a limitation on the lowest uncertainty that can be achieved with this method. The application of the disk-to-reference geometry correction factor resulted in an additional contribution of 0.6% to the 511 keV ( $^{22}\text{Na}$ ) efficiency uncertainty, illustrating the importance of using the same geometry for all the calibration sources to maximize accuracy. The uncertainty of the scatter-corrected photopeak counts ( $\Delta N_{photopeak}$ ) contributed to 0.6% for the 511 keV  $^{22}\text{Na}$  photopeak and ranged from 1.2% to 1.9% for  $^{152}\text{Eu}$  photopeaks. The increase in  $\Delta N_{photopeak}$  for  $^{152}\text{Eu}$  is due to the presence of high scatter under the photopeak (Figure 2.4). The uncertainty of the scatter-corrected photopeak counts may be minimized by considering the following: 1) long enough acquisition times of the energy spectrum so that the statistical errors in the photopeak counts are minimized; 2) precisely measuring the source-to-detector distance so that the variability due to positioning of the source is decreased and; 3) when available, measuring efficiency using photopeaks for which the presence of scatter is low compared to the intensity of the peak.

### **2.3.2.2 Uncertainties of Thyroid-Probe Activity Measurements**

The uncertainties of the samples' activities measured with the TP (Table 2.7) ranged from 6.6% to 12.7%. The largest uncertainties were obtained when the activity was estimated using photopeaks with low intensity and/or very high scatter counts (relative to the photopeak counts) such as the 478 keV and 633 keV  $^{188}\text{Re}$  photopeaks, and the 122 keV  $^{57}\text{Co}$  photopeak (Figure

2.8). In the case of activities determined with the most intense photopeaks, the uncertainties ranged from 6.6% to 8.1%.

The largest contribution to the TP-based activity uncertainty was the uncertainty of the vial-to-reference geometry factor which ranged from 3.4% to 4.8%. This uncertainty, however, could be minimized if the dimensions of the vial geometry were measured with more precision. The second largest contribution to the uncertainty of the sample's activity was the uncertainty of the scatter-corrected photopeak counts (which ranged from 1% to 5.6%), followed by the uncertainty of the fit efficiency (ranging from 1.8% to 2.9%). Lastly, the uncertainties associated with the photon yields were usually low, except for the uncertainty of the 155 keV  $^{188}\text{Re}$  and 364 keV  $^{131}\text{I}$  photon yields, which represented a 2.3% and 2% relative uncertainty, respectively. The uncertainty of the decay factors  $DF$ , which are related to the uncertainty of the isotope half-life, were negligible in all cases.

The most precise measurements were obtained when the photopeaks with the largest number of counts were used. In addition to our limitation in the knowledge of the nuclear data, there is a lower limit to the activity uncertainty set up by the uncertainty of the TP efficiency. It is therefore crucial to precisely and accurately determine the efficiency of the TP in order to optimize activity measurements, and eventually DC settings.

In the best-case scenario, when the source geometry is the same as the reference geometry (i.e.,  $\Delta\kappa$  would be zero), the lowest uncertainty of the TP based activity would range from 3% to 4% for the isotopes investigated. This uncertainty, however, is still higher than uncertainties obtained by other techniques such as liquid scintillation counting which may yield 1% uncertainty for  $^{188}\text{Re}$  activity measurements [89]. Therefore, we recommend to use these other

techniques that allow for more accurate and precise measurements of the sample activity if they are available at the NM department.

### 2.3.2.3 Uncertainties of Dose Calibrator Settings

For the case of  $^{188}\text{Re}$ , the relative uncertainties of the DC settings were 6.16% and 6.67% for the Atomlab 100plus and the Capintec CRC-55tR, respectively. These uncertainties were a combination of the uncertainty of the sample activity (6.15%), the uncertainty of the DC response (DC repeatability) and the propagation of the uncertainty through the fit. Table 2.6 shows the contribution of each individual component to the DC settings uncertainty. The main factor limiting the uncertainty of the DC settings was the uncertainty of the sample activity.

The experimentally determined dial settings not only depend on the sample activity, but also on the parameters of the fit used for the calibration curve method. Therefore, the uncertainty of the activity readings using the newly determined settings ( $\Delta A_{DS}$ ) depends on the dial setting uncertainty propagated through the equation of the fit ( $A'_{app} = c \times DS + d$ ). For Atomlab 100plus, a 6.16% uncertainty on the DS settings resulted in a 6.26% uncertainty of the activity readings. For Capintec CRC-55tR, a 6.67% uncertainty of the DS settings is translated into 6.94% uncertainty of the activity reading, showing a greater impact of the variability of the calibration curve (i.e., larger uncertainty of the parameters of the fit  $c$  and  $d$ ) on the final uncertainty.

Being able to determine uncertainties of the method is essential to understand its limitations. Having 6.2% relative expanded uncertainty ( $k=2$ ) of the DC settings (as in the case of  $^{188}\text{Re}$ ) means that the TP method is able to provide DC settings sensitive to source geometry in situations where the DC response variations are larger than, at least, 3.1% (i.e., the DC uncertainties partially overlap). If the response of the DC settings is less than 3.1% to changes in

source geometry, the TP method would not be sensitive enough to yield two different DC settings.

**Table 2.6 Top: expanded uncertainty components (k = 2, at 95% confidence level) of the TP-based  $^{188}\text{Re}$  activity. Bottom: resulting uncertainties of  $^{188}\text{Re}$  activity,  $^{188}\text{Re}$  DC dial settings and  $^{188}\text{Re}$  DC activity readings using the TP-based dial settings.**

	<b>Atomlab 100plus</b>	<b>Capintec CRC-55tR</b>
<b>Uncertainty component of A:</b>		
		%
<b>Corrected photopeak counts</b> <b>(<math>\Delta N_{photopeak}</math>)</b>		1.86
<b>Fit efficiency at 155 keV (<math>\Delta\epsilon'</math>)</b>		2.57
<b>Geometry factor (<math>\Delta\kappa</math>)</b>		4.74
<b>Decay factor (<math>\Delta DF</math>)</b>		0.05
<b>Photon yield (<math>\Delta Y</math>)</b>		2.31
<b>Resulting uncertainty:</b>		%
<b><math>^{188}\text{Re}</math> TP-based activity (<math>\Delta A</math>)</b>		6.15
<b><math>^{188}\text{Re}</math> dial setting (<math>\Delta DS</math>)</b>	6.16	6.67
<b><math>^{188}\text{Re}</math> dose calibrator reading</b>	6.26	6.94
<b>using TP-based settings (<math>\Delta A_{DS}</math>)</b>		

### 2.3.3 Accuracy of Thyroid-Probe Activity Measurements

The energy spectra measured with TP and corresponding to the  $^{99m}\text{Tc}$ ,  $^{188}\text{Re}$ ,  $^{131}\text{I}$  and  $^{57}\text{Co}$  sources are shown in Figure 2.8. For the  $^{188}\text{Re}$  energy spectrum, two low intensity photopeaks are visible (633 keV and 478 keV). However, due to poor detector energy resolution and its low efficiency at high energies, the selection of good energy-window settings for these two peaks was difficult. A similar situation was encountered with the 637 keV and the 284 keV photopeaks of  $^{131}\text{I}$  which were lying on top of a very large background. The energy spectrum of  $^{57}\text{Co}$  shows

the 122 keV peak. Although not visible, the shape of the 122 keV high-energy tail indicates the presence of the 136 keV peak.

Table 2.7 compares these isotope activities determined using the HPGe-based  $\gamma$ -ray spectroscopy method and with the thyroid-probe. Very good accuracy (errors below 3.8%) was found when the isotope activity was estimated using its most intense photopeak such as the 140 keV  $^{99m}\text{Tc}$  photopeak, the 155 keV of  $^{188}\text{Re}$  photopeak and the 364 keV  $^{131}\text{I}$  photopeak. The accuracy of the 122 keV  $^{57}\text{Co}$  photopeak was lower (7.5% error), reflecting the challenges of determining the proper window settings due to the presence of two overlapping photopeaks. Similar situation occurs for the 637 keV  $^{131}\text{I}$  photopeak, which partially overlaps with a lower intensity photopeak at 721 keV.

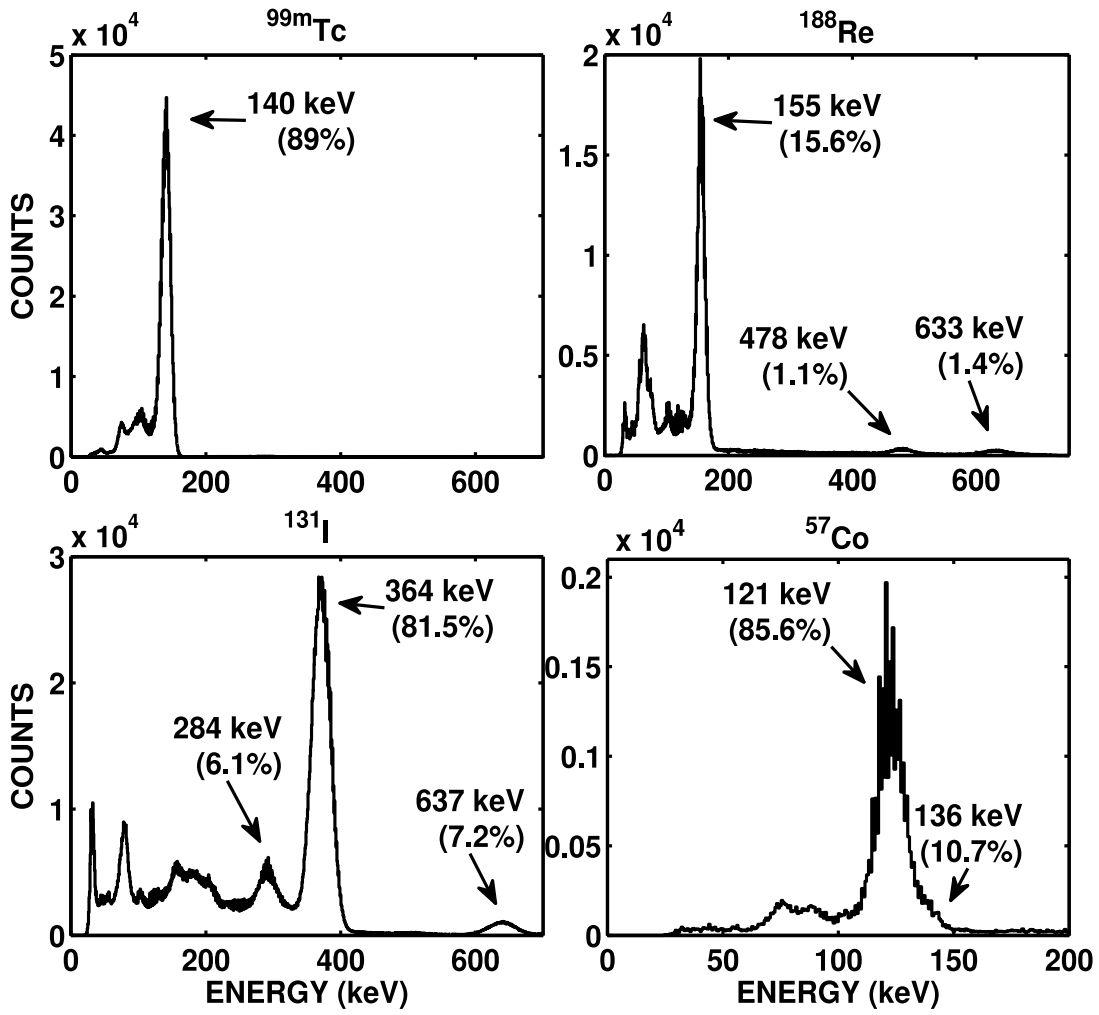


Figure 2.8 Energy spectra of  $^{99m}\text{Tc}$ ,  $^{188}\text{Re}$ ,  $^{131}\text{I}$  and  $^{57}\text{Co}$  measured with the thyroid-probe and used to evaluate accuracy of activity estimates.

**Table 2.7 Comparison between activity measured with HPGe and activity measured with the thyroid-probe for  $^{99m}\text{Tc}$ ,  $^{188}\text{Re}$ ,  $^{131}\text{I}$  and  $^{57}\text{Co}$ . All the reported uncertainties are expanded ( $k = 2$ ) at 95% confidence interval.**

Isotope	Energy [keV]	$A_{TRUE}$ [MBq]	$A_{TP}$ [MBq]	% diff
$^{99m}\text{Tc}$	140	$1.166 \pm 0.006$	$1.12 \pm 0.08$	$-3.8 \pm 6.6$
$^{188}\text{Re}$	155	$0.241 \pm 0.005$	$0.236 \pm 0.014$	$-2.1 \pm 6.4$
	478		$0.231 \pm 0.030$	$-4.1 \pm 12.5$
	633		$0.243 \pm 0.030$	$+0.8 \pm 12.4$
$^{131}\text{I}$	284	$0.0401 \pm 0.0011$	$0.0359 \pm 0.0022$	$-10.5 \pm 7.4$
	364		$0.0389 \pm 0.0019$	$-3.0 \pm 7.1$
	637		$0.0363 \pm 0.0026$	$-9.5 \pm 8.1$
$^{57}\text{Co}$	122	$(3.38 \pm 0.09) \times 10^{-3}$	$(3.12 \pm 0.25) \times 10^{-3}$	$-7.6 \pm 9.5$
	122+136		$(3.01 \pm 0.23) \times 10^{-3}$	$-11.0 \pm 8.9$

### 2.3.4 Limitations and Practical Considerations in the Nuclear Medicine Department

## 2.4 Conclusions

A practical method, based on  $\gamma$ -ray spectroscopy, to determine DC settings using the thyroid-probe was described. A detailed analysis of the factors that affect the uncertainty of the dose calibrator settings determined with this method was performed. The accuracy of thyroid probe-based activity measurements was investigated.

Our results suggest that the largest source of uncertainty of the thyroid probe-based DC settings is due to the application of geometry correction factor, followed by the uncertainty in the photopeak corrected counts and the uncertainty of the TP efficiency calibration experiment. In order to minimize this uncertainty and improve accuracy of the TP efficiency determination, we

recommend the following: the use of accurately calibrated standard sources, precisely measured source-to-detector distance, acquisition times long enough to minimize statistical errors in photopeak counts, and the use of calibration sources with consistent geometries.

Our analysis shows that the thyroid probe method allows us to determine activities of the samples to within 5% of their true activities using the most intense photopeaks of the sample's emissions. In such situations, the expanded uncertainties of the measurements were as low as 6.6% (at 95% confidence level).

The described protocol was applied to determine the  $^{188}\text{Re}$  dial settings for two commercial dose calibrators (Atomlab 100plus and Capintec-CRC55tR). Dial settings obtained using the TP-method were compared to the manufacturer-recommended settings. For Atomlab 100plus, manufacturer-recommended settings over-estimate  $^{188}\text{Re}$  activity by 10% relative to thyroid-probe settings, which were shown to yield more accurate results confirmed by HPGe  $\gamma$ -ray spectroscopy. For Capintec-CRC55tR, differences larger than 20% were found between manufacturer recommendation and the thyroid probe method, in agreement with previous results [89].

In conclusion, this study shows that accurate (within 5% errors) and reproducible (with 6-8% expanded uncertainties at 95% confidence level) measurements of activity can be performed using a thyroid probe. Additionally, identifying the factors that impact the uncertainties of the dose calibrator settings enabled us to maximize accuracy of this method, and potentially of any similar method that may use alternative instruments available in the nuclear medicine department (such as gamma-camera or well-counter).

## Chapter 3: Characteristics of $\gamma$ -emissions and Bremsstrahlung production by $^{188}\text{Re}$ for SPECT/CT Quantification in Radionuclide Therapies

### 3.1 Introduction

Rhenium-188 is a suitable isotope for radionuclide therapies thanks to the characteristics of its nuclear decay. The abundance and energy range of the  $\beta$ -particles emitted by  $^{188}\text{Re}$  ( $E_{\text{max}} = 2.1 \text{ MeV}$ ;  $E_{\text{mean}} = 0.763 \text{ MeV}$ ) results in the delivery of high-radiation dose to tumor sites, while sparing surrounding healthy tissue (maximum  $\beta$ -range in tissue is 11.0 mm; mean  $\beta$ -range of 3.8 mm). Additionally, the emission of 155 keV photons by de-excitation of its daughter nucleus  $^{188}\text{Os}$  (Table 1.3) allows us to perform quantitative  $^{188}\text{Re}$  SPECT imaging which is essential to verify activity distributions in the patient body and to estimate tumor and healthy organ's radiation doses. However, the interaction of  $\beta$ -particles with tissue results in the emission of Bremsstrahlung (BRS) radiation which contributes to patient dose and may be detected by the gamma camera. As the popularity of radionuclide therapies using  $^{188}\text{Re}$  increases, the BRS effect following administration of  $^{188}\text{Re}$  radiopharmaceuticals becomes more relevant because it may influence both accurate SPECT/CT quantification and internal dose calculation.

The understanding of the BRS energy spectrum associated with  $^{188}\text{Re}$  emissions is fundamental to optimize image acquisition parameters and obtain accurate quantification of images. In particular, it is important to quantify the fraction of BRS detected photons in the  $^{188}\text{Re}$  photopeak window to determine if additional corrections for  $^{188}\text{Re}$  SPECT images are needed. Different simulation studies have been performed to investigate BRS emission from two commonly used isotopes in radionuclide therapies:  $^{90}\text{Y}$  [108–110] and  $^{131}\text{I}$  [111]. Additionally, Monte-Carlo (MC) simulations were used to analyze primary and scattered components in  $^{177}\text{Lu}$ ,

$^{131}\text{I}$  and  $^{90}\text{Y}$  planar images [112]. To the best of our knowledge, no detailed studies of BRS production and  $\gamma$ -emissions for  $^{188}\text{Re}$  have been performed.

The purpose of this study was to investigate: (1) the characteristics of BRS spectra produced in tissue by  $^{188}\text{Re}$  and; (2) the characteristics of the  $^{188}\text{Re}$  energy spectra detected by a typical SPECT camera (SymbiaT, Siemens Medical, Germany) with low energy high resolution (LEHR), medium energy low penetration (MELP) and high energy (HE) collimators. The features of both BRS production and detected energy spectra with SPECT were obtained using MC simulations of a *Jaszczak* phantom filled with water. The MC model of the SPECT system was validated against experimental measurements of the  $^{188}\text{Re}$  detected energy spectra acquired from the same *Jaszczak* phantom.

## 3.2 Materials and Methods

### 3.2.1 Simulation of Spectra Detected by SPECT Camera

#### 3.2.1.1 Camera Modeling

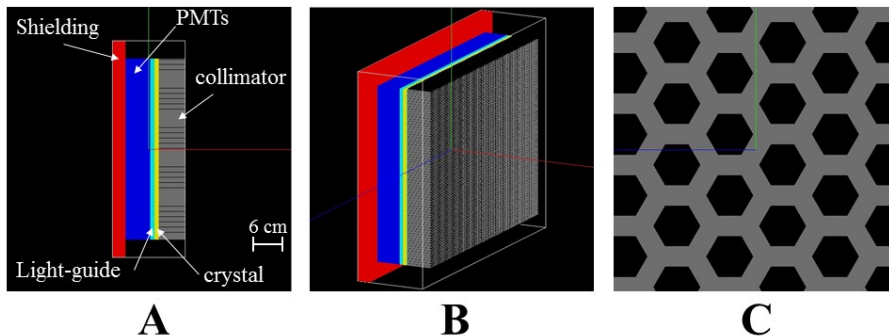


Figure 3.1 Geometry of SPECT camera model implemented in GATE. (A) lateral view, (B) 3-D surface rendered view and, (C) magnified frontal view showing the collimator holes. Note: the lateral shielding volume surrounding the camera head is not shown in these views.

A SymbiaT (Siemens Healthcare, Erlangen, Germany) SPECT camera with LEHR, MELP, and HE collimators was modeled using the MC code GATE v6.1 [53,54]. The

collimator's geometries were obtained from the manufacturer datasheets (Table 3.1). The camera detector was modeled as a 3/8" Sodium-Iodide (NaI) crystal covered by a 0.5 mm aluminum layer placed at the front. The back-compartment region of the detector contained a 0.95 cm thick light-guide made of glass followed by a 5.65 cm uniform material mix (23% glass, 56% vacuum and 21% air [113]) that modeled the photomultiplier tubes. The camera head shielding was modeled as a lead layer with a thickness of 4 cm at the sides and 3 cm at the back [114]. The geometry of the camera simulated with GATE is shown in Figure 3.1.

The  $^{188}\text{Re}$  decay data was built-in in GATE, and it is based on the Evaluated Nuclear Structure Data File (ENSDF) database [115]. The interactions of radiation were modeled using the standard electromagnetic physics list builder ("emstandard\_op3") of GATE. The physics list includes modelling of photoelectric processes, Compton and Rayleigh scattering, pair production, electron ionization and scattering, BRS and electron-positron annihilation. The detector energy resolution  $R$  (full width half-maximum, FWHM) was set at  $R_0 = 10\%$  for the reference energy  $E_0 = 140$  keV. The dependence of resolution  $R$  with photon energy was modeled as an inverse square root law ( $R(E) = R_0 E_0 / \sqrt{E}$ ). Only photons which deposited energies between 50 keV to 700 keV in the detector were recorded.

**Table 3.1 Characteristics of the SymbiaT LEHR, MELP and HE collimators. Data obtained from manufacturer datasheets [116]. Note: the LEHR, MELP and HE collimator specifications were determined using  $^{99\text{m}}\text{Tc}$ ,  $^{67}\text{Ga}$  and  $^{131}\text{I}$  sources, respectively.**

Collimator type	Hole diameter [cm]	Septal length [cm]	Septal thickness [cm]	Sensitivity @10 cm [cpm/ $\mu\text{Ci}$ ]	Geometric resolution @10 cm [mm]	System resolution @10 cm [mm]
LEHR	0.111	2.405	0.016	202	6.4	7.5
MELP	0.294	4.064	0.114	275	10.8	12.5
HE	0.400	5.970	0.200	135	13.2	13.4

### 3.2.1.2 Phantom Simulations

A total of three simulation runs (one for each collimator), modeling experimental acquisitions, were performed. The geometry of a *Jaszczak* phantom (radius = 11.1 cm; height = 19.5 cm) containing a hollow plastic sphere (radius = 1.0 cm; shell thickness = 0.1 cm) placed at the center of the phantom was built in GATE. The phantom body was filled with water and the distance from the center of the sphere to the collimator surface was set to 25 cm. The sphere body was filled with a uniform activity of  $^{188}\text{Re}$  dissolved in water.

From the simulation runs, the following data were recorded at three successive levels:

1. The total number and energy spectra of photons generated inside the *Jaszczak* phantom.
2. The total number of photons that were not absorbed and escaped the phantom.
3. The energy spectra of photons detected by the camera for the three collimators.

At the first two levels, the total BRS yield ( $TBY$ ), defined as the ratio of photons created by the BRS process ( $\gamma_{Bremss}$ ) relative to the total number of  $^{188}\text{Re}$  decays ( $N$ ), was evaluated using the following formula:

$$TBY = \frac{\gamma_{Bremss}}{N}. \quad (3.1)$$

The parameter  $\gamma_{Bremss}$  included not only BRS photons generated by the  $\beta$ -particles emitted by  $^{188}\text{Re}$ , but also those generated by electrons created in secondary processes, such as ionization and internal conversion. In addition, the total non-BRS yield ( $NBY_i$ ) was estimated, where  $NBY_i$  was defined as the ratio of photons produced by processes other than BRS ( $i = \text{“radioactive”}$  for photons from  $^{188}\text{Os}$  de-excitation;  $i = \text{“X-ray”}$  for photons produced by photoelectric absorption inside the phantom) to  $N$ :

$$NBY_i = \frac{\gamma_i}{N}. \quad (3.2)$$

The  $NBY_{radioactive}$  was further sub-divided into 155-keV photons (which are used for imaging  $^{188}\text{Re}$  with SPECT), low-energy photons ( $< 155$  keV) and high-energy photons ( $>155$  keV). Additionally, the mean energies of the BRS photons generated inside the phantom ( $MBE_{gen}$ ), as well as the mean energy of those BRS photons escaping the phantom ( $MBE_{out}$ ), were calculated. The difference of the total number of photons recorded at levels 1 and 2 reflects the effect of photon attenuation in the *Jaszczak* phantom.

At the third level, the energy spectrum recorded by the camera was simulated for all three collimators. In this case, the detected photons were separated into the following components:

- Primary:  $\gamma$ -photons generated by the radioactive decay of the  $^{188}\text{Re}$  source that did not interact with any component of the system and whose energy was fully deposited in the detector.
- Scatter: photons emitted from the  $^{188}\text{Re}$  decay that scattered with one, or more parts of the system before being detected. The origin of scattered photons was further categorized into 155-keV self-scattered and high energy downscattered photons. This group also includes photons that scatter in the detector crystal and deposit only a fraction of their initial energy.
- Bremsstrahlung: photons that were produced by Bremsstrahlung process when  $\beta$ -particles or secondary electrons interacted with the surrounding material.
- X-rays: photons that were produced by lead atomic de-excitations after photoelectric absorption in the collimator or shielding material.

GATE includes the so-called *actors* or sets of tools that allow the user to interact with the simulation and collect different types of information. The *phase space actor* was used to

compare the production of photons inside the phantom with those that exit the phantom (i.e., levels 1 and 2). For level 3, a new actor was coded to correctly identify scattered photons, in particular those that scattered in the crystal and deposited only part of their energy, and to identify the process which generated them (e.g. radioactive vs. BRS). For the first two levels of analysis,  $2 \times 10^7$   $^{188}\text{Re}$  decays were simulated. For level 3,  $3 \times 10^9$  decays were launched. The simulations were performed using a 64-core computer with 128 GB of RAM, and all the cores were used at the same time using parallel computing. The simulation results were validated against the experimental energy spectrum detected by the gamma camera acquisition of the *Jaszczak* phantom which was scanned under the same conditions as the simulations.

Finally, simulated planar images of the *Jaszczak* phantom for the three collimators were collected using the 155-keV photopeak window with 20% window width. Additionally, line profiles were drawn through the center of the  $^{188}\text{Re}$  source. The relative numbers of primary, scattered, and BRS photons measured in the entire image and in a circular ROI with 5.6 cm diameter drawn around the source (referred as to *source ROI*) was determined for each collimator acquisition.

### **3.2.2 Phantom Experiments**

In order to validate the simulations, three measurements of the phantom spectra were performed at the Nuclear Medicine department of the Vancouver General Hospital (Vancouver, Canada) using the same SymbiaT SPECT camera which was modeled in our simulations. The experimental conditions (i.e., phantom sizes, acquisitions geometry and collimator) were identical to those used in the simulations (Section 3.2.1.2). The activity placed in the  $^{188}\text{Re}$  sphere was 62.1 MBq.

The spectra were collected for each of the three collimators, namely LEHR, MELP and HE. ASCII files containing the measured energy spectra were exported directly from the manufacturer's computer and rescaled to match the corresponding simulated spectra.

Unfortunately, the camera does not provide the information about the duration of spectrum measurement (probably because energy spectra are only measured and visualized for quality control purposes, to check location and shapes of the photopeaks and to help the setup of the energy windows). Due to this problem, it was not possible to match the exact number of decays that occurred during spectra acquisition with the number of the simulated events. Therefore, the energy spectra were collected by visually inspecting their shapes until the number of counts was such that no apparent changes in shapes were observed and then, they were normalized dividing the counts in each bin by the sum of counts in the energy interval from 100 keV to 500 keV [109]. Since the low energy parts of the spectra were affected by both the energy cut-off set on the physical camera and the camera model used in simulations [113], only energy higher than 100 keV were used for normalization.

### 3.3 Results

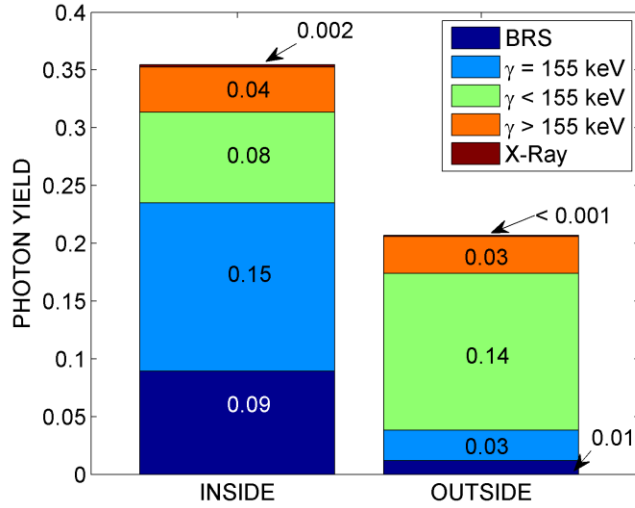


**Figure 3.2 Photon yields of Bremsstrahlung ( $TBY$ ),  $\gamma$ -particles ( $NBY_{radioactive}$ ) and X-rays ( $NBY_{X-ray}$ ) generated by the  $^{188}\text{Re}$  decay source inside the simulated Jaszczak phantom (INSIDE), and the corresponding yields of photons that escaped the phantom (OUTSIDE).**

Figure 3.2 presents the BRS (Equation 3.1) and non-BRS yields (Equation 3.2) calculated using GATE simulation of the  $^{188}\text{Re}$  source for photons generated inside the *Jaszczak* phantom, and those which escaped the phantom. The energy spectrum of all photons produced inside the *Jaszczak* phantom and that of photons that escape of the phantom is shown in Figure 3.3. The mean energies of BRS photons which were generated in the phantom ( $MBE_{gen}$ ) as well as those which left the phantom ( $MBE_{out}$ ) were 32.1 keV and 120.1 keV, respectively.

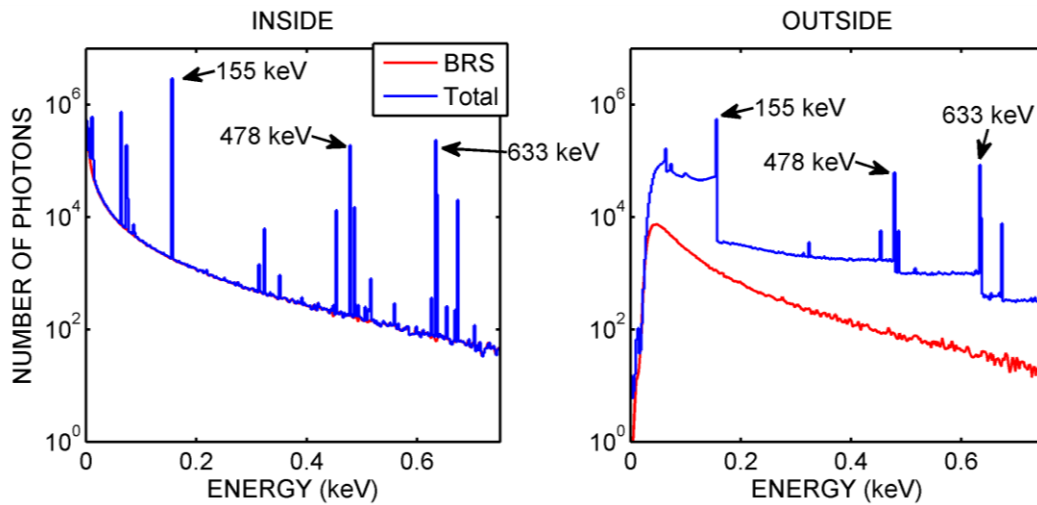


Figure 3.3 Energy spectra of (A: INSIDE) total photons produced inside the Jaszczak phantom after  $^{188}\text{Re}$  decay and (B: OUTSIDE) total photons that escaped the phantom. The contribution from BRS photons is also shown in both cases.

Figure 3.4 compares the measured and simulated energy spectra for the  $^{188}\text{Re}$  source acquired with LEHR, MELP and HE collimators. Figure 3.5 shows the components of the simulated spectra presented in Figure 3.4.

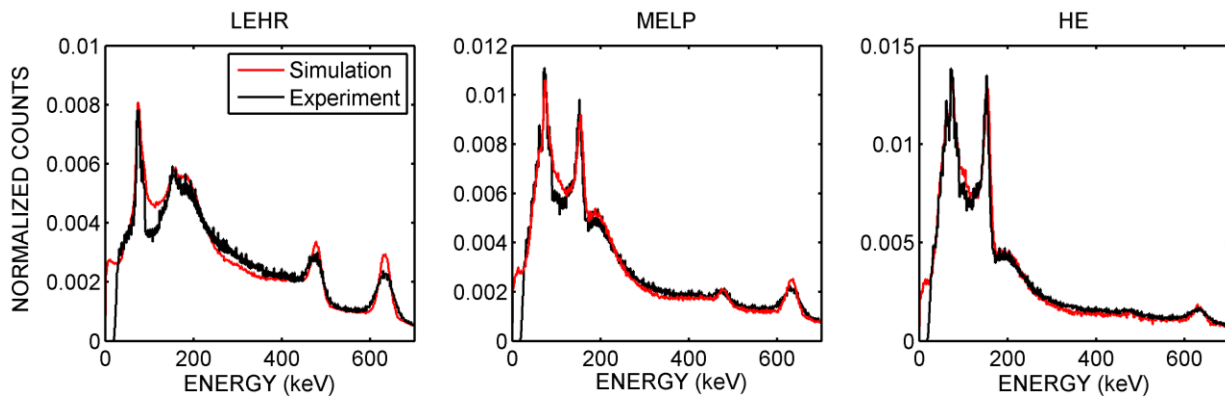


Figure 3.4 Comparison between experimental and simulated  $^{188}\text{Re}$  energy spectra for LEHR, ME and HE collimator.

Figure 3.6 shows the profiles obtained from the planar images of the  $^{188}\text{Re}$  source placed in the Jaszczak phantom for the 20% energy window set around the 155-keV photopeak. The

spatial distributions of primary, scattered and BRS photons are separately displayed. Table 3.2 summarizes the relative contributions of primary, scatter and BRS photons to the entire projection images and to the *source ROI*.

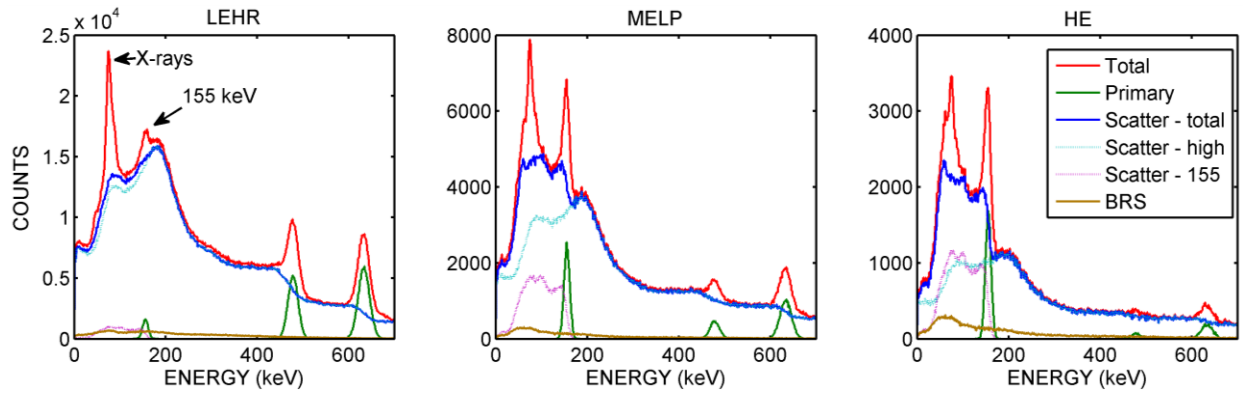


Figure 3.5 Analysis of different components of the simulated  $^{188}\text{Re}$  energy spectra acquired with LEHR, ME and HE collimators.

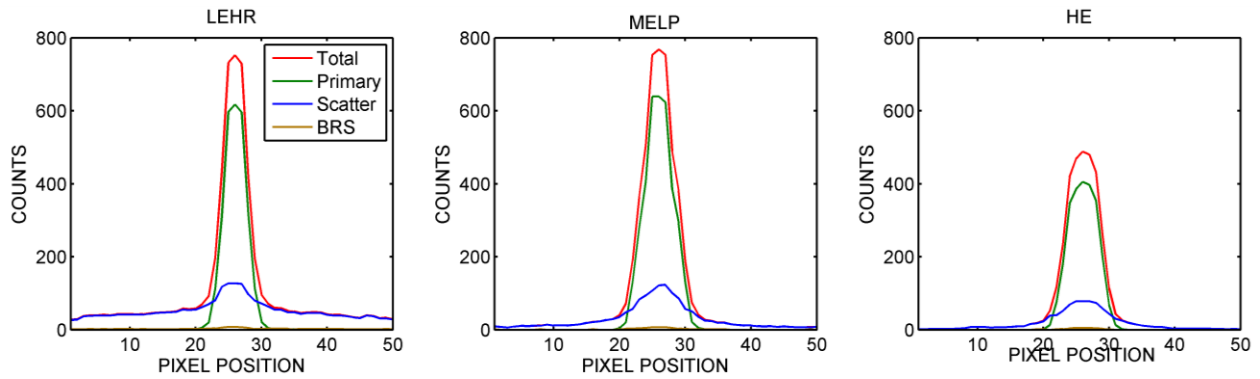


Figure 3.6 Profiles obtained from  $^{188}\text{Re}$  planar images using a 20% width window set around the 155 keV photopeak.

**Table 3.2 Relative contributions of primary, scatter and BRS photons to the  $^{188}\text{Re}$  image acquired using 20% wide energy window set on the 155 keV photopeak. Contributions to the entire image and the *source ROI* were estimated.**

Collimator	Relative contributions to the entire image			Relative contributions to the <i>source ROI</i>		
	Primary [%]	Scatter [%]	BRS [%]	Primary [%]	Scatter [%]	BRS [%]
LEHR	5.2	91.1	3.7	72.0	26.5	1.4
MELP	23.5	74.0	2.5	79.4	19.5	1.2
HE	36.1	64.6	2.3	80.3	18.5	1.2

### 3.4 Discussion

#### 3.4.1 Comparison of Simulations and Phantom Experiments

Direct quantitative comparison of the simulated and experimental spectra was difficult because normalization, which had to be applied here, was rather arbitrary. Additionally, the camera modeling used in the simulation was approximate and did not fully reflect the details of the geometry of our experimental studies. Despite these limitations, the shapes of the spectra obtained from simulations reproduce relatively well those from experimental measurements (Figure 3.4). The differences seen in all spectra at very low photon energies, where the simulations overestimate the measured spectra, are due to the fact that most SPECT cameras have a cut-off energy below which no photons are accepted. For the Siemens SymbiaT camera which was used in this study, the cut-off value is set around 20 keV.

In the range of photon energies between 100 keV and 120 keV, simulations exceed experimental data suggesting increased number of scattered photons in the simulations. This effect is probably due to discrepancies in the modeled camera geometry. A detailed examination of the relationship between the accuracy of camera modeling (with medium energy general

purpose collimator) and the shapes of the energy spectra simulated by GATE was performed by Rault *et al.* [113]. The camera model used in our simulation would correspond to the “intermediate model” used in Rault’s study. Although direct comparison of the simulation results is impossible because none of the radioisotopes which were simulated by us were included in Rault’s study, the general trends are very similar. In particular, similar excess of scattered photons in the 100-120 keV region as seen in our study, was also observed in  $^{131}\text{I}$  and  $^{18}\text{F}$  spectra simulated by Rault. Overall, the agreement between the simulated and experimental  $^{188}\text{Re}$  spectra is good, best for the HE collimator.

### 3.4.2 Quantitative Analysis of $^{188}\text{Re}$ Bremsstrahlung Simulations

At the level 1 and 2 of the simulations, the number of photons produced inside the phantom, and those that escaped the phantom (Figure 3.2) were evaluated and the following characteristics were observed:

- Approximately 9 BRS photons are produced per 100 decays of  $^{188}\text{Re}$  in tissue, from which only 1 BRS photon is able to escape the phantom. The yield of BRS photons escaping the phantom is much lower than that of non-BRS photons, which account to approximately 20 photons per 100 decays of  $^{188}\text{Re}$ . However, out of these 20 photons, only 3 have the energy of 155 keV, useful for SPECT imaging. The remaining photons that escape the phantom have mostly low energies ( $< 155$  keV) and correspond to scatter photons.
- The *MBE* of BRS photons that escaped the phantom relative to *MBE* of photons which were generated in the phantom is significantly shifted towards higher energies (similar to “beam hardening” of X-rays), indicating that majority of BRS photons have very low energy, as seen in Figure 3.3 A and are absorbed in the water filling the phantom.

- The energy spectra of photons generated inside the phantom illustrates the complexity of  $^{188}\text{Re}$  decay, which shows numerous high-energy gamma emissions. Some of these emissions have energies as high as 2.1 MeV [14] (not shown in Figure 3.3). The scatter interactions of high-energy and 155 keV photons in the phantom volume results in an energy spectrum of “escaping” photons dominated by the low-energy (<155 keV) photons (Figure 3.2 and Figure 3.3).
- The fraction of  $^{188}\text{Re}$ -BRS photons that leave the phantom relative to the total number of photons recorded outside the phantom is 5%.

### 3.4.3 Spectra Analysis and Optimization of Acquisition Parameters

Simulations provide an excellent opportunity to isolate groups of photons that were created through different effects, with or without scatter in the media, and to analyze their relative contributions to the spectra (Figure 3.5). Such analysis may be very helpful in identifying acquisition parameters (collimators and energy windows) which would lead to best quality images.

The contribution from BRS to the 155 keV photopeak window  $^{188}\text{Re}$  is very low, much lower than that from other photons. The number of detected BRS photons never exceed 4% of the total detected photons in the entire projection image (Table 3.2), and decreased to 1% - 1.5% when only the source ROI was considered. Therefore, since BRS contribution to the photopeak counts is small, the selection of collimator and energy windows can be based entirely on the analysis of  $^{188}\text{Re}$ 's  $\gamma$ -emissions. The following paragraph summarizes both current practice and the recommendations based on this study.

Traditionally, the 155 keV peak is used in imaging  $^{188}\text{Re}$  [117]. Considering its relatively low energy, close to the 140 keV of  $^{99\text{m}}\text{Tc}$ , the use of LEHR collimator would seem to be well

justified. However,  $^{188}\text{Re}$  numerous high energy emissions, although relatively weak, can easily penetrate this collimator. The contribution from these high-energy photons scattered in the patient and the camera is responsible for substantial background visible in Figure 3.6. In our simulated spectra, the scatter component for the LEHR collimator was greater than 90% in the entire image but decreased to 26% when the ROI was chosen around the source. In both, the entire image and ROI, the primary photon component is higher for the MELP than for LEHR collimator, and even more so for the HE (Table 3.2). Considering only counts in the ROI, the ratio of primaries to scatter increased even more with the HE collimator, providing the best ratio, by 5.7% greater than MELP. Therefore, based on these results, the use of MELP or HE collimators is recommended for  $^{188}\text{Re}$  imaging. The advantage of using MELP over HE collimator would be its higher sensitivity and better resolution; however, more septal penetration was observed in the MELP than in HE images.

It is important to note that the geometry used in these simulations (i.e., sphere located at the center of a Jaszczak phantom) might not be representative of other possible activity distributions found in patients studies. Therefore, the obtained BRS, primary and scatter photon fractions reported in this study might differ from other cases. Despite these differences, it is expected the trends observed in our simulation study (i.e., BRS fraction is small compared to  $\gamma$ 's) will also be observed for other activity distributions.

### **3.5 Conclusions**

The aim of this study was to investigate the characteristics of  $\gamma$ -emissions and BRS produced in tissue by  $^{188}\text{Re}$ . This was done in order to improve our understanding of the energy spectra acquired during medical imaging studies as this would allow us to identify camera configuration which would result in best quality and quantitative accuracy of images.

The simulations showed not only that  $^{188}\text{Re}$  BRS yield is very low (below 9%), but also that most of the created BRS photons have energies below 50 keV. For this reason, when imaging  $^{188}\text{Re}$ , BRS contributions to the energy spectra detected by the camera would be less than 4%. However, background of scattered high-energy photons must be corrected for when quantitative activity determination is required. This background is especially pronounced in studies performed with LEHR collimator.

The analysis of  $^{188}\text{Re}$  simulated spectra indicates that optimal imaging conditions for this isotope will be achieved when using HE collimator.

## Chapter 4: $^{188}\text{Re}$ Image Performance Evaluation of a Pre-Clinical Multi-Pinhole SPECT/PET/CT system

### 4.1 Introduction

Evaluation of new radiopharmaceuticals often involves small animal imaging studies using high resolution pre-clinical SPECT [118] and CT systems [119] aiming to establish the radiotracers' pharmacokinetics, targeting ability and potential toxicity in different organs [120]. To accurately quantify tracer uptake, imaging systems are required to provide users with high resolution, statistically robust images. Many pre-clinical SPECT and/or PET imaging systems have been evaluated for this purpose, with different radioisotopes [121–126]. One of such state-of-the-art scanners is the VECTor/CT (MILabs, Utrecht, The Netherlands), a pre-clinical SPECT/PET/CT system that uses multi-pinhole collimators and is able to achieve submillimeter spatial resolution [127,128]. VECTor's quantitative capabilities have been demonstrated for isotopes such as  $^{99\text{m}}\text{Tc}$ ,  $^{111}\text{In}$ ,  $^{125}\text{I}$ ,  $^{201}\text{Tl}$  [129,130] and most recently, for  $^{131}\text{I}$  [131]. Additionally, image quality for  $^{99\text{m}}\text{Tc}$  [132,133],  $^{18}\text{F}$  [134] and simultaneous imaging of  $^{99\text{m}}\text{Tc}$  and  $^{18}\text{F}$  [135,136] have been investigated. Similarly, de Swart *et al.* [137] evaluated the feasibility of imaging  $^{213}\text{Bi}$ , a SPECT isotope emitting high energy gammas. At this time, however, no systematic studies of VECTor camera performance for  $^{188}\text{Re}$  have been reported. Although its 155 keV gamma emissions seem to be perfectly suited for SPECT imaging using low energy collimators,  $^{188}\text{Re}$  also emits several high-energy photons (similar to  $^{213}\text{Bi}$ ) which have low intensities but can still negatively impact the quantitative accuracy of the images.

The goal of our study was to investigate  $^{188}\text{Re}$  image quality and accuracy of data quantification obtained with the VECTor/CT camera by performing a series of phantom

experiments using two multi-pinhole collimators: the Ultra High Resolution rat-size Collimator (UHRC); and the High Energy Ultra High Resolution mouse-size Collimator (HE-UHRC). The camera performance for imaging  $^{188}\text{Re}$  was compared with that for  $^{99\text{m}}\text{Tc}$  (which was considered the gold-standard) using similar phantom configurations and/or the published data. Additionally, energy spectra acquired experimentally and those from Monte-Carlo simulations were analyzed to help us to understand the challenges of  $^{188}\text{Re}$  imaging using the two multi-pinhole collimators. Finally, the characteristics of the ex-vivo images of a *C57BL/6*-mouse injected with biodegradable microspheres [75] labelled with  $^{188}\text{Re}$  were evaluated. Although this study focuses on  $^{188}\text{Re}$  imaging using VECTor/CT, the results might also be relevant for other imaging system based on pinhole when studying isotopes that emit multiple high-energy photons such as  $^{67}\text{Ga}$ ,  $^{123}\text{I}$  or  $^{124}\text{I}$ .

## **4.2 Materials and Methods**

### **4.2.1 The VECTor/CT System**

#### **4.2.1.1 VECTor/CT**

The phantom experiments were performed using VECTor/CT, a small animal SPECT/PET/CT camera, located at the Centre for Comparative Medicine in Vancouver, BC, Canada. The VECTor system is capable of imaging both SPECT and PET radiotracers [135]. Additionally, the CT module provides anatomical information of the imaged animal and is used to create transmission maps for use in attenuation correction. VECTor consists of three large field-of-view (FOV) sodium iodide (NaI) detectors arranged in a triangular geometry (Figure 4.1). The direction of incoming photons is determined using focusing multi-pinhole collimators.

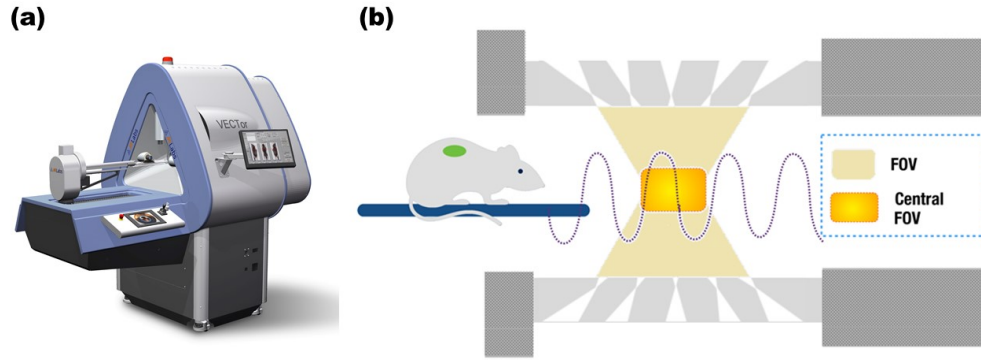


**Figure 4.1 (a) The VECTor/CT camera system (printed with permission of MILabs) (b) Cross-sectional diagram of the collimator geometry with the Field of View (FOV) and the Central Field of View (CFOV).**

Two types of multi-pinhole collimators were used in our study: The Ultra High Resolution rat-size Collimator (UHRC) [127] and the High Energy Ultra High Resolution mouse-size Collimator (HE-UHRC) [135]. In particular, the HE-UHRC is specifically designed to reduce collimator walls and pinhole edge penetration of higher energy gammas. Table 4.1 summarizes the main characteristics of the collimators.

**Table 4.1 Characteristics of UHRC and HE-UHRC geometry. All dimensions are in mm.**

	<b>Bore diameter</b>	<b>Wall thickness</b>	<b>Number of pinholes</b>	<b>Pinhole diameter</b>
<b>UHRC (rat size)</b>	98	15	75	1
<b>HE-UHRC (mouse size)</b>	48	43	192	0.7

The volume within the object which is simultaneously sampled by all the pinholes is referred to as the Central Field of View (CFOV) of the camera (Figure 4.1). To image objects with volumes larger than the VECTor’s CFOV (6 cm<sup>3</sup> for UHRC and 1 cm<sup>3</sup> for HE-UHRC), the

animal bed moves and stops inside the camera using so-called multi-planar or spiral trajectories [138], whereas the detectors and pinhole collimator remain stationary.

#### 4.2.1.2 Image Reconstruction and System Calibration

VECTor acquires data in a list-mode over a wide range of photon energies (30 to 1200 keV), which enables the user to select and test different energy-window settings. This post-processing is done while creating the projection data, after the animal scan is finished.

Additionally, this list-mode acquisition allows for the creation of datasets with different number of counts from a single experiment.

The photopeak and scatter/background window settings used to create  $^{188}\text{Re}$  and  $^{99\text{m}}\text{Tc}$  projections in our study are shown in Table 4.2. The lower and upper windows were used to correct for self-scatter, high-energy scatter and background of the photopeak data using the triple energy window (TEW) method [26]. The projection data were then reconstructed using a Pixel-based ordered subset expectation maximization (POSEM) algorithm [139] with 16 subsets and 6 iterations and a voxel size of  $0.4 \times 0.4 \times 0.4 \text{ mm}^3$ . After reconstruction, all images were corrected for attenuation using the CT-based non-uniform Chang method [130,140] (CT tube voltage = 60 kV, tube current = 615  $\mu\text{A}$ ).

**Table 4.2 Energy window settings used for reconstruction of  $^{188}\text{Re}$  and  $^{99\text{m}}\text{Tc}$  data. All the quantities are in keV.**

<b>Isotope</b>	<b>Photopeak window</b>	<b>Lower window</b>	<b>Upper window</b>
$^{188}\text{Re}$	(139.5,170.5)	(120.9,139.5)	(170.5,189.1)
$^{99\text{m}}\text{Tc}$	(119.9,154.1)	(111.3,119.9)	(154.1,162.7)

In order to obtain 3-D images of activity distribution, the reconstructed images were re-scaled using the experimentally determined calibration factor ( $CF$ ) that converts the voxel counts (arbitrary units) into the units of activity concentration (MBq/mL). The  $CF$  was obtained following the method described by Wu *et al* [129]. The details of our  $CF$  experiments are provided in the Appendix B.1.

#### 4.2.2 Phantom Experiments

The fact that the energies of  $^{99m}\text{Tc}$  and the main photopeak of  $^{188}\text{Re}$  (140 keV and 155 keV, respectively) are very similar may suggest that UHRC would be well suited for  $^{188}\text{Re}$  imaging as this collimator has been shown to yield accurate  $^{99m}\text{Tc}$  quantification [129,130]. However, since  $^{188}\text{Re}$  emits also high-energy photons, high-energy  $\beta$ -particles and associated Bremsstrahlung radiation in addition to the 155 keV gammas, the HE-UHRC may thus provide better image quality and image quantification. Although  $^{188}\text{Re}$  has already been imaged with VECTor using HE-UHRC [77,141], the advantages of using HE-UHRC over UHRC have not been investigated. Based on these considerations, imaging studies of  $^{188}\text{Re}$  were performed using both collimators.

Table 4.3 summarizes the three series of phantom experiments that were performed to assess image quality and image quantification. The image quality experiment aimed to determine the spatial resolution, contrast and contrast-to-noise ratio (CNR) using two different micro-*Jaszczak* phantoms (referred to as a.1 and a.2). Image quantification was evaluated in experiments with two phantom configurations: 1) a mouse-size phantom to assess quantification in animal whole-body scans and; 2) a multi-point source phantom to evaluate quantification accuracy at different levels of activity concentration and to assess potential cross-talk effects due to activity which is present outside of the currently imaged CFOV volume. Additionally, the

same phantom experiments were repeated for  $^{99m}\text{Tc}$  (imaged with both UHRC and HE-UHRC). The details of all the phantom experiments are described in Section 4.2.2.1 and Section 4.2.2.2.

**Table 4.3 Summary of phantom experiments performed to evaluate image quality and image quantification of  $^{188}\text{Re}$  with the VECTor camera.**

	<b>Phantom experiment</b>	<b>Experimental conditions</b>	<b>Objective</b>	<b>Isotope</b>	<b>Collimator</b>
<b>Image Quality</b>	Two different Micro- <i>Jaszczak</i> phantoms (a.1 and a.2)	Images were reconstructed using 100%, 25% and 2.5% of the total acquired counts	Measure spatial resolution, contrast and CNR at three level of noise	$^{99m}\text{Tc}$ and $^{188}\text{Re}$	UHRC and HE-UHRC
<b>Image Quantification</b>	Mouse-size phantom	Phantom body filled with air, water and hot (radioactive) water	Accuracy of quantification for whole-body animal scan	$^{99m}\text{Tc}$ and $^{188}\text{Re}$	UHRC and HE-UHRC
	Multi-point source phantom	Phantom body filled with water and hot (radioactive) water	Accuracy of quantification for small sources (lesion) of decreasing activity	$^{99m}\text{Tc}$ and $^{188}\text{Re}$	UHRC and HE-UHRC

#### 4.2.2.1 Image Quality

The spatial resolution of the system for  $^{188}\text{Re}$  and  $^{99\text{m}}\text{Tc}$  images was determined using two *Micro-Jaszczak* resolution phantoms containing 6 sectors of small diameter rods. Each sector of the phantom consisted of a set of equally sized capillaries with diameters ranging from 0.85 mm to 1.7 mm (phantom a-1) and 0.40 mm to 1.1 mm (phantom a-2) (Figure 4.2a). The space between the rods was equal to the rod diameter. Phantom a-1 was filled with 12 MBq of  $^{188}\text{Re}$  activity and was scanned for 90 minutes using UHRC and HE-UHRC. In order to obtain similar number of photons of 155 keV  $^{188}\text{Re}$  and 140 keV  $^{99\text{m}}\text{Tc}$  during the image quality phantom acquisitions, phantom a-1 was filled with 15.4 MBq of  $^{99\text{m}}\text{Tc}$  activity and was scanned for 10 min using UHRC and HE-UHRC. Phantom a-2 was filled with 14 MBq of  $^{188}\text{Re}$  activity and was scanned for 60 minutes using HE-UHRC. Similarly, phantom a-2 was filled with 57 MBq of  $^{99\text{m}}\text{Tc}$  and was scanned for 3 minutes using HE-UHRC. The acquired scan times resulted in approximately  $8 \times 10^9$  (155 keV) and  $9 \times 10^9$  (140 keV) photons emitted during  $^{188}\text{Re}$  and  $^{99\text{m}}\text{Tc}$  measurements, respectively. The resolution of the system was determined as the minimum rod diameter that could be clearly distinguished in the reconstructed image. Image contrast and CNR vs rod diameter were quantified using images of the same *Micro-Jaszczak* resolution phantoms following the method described by Walker *et al.* [134]. The details of this method are also described in the Appendix B.2.

The acquired list-mode data were post-processed to produce three projection sets with decreasing counts (equal to 100%, 25% and 2.5% of the total counts acquired in the original scans). The image contrast and CNR values were plotted against the rod diameter for these three decreasing levels of activity (corresponding to increasing noise).

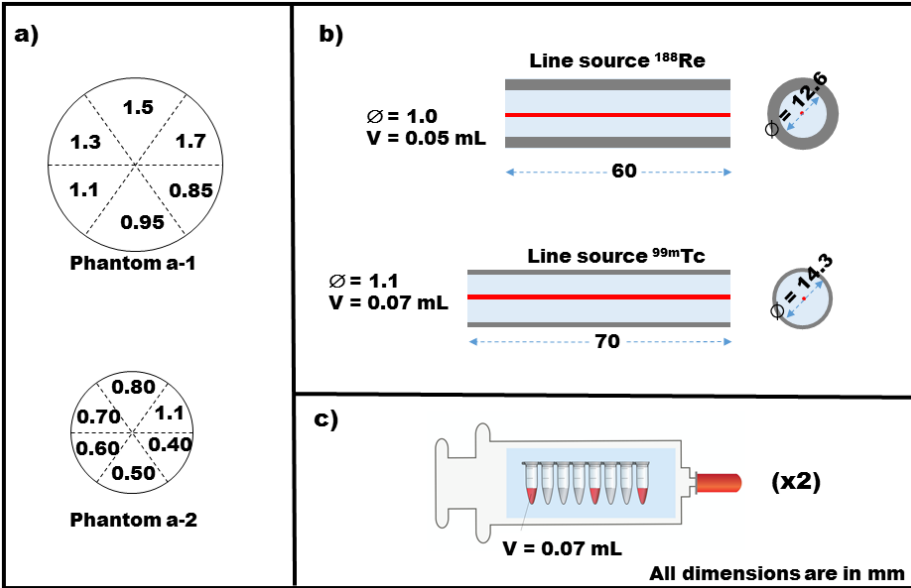


Figure 4.2 Geometry of (a) the two micro-*Jaszczak* phantoms, (b) the two line-source phantoms and (c) the multi-source phantom. Due to the arrangement of the small sources in the multi-source phantom, two syringes were needed in order to scan a total of 6 sources. All reported volumes (in mL) refer to the filling volumes. All dimensions are in mm.

#### 4.2.2.2 Image Quantification

##### 4.2.2.2.1 Mouse-size Phantom Experiments

Two cylindrical mouse-sized phantoms were custom-built to test the accuracy of  $^{99m}\text{Tc}$  (gold standard) and  $^{188}\text{Re}$  (isotope of interest) activity quantification for conditions modelling a whole-body animal scan. The phantoms contained a capillary tube (ID = 1.0-1.1 mm, volume = 0.05-0.07 mL) filled with activity, located along the central axis of a small cylinder (Figure 4.2b). For each experiment, the phantom was scanned three times: (1) with air in the phantom body to test the accuracy of reconstruction (Scan A), (2) with water in the phantom body to test the attenuation and scatter corrections (Scan B) and (3) with radioactive water (hot water) in the phantom body to test the accuracy of quantitation using the conditions of a real animal scan (Scan C).

**Table 4.4 Activities, source-to-background ratio and acquisition times for the mouse-size phantom experiments.**

	<b>Collimator</b>	<b>Line- source [MBq]</b>	<b>Line- source [MBq/mL]</b>	<b>Background [MBq/mL]</b>	<b>Source-to- Background ratio</b>	<b>Acquisition time [min]</b>
<sup>99m</sup> Tc	UHRC	13.8	203	2.3	88	10
	HE-UHRC					
<sup>188</sup> Re	UHRC	25	500	5.0	100	30
	HE-UHRC					

The activities of <sup>188</sup>Re and <sup>99m</sup>Tc filling the phantom insert (line-source) and the background activity concentrations are listed in Table 4.4 (adjusted to the time of Scan A), together with acquisition times used in these experiments. Overall, the total number of 155 keV photons emitted from the line-source during the <sup>188</sup>Re scans (approximately  $6.8 \times 10^9$ ) was comparable to the number of 140 keV photons emitted during the <sup>99m</sup>Tc acquisitions (approximately  $7.4 \times 10^9$ ).

#### **4.2.2.2.2 Multi-source Phantom Experiments**

The multi-source phantom was designed to evaluate the accuracy of activity quantification for different levels of activity concentration. The phantom (Figure 4.2c) consisted of 0.2 mL 8-strip Polymerase Chain Reaction (PCR) tubes placed inside a 20-mL plastic syringe. In total, six individual compartments of the PCR tubes were filled with decreasing amounts of <sup>188</sup>Re activity (70  $\mu$ L each volume), modelling different levels of uptake in organs or tumors in the animal. The space between two consecutive filled compartments was determined as shown in Figure 4.2c to ensure that only one source was visible within the CFOV of each individual acquisition. Since a maximum of three compartments were filled per PCR tube, two PCR tubes were required to scan

the total of six individual compartments. Two configurations for each PCR tube were imaged: a) with the syringe filled with water (cold-water scan) and b) filled with 1 MBq/mL of  $^{188}\text{Re}$  activity concentration (hot-water scan). The phantom was imaged with UHRC and HE-UHRC. Additionally, the cold-water and hot-water phantom experiment was repeated with  $^{99\text{m}}\text{Tc}$  activity using the UHRC and HE-UHRC.

The point-sources covered a relatively wide range of activities ranging from 0.3 MBq to 4.0 MBq (or 4.3 MBq/mL to 57.1 MBq/mL activity concentration) and were imaged individually (using appropriate FOV's), taking advantage of the targeting capabilities of multi-pinhole imaging with VECTor [142]. The acquisition time for each individual point-source was 5 minutes and 2 minutes for  $^{188}\text{Re}$  and  $^{99\text{m}}\text{Tc}$  scans, respectively.

#### 4.2.2.3 Data Processing for Image Quantification

The accuracy of image quantification was evaluated by calculating the percent difference between the activity recovered from the SPECT images ( $A_{SPECT}$ ) (reconstructed and rescaled using  $CF$  factor) and the true activity of the phantom, as measured with the dose calibrator ( $A_{TRUE}$ ):

$$\%_{diff} = \frac{A_{SPECT} - A_{TRUE}}{A_{TRUE}} \times 100. \quad (4.1)$$

For the mouse-size phantom experiments, the activity was evaluated for two different volumes-of-interest (VOIs). The first VOI (VOI A) was defined as a narrow cylinder (diameter = 5 mm, height = 70 mm) surrounding the line-source. To quantify the activity of the line source inside the VOI A, a 1% threshold was applied to segment the source in Scan A and Scan B, and 6% threshold for the Scan C. The 1% threshold was consistent with that used in  $CF$  determination. A larger threshold (6%) was applied to segment the source in the presence of

radioactive water in order to avoid the inclusion of the background counts into the calculation of the line source activity. The second VOI (VOI B) corresponded to a larger cylinder (diameter = 19 mm, height = 70 mm) that encompassed the entire phantom. The VOI B is used to evaluate quantification of the whole-body activity.

For the multi-source phantom experiments, the reconstructed activity concentration ( $C_{SPECT}^k$ ) for each individual source  $k$  ( $k=1-6$ ) was calculated from corresponding SPECT images as the mean voxel value inside a VOI drawn within each source boundaries. The VOI was defined as a cylinder (diameter = 2 mm, height = 3 mm) placed at the center of each source to avoid partial volume effects (i.e., spill out of activity).

The measured activity concentrations were compared with the true values. Following Vandeghiste *et al.* [125], two linear fits were applied to the measured data: one for the sources scanned in water and another for sources in radioactive background and accuracy of quantitation was evaluated by their slopes.

### **4.2.3 Ex-vivo Study**

A *C57BL/6*-mouse was injected intravenously with biodegradable microspheres [75] labelled with  $^{188}\text{Re}$ . The total injected activity was 1.7 MBq. One hour after injection, the mouse was scanned twice for 75 minutes (two static acquisitions) using the UHRC and the HE-UHRC. The mouse was euthanized prior to the image acquisition to prevent any changes in the microsphere distribution between scans.

The mouse images were reconstructed using the same parameters as used in the phantom experiments (Section 4.2.2). After intravenous injection, the microspheres are expected to accumulate mainly in the lungs and the liver [75]. For this reason, the lungs and liver uptake were evaluated from the SPECT images and compared to the total injected activity.

The animal study was carried out in compliance with the approved ethics protocol at the University of British Columbia.

#### **4.2.4 Understanding $^{188}\text{Re}$ and VECTor/CT**

##### **4.2.4.1 Analysis of the Measured Energy Spectra**

In order to understand the phenomena that may affect the performance of the VECTor camera for  $^{188}\text{Re}$  imaging studies, the measured energy spectra from the mouse-size phantom experiments were displayed and compared with those from  $^{99\text{m}}\text{Tc}$  scans. Since VECTor acquires data at multiple bed positions inside the FOV, the energy spectra were analyzed for each of these positions. Although the total volume scanned was the same using the two collimators, the resulting number of bed positions was different due to the differences in CFOV size between the collimators. In total, 35 and 174 bed positions were acquired during the mouse-size phantom scan using UHRC and HE-UHRC, respectively. Three examples of such energy spectra (for each isotope/collimator) are discussed in this manuscript. The three energy spectra corresponded to three bed positions with increasing number of counts in the photopeak (Figure 4.1 b).

##### **4.2.4.2 Monte-Carlo Simulations**

Two Monte-Carlo simulations of the VECTor system with a simplified model of UHRC were performed. In the first simulation, a  $^{188}\text{Re}$  point-source was placed at the centre of a cylindrical water phantom that modelled attenuation as it would be observed during a mouse scan. The phantom long axis was parallel to the collimator axis, and the centre of the phantom (i.e., the  $^{188}\text{Re}$  point-source) was positioned at the CFOV (i.e., the area of maximum sensitivity in the collimator). In the second simulation, the same source was placed 4 cm off-centre, representing a bed position of very low sensitivity. From each simulation, the detected energy

spectrum was recorded and separated into four different components according to the origin of the detected photons:

- Primary: photons emitted from the  $^{188}\text{Re}$  decay that did not interact with any component of the system and whose energy was fully deposited in the detector.
- Scatter: photons emitted from the  $^{188}\text{Re}$  decay that scattered with one, or more parts of the system before being detected. The origin of scattered photons was further categorized into 155 keV self-scattered and high energy down-scattered photons. This group also includes photons that scatter in the detector crystal and deposit a fraction of their initial energy.
- Bremsstrahlung: photons that were produced by Bremsstrahlung process when  $\beta$ -particles interacted with the surrounding material.
- Tungsten X-rays: photons that were produced by tungsten atom de-excitations after photo-electric absorption in the collimator or shielding material.

Additionally, each scattered photon was categorized according to the volume of its last interaction before being detected by the NaI crystal. The following scattering volumes were included in the analysis:

- Phantom: photons that scattered within the water cylinder volume.
- Aluminum-Layer: photons that scattered in the Aluminum layer, placed in front of the NaI detector.
- Collimator: photons that scattered in the Tungsten collimator tube.
- Back-compartment: photons that scattered in the back-compartment region that modeled the Photo-Multipliers tubes (PMTs), as well as the lead shielding material located behind the PMTs.

- Crystal: photons that only scattered in the NaI crystal, depositing a fraction of their initial energy.

The details of the Monte-Carlo simulation can be found in the Appendix B.3. The simulations were performed using GATE, version 6.1 [53,54]. The simulated spectra were validated by comparing them with the experimental  $^{188}\text{Re}$  energy spectra acquired with VECTOr using the UHRC. Furthermore, the simulated scatter-corrected count rate in the 155-keV photopeak (i.e., system sensitivity) of a  $^{188}\text{Re}$  point-source measured with UHRC was compared to the experimental measurements. The simulated sensitivity was multiplied by a factor of 5 to account for the differences between the UHRC (75 pinholes) and the simplified model of this collimator (15 pinholes) used in the simulations.

## 4.3 Results

### 4.3.1 Phantom Experiments

#### 4.3.1.1 Image Quality

Six trans-axial slices from the  $^{188}\text{Re}$  and  $^{99\text{m}}\text{Tc}$  SPECT images of the *Jaszczak* phantoms are displayed in Figure 4.3. The smallest visible rod size was 0.95 mm for  $^{188}\text{Re}$ -UHRC (phantom a-1). The resolution was slightly better for  $^{99\text{m}}\text{Tc}$ -UHRC, where the smallest visible rod size was 0.85 mm. Similarly, the smallest visible rod size was 0.60 mm for both  $^{188}\text{Re}$ -HE-UHRC and  $^{99\text{m}}\text{Tc}$ -HE-UHRC.

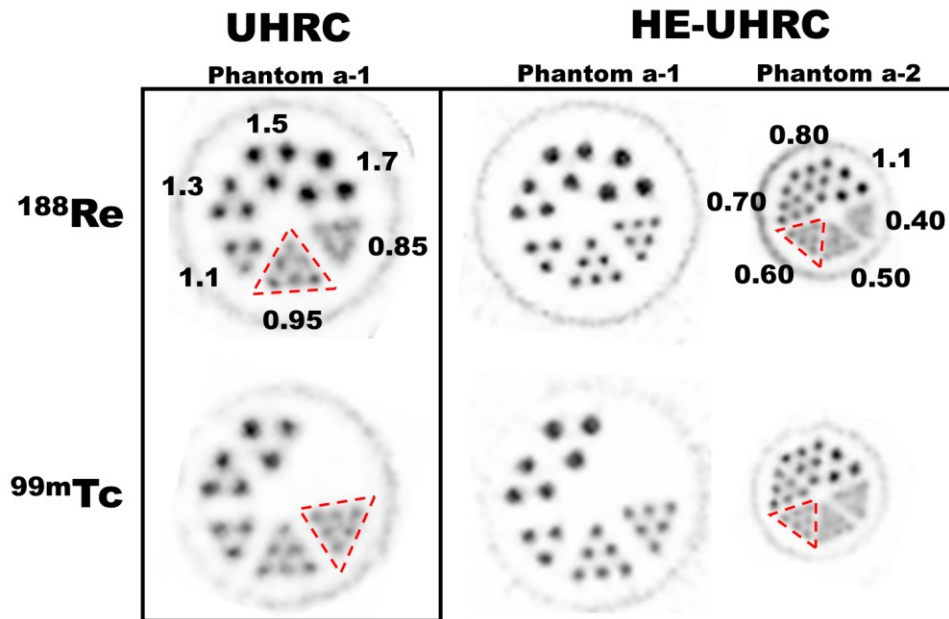


Figure 4.3 Transaxial slices from the SPECT images of the micro-*Jaszczak* resolution phantoms filled with  $^{188}\text{Re}$  and  $^{99\text{m}}\text{Tc}$ . The phantom rod diameters are shown in mm. The sector with the smallest distinguishable rods are highlighted with a red dashed triangle. Note: the largest rods (1.7 mm) of Phantom a-1 were not effectively filled with  $^{99\text{m}}\text{Tc}$ .

The image contrast and CNR as a function of rod size for different count levels are plotted in Figure 4.4. Scans with HE-UHRC produced images with better contrast than those observed for UHRC for both  $^{188}\text{Re}$  and  $^{99\text{m}}\text{Tc}$ . In the original scans (100% of counts), the contrast in the  $^{188}\text{Re}$ -UHRC image was 9% lower than in the  $^{99\text{m}}\text{Tc}$ -UHRC image for almost all rod sizes. The HE-UHRC scans yielded similar contrast for large rod sizes (0.95 mm – 1.5 mm) in  $^{188}\text{Re}$  and  $^{99\text{m}}\text{Tc}$  images, and lower contrast of  $^{188}\text{Re}$  images of small rod sizes (0.6 mm to 0.8 mm). The HE-UHRC scans also resulted in CNR values higher than those obtained with UHRC for the two isotopes investigated. Overall, CNR in  $^{188}\text{Re}$  images were comparable to those of  $^{99\text{m}}\text{Tc}$  with the

exception of very low counts reconstructions (2.5% of total counts), where  $^{99m}\text{Tc}$  HE-UHRC performed better (i.e., higher CNR) than  $^{188}\text{Re}$  HE-UHRC.

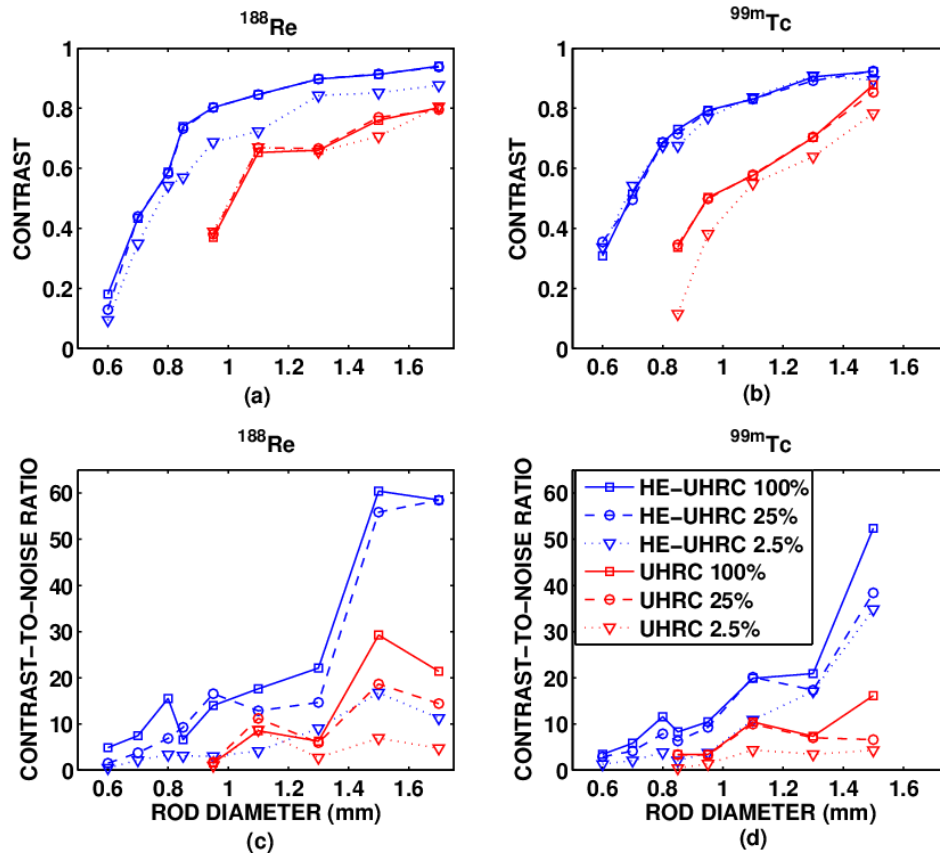


Figure 4.4 Contrast and contrast-to-noise ratio as a function of rod diameter and level of counts for  $^{188}\text{Re}$  (a, c) and  $^{99m}\text{Tc}$  (b, d), scanned using HE-UHRC and UHRC.

#### 4.3.1.2 Image Quantification

The results of the mouse-size phantom experiments are reported in Figure 4.5. The bar graphs represent the accuracy of activity quantification (calculated as the percentage error) of  $^{99m}\text{Tc}$  and  $^{188}\text{Re}$  phantoms. Quantification of activity within the line source (VOI A) resulted in average errors of less than 4% and 5% for  $^{99m}\text{Tc}$ -UHRC/HE-UHRC and  $^{188}\text{Re}$ -UHRC/HE-UHRC, respectively. When the region of interest was extended to cover the entire phantom (VOI B), the total activity calculated in the  $^{188}\text{Re}$ -UHRC image overestimated the true total activity by

+48% on average. The use of HE-UHRC improved the quantification of the total body activity, resulting in +20% overestimation. For  $^{99m}\text{Tc}$ , errors were as high as 9%.

Figure 4.6 summarizes the results of the multi-source phantom experiments. The lines of best fit show small deviations from the “optimum” quantification system (slope = 1) for both sources in water and sources in hot background.

Table 4.5 shows the slope values of the lines of best fit from the multi-source phantom experiments. For all cases, the deviation from the truth (slope = 1) were less than 6%.

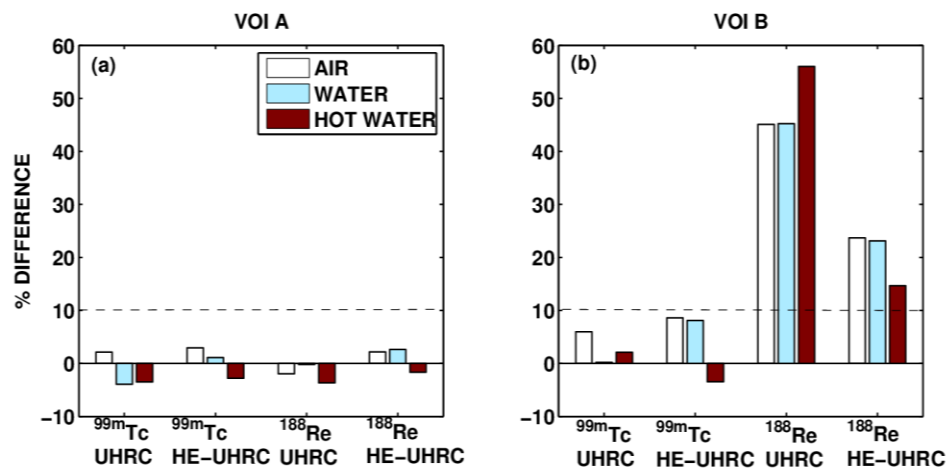


Figure 4.5 Quantification accuracy of  $^{99m}\text{Tc}$ -UHRC,  $^{99m}\text{Tc}$ -HE-UHRC,  $^{188}\text{Re}$ -UHRC and  $^{188}\text{Re}$ -HE-UHRC line source phantom experiments for VOI A (a) and VOI B (b). The dashed horizontal line shows the 10% error level.

Table 4.5 Summary of slope values obtained from linear fits to the multi-source phantom quantification experiment data

	Slope value Water	Slope value Hot water
$^{99m}\text{Tc}$ UHRC	1.004±0.004	0.990±0.003
$^{99m}\text{Tc}$ HE-UHRC	0.957±0.002	0.953±0.002
$^{188}\text{Re}$ UHRC	0.999±0.004	0.993±0.004
$^{188}\text{Re}$ HE-UHRC	0.984±0.003	0.976±0.003

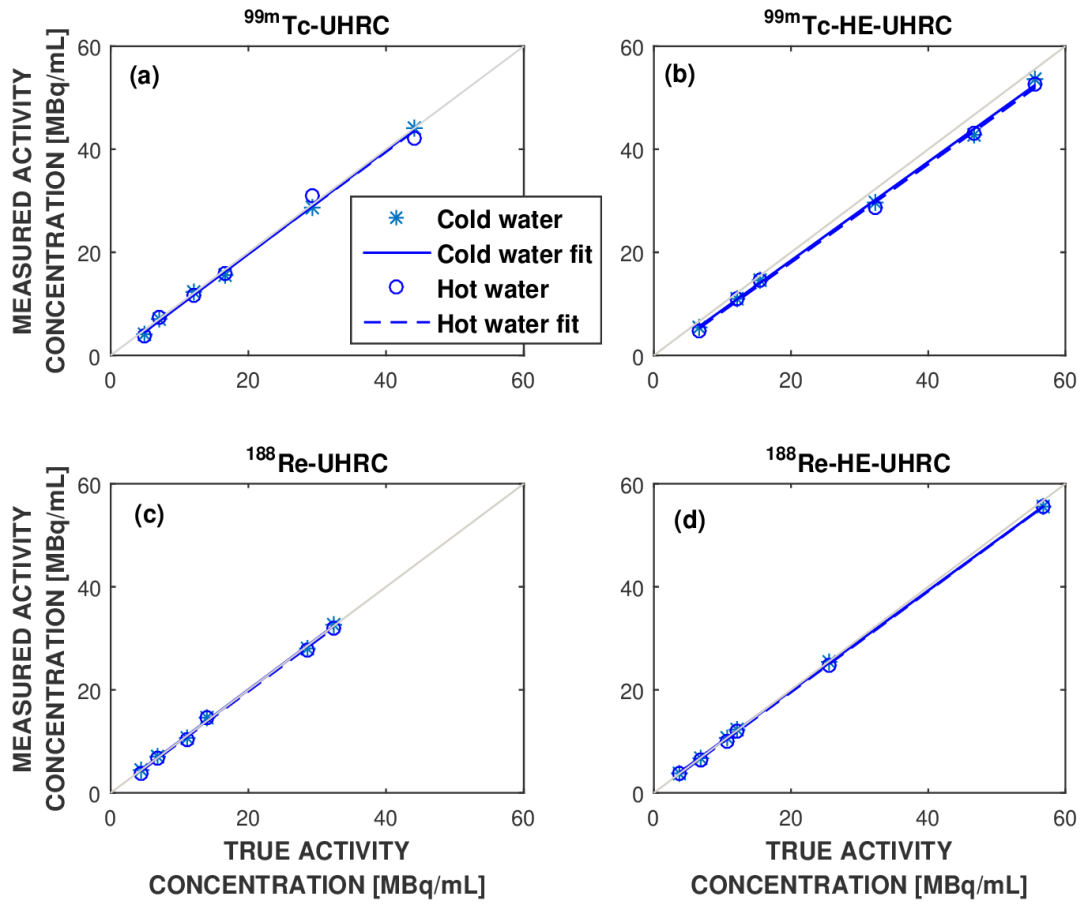


Figure 4.6 Quantification accuracy of  $^{99m}\text{Tc}$ -UHRC (a),  $^{99m}\text{Tc}$ -HE-UHRC (b),  $^{188}\text{Re}$ -UHRC (c) and,  $^{188}\text{Re}$ -HE-UHRC (d) multi-source phantoms as a function of activity concentration. A line of best fit is plot for sources in water and in the presence of 0.85 MBq/mL to 1 MBq/MI background activity.

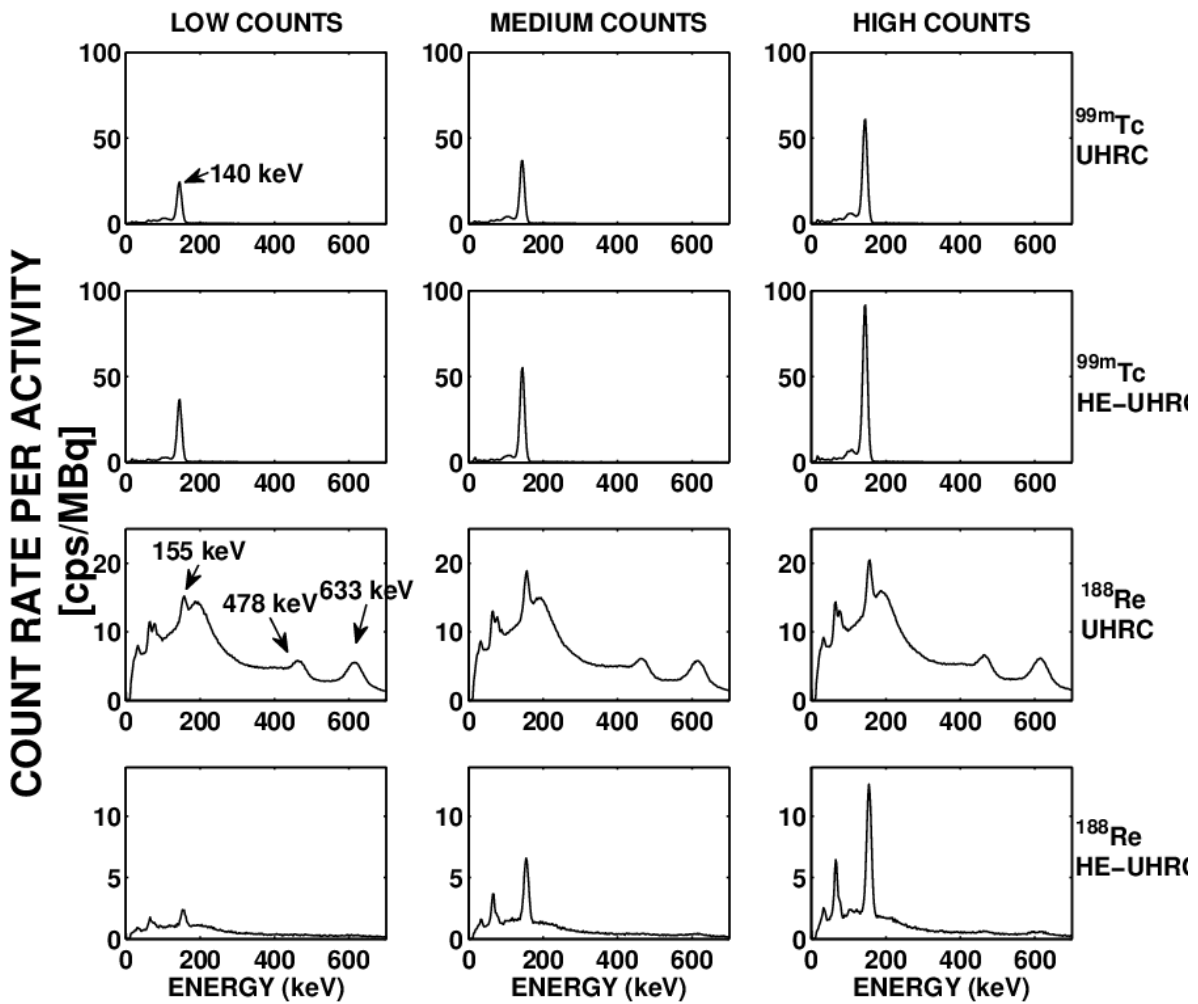


Figure 4.7 Energy spectra from  $^{99m}\text{Tc}$ -UHRC,  $^{99m}\text{Tc}$ -HE-UHRC,  $^{188}\text{Re}$ -UHRC and  $^{188}\text{Re}$ -HE-UHRC acquisitions of a line-source in a (cold) water phantom obtained at three different bed positions corresponding to different count-rate levels. For each isotope and collimator, the count-rates in the energy spectra were divided by the phantom activity.

### 4.3.2 Understanding $^{188}\text{Re}$ and VECTor/CT

#### 4.3.2.1 Experimental Energy Spectra

Figure 4.7 shows the acquired energy spectra for the  $^{99m}\text{Tc}$ -UHRC,  $^{99m}\text{Tc}$ -HE-UHRC,  $^{188}\text{Re}$ -UHRC and  $^{188}\text{Re}$ -HE-UHRC scans of the line source phantom in (cold) water at three bed

positions. The number of counts in the 140 keV  $^{99m}\text{Tc}$  and the 155 keV  $^{188}\text{Re}$  photopeaks increases as the source on the bed is moved towards positions where the sensitivity increases (i.e., close proximity to CFOV). The same is not true, however, for the 478 keV and 633 keV photopeaks in the  $^{188}\text{Re}$ -UHRC spectra. In this case, the number of counts remains nearly constant, indicating that the UHRC is not effectively stopping high-energy photons as they are being detected at the same rate at any bed position. Three interesting phenomena are observed in the  $^{188}\text{Re}$ -UHRC energy spectra: 1) contribution from scattered photons is larger than that of  $^{99m}\text{Tc}$ -UHRC,  $^{99m}\text{Tc}$ -HE-UHRC and  $^{188}\text{Re}$  HE-UHRC; 2) scatter vary very little across bed positions and; 3) the relative intensity of the 155 keV photopeak with respect to the background is very low. The use of HE-UHRC for  $^{188}\text{Re}$  imaging resulted in much cleaner (low background) spectrum and stronger intensity of the 155 keV photopeak in the spectrum (with respect to the background counts).

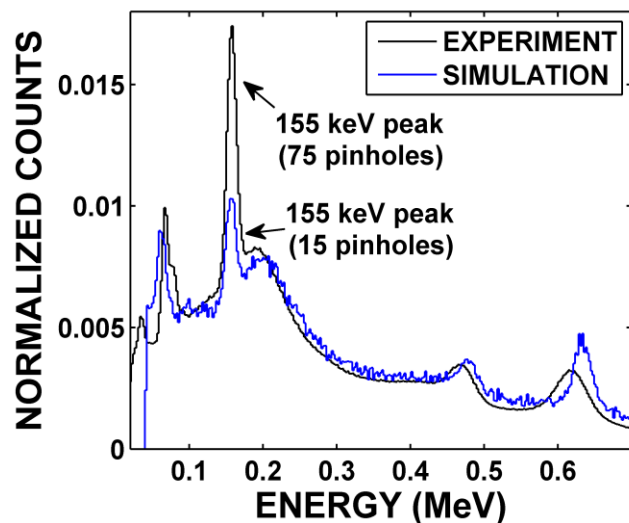


Figure 4.8 Comparison of experimental and simulated energy spectra of the  $^{188}\text{Re}$  point source scanned with UHRC. The energy spectra were normalized to the sum of counts in the energy interval from 100 keV to 700 keV.

### 4.3.2.2 Monte-Carlo Simulations

#### 4.3.2.2.1 Validation of Monte-Carlo Simulations

Figure 4.8 shows the experimental and simulated  $^{188}\text{Re}$  energy spectra of a point source that were used to validate the Monte-Carlo model of VECTor-UHRC. Overall, the most important features of the  $^{188}\text{Re}$  energy spectrum are well reproduced by the simulations with the exception of the intensity of the 155-keV peak, which is lower in the simulations due to the fact that number of simulated pinholes (15 pinholes) was 5 times lower than in the real system (75 pinholes). Additionally, there is a small mismatch between the energies of the simulated and experimental 478 keV and 633 keV photopeaks (probably caused by a loss of linearity in the detector energy calibration). The measured and the simulated  $^{188}\text{Re}$ -UHRC sensitivities were 144 cps/MBq and 176 cps/MBq, respectively.

#### 4.3.2.2.2 Analysis of $^{188}\text{Re}$ Emissions and Scatter Volumes

Figure 4.9 (a-b) presents the components of the simulated  $^{188}\text{Re}$  energy spectrum for a source being at the CFOV and 4 cm off-center. The simulations indicate that the majority of scattered photons detected on  $^{188}\text{RE}$ -UHRC scans originated from the high-energy emissions. Only a small fraction of photons corresponds to self-scatter from the 155 keV emissions. The 155 keV photopeak disappears in spectra collected outside the CFOV, indicating that UHRC successfully stops un-collimated 155 keV photons. On the contrary, 478 keV and 633 keV photopeaks intensities change very little regardless of the position of the source relative to the CFOV.

Based on the simulations, the fraction of Bremsstrahlung photons in the 155 keV photopeak window was estimated to be 3%, whereas the scattered photons accounted for 70-90%

of the total counts depending on the position of the source. The fraction of 155 keV primary photons ranged from 23% (highest sensitivity) to 0% (source completely outside FOV).

Figure 4.9-c shows that majority of detected scattered events (approximately 69%) scattered in the crystal (i.e., high-energy photons that only deposit a fraction of their energy in the NaI detector). Scatter in the phantom accounts for only 1.4% of the total detected scatter counts. The fraction of scatter in the collimator (13%) was similar to that in the back-compartment region of the system (15%).

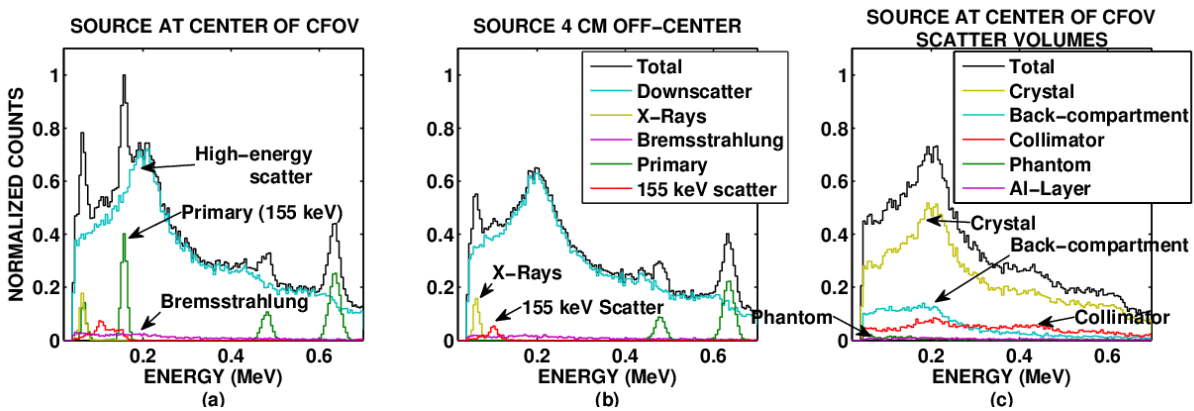
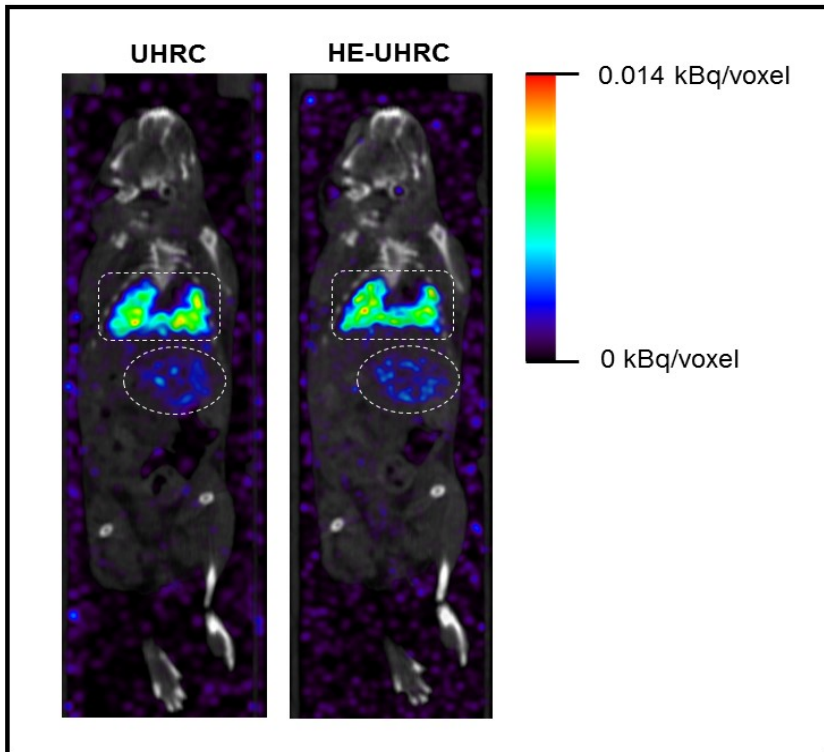


Figure 4.9 Monte-Carlo simulations of spectra components for the  $^{188}\text{Re}$ -UHRC acquisition of a point source (placed inside a cylindrical water phantom) at the center of CFOV (a), and 4 cm off-center (b). Sub-figure (c) shows the simulated spectra of scattered photons categorized by the location of their last interaction.

### 4.3.3 Ex-vivo Study

The  $^{188}\text{Re}$  microspheres distribution within the mouse, scanned with UHRC and HE-UHRC, is shown in Figure 4.10. Due to the very low injected activity (high level of noise), a Gaussian filter (FWHM = 1.0 mm) was applied to the reconstructed images. The quantitative analysis, however, was performed on the un-filtered data. Overall, both UHRC and HE-UHRC yielded similar spatial distribution of the microspheres' activity, showing the largest

accumulation in the lungs, followed by that in the liver. High levels of noise made determination of other organs' uptake difficult.



**Figure 4.10** Coronal slices of the fused SPECT/CT mouse scans showing the biodistribution of  $^{188}\text{Re}$  microspheres (1 hour after injection). Images were acquired using UHRC and HE-UHRC. The dashed lines indicate regions of uptake in the lungs and liver.

The activities in the lungs and the liver estimated from the SPECT images are reported in Table 4.6. The two collimators yielded comparable microsphere accumulation in both organs, with the HE-UHRC resulting in 10% higher activities than UHRC.

**Table 4.6 Distributions of the  $^{188}\text{Re}$ -labeled microspheres at 60 min after tail vein injection into the C57BL/6 mouse.**

	<b>Injected Activity [MBq]</b>	<b>Lungs Activity [MBq]</b>	<b>Liver Activity [MBq]</b>	<b>Lungs %ID</b>	<b>Liver %ID</b>
<b>UHRC</b>	1.70	1.13	0.27	66	16
<b>HE-UHRC</b>	1.70	1.26	0.33	74	19

#### **4.4 Discussion**

The spatial resolution of pinhole collimators depends on (a) the pinhole diameter and (b) the distances between object-pinhole and pinhole-detector [143] (i.e., bore diameter). Therefore, it was expected that HE-UHRC (0.7 mm diameter, 48 mm bore diameter) would perform better than UHRC (1.0 mm diameter, 98 mm bore diameter) for  $^{188}\text{Re}$  imaging. The important finding, however, was that spatial resolution of  $^{188}\text{Re}$  images was comparable to that of  $^{99\text{m}}\text{Tc}$  (for both collimators) despite the higher complexity of  $^{188}\text{Re}$  emissions. It is interesting to note that UHRC yielded slightly better resolution for  $^{99\text{m}}\text{Tc}$  than  $^{188}\text{Re}$  (0.85 mm vs 0.95 mm). Such degradation of  $^{188}\text{Re}$ -UHRC resolution is probably due to the large amount of scatter in the projection data, which potentially affects image contrasts (as seen in the experimental and simulated energy spectra, Figure 4.7 and Figure 4.9). The smallest discernible rod size for  $^{188}\text{Re}$ -HE-UHRC was the same as that of  $^{99\text{m}}\text{Tc}$ -HE-UHRC (0.6 mm), because the amount of scatter is substantially lower when imaging  $^{188}\text{Re}$  with HE-UHRC. Our values of  $^{99\text{m}}\text{Tc}$  spatial resolution are slightly larger than other published data: 0.80 mm for  $^{99\text{m}}\text{Tc}$ -UHRC [127] and 0.50 mm for  $^{99\text{m}}\text{Tc}$ -HE-UHRC [135]. We believe that these differences in resolution may have been caused by differences in counting statistics (lower activity and/or lower imaging time in our experiments that would decrease the ability to distinguish small rods in the resolution phantom). No

smoothing filter was applied in our study. Additionally, our spatial resolution was determined from 0.17 mm thick SPECT slices, whereas the cited studies used 3 mm thick slices.

Image contrast decreased considerably for rod sizes near the resolution limit of each collimator. Thus, it is meaningful to compare contrast (and CNR) between the two collimators for larger rods (>1.1 – 1.7 mm). In such scenario,  $^{188}\text{Re}$  HE-UHRC resulted in a 15-30% better contrast with respect to  $^{188}\text{Re}$  UHRC (Figure 4.4 a). The evaluation of CNR illustrated the effect of noise on image quality (Figure 4.4 c-d). For low noise levels and large objects,  $^{188}\text{Re}$  HE-UHRC yielded CNR values ranging from 13 to 60, whereas  $^{188}\text{Re}$  UHRC ranged from 2 to 30 which represents an approximately 55% reduction. For images with a very low number of counts, both collimators yielded CNR values below 10 for most of the rod-sizes. The comparison of  $^{188}\text{Re}$  contrast and CNR with those of  $^{99\text{m}}\text{Tc}$  allowed us to investigate the effect of  $^{188}\text{Re}$  high-energy scatter on image quality. In particular, the use of UHRC for  $^{188}\text{Re}$  imaging (i.e., imaging strongly affected by large amount of down-scattered high-energy photons) resulted in 9% lower contrast than  $^{99\text{m}}\text{Tc}$  UHRC for all rod sizes. However, nearly identical contrast was obtained in  $^{188}\text{Re}$  HE-UHRC and  $^{99\text{m}}\text{Tc}$  HE-UHRC images of large objects (>0.80 mm), where the amount of detected scatter in both  $^{188}\text{Re}$  and  $^{99\text{m}}\text{Tc}$  energy spectra was comparable. Interestingly, the CNR values from images of  $^{188}\text{Re}$  and  $^{99\text{m}}\text{Tc}$  were similar, with  $^{188}\text{Re}$  images showing slightly higher CNR for some rod sizes. This finding suggests that although contrast of  $^{188}\text{Re}$  images was lower than that of  $^{99\text{m}}\text{Tc}$ , the  $^{188}\text{Re}$  images were smoother than  $^{99\text{m}}\text{Tc}$  ones (i.e., lower variability within the pixel values), resulting in similar CNR values for both isotopes.

The results of the line-source phantom experiments demonstrated that the VECTor system with both UHRC and HE-UHRC accurately quantified  $^{188}\text{Re}$  activity in experiments modelling the whole-body mouse scan. The level of accuracy was similar to that achieved for other isotopes

[125]. The fact that the measured  $^{188}\text{Re}$  activity in the whole phantom (VOI B, Figure 4.5 b) greatly over-estimates the true value is due to the presence of a non-negligible background signal in areas of the image where the activity should be zero. In order to better illustrate this problem, off-axis line profiles of activity concentration were drawn in the SPECT images of the line-source in air for  $^{188}\text{Re}$  UHRC/HE-UHRC and  $^{99\text{m}}\text{Tc}$  UHRC/HE-UHRC. Figure 4.11 shows these profiles (a-d), as well as coronal slices from the reconstructed images (e-h). The profile along the  $^{188}\text{Re}$  UHRC image (Figure 4.11 c) shows background values as high as 0.54 MBq/mL (0.17 MBq/mL on average), whereas  $^{188}\text{Re}$  HE-UHRC line profile shows lower values (maximum 0.48 MBq/mL, average 0.09 MBq/mL). This background was mostly uniform across the entire image, as can be seen in Figure 4.11 g-h. Additionally, substantial amount of background seems to be visible at the edges of the  $^{188}\text{Re}$  UHRC phantom image which might be due to scatter (or back-scatter) of  $^{188}\text{Re}$  emissions with the collimator walls. None of these effects were observed in the  $^{99\text{m}}\text{Tc}$  scans (Figure 4.11 a-b, e-f), suggesting that this additional “undesired” background counts/noise in  $^{188}\text{Re}$  images are mostly related to emissions other than its 155 keV photopeak. These are primary and scattered high-energy photons which penetrate the collimator and Bremsstrahlung radiation which may also contribute to the photopeak window. The analysis of the energy spectra from Monte-Carlo simulations completed our understanding of this issue, as discussed in the following paragraph.

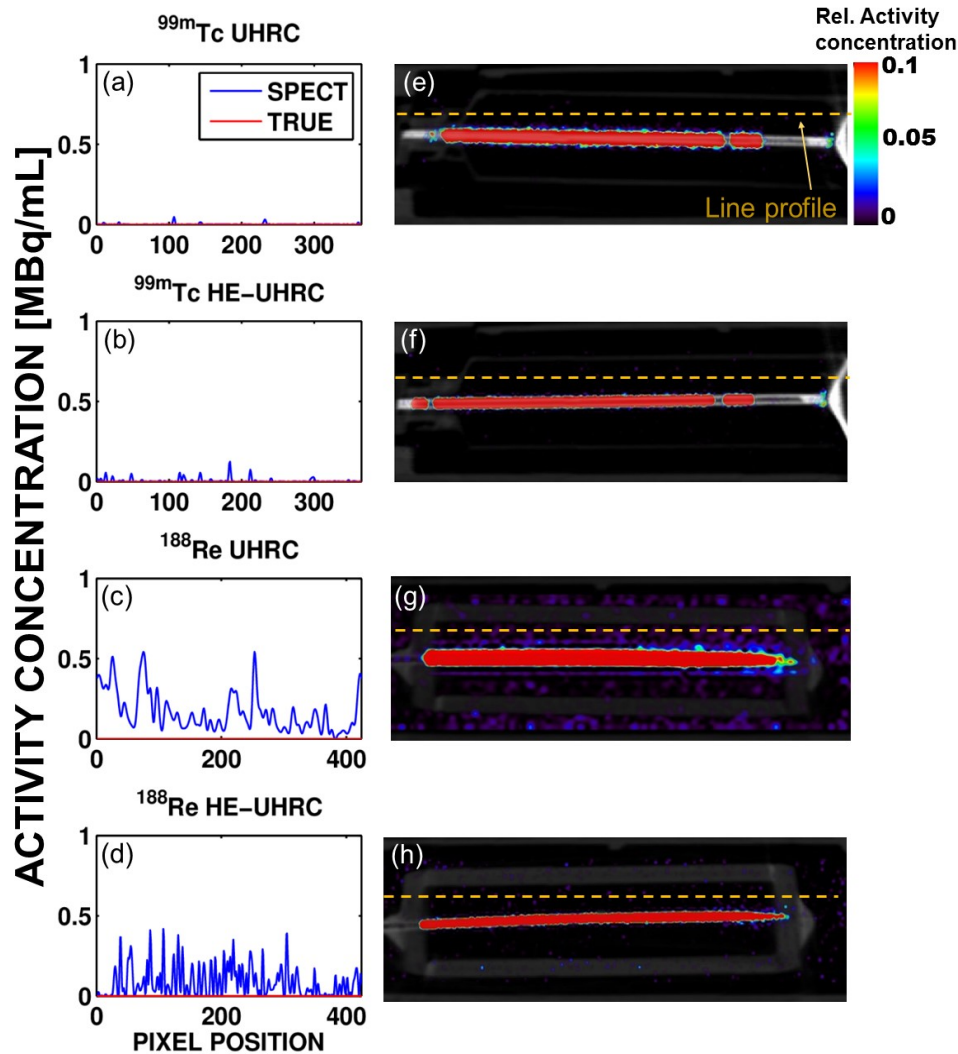


Figure 4.11 Activity concentration profiles drawn parallel to the main axis of phantom for the  $^{99m}\text{Tc}$  UHRC/HE-UHRC and  $^{188}\text{Re}$  UHRC/HE-UHRC SPECT images of the line source in air (a-d). Coronal slices of the fused SPECT/CT images of the line-source air phantoms (e-h). The color-map of SPECT images was re-scaled to 0.1 of the maximum value in each SPECT image to better visualize the background signal.

Figure 4.7 (third row) demonstrates that  $^{188}\text{Re}$  UHRC energy spectra are severely affected by scatter. Monte-Carlo simulations confirmed that the majority of photons detected within the  $^{188}\text{Re}$  UHRC photopeak window correspond to down-scattered photons from high-energy emissions (Figure 4.9 a - b). As a result, only a small fraction of 155 keV-collimated photons,

which contain meaningful spatial information about the source activity distribution, is detected at each bed position. At bed positions with low collimator sensitivity, the intensity of the 155 keV peak is very low compared to the scatter background (Figure 4.7:  $^{188}\text{Re}$  – UHRC, Low Counts). In such conditions, the majority of photons in the photopeak window are due to high-energy photons which are penetrating the UHRC collimator walls and scattering in the NaI crystal, as shown in Figure 4.9 c. The fraction of detected photons that scattered in the phantom is negligible because phantom scatter occurs more often for low energy photons (155 keV or X-rays). Photons of these low energies will likely be absorbed within the collimator walls and no longer be detected.

The use of HE-UHRC appreciably improved the quality of  $^{188}\text{Re}$  projection data, increasing the relative intensity of the 155 keV photopeak relative to the background (Figure 4.7- fourth row). Figure 4.7 (first and second row) illustrates the optimum case of  $^{99\text{m}}\text{Tc}$ , where the amount of scatter is minimal.

The projection data were corrected for scatter using the triple energy window (TEW) method. However, this method is just an approximation and does not necessarily model the spatial distribution of scatter. As a consequence, not all the scattered photons are effectively removed from the  $^{188}\text{Re}$  projection data (in particular, high-energy down-scatter) resulting in scattered counts reconstructed as true counts, increasing the background counts in  $^{188}\text{Re}$  images. Quantitatively, these “spurious” counts are identified as 155 keV emissions in the image, which explains the large overestimation of the true activity in the mouse-size phantom experiments (Figure 4.5, VOI B for UHRC). Our analysis suggests that a more sophisticated scatter correction method that accounts for collimator penetration may be required to further improve  $^{188}\text{Re}$  image quality and reduce noise. Nonetheless, quantification of activity within a small VOI surrounding

the object of interest (for example, a tumor), will be accurate for both  $^{188}\text{Re}$  UHRC and HE-UHRC. Imaging  $^{188}\text{Re}$  with UHRC might be problematic for image-based biodistribution studies where uptake in different organs are calculated using SPECT. In such cases, for instance, organs with very low uptake might yield an increased activity due to the presence of this “spurious” background signal. In order to address this issue, we recommend the following (in case when a high-energy collimator is not available): 1) quantify the average contribution from the background signal in areas where activity is known to be zero such as outside the animal body and; 2) subtract this estimated background concentration from the measured organ uptake.

It should be noted that our simulation of the UHRC has limitations. The most important is that only the central ring of pinholes was modelled (15 pinholes), whereas the real collimator contains 5 rings (75 pinholes in total). As a consequence, the simulated collimator sensitivity for 155 keV photons is expected to be lower than the experimental one, as it can be observed in the normalized energy-spectra of Figure 4.8. When taking into account the difference in number of pinholes, the  $^{188}\text{Re}$  UHRC simulated sensitivity of the 155-keV photopeak remained in relatively good agreement with the experiment (176 cps/MBq vs 144 cps/MBq, +22% difference). The over-estimation of simulated sensitivity might be due to the assumption that all pinholes have the same sensitivity. This assumption might not be true for pinholes located at the outer rings of the collimator, where collimated photons are projected onto the edge of the detector planes. Nonetheless, the simulated UHRC served as a good model to illustrate the relative variations of intensities of scatter, Bremsstrahlung and primary photons as the source moves inside the camera FOV (Figure 4.9 a-b) as well as to provide information about the location of scatter events within system (Figure 4.9 c). The features obtained in our simulated  $^{188}\text{Re}$  VECTor detected energy spectrum (in particular, large amounts of high-energy down-scatter and low detected

bremsstrahlung) were also reported by Uribe et al. [144] for simulations of  $^{188}\text{Re}$  clinical SPECT cameras using low energy high resolution (LEHR) collimators. Monte-Carlo simulations suggest that Bremsstrahlung photons in  $^{188}\text{Re}$  do not degrade image quantification due to their low yield and detection fraction compared to the other photons. For pure-beta emitters such as  $^{90}\text{Y}$  or  $^{32}\text{P}$ , Bremsstrahlung radiation has been recently shown to be useful for small animal planar imaging [145].

The mouse study (Figure 4.10) served as an illustration for  $^{188}\text{Re}$  small animal imaging using VECTor with UHRC and HE-UHRC. The image quality experiments showed that, at very low levels of activity, there was no major advantage of using HE-UHRC over UHRC for  $^{188}\text{Re}$  (Figure 4.4). In such conditions, the high noise that dominates the images is due to very low count statistics while other image-degrading effects are less important. Such noise (due to low statistics) degrades image quality and image quantification. In particular, it resulted in higher level of uptake in lungs and liver measured in our  $^{188}\text{Re}$  HE-UHRC animal image, compared to  $^{188}\text{Re}$  UHRC. Counting statistics could have been improved by using the targeting capabilities of VECTor and focusing the scan on the abdominal area of the animal. The low  $^{188}\text{Re}$  injected activity (1-2 MBq) was a limitation in our ex-vivo mouse experiment. It was due to the low  $^{188}\text{Re}$  concentration available in our  $^{188}\text{W}/^{188}\text{Re}$  generator combined with a low labelling yield of the microspheres. Since  $^{188}\text{Re}$  microspheres are intended for the therapeutic use, it is expected that larger doses will be administered in future animal studies. Nevertheless, we have learned that imaging very low  $^{188}\text{Re}$  activities becomes extremely challenging (compared to  $^{99\text{m}}\text{Tc}$ ) as large number of down-scattered photons combined with the low signal from 155 keV photons results in images with high noise and low contrast.

As the interest in radionuclide therapies has grown over the last years, new isotopes with complex emissions are being investigated for imaging and/or therapeutic applications [137],[146]. Similar to  $^{188}\text{Re}$ , some of these isotopes (e.g.  $^{67}\text{Ga}$ ,  $^{213}\text{Bi}$ ,  $^{124}\text{I}$ ) emit multiple high-energy photons which potentially may affect the quality of images. For such isotopes, there may be situations in which image degradation effects similar to those discussed in this paper may be observed. In particular, such degradation may occur for systems based on pinhole collimation where the pinhole FOV is small compared to the object's size. In such systems, if the collimator is not thick enough, due to penetration of high-energy photons through the collimator walls, the projection data will contain a large fraction of scattered high-energy photons which originated in areas outside the pinhole FOV.

#### **4.5 Conclusions**

Despite the presence of large number of down-scattered photons detected within the 155 keV photopeak window, VECTor ultra-high resolution and high-energy ultra-high resolution collimators produced  $^{188}\text{Re}$  images with submillimeter spatial resolution and high accuracy of activity quantification (errors below 10% for quantification of activity within small VOIs around the radioactive object of interest), comparable to  $^{99\text{m}}\text{Tc}$ . The main difference from  $^{99\text{m}}\text{Tc}$  images, however, was the presence of high background in images mainly caused by high-energy photons penetrating the collimator. Such background signal resulted in more than 20% overestimation of activity in the entire field of view for both collimators. The use of High-Energy Ultra High Resolution collimator optimized both image quality and image quantification of  $^{188}\text{Re}$  in VECTor/CT.

In the context of theranostic applications, the reliable quantification of  $^{99m}\text{Tc}$  and  $^{188}\text{Re}$  becomes very important to ensure good treatment planning (using the diagnostic isotope) and to perform accurate post-therapy dosimetry calculations.

## Chapter 5: Accuracy of Activity Quantification and Image-Based Dosimetry Calculations for $^{188}\text{Re}$ SPECT/CT

### 5.1 Introduction

Accurate measurements of  $^{188}\text{Re}$  activity using clinical SPECT cameras is challenging due to the complex decay scheme of this isotope (Table 1.3). Considering  $\gamma$ -emissions,  $^{188}\text{Re}$  emits, in addition to the 155 keV photon, high-energy photons which result in large amounts of down-scattered events within the photopeak energy window [144,147]. Furthermore, these high-energy photons also cause high levels of collimator septal-penetration. To minimize these problems, the use of medium energy (ME) or high energy (HE) collimators to image  $^{188}\text{Re}$  has been recommended [117]. However, poor spatial resolution of these collimators results in strong partial volume effects. On a positive note, although the interactions of  $\beta$ -particles (emitted from the  $^{188}\text{Re}$  decay) with tissue produce Bremsstrahlung radiation, its contribution to the detected signal in the gamma camera is negligible (see Chapter 3) [144].

Given the problems described above, it is expected that accuracy of  $^{188}\text{Re}$  SPECT activity quantification will be influenced by the choice of the collimator, the image acquisition parameters and the accuracy of the corrections for image-degrading factors implemented in the reconstruction algorithm.

Several studies have investigated quantitative capabilities of SPECT for imaging radionuclide therapy isotopes other than  $^{188}\text{Re}$ , such as  $^{131}\text{I}$  [42],  $^{177}\text{Lu}$  [29,148] and  $^{90}\text{Y}$  [108,149]. Regarding  $^{188}\text{Re}$ , Hambye *et al* 2002 [56] performed a phantom study to investigate the differences between the image quantification capabilities of  $^{188}\text{Re}$  and  $^{99\text{m}}\text{Tc}$ . The authors concluded that the accuracy of target-to-background activity estimation in the phantom was

significantly lower for  $^{188}\text{Re}$  than for  $^{99\text{m}}\text{Tc}$ , mostly due to the presence of downscattered photons recorded in the  $^{188}\text{Re}$  photopeak.

Another phantom study (Chaudakshetrin *et al* 2004 [150]) showed that quantification of  $^{188}\text{Re}$  activity using a 2-D imaging method can be reasonably accurate, with errors below 25%. This method was applied to perform patient-specific dosimetry for  $^{188}\text{Re}$  therapy of liver cancer [57].

More recently, Shcherbinin *et al* 2013 [38] demonstrated the feasibility of accurate quantification of  $^{188}\text{Re}$  SPECT images using phantom experiments. However, the experimental conditions of this phantom study (phantom geometry and activity levels) did not resemble those used in typical  $^{188}\text{Re}$  therapies. Additionally, the images were corrected for scatter using an analytical method [30], which is not available in clinical scanners. For these reasons, the quantitative accuracy of  $^{188}\text{Re}$  SPECT imaging for clinically relevant situations and using standard reconstruction methods available in clinical scanners still remains unknown.

In this work we performed a series of phantom experiments aiming to expand and complement those performed by Shcherbinin *et al* 2013. In this context, the objectives of our study were:

- 1) To evaluate the accuracy of image quantification for  $^{188}\text{Re}$  SPECT studies acquired under clinically relevant conditions. and reconstructed using the standard ordered subset expectation maximization (OSEM) [151] algorithm with the three clinically available corrections CT-based attenuation, triple-energy window (TEW) scatter and resolution recovery.
- 2) To evaluate the performance of the TEW scatter correction method using two different scatter window settings.

- 3) To determine the parameters of the dead-time correction method for  $^{188}\text{Re}$  SPECT.
- 4) To evaluate and compare the accuracy of  $^{188}\text{Re}$  dosimetry estimates performed using the OLINDA method [47] and the point-dose kernel (PDK) method [152].

Additionally, Monte-Carlo simulations of a phantom filled with  $^{188}\text{Re}$  and scanned with a commercial SPECT system were performed. The goal of these simulations was to better understand the results of the quantification experiments (objectives 1-3), and to calculate the reference dose to be used to evaluate the accuracy of the  $^{188}\text{Re}$  image-based dosimetry (objective 4).

## 5.2 Materials and Methods

The accuracy of  $^{188}\text{Re}$  SPECT activity quantification and dosimetry calculations was investigated through phantom experiments and Monte-Carlo simulations. To this end, three series of phantom experiments were performed:

- a) **Quantification experiments** - to evaluate the accuracy of the reconstructed activity distribution of  $^{188}\text{Re}$  with compensation for attenuation (AC), scatter (SC), resolution recovery (RR) and dead-time losses (DT);
- b) **Dead-time experiments** - to determine the dead-time correction factors to be applied on  $^{188}\text{Re}$  SPECT high-activity studies;
- c) **Calibration experiments** - to determine the camera normalization factor that converts corrected counts in the reconstructed image into the units of activity (or activity concentration).

The  $^{188}\text{Re}$  images from the quantification experiments were subsequently used to determine the average absorbed dose-rates (AADRs) for each of the individual phantom inserts.

Additionally, two series of Monte Carlo simulation studies were done using GATE v7.1 [53]:

- a) **Tests of the TEW scatter correction** - the  $^{188}\text{Re}$  planar acquisitions of a sphere and a point source as would be acquired with the SPECT camera equipped with medium energy and high energy collimators were simulated to investigate the performance of the TEW scatter correction method and;
- b) **Dosimetry calculation** - the dose deposited in the phantom which was used in our quantification experiments was simulated to determine the reference radiation dose rate for evaluation of the accuracy of image-based dosimetry.

The details of the phantom experiments and the dosimetry calculations are described in the following sub-sections.

## 5.2.1 $^{188}\text{Re}$ Phantom Experiments

### 5.2.1.1 Quantification Experiments

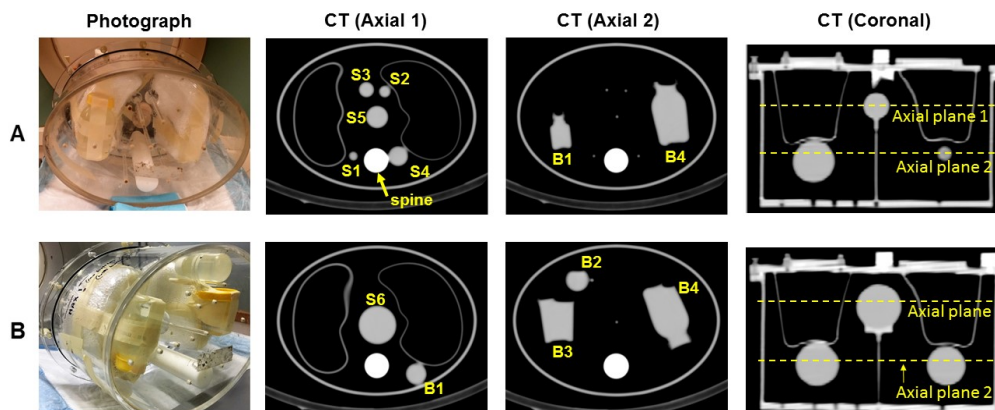


**Figure 5.1** Photographs, axial and coronal CT slices of the thorax phantom (from the experiment with phantom filled with air) with the two configurations of spheres and bottles (A and B) used in the quantification experiments. The spheres and bottles are labeled as S1-S6 and B1-B4, respectively.

The accuracy of quantification of  $^{188}\text{Re}$  SPECT was investigated using a thorax phantom (Data Spectrum Corporation, USA) with lungs (filled with lung-equivalent material) and spine inserts (filled with bone-equivalent material). The phantom was scanned in two configurations: A) containing a set of five spheres (labeled as S1-S5) and two bottles (B1 and B4) and B) containing a set of four bottles (labeled as B1-B4) and one sphere (S6). These objects model lesions of different sizes located at different positions inside the body (Figure 5.1). To test the accuracy of quantification under the challenging attenuation and scattering conditions, some of the objects were placed at locations resembling regions with non-uniform distribution of tissue density such as between the spine and the lungs (Figure 5.1). The information about the phantom experimental conditions, including object volumes and activities are summarized in Table 5.2.

The  $^{188}\text{Re}$  activities were measured using an Atomlab 100plus dose calibrator (Biodex, USA) available at our Nuclear Medicine department at Vancouver General Hospital (VGH). The  $^{188}\text{Re}$  dose calibrator dial setting number ( $76.5 \pm 4.8$ ) was determined experimentally using the thyroid-probe method described in Chapter 2 [153]. Both phantom configurations were scanned under three conditions: 1) with empty background (air) - to investigate the quantification with minimal scatter and attenuation; 2) with the phantom body (background) filled with water (water) - to investigate the performance of attenuation and scatter corrections and; 3) with the background filled with a  $^{188}\text{Re}$  solution (hot-water), to evaluate the accuracy of quantification in conditions similar to those of a real patient scan. The source-to-background ratio (SBR) in the hot-water scan was 7:1, which represents an intermediate value of Tumor-to-Normal liver ratio in  $^{188}\text{Re}$  radioembolization therapies, as measured in clinical and pre-clinical studies [154].

All phantom experiments were performed using a SymbiaT (Siemens Medical, Germany) SPECT/CT camera at VGH. The acquisitions were performed twice: with the medium-energy low penetration (ME) and the high-energy (HE) collimators. The collimator specifications are shown in Table 3.1.

In order to investigate the effect of the scatter-energy window width on the accuracy of quantification of the reconstructed images, the projection data from the phantom experiment with configuration A was acquired using the 155 keV photopeak energy window and the two sets of scatter windows referred to as “narrow” and “wide” (Table 5.1). The projection data from the phantom with configuration B was acquired using the 155 keV photopeak and the “narrow” window settings only.

The acquisition matrix was 128x128 and a total of 90 projections were acquired for each scan using non-circular orbits. The projection time was 5 seconds for the scans in air, and 10 seconds for the scans in water and hot-water. At the scan time, the sum of activity in the phantom inserts (spheres and bottles) was 697 MBq and 575 MBq for A and B configurations, respectively. The total activity in the entire phantom, including the hot background, was 1193 MBq for phantom B, whereas only 491 MBq for phantom A because this scan was performed two days after the air/water acquisitions due to an unexpected mechanical problem of the camera.

**Table 5.1 Energy window settings (narrow and wide) for the <sup>188</sup>Re quantification and the dead-time phantom experiments. Extra windows SLE (spectrum at low energies) and SHE (spectrum at high energies) were used to measure the count-rate in the entire energy spectrum. Values are given in keV.**

	<b>Photopeak</b>	<b>Lower Scatter</b>	<b>Upper Scatter</b>	<b>Extra SLE</b>	<b>Extra SHE</b>
<b>Narrow</b>	139.5-170.4	132.6-139.4	170.4-180.6	N/A	N/A
<b>Wide</b>	139.5-170.4	125.8-139.4	170.4-204.2	N/A	N/A
<b>Dead-time</b>	139.5-170.4	132.6-139.4	170.4-180.6	17.5-132.5	183.5-687.5

**Table 5.2 Details of  $^{188}\text{Re}$  phantom quantification experiment. SBR = Source-to-background ratio.**

<b>Phantom Configuration</b>	<b>Object label</b>	<b>Object diameter [cm]</b>	<b>Object volume [mL]</b>	<b>Object activity [MBq]</b>	<b>Object activity concentration [MBq/mL]</b>	<b>Background conditions</b>	<b>Total Activity in Phantom [MBq]</b>	<b>Notes</b>
A	S1	1.56	2	6.8	3.5	Air	697	<ul style="list-style-type: none"> <li>• B1 and B4 placed under lungs</li> <li>• S1 and S4 placed between spine and lungs</li> </ul>
	S2	1.97	4	13.8		Cold water	664	
	S3	2.48	8	28.3		Hot water	491	
	S4	3.13	16	55.6		(SBR = 7:1)		
	S5	3.37	20	69.4				
	B1	2.54	34	117.8				
	B4	5.64	197	405.3	2.1			
B	B1	2.54	33	33.1	1.0	Air	575	<ul style="list-style-type: none"> <li>• B3 and B4 placed under lungs</li> </ul>
	B2	3.15	75	75.9		Cold water	554	
	B3	4.69	142	146.5		Hot water	1193	
	B4	5.64	196	204.0		(SBR = 7:1)		
	S6	6.03	111	115.6				

### 5.2.1.2 Dead-time Experiments

Dead-time correction factors (DTCF) for  $^{188}\text{Re}$  imaged on the SymbiaT camera equipped with ME and HE collimators were obtained following the method described by Celler *et al* 2014 [155]. This method requires the determination of the calibration curves corresponding to the losses of primary photons due to dead-time as a function of increasing activity in the imaged object (patient or phantom). We are interested in dead-time losses of primary photons because only these photons are used in the creation of quantitative images. The experimental procedures used in the dead-time experiments were as follows:

- A 20 MBq/mL  $^{188}\text{Re}$  master solution was prepared by diluting 4.5 GBq of  $^{188}\text{Re}$  into 230 mL of water.
- This master solution was dispensed into 17 syringes with the following distribution: ten syringes were filled with 100 MBq each, four syringes were filled with 250 MBq each, one was filled with 500 MBq and two with 1000 MBq each. The exact activity in each syringe was measured using our Atomlab 100plus dose-calibrator.
- In a series of experiments, the content of each of these syringes was sequentially dispensed into a 300-mL bottle that was placed off-center inside a water filled Jaszczak phantom. As a result, the bottle activity increased from 0 MBq to 1000 MBq (in 10 steps, 100 MBq each), from 1000 MBq to 2000 MBq (in 4 steps, 250 MBq each), from 2000 MBq to 2500 MBq (in 1 step, 500 MBq) and from 2500 MBq to 4500 MBq (in 2 steps, 1000MBq each).
- For each activity level, planar scans were performed with camera heads in a  $180^\circ$  configuration. Both ME and HE collimators were used in these scans. The distance between the collimator and the center of the bottle was 35 cm and 25 cm for head 1 and

head 2, respectively. This geometry created different photon flux and different scattering conditions for head 1 and head 2. The energy window settings for the planar acquisitions are shown in Table 5.1. In total, the data were acquired in five energy windows covering the entire energy spectrum measured by the camera (18 keV to 700 keV). To minimize errors due to counting statistics, the acquisition times of planar images ranged from 5 minutes (for activities lower than 500 MBq) to 1 minute (for activities higher than 1500 MBq).

- For each individual planar image, the observed primary photons count-rate was determined as the collected count-rate in the 155-keV photopeak window corrected for scatter using the TEW method. The true primary count-rate was estimated by linear extrapolation of the observed primary photon count-rates from acquisitions where the measured count-rate in the entire spectrum was less than 50 kct/s (i.e., camera dead-time was negligible, Figure 5.2, A-B).
- The “observed” vs “true” primary photon count-rates were plotted and the data for each detector head were fitted to the paralyzable + non-paralyzable model [156]:

$$R_O = \frac{R_T}{\exp[\tau_P R_T] + (\tau_{NP} - \tau_P) R_T} \quad (5.1)$$

where  $R_O$  and  $R_T$  represent the “observed” and the “true” primary photon count-rates, respectively;  $\tau_P$  and  $\tau_{NP}$  represent the paralyzable and non-paralyzable camera dead-time values (in seconds). Curve fitting was performed using a non-linear least squares method applying the “trust-region” algorithm on MATLAB (Mathworks, USA). The phantom calibration curves are shown in Figure 5.2 A-B.

- From the phantom calibration curves, for each observed count-rate of primary photons, the DTCF can be calculated as the ratio of the “observed” to the “true” primary photon count-rates.
- In order to determine the DTCF to be applied to the reconstructed images, the value of this factor had to be determined (and tabulated) as a function of the total count-rates corresponding to the observed primary photon losses. This was done by relating the values of the observed primary photons count-rates to the corresponding total observed count rates.

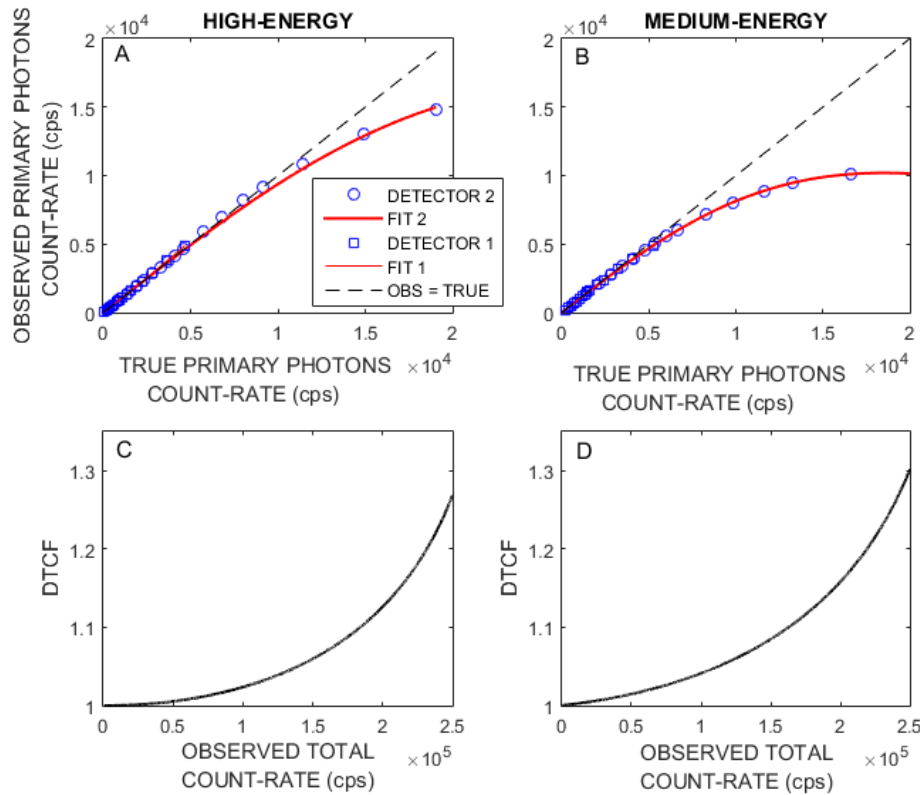


**Figure 5.2 A-B) Phantom calibration curves used to determine dead-time correction factors (DTCF) for HE and ME collimators. C-D) DTCF as a function of the observed total count-rate for HE and ME collimators. Fit parameters of HE dead-time:  $\tau_p = 3.4 \times 10^{-5}$  s;  $\tau_{NP} = 3.7 \times 10^{-14}$  s. Fit parameters of ME dead-time:  $5.4 \times 10^{-5}$  s;  $\tau_{NP} = 5.3 \times 10^{-6}$  s.**

When performing the dead-time correction for the subsequent patient (or phantom) study, first the “observed” total count-rate (recorded in the entire spectrum) has to be estimated, as the measured count rate averaged over all the tomographic projections. Subsequently, the dead-time correction factor corresponding to this total count rate has to be evaluated using the tabulated DTCF values (determined in the previous phantom experiments). Finally, this correction factor has to be applied to the SPECT image reconstructed using primary photons only. The DTCF curves obtained for ME and HE collimators are shown in Figure 5.2 C-D.

### 5.2.2 Monte-Carlo Simulations for $^{188}\text{Re}$ SPECT

Parallel to the experimental acquisitions, Monte Carlo simulations of the SPECT system were performed. The model of the SymbiaT camera included the following elements: the ME and HE collimators (Table 3.1); a 9.5 cm thick NaI detector covered by a 0.05 cm thick aluminum layer at the front; a back-compartment region (light-guide and photo-multiplier tubes) and; lead shielding around the scanner head. The model of the camera was validated in Chapter 3 [144].

The planar images of a  $^{188}\text{Re}$  point-like source (0.15 cm radius) in air, a sphere filled with a  $^{188}\text{Re}$  solution (1.0 cm radius) placed in air, and the same sphere placed inside a Jaszczak phantom filled with water were simulated. For each source, the projections of the true scattered photons detected in the photopeak window and those of scattered photons, which would be acquired using narrow and wide settings of the energy windows used with the TEW scatter correction, were generated. Additionally, the energy spectra that would be detected by the camera for each source type were simulated. A total of  $1.2 \times 10^9$  and  $3 \times 10^9$   $^{188}\text{Re}$  decays were simulated for the point source and the sphere, respectively. The  $^{188}\text{Re}$  decay data in GATE is based on the Evaluated Nuclear Structure Data File (ENDSF) database [115]. The physics of

photon interactions included photoelectric processes, Compton and Rayleigh scattering, pair production, electron ionization and scattering, Bremsstrahlung and electron-positron annihilation.

### **5.2.3 Image Reconstruction, Data Processing and Camera Calibration**

The tomographic reconstructions were performed using the standard ordered subsets expectation maximization (OSEM) algorithm [23] with 10 subsets and 8 iterations. Our previous tests (not described here) indicate that these reconstruction parameters provide a good compromise between the recovery of small and large reconstructed objects and the speed of the reconstruction, and are similar to those typically used in clinics. The corrections for attenuation (using the CT-based attenuation map), scatter (using the TEW method with two sets of scatter window settings, see Table 5.1), and resolution recovery (as described in Section 1.2.4 and in Blinder *et al* 2001 [37]) were applied. Since the amount of Bremsstrahlung photons present in the photopeak window of  $^{188}\text{Re}$  tomographic projections is negligible (see Chapter 3) [144], no further corrections were required.

The counts in the reconstructed SPECT images were corrected for dead-time losses (as described in Section 5.2.1.2) and then converted into units of activity using the experimentally measured calibration factor (CF). The CFs for ME and HE collimators were determined using planar acquisitions of a 12 MBq  $^{188}\text{Re}$  point source. These planar images were corrected for background from high-energy scattered photons using the TEW with “narrow” and “wide” scatter windows (Table 5.1). In the analysis of images for the camera calibration, the counts recorded in the entire image were used (a 1% threshold was applied).

The quantification accuracy of  $^{188}\text{Re}$  images was evaluated in terms of the recovery coefficients (RC), which represent the ratio of the measured activity in each object in the

reconstructed image to this object's true activity, as determined using the dose calibrator. The recovery curves (i.e., RC vs object volume) were determined for each phantom configuration (A and B), both scatter energy window settings ("narrow" and "wide" window) and all scanning conditions (air, water and hot-water).

To quantify the individual object's activity, three segmentation methods were applied. First, a fixed 1% threshold (consistent with that used in the camera calibration measurement) was applied to the SPECT image of the objects in cold background (Air and Cold-water images). This segmentation method was implemented to investigate the quantification accuracy of objects without the influence of partial volume effects (PVEs) as in this case the resulting volumes were large enough to account for the spill-out of activity. However, for obvious reasons, the 1% threshold could not be used for hot-water phantoms.

Moreover, the object's activities in Air, Cold- and Hot-water images were quantified by applying a fixed 40% threshold, which is often used in clinical settings [157,158] and; b) by delineating (in 3D) the object's boundaries based on its physical shape from CT images.

Additionally, since the accuracy of a small object's activity quantification can be strongly influenced by the segmentation method due to partial volume effects (especially for objects in hot-water), the accuracy of activity quantification in the whole phantom was evaluated for all phantom configurations. The total activity in the entire phantom was determined by applying a 1% fixed threshold to the SPECT image. This approach allowed us to evaluate the accuracy of activity quantification independent of the segmentation method. The quantification errors were estimated as the percent difference between the total phantom activity recovered in the reconstructed image and its true activity

## 5.2.4 Image-Based Dosimetry Calculations

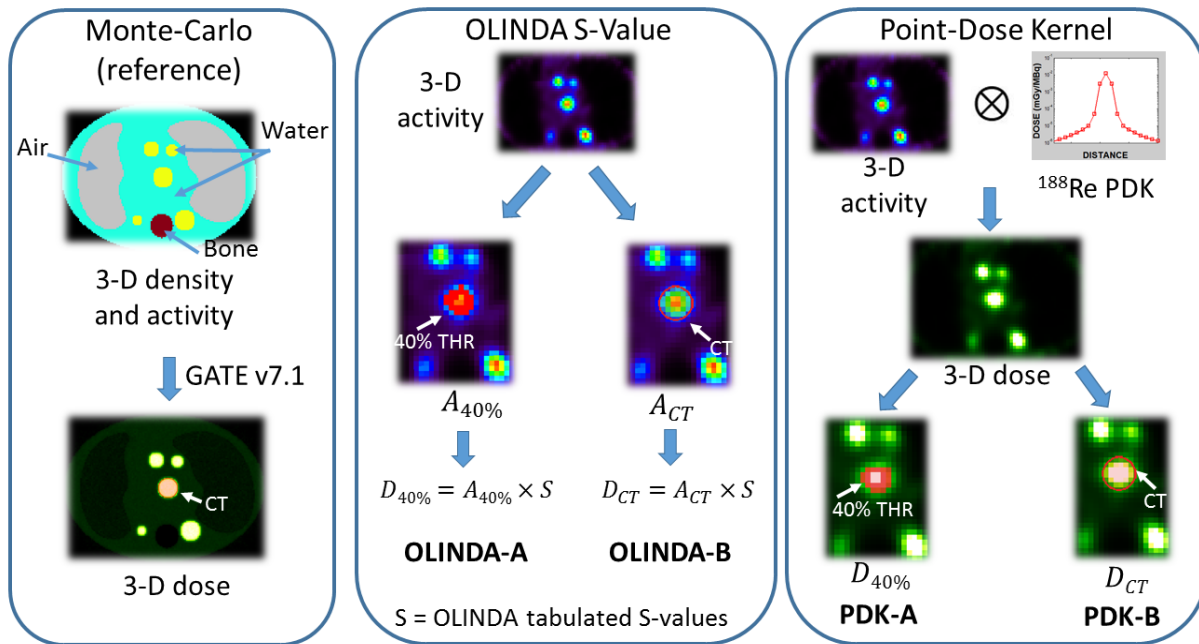


**Figure 5.3** Diagrams showing the two image-based dosimetry approaches that were investigated in this study (OLINDA S-Value and point-dose kernel) and compared to the reference dose obtained from the Monte Carlo-based calculation. For OLINDA and point dose kernel, the volumes of interests were segmented using two methods: a fixed 40% threshold and CT-based boundaries.

Subsequently, the  $^{188}\text{Re}$  images of the hot-water phantoms (Section 5.2.1.1) were used to estimate the spheres' and bottles' average absorbed dose-rates (AADRs). The AADRs were calculated using two methods: (a) OLINDA S-Value for spheres and (b) point dose kernel (PDK). These two methods were selected to investigate how their different use of segmentation affects their accuracy. For an OLINDA-type calculation, the segmentation is applied to the images of activity distribution while in PDK calculations, where the 3D dose (or dose-rate) maps are created, the determination of the average organ/tumour dose requires segmentation of these maps. The accuracy of image-based dosimetry estimates was calculated as the percent error between the AADRs estimated from  $^{188}\text{Re}$  images and the reference AADRs calculated with

Monte-Carlo (Section 5.2.4.3). Diagrams that summarize the sequences of procedures used in the two dosimetry methods are shown in Figure 5.3. The details of these methods are described in the following paragraphs.

#### **5.2.4.1 OLINDA S-Values Method**

The AADR for each object in the phantom was estimated as the product of this object's activity and a volume-dependent S-Value. OLINDA/EXM 1.1 sphere model was used to obtain the tabulated S-Values for each object in units of mGy/MBq. These S-Values were subsequently re-scaled to yield average absorbed dose per unit activity and per unit time (i.e., mGy/MBq/s). The object's activity was obtained from the  $^{188}\text{Re}$  quantitative SPECT image by applying a fixed 40% threshold (method OLINDA-A), as well as by segmenting the object using its physical boundaries based on the CT image (method OLINDA-B).

#### **5.2.4.2 Point Dose Kernel (PDK) Method**

In parallel, the quantitative SPECT images of the hot-water phantoms (i.e., 3-D activity distribution) were convolved with a 3-D  $^{188}\text{Re}$  PDK, resulting in 3-D dose-rate maps. The PDK was generated with the Monte-Carlo code GATE v7.1 by simulating a  $^{188}\text{Re}$  point source placed at the center of a uniform water phantom. This phantom was voxelized using a 31 x 31 x 31 matrix, with cubic voxels of 4.79 mm in size (identical to voxel sizes of the reconstructed SPECT images). The phantom dimensions (half-length = 77 mm) were much larger than the  $\beta$ -particles' maximum range (11 mm), to ensure that the kernel includes all dose-deposition due to  $\beta$ -particles and most of the dose due to  $\gamma$ -particles. The units of the PDK were dose per unit activity per unit time (mGy/MBq/s). Subsequently, the average absorbed dose-rate for each object was obtained by segmenting these 3-D dose-rate maps. Similar to the OLINDA method, two segmentation approaches were used: a fixed 40% threshold (method PDK-A) and the

physical object's boundaries from CT (method PDK-B). The AADRs were calculated as the average voxel value within the segmented volumes.

#### **5.2.4.3 Monte-Carlo Simulations for $^{188}\text{Re}$ Dosimetry Calculations**

In order to evaluate the accuracy of  $^{188}\text{Re}$  image-based dosimetry estimates, the reference AADR was calculated using the full Monte-Carlo simulation of a voxelized version of the hot-water thorax phantom. The voxelized phantom (127 x 168 x 85, 1.95 mm voxel size) was created from CT-images of the real phantom filled with the true activity distributions (as measured with the dose-calibrator) for each object inside the phantom for configurations A and B (Figure 5.3). For simplicity, only three different materials were defined in the phantom simulations: air for the lungs, bone for the spine insert and water for the remaining volume (spheres, bottles and background).

A total of  $3 \times 10^8$   $^{188}\text{Re}$  decays were simulated for each phantom configuration and the dose deposited per unit time at each voxel within the phantom was recorded using the “dose actor” function in GATE. Subsequently, the spheres and bottles were segmented on the 3-D Monte-Carlo dose distribution map using their true boundaries. The reference AADRs were calculated as the average voxel value within the segmented volumes. The statistical uncertainty (obtained using the GATE “dose-uncertainty” actor) of the Monte-Carlo absorbed dose calculations was less than 1.3% for voxels within the spheres and bottles and less than 5% for voxels belonging to the phantom background.

### **5.3 Results**

#### **5.3.1 Measurements of Camera Dead-time Factors**

Figure 5.2 A-B shows the primary photons' count losses due to the dead-time for ME and HE collimators, measured with both camera detectors. These curves represent the observed

count-rates of primary photons (i.e., TEW-scatter corrected photopeak photons) as a function of the true primary photons count-rates. Because we used an additional 10 cm of water between the source and detector 1 (as compared to source-detector 2), detector 1 count-rates were not sufficiently high to generate any visible camera dead-time when using HE or ME collimator. For detector 2, the primary photon count-losses were observed with both HE and ME collimators and the measured dead-time was modelled as a combination of paralyzable and non-paralyzable system (Equation 5.1).

The DTCF estimated from the HE and ME calibration curves were tabulated and plotted as a function of the total observed count-rate (Figure 5.2 C-D).

### 5.3.2 <sup>188</sup>Re Quantification

The experimentally determined camera calibration factors, required to convert the reconstructed image counts into activity values when using TEW-narrow energy window settings were equal to 0.840 cpm/kBq and 1.137 cpm/kBq for HE and ME collimators, respectively. The use of wide window settings for scatter correction of the calibration scan yielded slightly larger calibration factors, 0.853 cpm/kBq (HE) and 1.161 cpm/kBq (ME).

The activity recovery curves (i.e., ratio of reconstructed to true object's activity) determined from the <sup>188</sup>Re SPECT images of objects segmented with the 1% threshold, the 40% threshold and the CT-based volume-of-interests (VOIs) are shown in Figure 5.4. Data acquired with HE collimator and reconstructed using narrow TEW energy windows yielded relatively accurate RCs (errors below 7%) for objects in air (average RC =  $0.95 \pm 0.03$ ) and water (average RC =  $1.07 \pm 0.02$ ) segmented with the 1% threshold method. The use of ME collimator combined with the 1% threshold segmentation and narrow TEW settings resulted in RCs consistently lower than those of HE, with RC average values of  $0.86 \pm 0.04$  and  $1.00 \pm$

0.05 for sources in Air and Cold-water, respectively. The RCs were mostly independent of the object size for objects larger than 30 mL (>2.5 cm in diameter), scanned in cold background (Air and Cold-water) and segmented using a 1% fixed threshold. Although the same segmentation was applied for images in Air and Cold-water, the RCs of objects in Cold-water were approximately 8% higher than RCs of objects in air. This 8% difference was observed at all objects sizes and for both collimators.

The 40% fixed threshold method resulted in substantial underestimation of activities of most objects (RCs were always below 0.80) scanned using all experimental conditions and both collimators. The CT-based segmentation yielded slightly higher RCs than the 40% threshold method but still these RCs ranged from 0.60 (for objects with 2-3 cm in diameter) to 0.85 (for large objects), resulting in underestimation of the activities higher than 10%.

For objects in cold background, the use of wide scatter windows for TEW scatter correction resulted in RCs approximately 5% to 10% higher than those obtained with narrow scatter window settings. This trend was observed in images acquired with both collimators. In the case of hot-background, the effect of the scatter window width on the RCs was more noticeable for ME collimator and large objects.

Overall, the analysis of the RCs suggests that the use of HE collimator results in  $^{188}\text{Re}$  SPECT images with better quantification accuracy than those acquired with ME collimator.

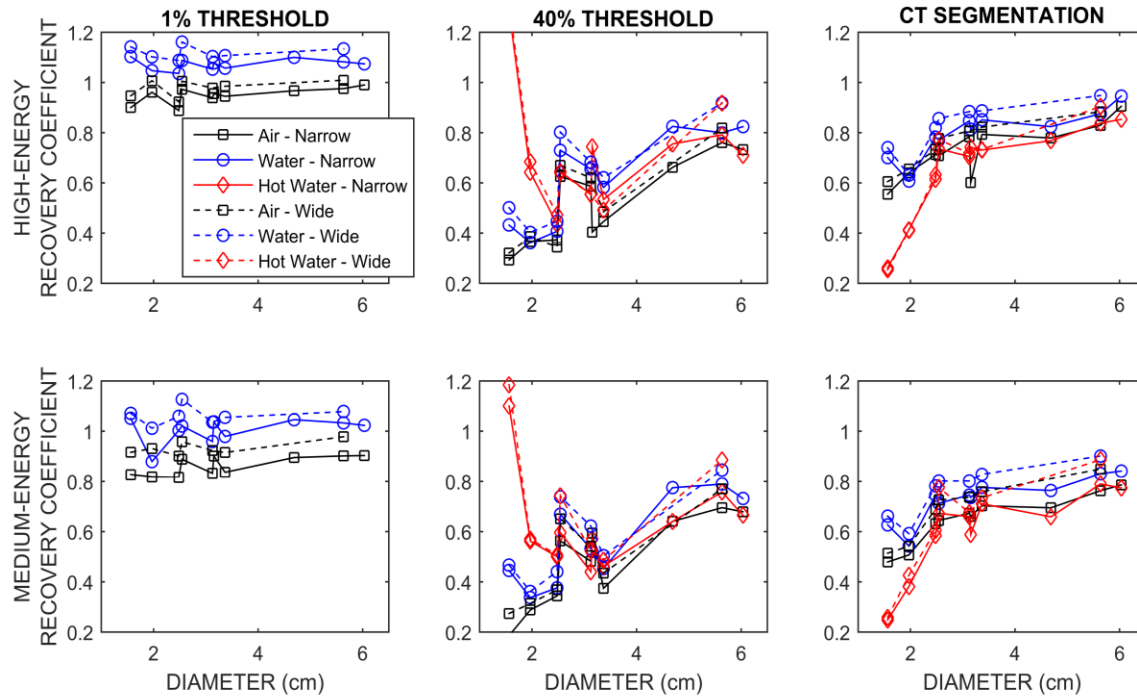


**Figure 5.4 Recovery curves (RC) of air, water and hot-water phantoms scanned with high-energy and medium-energy collimators and reconstructed the narrow (solid-line) and wide (dashed line) scatter window settings. Note: data with wide scatter windows settings were available for phantom configuration A only.**

The quantification accuracies (i.e., percent errors) of the activity measurements in the entire SPECT images of the thorax phantom with and without DTCF are reported in Table 5.3 and are summarized in the box-plots of Figure 5.5. The activity values measured with the dose-calibrator were decay corrected to the beginning of each scan. For experiments where activities were high enough to cause dead-time losses (only acquisitions with ME in our study), including DTCFs improved the accuracy of activity quantification (errors decreased from 18% to <10%, Figure 5.5 B). The application of DTCF was particularly important for ME collimator acquisitions, where the estimated camera dead-time losses of primary photons were as high as 13.9% (phantom B, ME hot-water in Table 5.3). For the phantom images acquired with HE

collimator, the estimated DTCFs were always lower than 2% and the change in quantification accuracy was negligible (Figure 5.5 A).

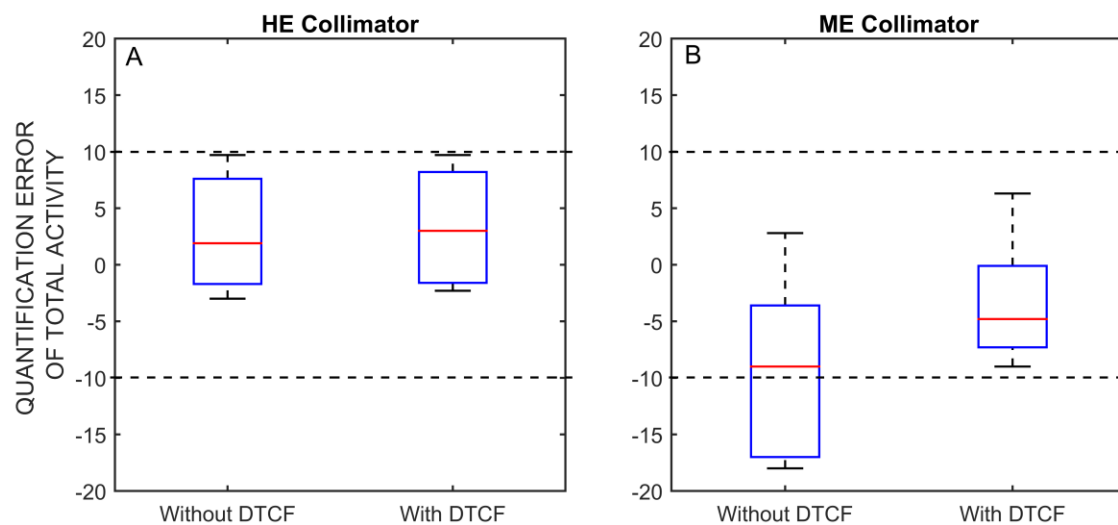


**Figure 5.5** Box-plots summarizing the quantification errors of the total activity measured in the SPECT images of the phantoms with and without dead-time corrections. The dashed lines show the  $\pm 10\%$  error limits.

**Table 5.3 Phantom activities, estimated dead-time correction factors and percentage errors of total phantom activity quantification. Note: Phantom A, Hot-Water has relatively low activity as it was scanned three half-lives later after Air and Water measurements.**

<b>Phantom Configuration - Collimator</b>	<b>Background Conditions</b>	<b>True Total Activity [MBq]</b>	<b>Estimated DTCF [%]</b>	<b>Reconstructed Activity with no DTCF [MBq]</b>	<b>Reconstructed Activity with DTCF [MBq]</b>	<b>% error with no DTCF</b>	<b>% error with DTCF</b>
A-ME	Air	713	9.7	592	649	-17	-9.0
	Water	648	3.7	625	647	-3.6	-0.1
	Hot-water	525	2.7	474	487	-9.7	-7.3
A-HE	Air	697	0.7	676	681	-3.0	-2.3
	Water	664	0.6	714	718	+7.6	+8.2
	Hot-water	491	0.2	483	483	-1.7	-1.6
B-ME	Air	586	5.8	537	568	-8.3	-3.0
	Water	563	3.4	579	599	+2.8	+6.3
	Hot-water	1227	13.9	1006	1146	-18	-6.6
B-HE	Air	575	0.6	591	594	+2.7	+3.3
	Water	554	0.3	608	608	+9.7	+9.7
	Hot-water	1193	1.6	1206	1225	+1.1	+2.7

### 5.3.3 Image-Based Dosimetry

Figure 5.6 evaluates the accuracy of  $^{188}\text{Re}$  image-based dosimetry calculations using the four investigated methods (OLINDA-A, OLINDA-B, PDK-A and PDK-B). The dosimetry calculations were performed using images of the hot-water phantom only since these represent the most realistic conditions, best approximating those of  $^{188}\text{Re}$  therapy scans.

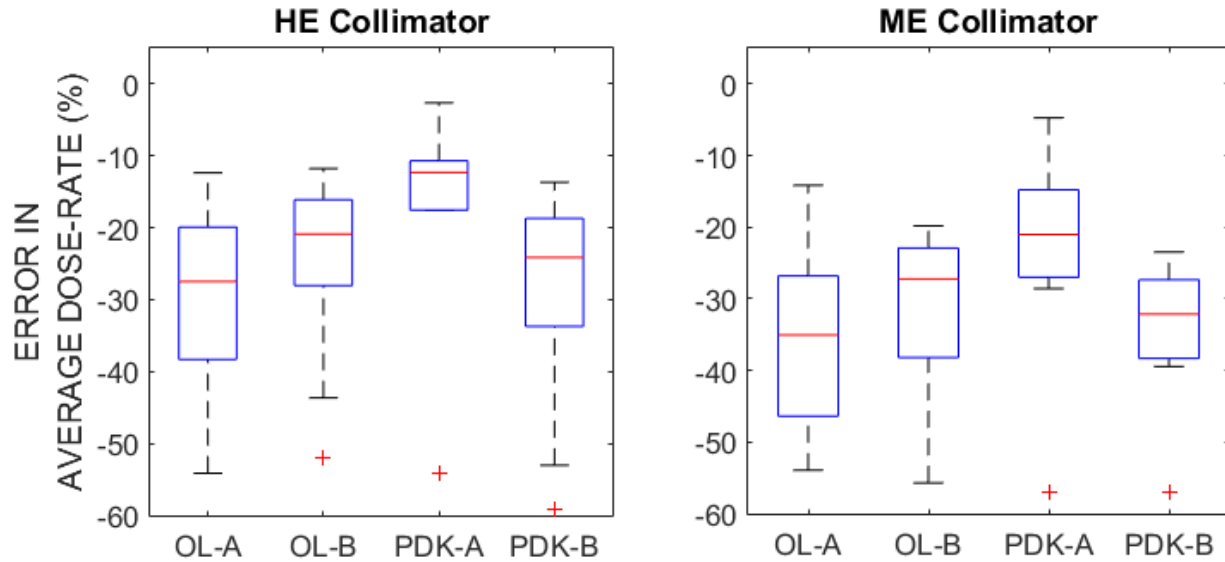


**Figure 5.6 Percent errors of the average absorbed dose-rates calculated using: OLINDA S-Values with 40% threshold segmentation (OL-A), OLINDA S-Values with CT-based segmentation (OL-B), point dose kernel with 40% threshold segmentation (PDK-A) and point dose kernel with CT-based segmentation (PDK-B).**

All dosimetry methods underestimated the average absorbed dose rates (AADR) by more than 10%, as shown by the negative error values on the box plots in Figure 5.6. For images obtained with HE collimator, the average errors for OLINDA-A and OLINDA-B were equal to -30% (range -54% to -12%) and -22% (range -43% to -11%), respectively. The average error for AADR estimated using PDK-B method was -29% (range -59% to -14%) while PDK-A yielded the most accurate results, with an average error of -15% (range -18% to -3%). The errors of PDK-A decreased to -10% on average when only objects with large volumes (>30 mL) were considered.

As expected, the AADR estimated from ME collimator images were lower than those obtained with HE which was consistent with the trend of RCs observed in ME and HE images.

## 5.4 Discussion

### 5.4.1 Accuracy of $^{188}\text{Re}$ SPECT Image Quantification

Figure 5.2 C-D shows that, for the same observed total count-rate, the count losses of primary photons for ME collimator were only slightly larger (i.e., higher DTCF) than those for the HE collimator. This result agrees with our hypothesis that primary photon dead-time losses depend mostly on the total observed count-rate. However, the same total observed count rates for ME and HE result from much lower activity when ME collimator is used, partly due to its higher septal penetration. Therefore, the losses of primary photons due to dead time for ME are typically substantially higher than those of HE at the same activity level (Figure 5.5 and Table 5.3).

Our analysis of RCs for objects with different sizes placed in a cold background (air and water phantom) and segmented with a 1% fixed threshold allowed us to investigate the quantification accuracy of  $^{188}\text{Re}$  image reconstructions without the influence of the partial volume effects (PVE). Additionally, the measurements of objects in air and water helped us to compare the performance of attenuation and the TEW scatter corrections in these conditions.

It is interesting to notice that, regardless of the segmentation method, the RCs for objects in water were always higher than those of objects in air. To clarify this issue, we investigated the performance of the TEW scatter corrections using Monte-Carlo simulations (Section 5.2.2). A point source in air (modeling the conditions of the calibration acquisition), and a 2-cm diameter sphere placed in air and water (modeling the experiment) were simulated. Figure 5.7 shows the differences between the simulated true scatter, the simulated TEW-narrow scatter estimate, and the simulated TEW-wide estimate (for simulations with HE collimator). The analyses of the simulated energy spectra and the projections of scattered photons show that for sources in air the

number of photons in the TEW-scatter windows exceeds the true scattered photons. Therefore, the reconstructed activity is lower than the true activity. However, this situation is reversed for the sphere placed in water, where simulations indicate that TEW-scatter windows seriously underestimate the true scatter. Similar results were obtained for simulations with ME collimator (Figure 5.8).

The Monte-Carlo simulations also revealed that scatter estimates using the wide energy window settings are slightly lower than those obtained with narrow TEW settings (Figure 5.7 and Figure 5.8). This effect is mostly due to the substantial contribution of the tails of the photopeak into narrow scatter windows. Therefore, the RCs for images reconstructed with narrow TEW settings are consistently lower than RCs for images with wide settings. This result is not as pronounced for scans in cold water, where the effect of underestimation of scatter by TEW dominates and, amplified by attenuation correction, causes RC to be 8-10% higher than 1.

The TEW method, although simple and practical, only approximates the true scatter and its performance depends on the object scattering conditions (see Figure 5.7, sphere in air and water). Robinson *et al* 2016 [27] also reported a similar overestimation of activity due to TEW in a phantom study using  $^{177}\text{Lu}$ . To compensate for the differences between the estimated scatter and the true scatter, the use of scaling factor was suggested [42,159].

The investigation of quantification accuracy for scans of objects placed in hot background (which represents clinically realistic conditions), underlines the importance of an adequate segmentation method. The RCs for objects segmented using the 40% threshold clearly show that this segmentation fails to recover the true objects' activities in both HE and ME collimator images. This is caused by the partial volume effects. Although the loss of resolution was compensated in our reconstruction algorithm, the implemented method did not model septal

penetration. Septal penetration of high-energy photons was substantial in both these cases [144]. Additionally, the 40% threshold method yielded noisy RCs (i.e., RCs that did not increase “smoothly” with object’s diameter). Such variability in RCs could be due to the fact that the size and shape of the segmented VOIs were very sensitive to the statistical noise, the shape of the object and the activity distribution within the segmented object. Although the objects in our study were filled with uniform activity, the use of resolution recovery during reconstruction created Gibbs artefacts (displayed as “horns” at the edges of large objects, or as a “peak” in the center of small objects) which resulted in non-uniformities of activity in the SPECT image of these objects. The Gibbs artefacts are rarely apparent in patient studies, however, they may influence activity distribution and this analysis illustrates the variability of accuracy of activity quantification using a fixed thresholding method.

For CT-based segmentation, the activity RCs were approximately 5% higher (on average) than those obtained with the 40% threshold segmentation because CT-derived VOIs were consistently larger than those obtained with the 40% threshold method. The recovery values were always below 0.85 except for the large objects (> 100 mL) reconstructed with wide TEW energy settings.

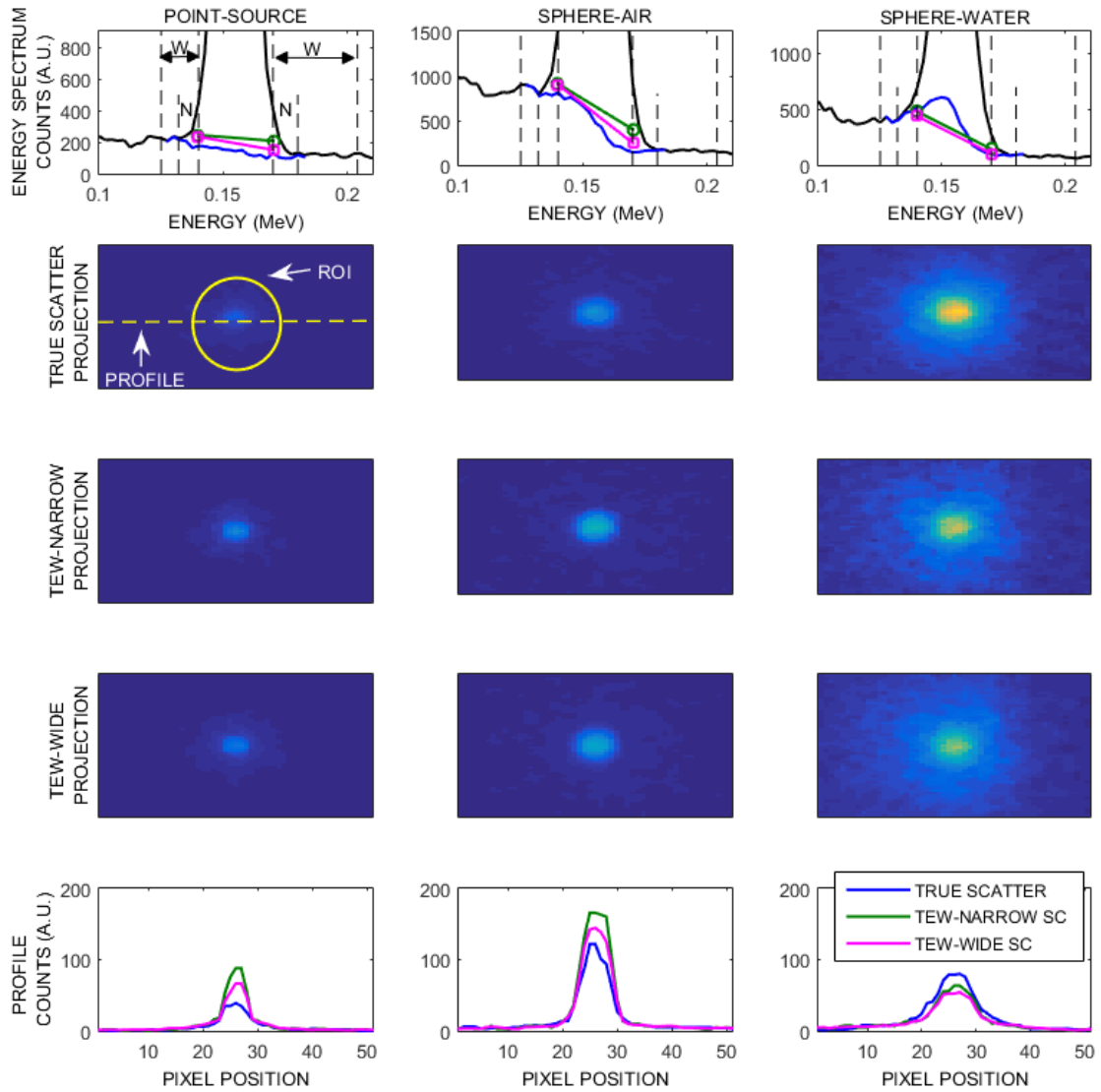


Figure 5.7 Comparison of simulated true scatter, simulated TEW-narrow scatter estimate and simulated TEW-wide scatter estimate from a  $^{188}\text{Re}$  point-source and a 2.0 cm diameter sphere filled with  $^{188}\text{Re}$  in air and water and scanned using HE collimator. Row 1: simulated energy spectra obtained from counts within a 5.0 cm diameter circular ROI around the source center. The wide (W) and narrow (N) scatter window settings are indicated with vertical dashed lines. Row 2-4: Simulated projection images. Row 5: profiles along the simulated projection images.

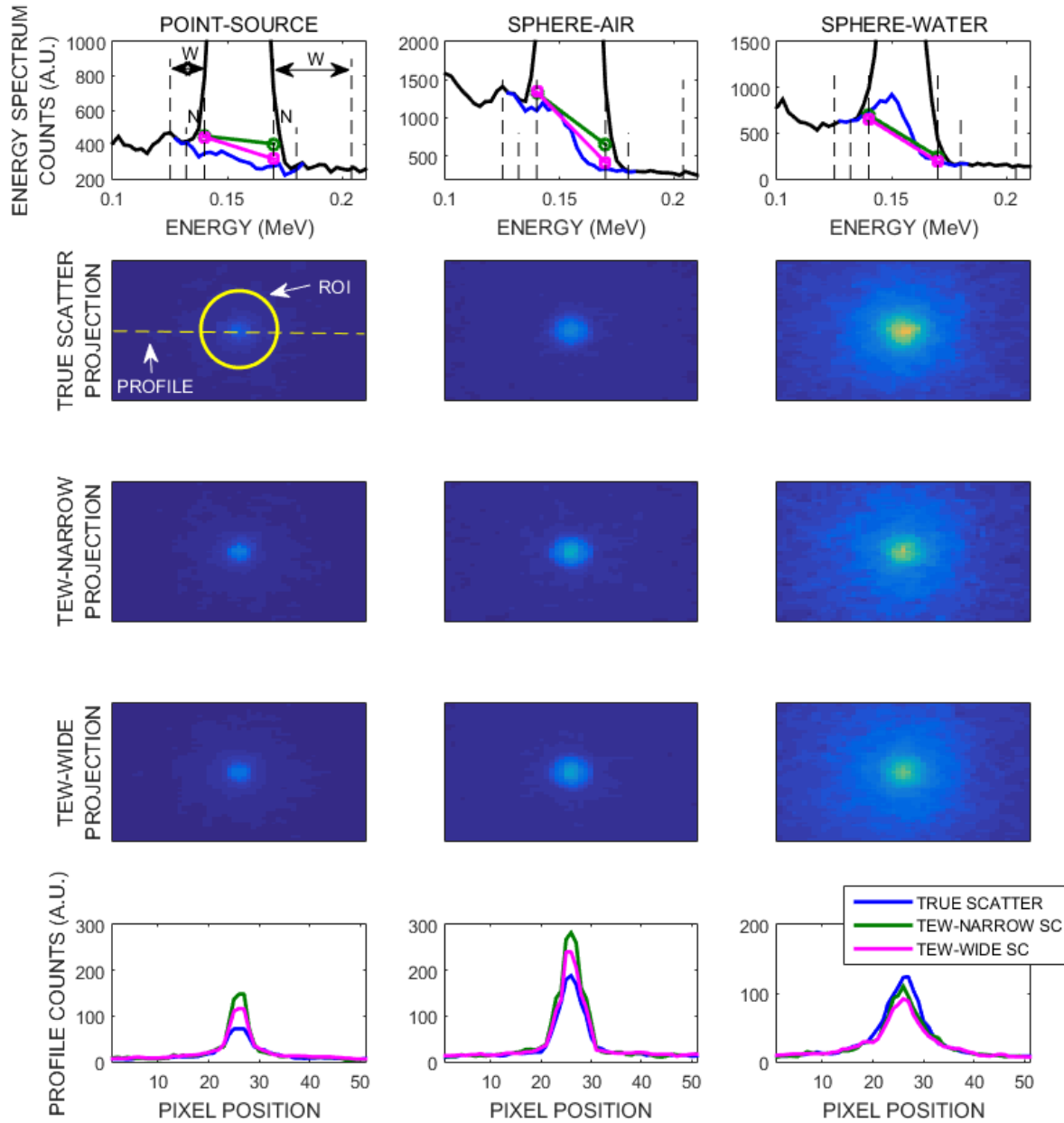


Figure 5.8 Comparison of simulated true scatter, simulated TEW-narrow scatter estimate and simulated TEW-wide scatter estimate from a  $^{188}\text{Re}$  point-source and a 2.0 cm diameter sphere filled with  $^{188}\text{Re}$  in air and water and scanned using ME collimator. Row 1: simulated energy spectra obtained from counts within a 5.0 cm diameter circular ROI around the source center. The wide (W) and narrow (N) scatter window settings are indicated with vertical dashed lines. Row 2-4: Simulated projection images. Row 5: profiles along the simulated projection images.

In terms of the quantification accuracy of total activity measurements in the entire phantom, the point source calibration method applied to  $^{188}\text{Re}$  images reconstructed with CT-based attenuation corrections, TEW-narrow scatter correction, resolution recovery and dead-time corrections resulted in errors below 10% for all the investigated phantom configurations (Figure 5.5 and Table 5.3). The accuracy achieved in this study for  $^{188}\text{Re}$  is similar to that reported by other phantom studies of  $^{99\text{m}}\text{Tc}$ ,  $^{111}\text{In}$ ,  $^{131}\text{I}$  [17] and  $^{177}\text{Lu}$  [29,148], demonstrating that the standard reconstruction with corrections yields relatively accurate quantification of  $^{188}\text{Re}$  total activities. The remaining challenge, however, is image segmentation and partial volume effect corrections on nuclear medicine images.

Due to septal penetration of high-energy photons the dead-time losses for the ME collimator were as high as 14% (Table 5.3) for 1.2 GBq activity, a typical dose in  $^{188}\text{Re}$  radioembolization procedures [44]. The use of the HE collimator considerably decreased septal penetration and minimized the DT losses. In our study, the applied DTCFs did not completely recover the activity of ME images (Table 5.3), causing RCs to be slightly lower than those of the HE images, but still below  $\pm 10\%$  (Figure 5.5 B).

One limitation of the proposed dead-time correction method is that it estimates the DTCF based on the count-rate of the whole energy spectrum averaged over all the acquired tomographic projections which may not apply to patient studies that show large variations in the count-rate across different projection angles. However, these deviations in DTCF will be small and will only marginally affect the overall DT corrections (which for HE collimator usually remain below 10%). Additionally, despite this limitation, the simplicity of this approach and the resulting improvement of activity quantification (especially for high-activity studies acquired with ME scans) seems to justify its potential use in clinics.

Another factor that needs to be considered for image quantification is the camera calibration factor. Different methods for camera calibration have been proposed [8,148]. The point source planar method is a simple method and it is expected to provide accurate estimates of activity if all the image-degrading factors are properly compensated during the reconstruction [29]. Alternatively, if the reconstruction algorithm is not fully quantitative, a calibration factor derived from a tomographic acquisition of a large phantom filled with activity is recommended as it is expected that in this case both the calibration phantom and patient images would suffer from the same quantification inaccuracies [8]. In our study, the camera calibration factor was determined using the planar image of a  $^{188}\text{Re}$  point source scanned in air, with corrections for scatter using TEW. The TEW method was required to remove the down-scattered high-energy photons recorded in the photopeak window of the planar calibration image.

#### **5.4.2 Accuracy of $^{188}\text{Re}$ SPECT Image-Based Dosimetry**

The determination of the absorbed dose in an entire organ or tumour requires segmentation of this organ/tumour volume (volume of interest, VOI). With the reconstruction techniques used in this study, both the 40% fixed threshold (OLINDA-A and PDK-A) and CT-based segmentations (OLINDA-B and PDK-B) under-estimated the absorbed doses by more than 10%.

For the PDK-A, the average errors in AADRs were much lower than those obtained with OLINDA-A (average errors were equal to -15% and -30%, respectively). On the other hand, when CT-segmentation was applied, the errors of AADRs estimated with OLINDA-B (average error of -22%) and PDK-B (average error of -29%) were similar to each other. Please note that since our reference dose obtained from MC simulations was estimated using true volumes of the objects (which is equivalent to CT-based segmentation), these errors must be attributed to other causes than segmentation. Indeed, in our case these errors had different origins. For the

OLINDA-B method, the dose was underestimated because the CT volumes were not large enough to completely recover the objects' activities (due to partial volume effect). For the PDK-B method, the convolution with the dose kernel on the activity map (which was already suffering from partial-volume effects) decreased the average dose value within the segmented object' volume.

The analysis of the impact of image segmentation on the activity map (OLINDA) or dose-rate map (PDK) helped us understand why PDK-A yield better dose-rate estimates than all other methods. For the investigated SBR of 7:1, the 40% threshold delineated smaller volumes than those found within CT-based boundaries (as illustrated in Figure 5.3). These smaller volumes did not include many voxels belonging to the dose fall-off tails, so the resulting calculated average dose-rates were less affected by the partial volume effect. It is important to note, however, that this result cannot be generalized to other scans, as the difference between VOI obtained with 40% threshold and that from CT-image will depend on the SBR, as well as on the activity distribution within the organ of interest.

In summary, our results illustrate the variability of dose-estimates and emphasize the need for better segmentation methods.

The use of the PDK method for image-based dosimetry calculations offers the possibility to investigate dose profiles, dose-volume histograms (DVH), and other parameters such as  $D_{90}$  (commonly used in external beam radiotherapies). There is evidence that suggests that average absorbed dose might not be predictive of deterministic effects like tumor-control and organ toxicities [8]. For instance, Shcherbinin *et al* 2013 determined that  $D_{90}$  tumor dose correlates better to patient response than the average tumor dose for patients receiving  $^{188}\text{Re}$ -Human Serum Albumin radioembolization.

The analysis of these parameters on SPECT-based dose maps, however, must be done carefully. Firstly, the images compensated for resolution loss may display Gibbs artefacts [160] which are displayed as “horns” at the edges of large objects with sharp boundaries (Figure 5.9 E); or as a “peak” at the center of small objects (Figure 5.9 B). The presence of Gibbs artefacts may impact the accuracy of the DVH [161]. To illustrate the severity of this problem for  $^{188}\text{Re}$ , dose-rate profiles and DVHs for the 20 mL and 110 mL spheres inside the hot water phantom were generated and compared to the reference values obtained from Monte-Carlo (Figure 5.9).

Additionally, large differences are observed in DVHs generated from dose-maps derived from images with and without resolution recovery. Using these DVHs, the  $D_{90}$  values can be determined. For example, the estimated  $D_{90}$  doses obtained from DVHs of images compensated for resolution (i.e., affected by Gibbs artefacts) were 22 Gy and 6.8 Gy for the small and large sphere, respectively. These estimates, however, decreased to 13.5 Gy (small sphere) and 5.6 Gy (large sphere) if no resolution recovery is applied. The reference  $D_{90}$  doses obtained from Monte-Carlo derived DVHs were 30.7 Gy and 8.8 Gy for the 20-mL and the 110-mL sphere, respectively. These large variabilities in the DVHs and  $D_{90}$ , which depends on the resolution recovery and the segmentation method, reflect the importance of investigating the accuracy of the image reconstruction and dosimetry method to be applied in clinical studies. Although not discussed here, other factors such as noise and reconstruction parameters (iteration numbers) might also affect the accuracy of the DVHs [161]. For example, the convergence rate for objects in hot background might be lower than that of objects in cold background. As a result, images of objects in hot-background might yield lower RCs (and hence, dose estimates) than images in cold background if the same number of subsets and iterations are used.

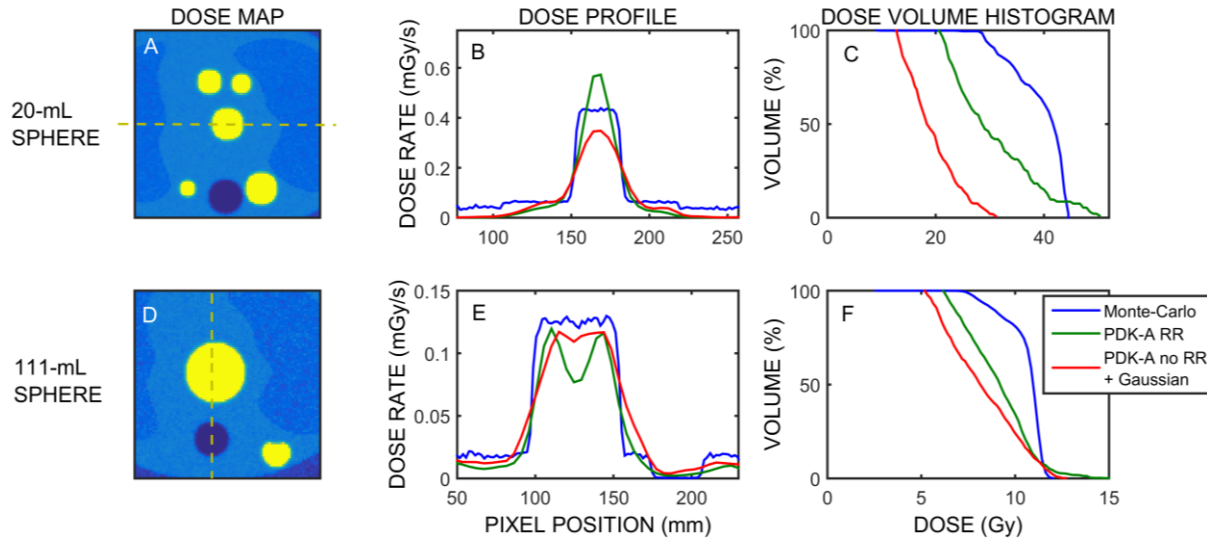


**Figure 5.9 (A,D) Monte-Carlo dose-maps showing the 20-mL sphere and the 111-mL sphere in hot water; (B,E) Dose-profiles along the 20-mL sphere and the 111-mL sphere for three cases: Monte-Carlo dose-map, dose-map obtained from images reconstructed with (“PDK-A RR”) and without resolution recovery + filtered with a 5-mm Gaussian kernel (“PDK-A no RR + Gaussian”); (C,F) Dose volume histograms calculated for the 20-mL and 111-mL spheres derived from images with and without resolution recovery. The cumulated dose was calculated from the dose-rate map, assuming the physical decay of  $^{188}\text{Re}$  only.**

## 5.5 Conclusions

In this work, the accuracy of activity quantification and image-based dosimetry calculations of  $^{188}\text{Re}$  was evaluated using phantoms and Monte-Carlo simulations. The experimental conditions resembled those of typical  $^{188}\text{Re}$  radioembolization therapy scans.

In conclusion, good accuracy of activity quantification (errors below 10%) was obtained for the entire phantom and for objects scanned in cold background (air and water) when reconstruction was performed with OSEM (10 subsets, 8 iterations), with CT-based attenuation correction, TEW scatter corrections with narrow scatter windows, resolution recovery and dead-time correction was applied. However, the accuracy of activity quantification for objects placed in hot water was strongly influenced by the applied segmentation method. Substantial errors

(20% and higher) were observed when object activities were determined using the 40% thresholds or object boundaries were obtained from CT images. The use of a ME collimator resulted in large dead-time losses that decreased quantification accuracy despite the fact that the dead-time correction was applied. The Monte-Carlo simulations confirmed that TEW scatter correction applied to  $^{188}\text{Re}$ , although practical, yields only approximate estimates of the true scatter.

In terms of image-base dosimetry, the errors of the  $^{188}\text{Re}$  average absorbed dose rates were larger than 10% for both dosimetry methods used in this study. However, our analysis suggests that these errors are not related to SPECT quantitation, but were mostly due to partial volume effects and were further exacerbated by the poor segmentation methods.

For patient-specific dose calculations of  $^{188}\text{Re}$  therapies, the use of improved segmentation methods, such as the iterative adaptive threshold [162], potentially could reduce these errors. Alternatively, the errors in dose estimates can be decreased by applying correction factors for partial-volume effects, for example by using coefficients derived from the recovery curves.

In spite of this somehow limited accuracy of dose calculations, in our opinion patient specific image based dosimetry does provide information which is sufficient and crucially important and will allow physicians to correlate administered activities and doses delivered to tumours and critical organs with the therapy outcomes.

## Chapter 6: Image-Based Dosimetry of Patients Undergoing $^{188}\text{Re}$ -Lipiodol Trans-arterial Radioembolization

### 6.1 Introduction

The Canadian Cancer Society reports that the incidence of primary liver cancer (hepatocellular carcinoma) and secondary liver cancer, with the most common form being metastatic colorectal carcinoma, are on the rise [163]. These types of cancers are one of the leading causes of cancer related deaths worldwide [164]. For patients suffering from primary or secondary liver cancer, resection represents the therapy of choice, but only a minority of patients fulfil the criteria for resection surgery or liver transplantation [165]. When surgery is not an option, other treatment strategies are being used such as systemic chemotherapy for liver metastases [166], hepatic arterial embolization (with or without chemotherapy), radiofrequency ablation [167] or brachytherapy [168]. External beam radiotherapy might also be effective but can only be applied in localized disease. Another alternative for these patients is the use of radioembolization with radioactive particles.

The majority of radioembolization procedures involve the use of  $^{90}\text{Y}$ -microspheres (glass or resin) [169]. The high-energy of  $^{90}\text{Y}$   $\beta$ -emissions (Table 1.2) makes this isotope suitable for treating tumors. However, since  $^{90}\text{Y}$  is a pure  $\beta$ -emitter, imaging the microsphere biodistribution within the patient is commonly performed with Bremsstrahlung SPECT, which is not optimal for quantitative measurements [170]. Alternatively, quantitative  $^{90}\text{Y}$  imaging can be achieved using PET/CT [171], but this imaging procedure has some drawbacks. Due to the very low emission yield of positrons by  $^{90}\text{Y}$ , these PET images suffer from high levels of noise, and also PET/CT scanners are less common than SPECT/CT in nuclear medicine departments due to their high

cost. Additionally, the commercially available  $^{90}\text{Y}$  microspheres are expensive, making this treatment option inaccessible in some cases, especially for developing countries where hepatocellular carcinoma has high prevalence in the population [44].

The use of  $^{188}\text{Re}$  for radioembolization offers advantages with respect to  $^{90}\text{Y}$ . As demonstrated in Chapter 5, its 155 keV  $\gamma$ -emissions allows performance of quantitative  $^{188}\text{Re}$  SPECT and image-based dosimetry. In addition, the availability of  $^{188}\text{Re}$  through the generator makes the treatment less costly and more practical as  $^{188}\text{Re}$  can be produced on site. Overall,  $^{188}\text{Re}$  is a very attractive isotope for Radioembolization.

The main clinical experience with  $^{188}\text{Re}$  radioembolization comes from on a large study sponsored by IAEA that involved 8 countries [44,72]. In this study, 185 patients received radioembolization using  $^{188}\text{Re}$ -Lipiodol. Among these patients, 25% of them showed objective response (tumor size reduction by 50%, as seen on CT); stable disease was observed in 53% and tumor progression in 22%. Overall, this multi-center study showed that  $^{188}\text{Re}$ -Lipiodol is a safe and cost-effective method to treat primary HCC. An alternative carrier to deliver  $^{188}\text{Re}$  in radioembolization studies is Human Serum Albumin (HSA). Two small  $^{188}\text{Re}$ -HSA clinical studies with 10 and 13 patients were carried out in Germany and Poland, respectively [70,71]. In the German study, Liepe *et al* [70] reported that 2 out of 10 patients showed partial response to therapy, 5 out of 10 showed stable disease, and 3 out of 10 showed disease progression. Similarly, Nowicki *et al* [71] reported a partial response in 1 out 13 patients, stable disease in 7 out of 13 and disease progression in 5 patients. The slightly worse outcomes in the European studies (relative to the IAEA trial) can be related to the fact that these studies included patients with HCC and colorectal liver metastases, whereas the IAEA study mostly included patients with HCC, which has better prognosis than the secondary liver cancer.

The organs at risk during  $^{188}\text{Re}$  radioembolization therapies are the lungs, the liver and the bone marrow with maximum tolerated doses of 12 Gy, 30 Gy and 1.5 Gy, respectively [57]. Zanzonico *et al* [57] developed a clinical algorithm to estimate the patient-specific therapeutic activity for  $^{188}\text{Re}$ -Lipiodol radioembolization. In this protocol, a pre-treatment  $^{188}\text{Re}$  ‘scout’ planar scan is used to estimate the maximum injected activity (i.e., the therapeutic dose) that would result in organs-at-risk doses below the tolerance limits. The protocol was applied to the IAEA study. Despite the efforts by the IAEA team to perform patient-specific treatment planning and the reported promising results, there is still room for optimization. Firstly, the treatment planning in the IAEA study was based on a single  $^{188}\text{Re}$  whole-body planar image which had limited quantitative accuracy due to the lack of depth information and proper quantification, which could lead to sub-optimal prediction of therapeutic activities. Secondly, the protocol relied on the assumption that biological clearance of  $^{188}\text{Re}$  Lipiodol by tumor and other organs was very low and therefore, the effective clearance was modelled by the physical half-life of  $^{188}\text{Re}$ . This assumption, which was based on  $^{131}\text{I}$ -Lipiodol studies [172], was not confirmed during the clinical study due to the lack of patient images at multiple time points after  $^{188}\text{Re}$ -Lipiodol administration.

Applying quantitative SPECT to  $^{188}\text{Re}$  therapies not only would improve the treatment planning, but would also allow us to perform accurate calculations of doses absorbed by tumors and organs at risk. The current dose-limits for lung, liver and marrow are inferred from external beam radiotherapy. There is a growing evidence that radiobiology and tissue response in radionuclide therapies are different from those in external beam therapies because of the differences in dose rates and dose distributions [173,174]. Furthermore, the availability of 3-D dose distribution would allow us to investigate the relationship between Dose-Volume

Histograms (DVHs) or  $D_{90}$  doses and the patient response to therapy. In some cases, it has been shown that these parameters are better predictors of biological response than the mean absorbed doses [8,71].

The objective of this study was to apply the quantitative methods developed in this thesis to perform patient-specific dosimetry of patients undergoing  $^{188}\text{Re}$ -Lipiodol radioembolization. For the scope of the thesis, this work is intended as an illustration of the capabilities of these methods allowing us to discuss their practical limitations. The data presented in this study have been obtained in the scope of the collaboration between the Medical Imaging Research Group (Vancouver, Canada) and the Nuclear Medicine department at Kovai Center Medical Hospital (Coimbatore, India). In this study, the following objectives are being addressed:

- 1) Determination of the effective half-life of  $^{188}\text{Re}$  Lipiodol in tumors and organs at risk.
- 2) Determination of average absorbed radiation dose to tumor and organs at risk based on quantitative SPECT imaging. In the future, the correlation between the average doses and biological response will be investigated.
- 3) Comparison of the  $^{188}\text{Re}$ -Lipiodol radioembolization average absorbed tumor/organ doses obtained with two dosimetry methods: OLINDA and Voxel S-Value.
- 4) Investigation of the correlation between DVHs (and/or other parameters derived from 3-D data) and the biological response.

Up to date, only four patients' data have been analyzed. Therefore, the results that are presented here must be considered only as an illustration of the application of the  $^{188}\text{Re}$  quantitative methods.

## 6.2 Materials and Methods

### 6.2.1 Preparation of $^{188}\text{Re}$ -Lipiodol

Rhenium-188, in the form of sodium perrhenate ( $\text{Na}^{188}\text{ReO}_4$ ), was eluted from a  $^{188}\text{W}/^{188}\text{Re}$  generator (iTG – Isotopen Technologien München, Germany) using a 0.9% NaCl solution. Rhenium-188 Lipiodol labelling was performed using Rhenium-4-hexadecyl-4,-7-diaza-1,-10-decaedithiol Lipiodol 188 ( $^{188}\text{Re}$ -HDD-Lipiodol) labelling kits, following the procedure described previously in Paeng *et al* 2003 [175]. The labelling kits were obtained from Seoul National University Hospital, Korea. Routine quality control testing for radiochemical purity was done prior to patient injection, consisting mainly in thin layer chromatography.

The activity of  $^{188}\text{Re}$  was measured prior to the labelling procedure using a Capintec CRC-25 R dose calibrator (Capintec, USA). Based on our findings from Chapter 2 (Section 2.3.1.2), and the published data [89], the dose calibrator dial settings were set to  $621 \times 10$ .

### 6.2.2 Patient Selection Criteria

Patients with histologically proven hepatocellular carcinoma (HCC) who fell under Child-Pugh class A with adequate bone marrow & liver function were selected for the study. Only patients who demonstrated uni-lobular involvement in contrast-enhanced CT (CCT) images were included in the study. The patients with extra-hepatic metastases, chronic kidney disease and significant co-morbidities were excluded from the study. A written informed consent was obtained from all the patients before taking part in the study.

Up to date, a total of 4 patients (2 males and 2 females) with a mean age of 49 years (range 20 years to 71 years) have been included in the presented work. The radioembolization treatment and all the image acquisitions were performed at the nuclear medicine department in Kovai Medical Centre Hospital (KMCH) (Coimbatore, India).

### 6.2.3 Treatment Planning and Imaging Protocol

For each patient, the image protocol consisted of a diagnostic CCT and a series of 2 to 3 nuclear medicine acquisitions performed at  $t_1 = 3$  hours,  $t_2 = 12$  hours and  $t_3 = 48$  hours post-administration of  $^{188}\text{Re}$ -Lipiodol.

The therapeutic activity of  $^{188}\text{Re}$ -Lipiodol was calculated empirically based on the patient's tumor volume determined on the diagnostic CCT image. Approximately, 37 MBq (1 mCi) of  $^{188}\text{Re}$  was administered per mL of tumor. For very small tumors, the dose per unit volume was increased up to 92.5 MBq/mL (2.5 mCi/mL) whereas for very large tumors, the dose was decreased to approximately 14.8 MBq/mL (0.4 mCi/mL).

For each nuclear medicine acquisition, a whole-body anterior/posterior planar scan and a SPECT/CT scan of the lungs-abdominal area were performed using a SymbiaT SPECT/CT camera (Siemens Medical, Germany) equipped with the HE collimator. In order to acquire an image of the whole-body, the speed of the patient-bed was set to 15 cm/min. During SPECT acquisitions, a total of 32 projections (20 seconds/view) were acquired over 360 degrees around the patient (angular step =  $360/32 = 11.25$  degrees). The nuclear medicine data were collected using the quantitative "narrow" energy window settings (Section 5.2.1.1, Table 5.1). In addition, a low-dose CT was also acquired to be used for attenuation correction of the SPECT images. The details of each patient's protocol (administered activity, tumor volume and imaging times) are reported in Table 6.1.

**Table 6.1 Administered  $^{188}\text{Re}$ -Lipiodol activities, tumor volumes and imaging protocols of the four patients investigated in this study. The tumor volumes (reported by the physicians) were determined from diagnostic contrast enhanced CT images.**

	<b>Injected Activity [MBq]</b>	<b>Tumor Volume [cc]</b>	<b>Whole-body Scans</b>	<b>SPECT/CT Scans</b>	<b>Acquisition # 1 [h]</b>	<b>Acquisition # 2 [h]</b>	<b>Acquisition # 3 [h]</b>
<b>Patient 01</b>	1296	22	2	2	1.3	27.7	N/A
<b>Patient 02</b>	1527	10	2	2	4.6	27.3	N/A
<b>Patient 03</b>	1918	400	3	3	3.1	24.7	49.2
<b>Patient 04</b>	5239	600	2	2	4.2	29.1	N/A

#### **6.2.4 Image Reconstruction, Camera Calibration and Activity quantification**

The whole-body planar data were processed according to the MIRD pamphlet No. 16 [43]. Since no transmission scans were available, attenuation and/or scatter corrections were not applied to these images. For this reason, the 2-D planar data were only used to determine the relative change in organ/tumor activities over time (i.e., shape of the time activity curve).

The patient's tomographic data were reconstructed using the  $^{188}\text{Re}$  quantitative protocol described in Chapter 5. The protocol consisted of standard OSEM reconstruction (8 subsets, 12 iterations) with corrections for attenuation (CT-based), scatter (TEW [26]), dead-time (based on the experimental phantom calibration, Section 5.2.1.2) and resolution recovery (RR) [37]. The number of subsets and iterations (8 subsets, 12 iterations) was slightly modified with respect to the phantom quantification experiments (10 subsets, 10 iterations) because patient data were acquired using 32 projections, which did not allow one to create 10 subsets.

The counts in the reconstructed images were converted into units of activity by applying the camera calibration factor (CF) determined with the point-source method (Section 5.2.3). The

details of this procedure, which was performed at KMCH, are as follows: a planar image of a 25 MBq point source of  $^{188}\text{Re}$  was acquired for 10 minutes using the “narrow” energy window settings. The counts corresponding to high-energy down-scattered photons were removed from the planar image using the TEW method. The counts in the final image, which represents primary photons only, were obtained by applying a 1% threshold on this image. As expected, the CF obtained for the SPECT/CT camera at KMCH was similar to that obtained for our SPECT/CT in Vancouver because the same SPECT/CT system, collimator and energy window settings were used in both centers. This CF, however, cannot be applied to the whole-body planar images because the counts in these images do not represent counts from primary photons only.

### **6.2.5 Dosimetry Protocols**

The goal of image-based dosimetry calculations is to determine the dose absorbed by tumor(s) and organs at risk on a patient-by-patient basis. For  $^{188}\text{Re}$ -Lipiodol radioembolization, the organs at risk include the normal liver, lungs and bone marrow. In addition, other organs that might uptake  $^{188}\text{Re}$ -Lipiodol are the stomach, kidneys, spleen and thyroid (Figure 6.1). In this study, the doses in these organs were estimated based on three quantitative protocols: the hybrid-OLINDA, the hybrid-Voxel S-Value and the purely SPECT-Voxel S-Value. These methods combine two imaging protocols (hybrid planar/SPECT and purely SPECT imaging, Section 1.3.2.2) to determine the time-integrated activity curves (TIACs) in source regions with two dosimetry methods (OLINDA and Voxel S-Value, Section 1.3.3), to calculate the average absorbed dose by target regions.

In all methods, the whole-body planar images from different time points were co-registered to the whole-body image at  $t_1$  using a rigid-registration algorithm. Similarly, rigid registration was also applied to the CT and the SPECT images. The image-registration, organ segmentation,

TIACs calculations and dosimetry estimates were performed using Q-Dose, a software for dosimetry calculations in radionuclide therapy (ABX-CRO, Germany). The details of each protocol are described in the following sub-sections.

#### **6.2.5.1 Hybrid Planar/SPECT – OLINDA**

In the hybrid planar/SPECT-OLINDA method, rough boundaries of the source-regions (organs/tumor) were first delineated on the whole-body planar images. Subsequently, within these boundaries, a 40% threshold was applied to determine the count-rate (and therefore, the relative activity) within each segmented region of interest (ROI). For each patient, the following source regions were segmented on planar data: tumor, entire liver, normal liver, lungs, kidneys, spleen, stomach, thyroid and urinary bladder (see Figure 6.1). The normal liver ROI was defined as the difference between the entire liver ROI and the tumor ROI. Since the planar images from different time-points were co-registered to each-other, the activity as a function of time (time-activity curve, TAC) was obtained for each source region. These curves only represent the relative activity change over time in each source organs. To determine the absolute time-activity curves, the source's absolute activities were determined using the SPECT images and the curves were re-scaled as described in Section 1.3.2.2. The boundaries of the source-organs that were visible on the SPECT/CT FOV (i.e., all the listed organs except for the thyroid and the urinary bladder) were manually delineated based on their physical size using the CT image which was co-registered to the SPECT data. The boundaries of tumors were obtained in two steps. Firstly, a rough boundary was manually drawn (on the CT) within the liver segment or lobe that contained the tumor (as reported by the physicians). Secondly, a fixed threshold was applied within this boundary on the SPECT image such that the recovered volume would equal the reported tumor

volume of Table 6.1 (Figure 6.3). The quality of this approach to tumor segmentation will be discussed with the nuclear medicine physicians at KMCH.

For each source region, the quantitative time-activity data were fit to a mono-exponential function:

$$A_{fit}(t) = a \times e^{-\frac{\ln 2}{T_{eff}}t} \quad (6.1)$$

where  $a$  and  $T_{eff}$  are the parameters of the fit. The quantity  $a$  represents the source region activity at time of injection ( $t = 0$ ). The quantity  $T_{eff}$  represents the effective half-life of  $^{188}\text{Re}$ -Lipiodol clearance in the source of interest, which is related to the physical half-life of  $^{188}\text{Re}$  ( $T_{phys} = 17 \text{ h}$ ) and the biological half-life ( $T_{bio}$ ):

$$\frac{1}{T_{eff}} = \frac{1}{T_{phys}} + \frac{1}{T_{bio}}. \quad (6.2)$$

This mono-exponential fit was only applied to time values between the first ( $t_1$ ) and the last acquired time-point ( $t_{last}$ ). Since three of the patients were only scanned twice, the mono-exponential function perfectly fitted the two data points  $t_1$  and  $t_2$ . For Patient 03, which was scanned three times, the mono-exponential function fitted the data well ( $R^2 = 0.997$ ). Between  $t = 0$  hours and  $t_1$ , the source activity was assumed to grow linearly. For  $t > t_{last}$ , the activity was extrapolated assuming a mono-exponential clearance following the  $^{188}\text{Re}$  physical decay. Figure 6.4 A shows the normalized tumor TACs of the four patients investigated in this study. The total number of decays within each source-region were calculated by analytical integration of the time-activity curves. The resulting TIACs were divided by the injected activity to determine the so-called “residence time”. The “residence time”, combined with the model of a 70-kg human (male or female) phantom, was used to determine the average organ radiation dose using

OLINDA/EXM 1.1 [47]. In order to determine the tumor and the normal liver dose, the OLINDA sphere model was used. This model assumes that the tumor/normal liver activity is uniformly distributed within a sphere that has a volume equal to the segmented tumor/normal liver volumes.

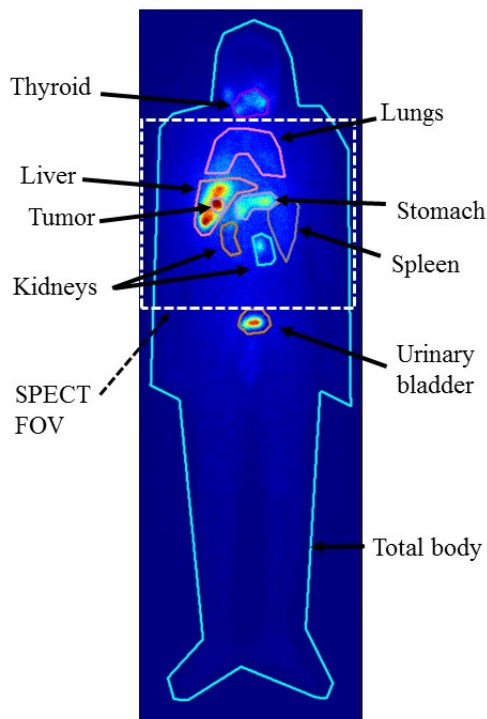


**Figure 6.1** Anterior whole-body view of Patient 01 showing the manually drawn organ's ROIs. Note: The thyroid and the urinary bladder were not visible on SPECT/CT.

#### **6.2.5.2 Hybrid Planar/SPECT – Voxel S-Value**

The imaging protocol, organ segmentation and time-activity curve determination of the hybrid planar/SPECT – Voxel S-Value method were identical to those of the hybrid-OLINDA method. The only difference between these two methods was the calculation of average organ/tumor doses. The hybrid – Voxel S-Value required the knowledge of the TAC for each voxel in the SPECT image. For a given segmented region, the shape of the TAC for each individual voxel was assumed to be that of the whole region. The absolute TAC for each voxel

was determined by re-scaling this relative-curve with this voxel activity. Subsequently, the area under each voxel's TAC was calculated. As a result, a 3-D map of the total number of  $^{188}\text{Re}$  decays at each particular voxel was obtained. Next, this 3-D map was convolved with the  $^{188}\text{Re}$  PDK (Section 5.2.4.2) yielding a 3-D dose-map. Finally, the average tumor/organ absorbed dose was calculated as the average voxel value within the segmented region (tumor/organ) of interest on the dose-map. In addition to average doses, the 3-D dose map was used to generate tumor and normal-liver DVHs. Due to large non-uniformity of density within the lung-tissue and lack of a  $^{188}\text{Re}$  PDK for this organ, the average doses absorbed by the lungs were not calculated with the Voxel S method.

### **6.2.5.3 Purely SPECT – Voxel S-Value**

With the purely SPECT – Voxel S-Value, the time-activity curves for each organ and tumor were determined solely from SPECT data. The rest of the procedure was identical to that of the hybrid Voxel S-Value method. Since SPECT and CT data were co-registered, and SPECT images from different time points were also co-registered to each-other, the organ/tumor boundaries that were drawn on the CT image at  $t_1$  were propagated to the remaining time points. Additionally, due to the limitations and inaccuracies of rigid-registration of soft-tissue organs, the segmented volumes at each time point were reviewed and edited.

### 6.3 Results

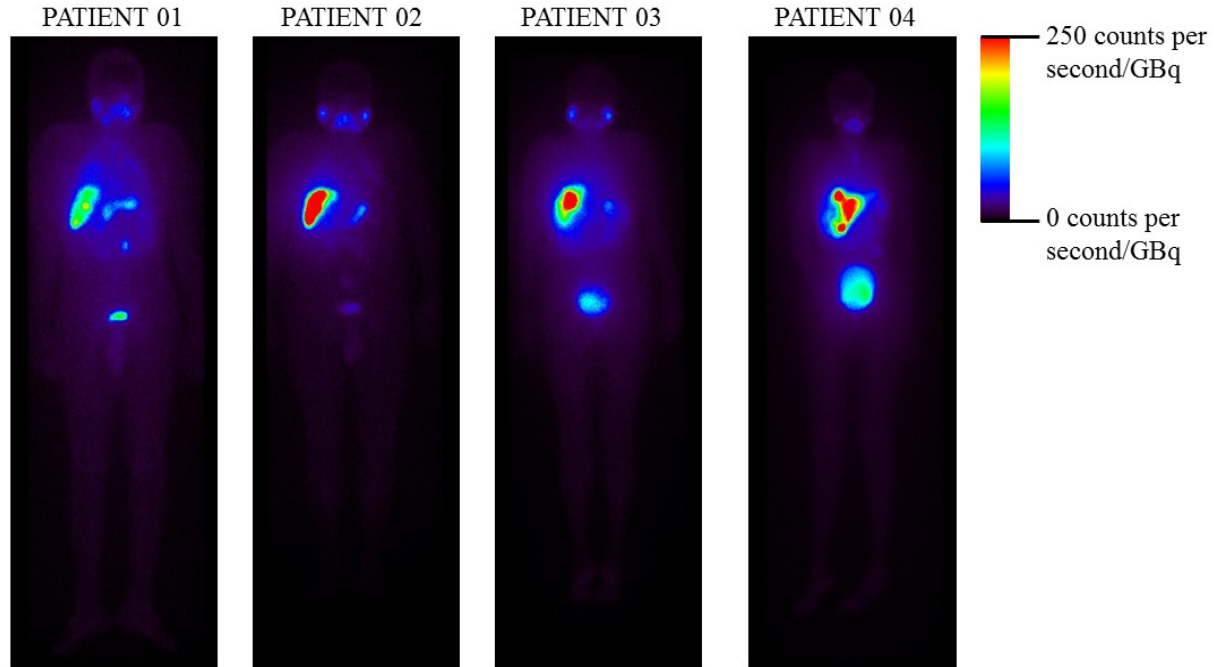


**Figure 6.2** Planar images of  $^{188}\text{Re}$ -Lipiodol biodistribution in the four patients investigated in this study. The images shown were acquired 3 hours post-administration of the radiopharmaceutical. For comparison purposes, the counts in each image were normalized by the corresponding injected activity.

Figure 6.2 shows the whole-body nuclear medicine images (anterior-view) of the four patients investigated in this study. The images were acquired approximately 3 hours after the administration of  $^{188}\text{Re}$  –Lipiodol. For the sake of comparison, the count-rate in each image was normalized to the corresponding injected activity. The maximum uptake of  $^{188}\text{Re}$ -Lipiodol is observed in the liver/tumor region. The thyroid and possibly the salivary glands also show large uptake, followed by those in the urinary bladder, the stomach, the kidneys, the spleen and the lungs.

Figure 6.3 shows coronal views from CT and fused SPECT/CT images of each patient. Since Lipiodol is radio-opaque, its presence in liver tissue is clearly visible on the CT images. The fused SPECT/CT images in Figure 6.3 also show the boundaries of the delineated tumor

volumes. It is very important to keep in mind that the following results concerning effective half-life, dose and DVH of tumors are based on the current segmentation method.

Table 6.2 reports the effective half-lives for each organ/tumor determined with the hybrid and the purely SPECT imaging protocols. Both the hybrid and the purely SPECT methods yielded very similar effective half-lives for all the regions of interest and patients investigated. On average, the tumor effective half-life was  $11.9 \pm 2.5$  h and  $12.3 \pm 1.4$  h for the hybrid and the pure SPECT method, respectively. The  $^{188}\text{Re}$ -Lipiodol retention in the normal liver ( $12.2 \pm 2.5$  h for hybrid,  $13.0 \pm 1.3$  h for purely SPECT) was similar to that observed in the tumor. The slowest observed clearance of  $^{188}\text{Re}$ -Lipiodol was found in the spleen ( $16.5 \pm 2.7$  h). The fastest clearance of  $^{188}\text{Re}$ -Lipiodol was observed in stomach ( $8.0 \pm 0.8$  h), thyroid ( $7.9 \pm 0.5$  h) and urinary bladder ( $6.8 \pm 1.6$  h).

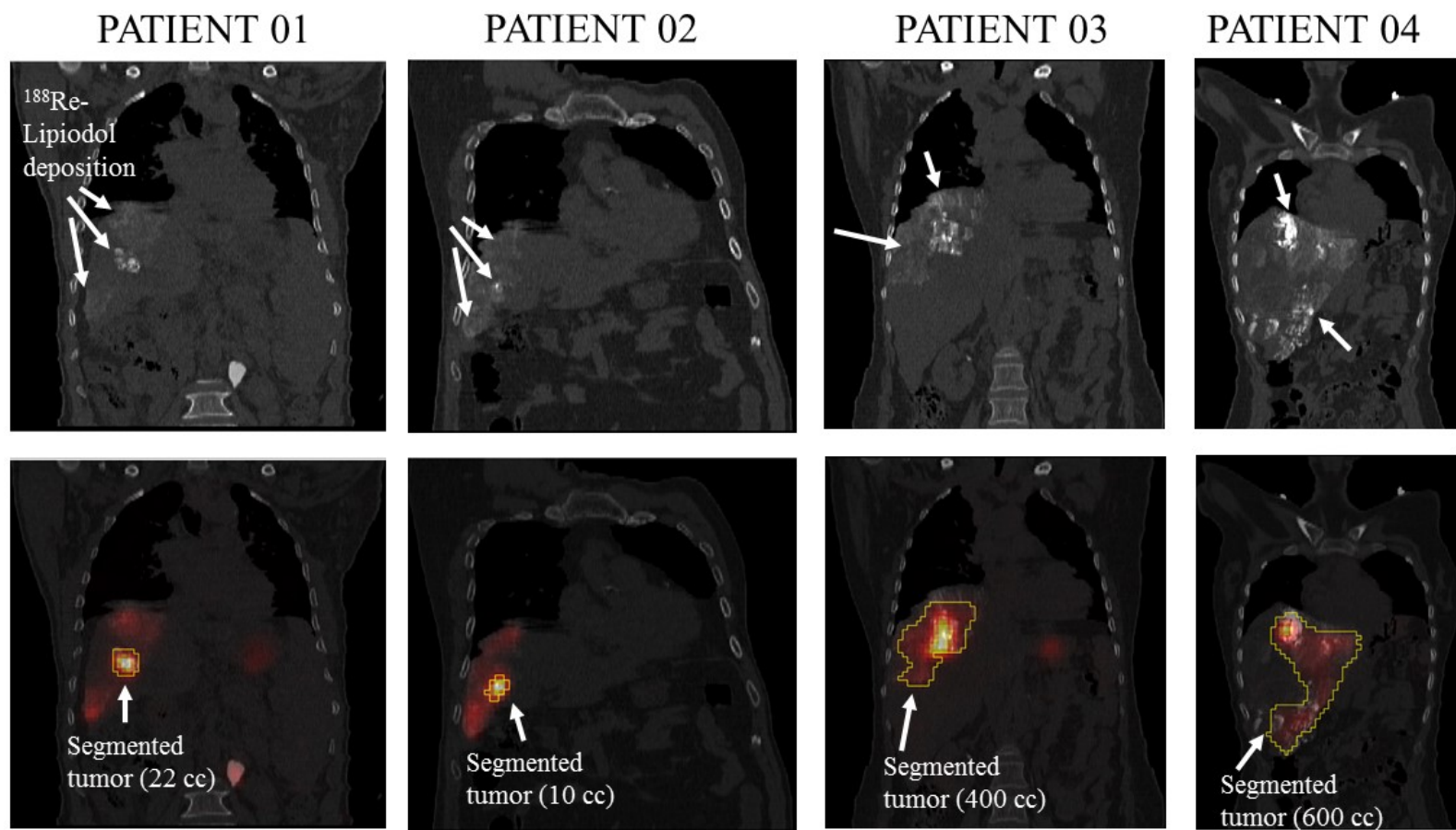
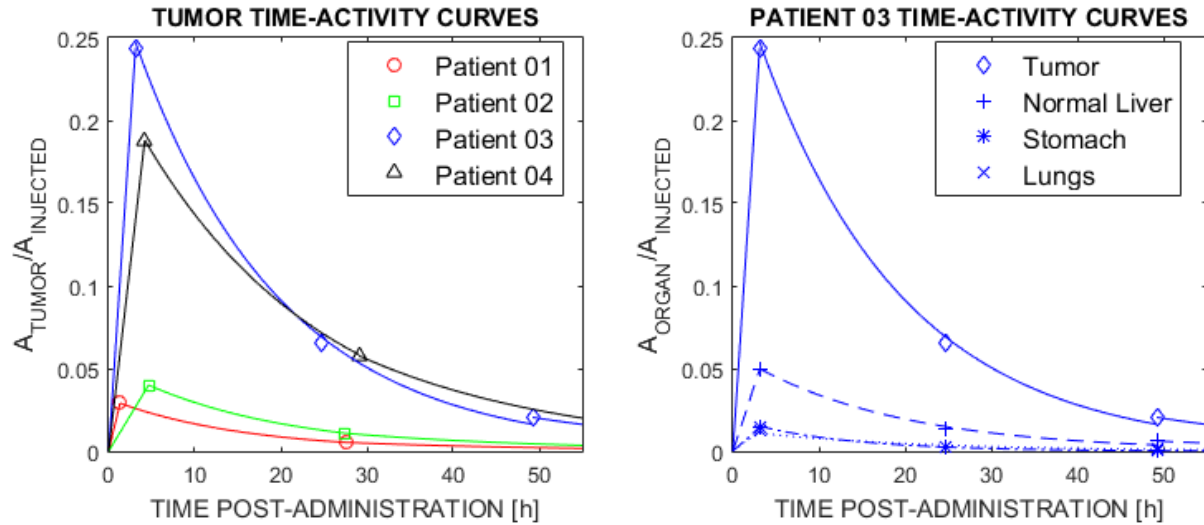


Figure 6.3 CT (top-row) and fused SPECT/CT (bottom-row) coronal slices showing the  $^{188}\text{Re}$ -Lipiodol biodistribution within the liver and the segmented tumor boundaries of the four patients investigated in this study.

**Table 6.2 Effective half-lives of tumor and organs at risk determined with the hybrid planar/SPECT method (H) and the purely SPECT method (P).**

	Tumor [h]		Normal Liver [h]		Stomach [h]		Lungs [h]		Kidneys [h] (Left/Right)		Spleen [h]		Thyroid [h]		Urinary bladder [h]	
	H	P	H	P	H	P	H	P	H	P	H	P	H	P	H	P
<b>Patient 01</b>	9.8	10.7	9.8	11.2	7.8	7.4	9.8	9.7	8.6	7.8	10.4	13.6	7.6	N/A	6.1	N/A
<b>Patient 02</b>	10.8	12.1	11.0	13.6	8.9	9.0	8.5	8.5	9.8	21.1	17.9	21.0	7.7	N/A	9.6	N/A
<b>Patient 03</b>	10.7	11.8	11.6	12.4	10.9	8.4	13.6	13.5	12.6	15.8	11.5	15.8	7.6	N/A	5.5	N/A
<b>Patient 04</b>	16.2	14.6	16.3	14.7	11.5	7.0	11.6	11.5	14.0	9.2	17.2	15.8	8.7	N/A	6.0	N/A
<b>Average [h]</b>	11.9	12.3	12.2	13.0	9.8	8.0	10.9	10.8	11.3	13.5	14.3	16.5	7.9	N/A	6.8	N/A
<b>SD [h]</b>	2.5	1.4	2.5	1.3	1.4	0.8	1.9	1.9	2.1	5.4	3.3	2.7	0.5	N/A	1.6	N/A



**Figure 6.4 Comparison of tumor time-activity curves for all the patients (A) and organ-time activity curves for Patient 03 (B). The time-activity curves were determined from purely SPECT data and were normalized by the injected activity. With this normalization, the area under these curves represents the residence time.**

The normalized tumor time-activity curves of each patient are shown in Figure 6.4 A. The presented tumor data of Figure 6.4-A indicates that, for very large tumors (Patient 03 and Patient 04), approximately 20% to 25% of the injected activity localized in the tumor volume at  $t_1$ . For very small tumors (Patient 01 and Patient 02), approximately 5% of the injected activity localized in the tumor site. Figure 6.4 B shows the differences between the tumor and the organ-at-risk time-activity curves of Patient 03, reflecting the higher concentration of  $^{188}\text{Re}$  in tumor with respect to normal liver, stomach or lungs.

Table 6.3 compares the tumor and organ doses per injected activity (averaged over all patients) estimated with the hybrid-OLINDA, hybrid-Voxel S and purely SPECT – Voxel S methods. On average, the coefficient of variation of the relative tumor and normal-liver doses estimated with the three methods was 2% and 5%, respectively. In terms of organ doses, the hybrid-Voxel S and the purely SPECT – Voxel S methods also yielded comparable results, with

an average percent difference (determined as  $\frac{DOSE_{hybrid}-DOSE_{pure}}{DOSE_{pure}} \times 100$ ) equal to +20%, -20% and -4% for stomach, kidneys and spleen doses, respectively. The hybrid-OLINDA method, however, yielded stomach doses substantially smaller than the Voxel-S methods. The opposite trend was observed for hybrid-OLINDA spleen doses. These differences are mostly due to the fact that OLINDA assumes that the activity is distributed uniformly in the standard organ geometry of an adult phantom (male or female), whereas Voxel-S methods account for the true volume and activity distribution to calculate the average dose. The stomach volumes of the standard phantoms used in OLINDA were often larger than those of the patients (determined from their CT images) whereas the OLINDA spleen volumes were usually smaller than those obtained from CT images. The dose-estimates obtained with OLINDA can be improved by introducing a scaling factor that takes into account the patient-specific organ mass.

**Table 6.3 Tumor and organs at risk doses per injected activity. The doses were determined with the Hybrid OLINDA, the Hybrid Voxel S and the Purely SPECT Voxel S methods. All quantities are expressed in mGy/MBq. Data are average  $\pm$  SD over the four patients. The quantities in parenthesis represent the range of values.**

	<b>Hybrid OLINDA</b>	<b>Hybrid Voxel S</b>	<b>Purely SPECT Voxel S</b>
<b>Tumor</b>	12.5 $\pm$ 13.1 (3.7 – 31.9)	11.9 $\pm$ 11.3 (3.4 – 27.8)	12.2 $\pm$ 12.7 (3.2 – 30.8)
<b>Normal Liver</b>	0.95 $\pm$ 0.72 (0.37 – 1.96)	0.85 $\pm$ 0.66 (0.33 – 1.76)	0.93 $\pm$ 0.78 (0.35 – 2.01)
<b>Stomach</b>	0.24 $\pm$ 0.08 (0.13 – 0.32)	0.66 $\pm$ 0.13 (0.53 – 0.81)	0.55 $\pm$ 0.16 (0.34 – 0.71)
<b>Lungs</b>	0.20 $\pm$ 0.07 (0.11 – 0.27)	N/A	N/A
<b>Kidneys</b>	0.24 $\pm$ 0.12 (0.07 – 0.34)	0.23 $\pm$ 0.13 (0.08 – 0.41)	0.29 $\pm$ 0.11 (0.20 – 0.45)
<b>Spleen</b>	0.45 $\pm$ 0.28 (0.10 – 0.54)	0.24 $\pm$ 0.17 (0.10 – 0.48)	0.25 $\pm$ 0.16 (0.11 – 0.45)

Regardless of the method, the calculated average dose in lungs and normal liver were well below the maximum tolerated values (30 Gy for liver, 12 Gy for lungs) in all the patients (Table 6.4). The dose absorbed by bone marrow, however, was not determined on this study. The absorbed tumor doses ranged from 9 Gy (Patient 03) to approximately 48 Gy (Patient 02). As shown in Figure 6.2, there was large accumulation of  $^{188}\text{Re}$  in the thyroid and salivary glands which might indicate that a fraction of  $^{188}\text{Re}$  (in the form of perrhenate) is dissociated from Lipiodol *in-vivo* and travels in the circulatory system. Unfortunately, neither the thyroid or salivary glands organs were visible on the SPECT/CT images. Therefore, accurate estimates of the absorbed doses are not available. Nevertheless, the absorbed dose to the thyroid was estimated semi-quantitatively using only the planar images. These estimations ranged from 3 Gy (Patient 01) to 12 Gy (Patient 04).

**Table 6.4 Radiation doses absorbed by tumor, normal liver and lungs calculated with the hybrid - OLINDA (H-O), the hybrid - Voxel S (H-VS) and the purely SPECT - Voxel S (P-VS) methods. All the quantities are in Gy.**

	Tumor			Normal Liver			Lungs		
	H-O	H-VS	P-VS	H-O	H-VS	P-VS	H-O	H-VS	P-VS
<b>Patient 01</b>	11.65	11.05	12.05	1.27	1.17	1.28	0.32	N/A	N/A
<b>Patient 02</b>	48.78	42.44	47.08	2.99	2.69	3.07	0.41	N/A	N/A
<b>Patient 03</b>	9.55	8.87	9.34	0.65	0.57	0.61	0.28	N/A	N/A
<b>Patient 04</b>	19.14	17.84	16.51	2.61	2.15	1.92	0.61	N/A	N/A

Figure 6.5 shows the tumor and normal-liver DVHs generated from the hybrid – Voxel S-Value method for each patient. The use of DVHs in this clinical study will be discussed with the physicians in the future.

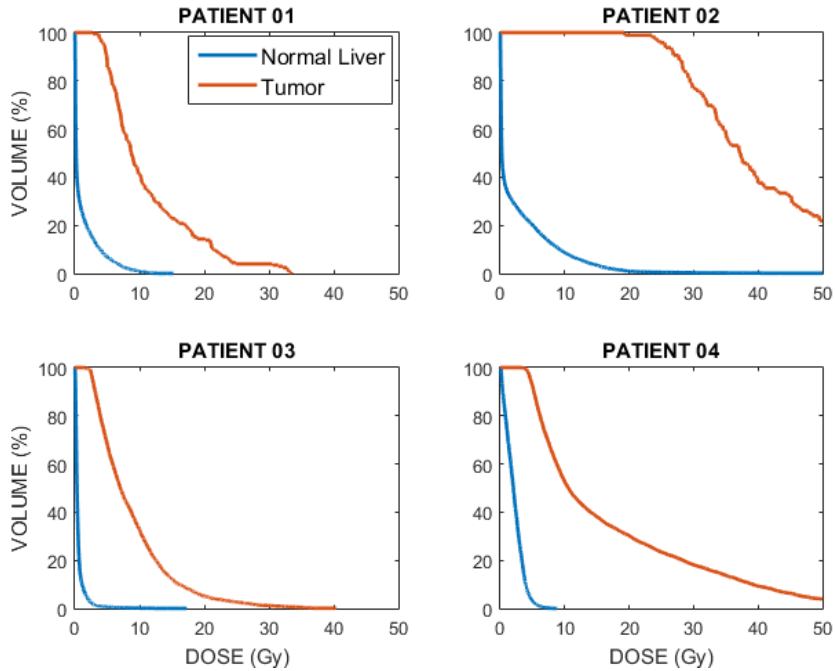


**Figure 6.5 Dose volume histograms (DVH) of tumor and normal liver volumes of the patients investigated in this study. For the sake of comparison, the dose-range on each DVH is set to [0Gy, 50Gy].**

## 6.4 Discussion

The presented patient data (only 4 patients) corresponds to a small subset of a large clinical study that includes 30 patients receiving  $^{188}\text{Re}$ -Lipiodol for treatment of primary HCC. For this reason, the trends and findings obtained with these data might not be representative for the complete patient dataset. Furthermore, the segmented tumor boundaries based on the fixed-threshold value that recovered the tumor volume (Table 6.1) might not correlate to the true physical tumor distribution. In order to evaluate the validity of our tumor segmentation, the diagnostic CCT images showing the true tumor volume are required. Despite these concerns, the preliminary analysis of the small dataset was very useful to identify the limitations of the

methods, optimize the imaging protocols and establish the final dosimetry tools to be used on the large patient group. Currently, these results are being discussed with the clinical team at KMCH.

One of the main assumptions of the treatment plan developed by Zanzonico *et al* [57] for the IAEA clinical trial was that  $^{188}\text{Re}$ -Lipiodol follows a mono-exponential clearance in tumor and organs at risk with an effective half-life of 17 h (i.e.,  $^{188}\text{Re}$  physical half-life). Our preliminary analysis indicates that tumor clearance is faster than 17h, with an average effective half-life of 12 hours, obtained with both hybrid imaging and pure-SPECT imaging protocols. It is worth noting that on a pre-clinical study of rabbits bearing liver tumors that received  $^{188}\text{Re}$ -HDD-Lipiodol radioembolization, the average effective half-life of  $^{188}\text{Re}$ -Lipiodol in tumor was also reported to be 12 hours [175]. Since Zanzonico *et al* treatment planning was based on estimates of the maximum tolerated-activity for lungs, normal liver and red marrow, assuming a ‘slow’ clearance of  $^{188}\text{Re}$ -Lipiodol provided a conservative prediction of the maximum injected activity. If our preliminary findings are proven to be true (once a larger set of patient data is analyzed), the current treatment planning for patients receiving  $^{188}\text{Re}$ -Lipiodol radioembolization could be improved. A ‘faster’ clearance of  $^{188}\text{Re}$ -Lipiodol by organs at risk could allow higher-administered activities than those prescribed in the IAEA study, were the average injected dose was 4 GBq (range 0.8 GBq to 13.5 GBq) and minimal side-effects were reported.

The estimated relative tumor doses (i.e., doses per injected activity) ranged from 3 mGy/MBq to 30 mGy/MBq (Table 6.3). For normal-liver, the relative doses ranged from 0.3 mGy/MBq to 2.0 mGy/MBq. These large inter-patient dose variations highlight the importance of performing patient-specific dose estimates for  $^{188}\text{Re}$ -Lipiodol therapies.

Up to date, the current imaging protocol includes both whole-body planar and SPECT/CT acquisitions at each time point. The preliminary data, however, indicates that similar estimates of

tumor and organs-at-risk doses were obtained using the hybrid and purely SPECT methods. Given the limited resources and time at nuclear medicine departments, it might be beneficial for these centers to update the  $^{188}\text{Re}$ -Lipiodol imaging protocol by including a series of whole-body acquisition to determine the shape of the time-activity curves, and only one quantitative SPECT/CT to determine absolute activities. However, if accurate estimates of doses to thyroid, urinary bladder and surrounding tissues are required, additional SPECT acquisitions of these areas of the body would be needed.

In the majority of patients of the IAEA study, the predicted radiation dose to normal liver (based on the planar ‘scout’ scan) was one of the factors that limited the maximum injected activity [72]. As seen in the whole-body scans of the presented patient data (Figure 6.2),  $^{188}\text{Re}$ -Lipiodol uptake is substantial not only in normal-liver, but also in lungs, stomach and thyroid. Additionally, the presence of  $^{188}\text{Re}$ -Lipiodol in blood can be used to estimate radiation dose to red-marrow [57]. Nevertheless, the relatively high-uptake of  $^{188}\text{Re}$ -Lipiodol by these organs and the potential tissue toxicities seem to be one additional limiting factors for this therapy.

Lipiodol, as an emulsion of iodized ethyl esters of fatty acid of poppy-seed oil, behaves like a chemical embolization agent with high-viscosity [176]. Promising candidates for trans-arterial radioembolization include Human-Serum Albumin [71] or bio-degradable polymer-based microspheres [9], which are physical embolization agents. As such, they mainly accumulate (and physically lodge) in the tumor vasculature, reducing the exposure to radiation for other organs such as lungs, normal-liver, stomach and bone-marrow.

## **6.5 Conclusions**

The image-based dosimetry calculations of four patients receiving  $^{188}\text{Re}$ -Lipiodol for the treatment of hepatocellular carcinoma were performed using the quantitative  $^{188}\text{Re}$  SPECT

reconstruction algorithm described in this thesis. The preliminary results indicate that tumor clearance of  $^{188}\text{Re}$ -Lipiodol might be faster than what was expected based on previous clinical studies. The estimated average absorbed doses to lungs and normal liver were well below the maximum tolerated doses, indicating that injected activity could potentially be increased to improve tumor control and partial response rates. The preliminary results illustrate the importance of accurate quantitative  $^{188}\text{Re}$  imaging to optimize radionuclide therapies.

## Chapter 7: Conclusions and Future Work

### 7.1 Conclusions

The objective of this thesis was to establish practical methods for quantitative measurements of  $^{188}\text{Re}$  activities in radionuclide therapies. In order to achieve this objective, five subprojects that covered a wide range of applications of  $^{188}\text{Re}$  in nuclear medicine (from pre-clinical studies to patient-specific dosimetry) were identified and performed.

- 1) A practical method to determine dose-calibrator dial settings using a thyroid probe was developed. The goal of this method was to ensure that measurements of administered activities in patient studies are accurate and that patients are not over/under-dosed. Compared to alternative methods based on sophisticated (and often, unavailable) equipment such as liquid-scintillation or HPGe  $\gamma$ -ray spectroscopy, this method uses equipment that is readily available in most of the nuclear medicine departments. The analysis of the accuracy showed that the thyroid-probe method yields sample's activity measurements within 5% of its true value. The method was applied to determine  $^{188}\text{Re}$  dial settings for two commercially dose-calibrators. In both cases, the method yielded  $^{188}\text{Re}$  dial settings that resulted in activity readings more accurate than those obtained with settings recommended by the instrument manufacturer.
- 2) A series of Monte-Carlo simulations of  $^{188}\text{Re}$  emissions were performed to investigate the influence of Bremsstrahlung on quantitative SPECT imaging. The simulations indicated that the contribution of Bremsstrahlung photons to the detected gamma-camera signal was negligible thus no specific corrections for Bremsstrahlung during image-reconstruction are needed. However, our results showed that the majority of detected photons in the  $^{188}\text{Re}$  photopeak corresponds to down-scattered high-energy photons. This

analysis allowed us to identify the camera configuration which would result in best quality and quantitative accuracy of  $^{188}\text{Re}$  images. Although the medium-energy collimator has better sensitivity than high-energy collimator, the use of a high-energy collimator maximizes the fraction of primary-to-scatter photons in the  $^{188}\text{Re}$  photopeak and it is therefore recommended for imaging this isotope.

- 3) The image performance of  $^{188}\text{Re}$  SPECT was assessed for VECTor/CT, a pre-clinical multi-pinhole system. The main goal of this project was to ensure that the results from image-based pre-clinical studies using  $^{188}\text{Re}$  are accurate and reliable. A series of phantom experiments were performed to evaluate the image quality and image quantification capabilities of VECTor equipped with two of its multi-pinhole collimators: the ultra-high resolution collimator and the high-energy ultra-high resolution collimator. In parallel, for comparison, the same phantom experiments were performed with the gold-standard  $^{99\text{m}}\text{Tc}$ . Despite the presence of large number of down-scattered photons detected within the 155 keV photopeak window, VECTor ultra-high resolution and high-energy ultra-high resolution collimators produced  $^{188}\text{Re}$  images with submillimeter spatial resolution and high accuracy of activity quantification (errors below 10% for quantification of activity within small VOIs around the radioactive object of interest), comparable to  $^{99\text{m}}\text{Tc}$ . This work also provided insight into the challenges of pinhole-based imaging of isotopes that emit high-energy photons.
- 4) We performed a series of phantom experiments to investigate the accuracy of activity quantification for  $^{188}\text{Re}$  SPECT studies acquired under clinically relevant conditions and reconstructed using the standard ordered subset expectation maximization (OSEM) algorithm with corrections available in many clinical systems. Using these quantitative

images, we also evaluated and compared the accuracy of  $^{188}\text{Re}$  image-based dosimetry estimates performed with the OLINDA method and the point-dose kernel method. As a gold-standard, to evaluate the accuracy of  $^{188}\text{Re}$  dosimetry, we performed Monte-Carlo simulations of a digital version of the phantoms used in this study. Additionally, we simulated a clinical SPECT system to test the performance of the TEW scatter correction method for  $^{188}\text{Re}$  imaging. We showed that good quantification accuracy is achieved when the  $^{188}\text{Re}$  projection data is acquired using HE or ME collimator, and reconstructed with OSEM (10 subsets, 8 iterations), CT-based attenuation correction, TEW scatter corrections with narrow scatter windows, dead-time corrections and resolution recovery. The Monte-Carlo simulations confirmed that TEW scatter correction applied to  $^{188}\text{Re}$ , although practical, yields only approximate estimates of the true scatter. In terms of image-base dosimetry, the OLINDA method and the PDK method underestimated the average absorbed dose-rates of  $^{188}\text{Re}$  by more than 10%. Our analysis suggests that these errors were mostly due to the poor segmentation methods. For patient-specific dose calculations of  $^{188}\text{Re}$  therapies, the use of improved segmentation methods, such as the iterative adaptive threshold [162], could potentially reduce these errors.

- 5) Finally, the quantitative  $^{188}\text{Re}$  SPECT method was applied to perform patient-specific dosimetry calculations of four patients receiving  $^{188}\text{Re}$ -Lipiodol radioembolization. This work is part of a large collaboration with the nuclear medicine department at Kovai Medical Center Hospital (Coimbatore, India). These preliminary results indicate that tumor clearance of  $^{188}\text{Re}$ -Lipiodol might be faster than what was expected from previous clinical studies. The estimated average absorbed doses to lungs and normal liver were

well below the maximum tolerated doses, indicating that injected activity could potentially be increased to improve tumor control and partial response rates.

## **7.2 Future Work**

### **7.2.1 Comparison of $^{188}\text{Re}$ -SSS/Lipiodol and $^{188}\text{Re}$ -HDD/Lipiodol in Vivo Dosimetry of Patients Undergoing Trans-Arterial Radioembolization**

The patient data presented in Chapter 6 is part of a large clinical study carried out at Kovai Medical Center Hospital (KMCH). In this study, approximately 30 patients received  $^{188}\text{Re}$  radioembolization therapy. Half of these patients received  $^{188}\text{Re}$ -HDD-Lipiodol, whereas the other half were treated with a different radio-conjugate known as  $^{188}\text{Re}$ -Super Six Sulphur-Lipiodol ( $^{188}\text{Re}$ -SSS-Lipiodol) [154]. The main differences between these two radio-conjugates is their in-vivo biodistribution and pharmacokinetics, which may potentially lead to differences in tumor and organ at risk absorbed doses.

The preliminary work presented in this thesis could be expanded by performing patient specific dosimetry for all the patients included in the study. A comparison between  $^{188}\text{Re}$ -HDD-Lipiodol vs  $^{188}\text{Re}$ -SSS-Lipiodol could be of great interest to determine which radio-conjugate results in larger tumor retention of Lipiodol while having the faster organ's clearance. In addition, the investigation of the correlation between the average tumor doses (and potentially, other parameters such as DVHs or  $D_{90}$ ) and the response to therapy (measured as patient survival, or tumor response) would also be important to further understand the efficacy of  $^{188}\text{Re}$  radioembolization therapies.

Given the strong interest on trans-arterial radioembolization using  $^{188}\text{Re}$  in developing countries such as India, Thailand and Mongolia, where the prevalence of hepatocellular carcinoma is very high, I believe there is also potential for further collaboration between the

Medical Imaging Research Group, the Hafeli Lab and the nuclear medicine department at KMCH. This collaboration could bring the recently developed bio-degradable microspheres at the Hafeli's Lab [9] into a clinical study at KMCH. In this collaboration, two interesting research topics could be explored: 1) to investigate the use of  $^{99m}\text{Tc}$ -labelled microspheres for diagnosis and treatment planning of  $^{188}\text{Re}$  radioembolization, and 2) to perform patient-specific dosimetry based on  $^{188}\text{Re}$ -SPECT and investigate the correlation between the tumor/normal liver doses and the patient response to the treatment.

### **7.2.2 Performance Evaluation of an Iterative Dual-threshold Segmentation Method for $^{188}\text{Re}$ Imaging: Phantom and Simulation Study**

In Chapter 5, the quantitative capabilities of  $^{188}\text{Re}$  SPECT were demonstrated. Under clinically relevant conditions (such as those of  $^{188}\text{Re}$  radioembolization scans), the measured activities on  $^{188}\text{Re}$  images were quantitatively accurate when these images were reconstructed using the standard OSEM algorithm with corrections that are available in many clinical scanners. However,  $^{188}\text{Re}$  images suffer from partial volume effects. As a result, image based dosimetry estimates have relatively large errors mostly due to the poor segmentation methods that are often used in clinical practice. The presented work could be expanded by investigating the performance of improved segmentation methods applied to  $^{188}\text{Re}$  SPECT such as the iterative adaptive dual-threshold (IADT) [162]. This method uses phantom calibration curves to determine the optimum threshold that should be applied to the image to recover the object's true activity or true volume under specific conditions of signal-to-background ratio. The IADT method, which was tested on  $^{99m}\text{Tc}$  and  $^{177}\text{Lu}$  SPECT images of phantoms, provided accurate estimates of object's activities and object's volumes. As  $^{188}\text{Re}$  images have worse image quality (i.e., large partial volume effects) than  $^{99m}\text{Tc}$  or  $^{177}\text{Lu}$  images due to the use of HE collimators, it

would be important to test the performance of the IADT method for  $^{188}\text{Re}$ . I would, however, propose to replace the phantom calibration curves experiments by Monte-Carlo simulations as physical phantoms are tedious, suffer from measurements errors and cause exposure to radiation dose. In addition, I would investigate the performance of the IADT on more realistic geometries such as simulated patient images of non-uniform activity distributions where the true organ activity and its volume are known.

## Bibliography

- [1] Zukotynski K, Jadvar H, Capala J, Fahey F. Targeted Radionuclide Therapy: Practical Applications and Future Prospects. *Biomark Cancer* 2016;8:35–8.
- [2] Browne E, Tuli JK. Nuclear Data Sheets for A = 99. *Nucl Data Sheets* 2011;112:275–446.
- [3] Tilley DR, Weller HR, Cheves CM, Chasteler RM. Energy levels of light nuclei A = 18-19. *Nucl Physics, Sect A* 1995;595:1–170.
- [4] Junde H, Xiaolong H, Tuli JK. Nuclear data sheets for A = 67. *Nucl Data Sheets* 2005;106:159–250.
- [5] Blachot J. Nuclear Data Sheets for A = 111. *Nucl Data Sheets* 2009;110:1239–407.
- [6] McCutchan EA. Nuclear Data Sheets for A = 68. *Nucl Data Sheets* 2012;113:1735–870.
- [7] Turner JE. Review article: Interaction of Ionizing Radiation with Matter. *Health Phys* 2004;86.
- [8] Dewaraja YK, Frey EC, Sgouros G, Brill a B, Roberson P, Zanzonico PB, et al. MIRD Pamphlet No. 23: Quantitative SPECT for Patient-Specific 3-Dimensional Dosimetry in Internal Radionuclide Therapy. *J Nucl Med* 2012;53:1310–25.
- [9] De La Vega JC, Saatchi K, Rodríguez-Rodríguez C, Esquinas PL, Bokharaei M, Moskalev I, et al. Development of Rhenium-188 Functionalized Microspheres as a Second Generation Radioembolization Agent for Hepatocellular Carcinoma Treatment. *Eur J Nucl Med Mol Imaging* 2016;43(Suppl 1).
- [10] Minarik D, Sjögren-Gleisner K, Linden O, Wingårdh K, Tennvall J, Strand S-E, et al. <sup>90</sup>Y Bremsstrahlung imaging for absorbed-dose assessment in high-dose radioimmunotherapy. *J Nucl Med* 2010;51:1974–8.
- [11] Khazov Y, Mitropolsky I, Rodionov A. Nuclear Data Sheets for A = 131. *Nucl Data*

- Sheets 2006;107:2715–930.
- [12] Kondev FG. Nuclear Data Sheets for  $A = 177$ . Nucl Data Sheets 2003;98:801–1095.
- [13] Browne E. Nuclear Data Sheets for  $A = 90$ . Nucl Data Sheets 1997;82:379–546.
- [14] Singh B. Nuclear Data Sheets for  $A = 188$ . Nucl Data Sheets 2002;95:387–541.
- [15] Browne E. Nuclear Data Sheets for  $A = 215, 219, 223, 227, 231$ . Nucl Data Sheets 2001;93:763–1062.
- [16] Bailey DL, Willowson KP. An evidence-based review of quantitative SPECT imaging and potential clinical applications. J Nucl Med 2013;54:83–9.
- [17] Shcherbinin S, Celler A, Belhocine T, Vanderwerf R, Driedger A. Accuracy of quantitative reconstructions in SPECT/CT imaging. Phys Med Biol 2008;53:4595–604.
- [18] Shcherbinin S, Piwowarska-Bilska H, Celler A, Birkenfeld B. Quantitative SPECT/CT reconstruction for  $^{177}\text{Lu}$  and  $^{177}\text{Lu}/^{90}\text{Y}$  targeted radionuclide therapies. Phys Med Biol 2012;57:5733–47.
- [19] Frey EC, Tsui BMW. Collimator-Detector Response Compensation in SPECT. In: Zaidi H, editor. Quant. Anal. Nucl. Med. imaging, New York, NY: Springer; 2006, p. 141–66.
- [20] Kessler RM, Ellis JR, Eden M. Analysis of emission tomographic scan data: limitations imposed by resolution and background. J Comput Assist Tomogr 1984;8:514–22.  
doi:10.1097/00004728-198406000-00028.
- [21] Kinahan PE, Defrise M, Clackdoyle R. Analytic Image Reconstruction Methods. In: Wernick MS AJ, editor. Emiss. Tomogr. Fundam. PET SPECT, London, UK: Elsevier Academic Press; 2004, p. 421–42.
- [22] Lalush DS, Wernick MN. Iterative Image Reconstruction. In: Wernick MS AJ, editor. Emiss. Tomogr. Fundam. PET SPECT., London, UK: Elsevier Accademic Press; 2004, p.

- 443–72.
- [23] Hudson HM, Larkin RS. Accelerated Image Reconstruction using Ordered Subsets of Projection Data. *IEEE Trans Med Imaging* 1994;13:601–9.
  - [24] Sheep LA, Vardi Y. Maximum Likelihood Reconstruction for Emission Tomography. *IEEE Trans Med Imaging* 1982;1:113–22.
  - [25] Koral KF, Swailem FM, Buchbinder S, Clinthorne NH, Rogers WL, Tsui BM. SPECT dual-energy-window Compton correction: scatter multiplier required for quantification. *J Nucl Med* 1990;31:90–8.
  - [26] Ogawa K, Harata Y, Ichihara T, Kubo A, Hashimoto S. A practical method for position-dependent Compton-scatter correction in single photon emission CT. *IEEE Trans Med Imaging* 1991;10:408–12.
  - [27] Robinson AP, Tipping J, Cullen DM, Hamilton D. The influence of triple energy window scatter correction on activity quantification for  $^{177}\text{Lu}$  molecular radiotherapy. *Phys Med Biol* 2016;61:5107–27.
  - [28] Dewaraja Y, Li J, Koral K. Quantitative I-131 SPECT with triple energy window compton scatter correction. *IEEE Trans Nucl Sci* 1998;45:3109–14.
  - [29] Uribe CF, Esquinas PL, Tanguay J, Gonzalez M, Gaudin E, Beauregard J-M, et al. Accuracy of  $^{177}\text{Lu}$  activity quantification in SPECT imaging: a phantom study. *EJNMMI Phys* 2017;4:2.
  - [30] Wells RG, Celler A, Harrop R. Analytical Calculation of Photon Distributions in SPECT Projections. *IEEE Trans Nucl S Cience* 1998;45:3202–14.
  - [31] Frey EC, Tsui BMW. A new method for modeling the spatially-variant, object-dependent scatter response function in SPECT. 1996 *IEEE Nucl Sci Symp Conf Rec*

- 1996;2:1082–6.
- [32] Dewaraja YK, Ljungberg M, Fessler JA. 3-D Monte Carlo-based scatter compensation in quantitative I-131 SPECT reconstruction. *IEEE Trans Nucl Sci* 2006;53:181–8.
- [33] Ouyang J, Fakhri G El, Moore SC. Fast Monte Carlo based joint iterative reconstruction for simultaneous Tc 99 m/I 123 SPECT imaging. *Med Phys* 2007;34:3263–72.
- [34] Eklund A, Dufort P, Forsberg D, LaConte SM. Medical image processing on the GPU - Past, present and future. *Med Image Anal* 2013;17:1073–94.
- [35] Nassiri MA, Carrier J-F, Després P. Fast GPU-based computation of spatial multigrid multiframe LMEM for PET. *Med Biol Eng Comput* 2015;53:791–803.
- [36] Beekman FJ, Eijkman EGJ, Slijpen ETP, Viergever MA, Borm GF. Object Shape Dependent PSF Model for SPECT Imaging. *IEEE Trans Nucl Sci* 1993;40:31–9.
- [37] Blinder S, Celler A, Wells RG, Thomson D, Harrop R. Experimental verification of 3D detector response compensation using the OSEM reconstruction method. 2001 IEEE Nucl Sci Symp Conf Rec 2001;4:2174–8.
- [38] Shcherbinin S, Grimes J, Bator A, Cwikla JB, Celler A. Three-dimensional personalized dosimetry for (188)Re liver selective internal radiation therapy based on quantitative post-treatment SPECT studies. *Phys Med Biol* 2013;59:119–34.
- [39] Celler A, Piwowarska-Bilska H, Shcherbinin S, Uribe C, Mikolajczak R, Birkenfeld B. Evaluation of dead-time corrections for post-radionuclide-therapy (177)Lu quantitative imaging with low-energy high-resolution collimators. *Nucl Med Commun* 2014;35:73–87.
- [40] Snyder WS, Ford MR, Warner GG, Watson SB. MIRD Pamphlet No. 11: Absorbed Dose per Unit Cumulated Activity for Selected Radionuclides and Organs. *Soc Nucl Med* 1975.
- [41] Bolch WE, Eckerman KF, Sgouros G, Thomas SR, MIRD SNM, Wesley C, et al. MIRD

- Pamphlet No . 21 : A Generalized Schema for Radiopharmaceutical Dosimetry —  
Standardization of Nomenclature. J Nucl Med 2009;50:477–85.
- [42] Dewaraja YK, Ljungberg M, Green AJ, Zanzonico PB, Frey EC, Bolch WE, et al. MIRD pamphlet No. 24: Guidelines for quantitative <sup>131</sup>I SPECT in dosimetry applications. J Nucl Med 2013;54:2182–8.
- [43] Siegel J a, Thomas SR, Stubbs JB, Stabin MG, Hays MT, Koral KF, et al. MIRD pamphlet no. 16: Techniques for quantitative radiopharmaceutical biodistribution data acquisition and analysis for use in human radiation dose estimates. J Nucl Med 1999;40:37S–61S.
- [44] Bernal P, Raoul JL, Vidmar G, Seregotov E, Sundram FX, Kumar A, et al. Intra-Arterial Rhenium-188 Lipiodol in the Treatment of Inoperable Hepatocellular Carcinoma: Results of an IAEA-Sponsored Multination Study. Int J Radiat Oncol Biol Phys 2007;69:1448–55.
- [45] O’Donoghue JA. Implications of nonuniform tumor doses for radioimmunotherapy. J Nucl Med 1999;40:1337–41.
- [46] He B, Wahl RL, Du Y, Sgouros G, Jacene H, Flinn I, et al. Comparison of residence time estimation methods for radioimmunotherapy dosimetry and treatment planning-Monte Carlo simulation studies. IEEE Trans Med Imaging 2008;27:521–30.
- [47] Stabin MG, Sparks RB, Crowe E. OLINDA/EXM: The Second Generation Personal Computer Software for Internal Dose Assessment in Nuclear Medicine. J Nucl Med 2005;46:1023–7.
- [48] Andersson M, Johansson L, Minarik D, Mattsson S, Leide-Svegborn S. An Internal Radiation Dosimetry Computer Program , IDAC 2 .0, for Estimation of Patient Doses From Radiopharmaceuticals. Radiat Prot Dosimetry 2013;162:299–305.

- [49] Bolch WE, Bouchet LG, Robertson JS, Wessels BW, Siegel J a, Howell RW, et al. MIRD pamphlet No. 17: the dosimetry of nonuniform activity distributions--radionuclide S values at the voxel level. Medical Internal Radiation Dose Committee. J Nucl Med 1999;40:11S–36S.
- [50] Kwok CS, Irfan M, Woo MK, Prestwich W V. Effect of tissue inhomogeneity on beta dose distribution of P-32. Med Phys 1987;14.
- [51] Lanconelli N, Pacilio M, Meo S Lo, Botta F, Dia a Di, Aroche L a T, et al. A free database of radionuclide voxel S values for the dosimetry of nonuniform activity distributions. Phys Med Biol 2012;57:517–33.
- [52] Yoriyaz, H, Stabin MG and DS. Monte Carlo MCNP-4B based absorbed dose distribution estimates for patient-specific dosimetry. J Nucl Med Nucl Med 2001;42:662–9.
- [53] Jan S, Santin G, Strul D, Staelens S, Assi K. GATE : a simulation toolkit for PET and SPECT. Phys Med Biol 2004;49:4543–61.
- [54] Jan S, Benoit D, Becheva E, Carlier T, Cassol F, Descourt P, et al. GATE V6: a major enhancement of the GATE simulation platform enabling modelling of CT and radiotherapy. Phys Med Biol 2011;56:881–901.
- [55] Rogers DWO. Low Energy Electron Transport with EGS. Nucl Instruments Methods Phys Res A 1984;227:535–48.
- [56] Hambye ASE, Dobbeleir AA, Vervaet AM, Knapp FFJ. Image quality with rhenium-188 and technetium-99m: Comparative planar and SPECT evaluation in a phantom study and implications for dosimetry. World J Nucl Med 2002;1:12–20.
- [57] Zanzonico PB, Divgi C. Patient-Specific Radiation Dosimetry for Radionuclide Therapy of Liver Tumors With Intrahepatic Artery Rhenium-188 Lipiodol. Semin Nucl Med

- 2008;38:30–9.
- [58] Argyrou M, Valassi A, Andreou M, Lyra M. Rhenium-188 production in hospitals, by w-188/re-188 generator, for easy use in radionuclide therapy. *Int J Mol Imaging* 2013;2013:290750.
- [59] Dash A, Knapp FF (Russ) J. An Overview of Radioisotope Separation Technologies for Development of W-188/Re-188 Radionuclide Generators Providing Re-188 to Meet Future Research and Clinical Demands. *RSC Adv* 2015;5:39012–36.
- [60] Stabin MG, Siegel J a. Physical Models and Dose Factors for Use in Internal Dose Assessment. *Health Phys* 2003;85:294–310.
- [61] Mirzadeh S, Knapp FF (Russ) J, Callahan AP. Production of Tungsten-188 and Osmium-194 in a Nuclear Reactor for New Clinical Generators 1992:2234–6.
- [62] Knapp FF (Russ) J, Mirzadeh S, Garland M, Ponsard B, Kuznetsov R. Reactor Production and Processing of Tungsten-188. *Prod. Long Lived Parent Radionuclides Gener.* 68Ge, 82Sr, 90Sr 188W, Vienna 2010: International Atomic Energy Agency; 2010.
- [63] Lambert B, de Klerk JMH. Clinical applications of 188Re-labelled radiopharmaceuticals for radionuclide therapy. *Nucl Med Commun* 2006;27:223–9.
- [64] Chen S, Xu K, Liu W, Yao Z, Chen K, Yin D, et al. Treatment of metastatic bone pain with rhenium-188 hydroxyethylidene diphosphonate. *Med Princ Pract* 2001;10:98–101.
- [65] Lange R, Overbeek F, de Klerk JMH, Pasker-de Jong PCM, van den Berk AM, Ter Heine R, et al. Treatment of painful bone metastases in prostate and breast cancer patients with the therapeutic radiopharmaceutical rhenium-188-HEDP. Clinical benefit in a real-world study. *Nuklearmedizin* 2016;55:1–8.
- [66] Shin K, Lee JC, Choi HJ, Jeong JM, Son M, Lee YJ, et al. Radiation synovectomy using

- 188Re-tin colloid improves knee synovitis as shown by MRI in refractory rheumatoid arthritis. *Nucl Med Commun* 2007;28:239–44.
- [67] Phaeton R, Jiang Z, Revskaya E, Fisher DR, Goldberg GL, Dadachova E. Beta emitters rhenium-188 and lutetium-177 are equally effective in radioimmunotherapy of HPV-positive experimental cervical cancer. *Cancer Med* 2016;5:9–16.
- [68] Werner M, Scheinert D, Henn M, Scheinert S, Bräunlich S, Bausback Y, et al. Endovascular brachytherapy using liquid Beta-emitting rhenium-188 for the treatment of long-segment femoropopliteal in-stent stenosis. *J Endovasc Ther* 2012;19:467–75.
- [69] Häfeli UO, Roberts WK, Meier DS, Ciezki JP, Pauer GJ, Lee EJ, et al. Dosimetry of a W-188/Re-188 beta line source for endovascular brachytherapy. *Med Phys* 2000;27:668–75.
- [70] Liepe K, Brogsitter C, Leonhard J, Wunderlich G, Hliscs R, Pinkert J, et al. Feasibility of high activity rhenium-188-microsphere in hepatic radioembolization. *Jpn J Clin Oncol* 2007;37:942–50.
- [71] Nowicki ML, Cwikla JB, Sankowski AJ, Shcherbinin S, Grimmes J, Celler A, et al. Initial Study of Radiological and Clinical Efficacy Radioembolization Using 188Re-Human Serum Albumin (HSA) Microspheres in Patients with Progressive, Unresectable Primary or Secondary Liver Cancers. *Med Sci Monit Int Med J Exp Clin Res* 2014;20:1353–62.
- [72] Sundram F, Chau TCM, Onkhuudai P, Bernal P, Padhy AK. Preliminary results of transarterial rhenium-188 HDD lipiodol in the treatment of inoperable primary hepatocellular carcinoma. *Eur J Nucl Med Mol Imaging* 2004;31:250–7.
- [73] Bernal P, Raoul JL, Stare J, Sereegotov E, Sundram FX, Kumar A, et al. International Atomic Energy Agency-Sponsored Multination Study of Intra-Arterial Rhenium-188-Labeled Lipiodol in the Treatment of Inoperable Hepatocellular Carcinoma: Results With

- Special Emphasis on Prognostic Value of Dosimetric Study. *Semin Nucl Med* 2008;38:40–5.
- [74] Verger E, Drion P, Bernard C, Duwez L, Hustinx R, Lepareur N, et al. Ga-68 and Re-188 Starch-Based Microparticles as Theranostic Tool for the Hepatocellular Carcinoma : Radiolabeling and Preliminary In Vivo Rat Studies. *PLoS One* 2016:1–17.
- [75] Häfeli UO, Saatchi K, Elischer P, Misri R, Bokharaei M, Renée Labiris N, et al. Lung perfusion imaging with monosized biodegradable microspheres. *Biomacromolecules* 2010;11:561–7.
- [76] De Decker M, Bacher K, Thierens H, Slegers G, Dierckx R a., De Vos F. In vitro and in vivo evaluation of direct rhenium-188-labeled anti-CD52 monoclonal antibody alemtuzumab for radioimmunotherapy of B-cell chronic lymphocytic leukemia. *Nucl Med Biol* 2008;35:599–604.
- [77] Lange R, de Klerk JMH, Bloemendal HJ, Ramakers RM, Beekman FJ, van der Westerlaken MML, et al. Drug composition matters: the influence of carrier concentration on the radiochemical purity, hydroxyapatite affinity and in-vivo bone accumulation of the therapeutic radiopharmaceutical 188Rhenium-HEDP. *Nucl Med Biol* 2015;42:465–9.
- [78] Valley J-F, Bulling S, Leresche M, Wastiel C. Determination of the efficiency of commercially available dose calibrators for beta-emitters. *J Nucl Med Technol* 2003;31:27–32.
- [79] Zimmerman BE, Cessna JT. Experimental determinations of commercial “dose calibrator” settings for nuclides used in nuclear medicine. *Appl Radiat Isot* 2000;52:615–9.
- [80] Ljungberg M, Celler A, Konijnenberg MW, Eckerman KF, Dewaraja YK, Sjögreen-Gleisner K. MIRD Pamphlet No. 26: Joint EANM/MIRD Guidelines for Quantitative 177

- Lu SPECT Applied for Dosimetry of Radiopharmaceutical Therapy. *J Nucl Med* 2016;57:151–62.
- [81] Bergeron DE, Cessna JT, Golas DB, Young RK, Zimmerman BE. Dose calibrator manufacturer-dependent bias in assays of I-123. *Appl Radiat Isot* 2014;90:79–83.
- [82] Jacobson AF, Centofanti R, Babalola OI, Dean B. Survey of the performance of commercial dose calibrators for measurement of I-123 activity. *J Nucl Med Technol* 2011;39:302–6.
- [83] Schrader H, Kossert K, Mintcheva J. Calibration of a radionuclide calibrator system as a Bulgarian standard for activity. *Appl Radiat Isot* 2008;66:965–71.
- [84] Zimmerman BE, Pipes DW. Experimental determination of dose calibrator settings and study of associated volume dependence in v-vials for Rhenium-186 perrhenate solution sources. *J Nucl Med Technol* 2000;28:264–70.
- [85] Zimmerman BE, Cessna JT, Millican M a. Experimental determination of calibration settings for plastic syringes containing solutions of Y-90 using commercial radionuclide calibrators. *Appl Radiat Isot* 2004;60:511–7.
- [86] Wastiel C, Valley J-F, Delaloye AB, Leresche M, Linder R, Sassowsky M, et al. Intercomparison of activity measurements for beta-emitters in Swiss nuclear medicine laboratories. *J Nucl Med Technol* 2005;33:238–42.
- [87] Santos JAM, Dias AG, Bastos AL. Characterization of geometric uncertainties of a dose calibrator during measurement of  $^{90}\text{Y}$  activity. *J Nucl Med Technol* 2011;39:125–30.
- [88] Zimmerman BE, Cessna JT, Schima FJ. The standardization of the potential bone palliation radiopharmaceutical  $\text{Sn-117m}(+4)\text{DTPA}$ . *Appl Radiat Isot* 1998;49:317–28.
- [89] Zimmerman BE, Cessna JT, Unterweger MP, Li AN, Whiting JS, Knapp FF. A new

- experimental determination of the dose calibrator setting for Re-188. *J Nucl Med* 1999;40:1508–16.
- [90] Zimmerman BE, Cessna JT. The standardization of Cu-62 and experimental determinations of dose calibrator settings for generator-produced Cu-62-PTSM. *Appl Radiat Isot* 1999;51:515–26.
- [91] Bergeron DE, Cessna JT, Zimmerman BE. Secondary standards for Ra-223 revised. *Appl Radiat Isot* 2015;101:10–4.
- [92] Cannata V, Ciofetta G, Garganese MC, De Felice P, Capogni M, Fazio A, et al. Experimental determination of the radionuclide calibrator setting for Technesium-99m, by using a primary standardisation method. *Nucl Med Commun* 2007;28:321–6.
- [93] Marengo M, Uccelli L, Cicoria G, Pasquali M, Gambaccini M, Duatti A. Calibration Factor for Activity Measurement of Re-188 with a Widely Used Model of Radionuclide Activity Meter. *First Eur. Conf. Med. Phys., Pisa, Italy: 2007.*
- [94] Beattie BJ, Pentlow KS, O'Donoghue J, Humm JL. A recommendation for revised dose calibrator measurement procedures for Zr-89 and I-124. *PLoS One* 2014;9:e106868.
- [95] ANSI. American National Standard Calibration and Usage of Thallium- Activated Sodium Iodide Detector Systems for Assay of Radionuclides. ANSI 1994:N42.12-1994.
- [96] Stabin MG. *Radiation Protection and Dosimetry: An Introduction to Health Physics.* Springer; 2007.
- [97] Firestone RB. Nuclear Data Sheets for A=22. *Nucl Data Sheets* 2005;106:1–88.
- [98] Martin MJ. Nuclear data sheets for A = 152. *Nucl Data Sheets* 2013;114:1497–847.
- [99] Bé M-M, Chisté V, Dulieu C, Browne E, Chechev V, Kuzmenko N, et al. *Table of Radionuclides.* Bureau International des Poids et Mesures; 2004.

- [100] Bhat MR. Nuclear data sheets for  $A = 57$ . Nucl Data Sheets 1998;85:415–536.
- [101] Capintec Inc. Capintec CRC-55t Owner's Manual - Revision K 2015.
- [102] Capintec Inc. CRC-15R Owner's Manual - Revision Y 2007.
- [103] Bevington PR, Robinson DK. Data Reduction and Error Analysis for the Physical Sciences. Second. New York: McGraw-Hill; 1992.
- [104] Abd-Elzaher M, Badawi MS, El-Khatib A, Abouzeid AT. Determination of Full Energy Peak Efficiency of NaI(Tl) Detector Depending on Efficiency Transfer Principle for Conversion Form Experimental Values. World J Nucl Sci Technol 2012;2:65–72.
- [105] Morgat C, Mazère J, Fernandez P, Buj S, Vimont D, Schulz J, et al. A phantom-based method to standardize dose-calibrators for new  $\beta^+$ -emitters. Nucl Med Commun 2015;36:201–6.
- [106] Dantas BM, Lucena EA, Dantas ALA, Araújo F, Rebelo AMO, Terán M, et al. A Protocol for the Calibration of Gamma Cameras to Estimate Internal Contamination in Emergency Situations. Radiat Prot Dosimetry 2007;127:253–7.
- [107] Maioli C, Bestetti A, Milani F, Cornalba GP, Tagliabue L, Di Benedetto D, et al. Evaluation of different counting methods for use in radiochemical purity testing procedures for Tc-99m-labelled radiopharmaceuticals. Appl Radiat Isot 2008;66:556–9.
- [108] Rong X, Du Y, Ljungberg M, Rault E, Vandenberghe S, Frey EC. Development and evaluation of an improved quantitative  $(90\text{Y})$  bremsstrahlung SPECT method. Med Phys 2012;39:2346–58.
- [109] Heard S, Flux GD, Guy MJ, Ott RJ. Monte Carlo Simulation of  $90\text{Y}$  Bremsstrahlung Imaging. IEEE Nucl Sci Symp Conf Rec 2004:3579–83.
- [110] Rong X, Frey EC. A collimator optimization method for quantitative imaging: application

- to Y-90 bremsstrahlung SPECT. *Med Phys* 2013;40:82504. doi:10.1118/1.4813297.
- [111] Autret D, Bitar A, Ferrer L, Lisbona A, Bardiès M. Monte Carlo modeling of gamma cameras for I-131 imaging in targeted radiotherapy. *Cancer Biother Radiopharm* 2005;20:77–84.
- [112] Ljungberg M. Monte Carlo simulations for therapy imaging. *J Phys Conf Ser* 2011;317:12016.
- [113] Rault E, Staelens S, Van Holen R, De Beenhouwer J, Vandenberghe S. Accurate Monte Carlo modelling of the back compartments of SPECT cameras. *Phys Med Biol* 2011;56:87–104. doi:10.1088/0031-9155/56/1/006.
- [114] Assié K, Gardin I, Véra P, Buvat I. Validation of the Monte Carlo simulator GATE for indium-111 imaging. *Phys Med Biol* 2005;50:3113–25.
- [115] Bhat MR. Evaluated Nuclear Structure Data File (ENSDF). *Nucl Data Sci Technol* 1992;817–21.
- [116] Siemens Medical Solutions G. Symbia S and T System Specifications. 2010.
- [117] Eary JF, Durack L, Williams D, Vanderheyden JL. Considerations for imaging Re-188 and Re-186 isotopes. *Clin Nucl Med* 1990;15:911–6.
- [118] Franc BL, Acton PD, Mari C, Hasegawa BH. Small-animal SPECT and SPECT/CT: important tools for preclinical investigation. *J Nucl Med* 2008;49:1651–63.
- [119] Clark DP, Badea CT. Micro-CT of rodents: State-of-the-art and future perspectives. *Phys Medica* 2014;30:619–34.
- [120] Kagadis GC, Loudos G, Katsanos K, Langer SG, Nikiforidis GC. In vivo small animal imaging: Current status and future prospects. *Med Phys* 2010;37:6421–42.
- [121] Liu X, Laforest R. Quantitative small animal PET imaging with nonconventional nuclides.

- Nucl Med Biol 2009;36:551–9.
- [122] Magota K, Kubo N, Kuge Y, Nishijima KI, Zhao S, Tamaki N. Performance characterization of the Inveon preclinical small-animal PET/SPECT/CT system for multimodality imaging. *Eur J Nucl Med Mol Imaging* 2011;38:742–52.
- [123] Goertzen AL, Bao Q, Bergeron M, Blankemeyer E, Blinder S, Canadas M, et al. NEMA NU 4-2008 Comparison of Preclinical PET Imaging Systems. *J Nucl Med* 2012;53:1300–9.
- [124] Sánchez F, Orero A, Soriano A, Correcher C, Conde P, González A, et al. ALBIRA: a small animal PET/SPECT/CT imaging system. *Med Phys* 2013;40:051906 (11 pp).
- [125] Vandeghinste B, Van Holen R, Vanhove C, De Vos F, Vandenberghe S, Staelens S. Use of a ray-based reconstruction algorithm to accurately quantify preclinical microspect images. *Mol Imaging* 2014;13:1–13.
- [126] Rodríguez-Villafuerte M, Yang Y, Cherry SR. A Monte Carlo investigation of the spatial resolution performance of a small-animal PET scanner designed for mouse brain imaging studies. *Phys Medica* 2014;30:76–85.
- [127] van der Have F, Vastenhouw B, Ramakers RM, Branderhorst W, Krah JO, Ji C, et al. U-SPECT-II: An Ultra-High-Resolution Device for Molecular Small-Animal Imaging. *J Nucl Med* 2009;50:599–605.
- [128] Ivashchenko O, van der Have F, Villena JL, Groen HC, Ramakers RM, Weinans HH, et al. Quarter-Millimeter-Resolution Molecular Mouse Imaging with U-SPECT+. *Mol Imaging* 2014;13:1–8.
- [129] Wu C, Van Der Have F, Vastenhouw B, Dierckx R a JO, Paans AMJ, Beekman FJ. Absolute quantitative total-body small-animal SPECT with focusing pinholes. *Eur J Nucl*

- Med Mol Imaging 2010;37:2127–35.
- [130] Wu C, de Jong JR, Gratama van Andel H a, van der Have F, Vastenhouw B, Laverman P, et al. Quantitative multi-pinhole small-animal SPECT: uniform versus non-uniform Chang attenuation correction. *Phys Med Biol* 2011;56:N183–93.
- [131] van der Have F, Ivashchenko O, Goorden MC, Ramakers RM, Beekman FJ. High-resolution clustered-pinhole <sup>131</sup>Iodine SPECT imaging in mice. *Nucl Med Biol* 2016;43:506–11.
- [132] Visser EP, Harteveld AA, Meeuwis APW, Disselhorst JA, Beekman FJ, Oyen WJG, et al. Image quality phantom and parameters for high spatial resolution small-animal SPECT. *Nucl Instruments Methods Phys Res A* 2011;654:539–45.
- [133] Ivashchenko O, van der Have F, Goorden MC, Ramakers RM, Beekman FJ. Ultra-High-Sensitivity Submillimeter Mouse SPECT. *J Nucl Med* 2015;56:470–5.
- [134] Walker MD, Goorden MC, Dinelle K, Ramakers RM, Blinder S, Shirmohammad M, et al. Performance Assessment of a Preclinical PET Scanner with Pinhole Collimation by Comparison to a Coincidence-Based Small-Animal PET Scanner. *J Nucl Med* 2014;55:1368–74.
- [135] Goorden MC, van der Have F, Kreuger R, Ramakers RM, Vastenhouw B, Burbach JPH, et al. VECTor: A Preclinical Imaging System for Simultaneous Submillimeter SPECT and PET. *J Nucl Med* 2012;54:306–12.
- [136] Miwa K, Inubushi M, Takeuchi Y, Katafuchi T, Koizumi M, Saga T, et al. Performance characteristics of a novel clustered multi-pinhole technology for simultaneous high-resolution SPECT/PET. *Ann Nucl Med* 2015:460–6.
- [137] de Swart J, Chan HS, Goorden MC, Morgenstern A, Bruchertseifer F, Beekman FJ, et al.

- Utilizing high-energy gamma photons for high-resolution  $^{213}\text{Bi}$  SPECT in mice. *J Nucl Med* 2015;486–92.
- [138] Vaissier PEB, Goorden MC, Vastenhouw B, van der Have F, Ramakers RM, Beekman FJ. Fast Spiral SPECT with Stationary -Cameras and Focusing Pinholes. *J Nucl Med* 2012;53:1292–9.
- [139] Branderhorst W, Vastenhouw B, Beekman FJ. Pixel-based subsets for rapid multi-pinhole SPECT reconstruction. *Phys Med Biol* 2010;55:2023–34.
- [140] Chang L. A Method for Attenuation Correction in Radionuclide Computed Tomography. *IEEE Trans Nucl Sci* 1978;25:638–43.
- [141] ter Heine R, Lange R, Breukels OB, Bloemendal HJ, Rummenie RG, Wakker AM, et al. Bench to bedside development of GMP grade Rhenium-188-HEDP , a radiopharmaceutical for targeted treatment of painful bone metastases. *Int J Pharm* 2014;465:317–24.
- [142] Branderhorst W, Vastenhouw B, van der Have F, Blezer ELA, Bleeker WK, Beekman FJ. Targeted multi-pinhole SPECT. *Eur J Nucl Med Mol Imaging* 2011;38:552–61.
- [143] Beekman F, van der Have F. The pinhole: gateway to ultra-high-resolution three-dimensional radionuclide imaging. *Eur J Nucl Med Mol Imaging* 2007;34:151–61.
- [144] Uribe CF, Esquinas PL, Gonzalez M, Celler A. Characteristics of Bremsstrahlung emissions of  $^{177}\text{Lu}$ ,  $^{188}\text{Re}$ , and  $^{90}\text{Y}$  for SPECT/CT quantification in radionuclide therapy. *Phys Medica* 2016;32:691–700.
- [145] Spinelli AE, Boschi F. Bremsstrahlung radiation detection for small animal imaging using a CCD detector. *Phys Medica* 2016;32:706–8.
- [146] Lehner S, Lang C, Kaissis G, Todica A, Zacherl MJ, Boening G, et al. I-124-PET

- Assessment of Human Sodium Iodide Symporter Reporter Gene Activity for Highly Sensitive In Vivo Monitoring of Teratoma Formation in Mice. *Mol Imaging Biol* 2015;17:874–83.
- [147] Esquinas PL, Rodríguez-Rodríguez C, Carlos De La Vega J, Bokharai M, Saatchi K, Shirmohammad M, et al. 188Re image performance assessment using small animal multi-pinhole SPECT/PET/CT system. *Phys Medica* 2017;33:26–37.
- [148] Ljungberg M, Celler A, Konijnenberg MW, Eckerman KF, Dewaraja YK, Sjogreen Gleisner K. MIRD Pamphlet No. 26: Joint EANM/MIRD Guidelines for Quantitative 177Lu SPECT applied for Dosimetry of Radiopharmaceutical Therapy. *J Nucl Med* 2015;9881:151–62. doi:10.2967/jnumed.115.159012.
- [149] Minarik D, Sjögren Gleisner K, Ljungberg M. Evaluation of quantitative (90)Y SPECT based on experimental phantom studies. *Phys Med Biol* 2008;53:5689–703.
- [150] Chaudakshetrin P, Osorio M, Padhy A, Divgi C, Zanzonico P. Rhenium-188-Lipiodol therapy of liver cancer: Optimization of conjugate-view imaging of Rhenium-188 for patient-specific dosimetry. *World J Nucl Med* 2004;3 (suppl.):S128–9.
- [151] Hudson HM, Larkin RS. Accelerated Image Reconstruction Using Ordered Subsets of Projection Data. *IEEE Trans Med Imaging* 1994;13:601–9.
- [152] Zanzonico PB. Internal radionuclide radiation dosimetry: a review of basic concepts and recent developments. *J Nucl Med* 2000;41:297–308.
- [153] Esquinas PL, Tanguay J, Gonzalez M, Vuckovic M, Rodríguez-Rodríguez C, Häfeli UO, et al. Accuracy, reproducibility, and uncertainty analysis of thyroid-probe-based activity measurements for determination of dose calibrator settings. *Med Phys* 2016;43:6309–21.
- [154] Lepareur N, Ardisson V, Noiret N, Garin E. (188)Re-SSS/Lipiodol: Development of a

- Potential Treatment for HCC from Bench to Bedside. *Int J Mol Imaging* 2012:Article ID:278306, 9 pages.
- [155] Celler A, Uribe C, Esquinas PL, Gonzalez M. Dead-time Corrections for Quantitation of Lu-177 SPECT/CT Radionuclide Therapy Studies. *Annu. Congr. Eur. Assoc. Nucl. Med.*, 2014.
- [156] Guirado D, Ramírez JC, De la Vega JM, Vilches M, Lallena AM. Quality control for system count rate performance with scatter in gamma cameras. *Phys Medica* 2012;28:254–61.
- [157] Erdi YE, Wessels BW, Loew MH, Erdi a K. Threshold estimation in single photon emission computed tomography and planar imaging for clinical radioimmunotherapy. *Cancer Res* 1995;55:5823s–5826s.
- [158] Biehl KJ, Kong F-M, Dehdashti F, Jin J-Y, Mutic S, El Naqa I, et al. 18F-FDG PET definition of gross tumor volume for radiotherapy of non-small cell lung cancer: is a single standardized uptake value threshold approach appropriate? *J Nucl Med* 2006;47:1808–12. doi:47/11/1808 [pii].
- [159] van Gils CAJ, Beijst C, van Rooij R, de Jong HWAM. Impact of reconstruction parameters on quantitative I-131 SPECT. *Phys Med Biol* 2016;61:5166–82.
- [160] Seret A, Nguyen D, Bernard C. Quantitative capabilities of four state-of-the-art SPECT-CT cameras. *EJNMMI Res* 2012;2:45.
- [161] Cheng L, Hobbs RF, Segars PW, Sgouros G, Frey EC. Improved dose-volume histogram estimates for radiopharmaceutical therapy by optimizing quantitative SPECT reconstruction parameters. *Phys Med Biol* 2013;58:3631–47.
- [162] Grimes J, Celler A, Shcherbinin S, Piwowska-Bilska H, Birkenfeld B. The accuracy and

- reproducibility of SPECT target volumes and activities estimated using an iterative adaptive thresholding technique. *Nucl Med Commun* 2012;33:1254–66.
- [163] Society CC. Canadian Cancer Society's Advisory Committee on Cancer Statistics. Canadian Cancer Statistics 2016. *Can Cancer Soc* 2016:1–132.
- [164] Organization WH. World Cancer Report 2014. 2014.
- [165] Liepe K, Kotzerke J. Advantage of Re-188-Radiopharmaceuticals in Hepatocellular Cancer and Liver Metastases. *J Nucl Med* 2005;46:1407–8.
- [166] Alberts SR, Wagman LD. Chemotherapy for Colorectal Cancer Liver Metastases. *Oncologist* 2008;13:1063–73.
- [167] Ellis L, Curley S, Tanabe K. Radiofrequency Ablation for Cancer: Current Indications, Techniques and Outcomes. New York, NY: Springer Verlag; 2004.
- [168] Ricke J, Wust P, Stohlmann A, Beck A, Cho CH, Pech M, et al. CT-guided interstitial brachytherapy of liver malignancies alone or in combination with thermal ablation: Phase I-II results of a novel technique. *Int J Radiat Oncol Biol Phys* 2004;58:1496–505.
- [169] Salem R, Thurston KG, Carr BI, Goin JE, Geschwind J-FH. Yttrium-90 microspheres: radiation therapy for unresectable liver cancer. *J Vasc Interv Radiol* 2002;13:S223–9. doi:10.1016/s1051-0443(07)61790-4.
- [170] Kennedy AS, Coldwell D, Nutting C, Murthy R, Wertman DE, Loehr SP, et al. Resin 90Y-microsphere brachytherapy for unresectable colorectal liver metastases: Modern USA experience. *Int J Radiat Oncol Biol Phys* 2006;65:412–25.
- [171] Willowson K, Forwood N, Jakoby BW, Smith AM, Bailey DL. Quantitative (90)Y image reconstruction in PET. *Med Phys* 2012;39:7153–9. doi:10.1118/1.4762403.
- [172] Madsen MT, Park CH, Thakur ML. Dosimetry of Iodine-131 Ethiodol in the Treatment of

- Hepatoma. *J Nucl Med* 1988;29:1038–44.
- [173] Bodei L, Cremonesi M, Ferrari M, Pacifici M, Grana CM, Bartolomei M, et al. Long-term evaluation of renal toxicity after peptide receptor radionuclide therapy with  $^{90}\text{Y}$ -DOTATOC and  $^{177}\text{Lu}$ -DOTATATE: The role of associated risk factors. *Eur J Nucl Med Mol Imaging* 2008;35:1847–56.
- [174] Pouget J-P, Lozza C, Deshayes E, Boudousq V, Navarro-Teulon I. Introduction to radiobiology of targeted radionuclide therapy. *Front Med* 2015;2:12.
- [175] Paeng JC, Jeong JM, Yoon CJ, Lee YS, Suh YG, Chung JW, et al. Lipiodol solution of Re-188-HDD as a new therapeutic agent for transhepatic arterial embolization in liver cancer: Preclinical study in a rabbit liver cancer model. *J Nucl Med* 2003;44:2033–8.
- [176] Nakajo M, Kobayashi H, Shimabukuro K, Shirono K, Sakata H, Taguchi M, et al. Biodistribution and In Vivo Kinetics of Iodine-131 Lipiodol Infused via the Hepatic Artery of Patients with Hepatic Cancer. *J Nucl Med* 1988;29:1066–77.
- [177] Vaissier PEB, Goorden MC, Vastenhouw B, van der Have F, Ramakers RM, Beekman FJ. Fast Spiral SPECT with Stationary gamma-Cameras and Focusing Pinholes. *J Nucl Med* 2012;53:1292–9.

## Appendices

### Appendix A - Supplementary Material for Chapter 3

#### A.1 Geometry Correction Factors

The  $\kappa_{VR}(E)$  factor was estimated as the ratio of the average photon transmission factor in the 0.6 cm thick solid acrylic disk  $\langle TF_{ref} \rangle$  (reference geometry) to the average photon transmission factor in the vial source  $\langle TF_{vial} \rangle$ :

$$\kappa_{VR}(E) = \frac{\langle TF_{ref} \rangle}{\langle TF_{vial} \rangle} \quad (\text{A.1})$$

The following approximations were made in the calculation of  $\kappa_{VR}(E)$ : the vial source was modelled as a water cylinder ( $R = 1.4 \text{ cm}$ ,  $h = 3.2 \text{ cm}$ ) of uniform activity; the reference source was modelled as a plastic cylinder ( $R = 1.3 \text{ cm}$ ,  $h_{ref} = 0.6 \text{ cm}$ ) with point source activity at its centre and; the photons were assumed to be emitted in the forward direction. Based on these approximations and the orientation of each source relative to the TP (Figure A.1), the value of  $\langle TF_{vial} \rangle$  did not depend on the height of the vial, and was defined by the following analytical expression:

$$\langle TF_{vial} \rangle = \frac{1}{A} \int_A \exp[\mu_w(E)l(x, y)] dA \quad (\text{A.2})$$

where  $A$  represents the cross-sectional circular area of the vial,  $\mu_w(E)$  represents the linear attenuation coefficient for photons of energy  $E$  in water and  $l(x, y)$  represents the path length (in the forward direction) traveled by a photon emitted from position  $(x, y)$  in the vial (Figure A.1).

The result of the 2-D integral of Eq. A.2 was calculated numerically as:

$$\langle TF_{vial} \rangle \approx \frac{1}{N} \sum_{y_i} \sum_{x_i} \exp \left[ \mu_w(E) \left( \sqrt{R^2 - y_i^2} - x_i \right) \right] \quad (\text{A.3})$$

where  $x_i$  and  $y_i$  represent the sampled points (0.03 cm step size) within the cross-sectional circular area of the vial source and  $N$  represents the total number of sampled points. The value of  $\langle TF_{ref} \rangle$  did not depend on the radius of the disk, and it was estimated as:

$$\langle TF_{ref} \rangle = \exp\left(-\frac{\mu_p(E)h_{ref}}{2}\right) \quad (\text{A.4})$$

where  $\mu_p(E)$  represents the linear attenuation coefficient for photons of energy  $E$  in plastic and  $h_{ref}$  represents the thickness of the reference disk source geometry (Table 2.1). Similarly,  $\kappa_{DR}(E)$  was calculated as

$$\kappa_{DR}(E) = \frac{\langle TF_{ref} \rangle}{\langle TF_{disk} \rangle} = \exp\left(\frac{\mu_p}{2} [h_{disk} - h_{ref}]\right) \quad (\text{A.5})$$

where  $h_{disk}$  represents the thickness of the  $^{22}\text{Na}$  disk source.

Lastly,  $\kappa_{TR}(E)$  was calculated using Equation A.4 and replacing the vial dimensions by the dimensions of the tube (i.e.,  $R = 0.6 \text{ cm}$ ).

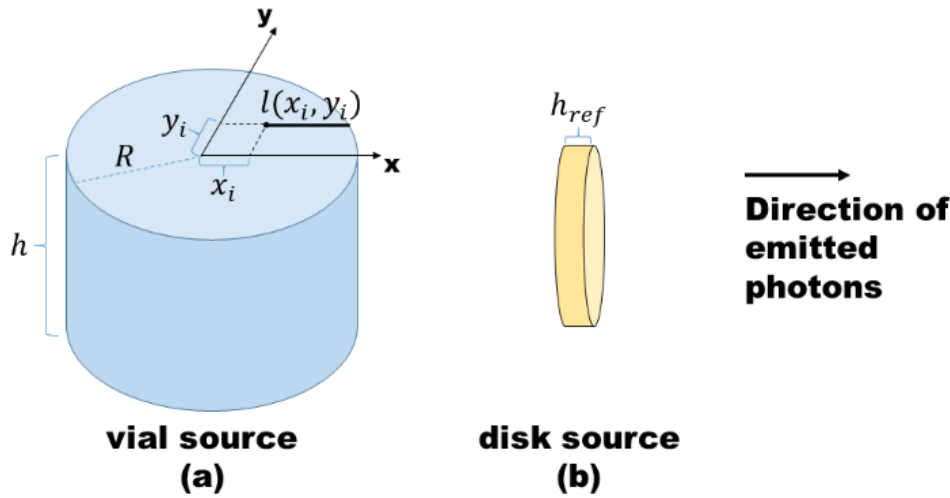


Figure A.7.1 Diagram of vial source and disk source used for geometry correction factor estimation.

## A.2 Uncertainties of Dose Calibrator Settings Determined with the Thyroid Probe

As discussed in Section 2.2.1, the method to determine DC settings for a new isotope (or a new sample geometry) using TP consists of the following three steps: 1) efficiency calibration of TP, 2) determination of activity of the new isotope sample using TP and, 3) determination of the DC dial settings for the new isotope. In this section, the formulas used to estimate the standard uncertainties (at a 68% confidence level) of each measuring step are derived.

### Uncertainties of Thyroid Probe Efficiency Curve

The uncertainty of the TP efficiency determination was calculated by applying the standard error propagation formula through equation 2.1:

$$\left(\frac{\Delta\epsilon}{\epsilon}\right)^2 = \left(\frac{\Delta N_{\text{photopeak}}}{N_{\text{photopeak}}}\right)^2 + \left(\frac{\Delta N_{\text{emitted}}}{N_{\text{emitted}}}\right)^2 + \left(\frac{\Delta\kappa}{\kappa}\right)^2 + \left(\frac{\Delta DT}{DT}\right)^2 + \left(\frac{\Delta f}{f}\right)^2. \quad (\text{A.6})$$

The  $\Delta N_{\text{photopeak}}$  value accounted for: 1) the uncertainty of the total detected counts in the photopeak ( $\Delta N_{\text{detected}}$ ) and 2) the uncertainty of  $N_U$  and  $N_L$ , propagated through the scatter-correction formula (equation 2.2):

$$(\Delta N_{\text{photopeak}})^2 = (\Delta N_{\text{detected}})^2 + \left(\frac{W_{\text{detected}}}{2}\right)^2 \left(\frac{\Delta N_U^2}{W_U^2} + \frac{\Delta N_L^2}{W_L^2}\right) \quad (\text{A.7})$$

where  $\Delta N_{\text{detected}}$ ,  $\Delta N_U$  and  $\Delta N_L$  were estimated as the standard deviations ( $\sigma_i$ ) of  $N_{\text{detected}}$ ,  $N_U$  and  $N_L$ , respectively, added in quadrature with the uncertainty of the ambient background counts of each corresponding energy window ( $\Delta N_{\text{bkg}-i}$ ):

$$(\Delta N_{\text{detected}})^2 = \sigma_{\text{detected}}^2 + (\Delta N_{\text{bkg-detected}})^2. \quad (\text{A.8})$$

The standard deviations of  $N_{\text{detected}}$ ,  $N_U$  and  $N_L$  were calculated from repeated measurements of the isotope's energy spectra. The uncertainty of  $N_{\text{bkg}-i}$  was estimated as  $\sqrt{N_{\text{bkg}-i}}$  (Poisson

statistics). As a result, the uncertainty in the photopeak corrected counts ( $\Delta N_{photopeak}$ ) accounts for the statistical fluctuations in the number of counts in each energy window (Poisson statistics), the uncertainty due to ambient background subtraction and the variability in counts due to source positioning. Errors in window settings were ignored.

Considering the definition of  $N_{emitted}(E)$  (Equation 2.4), the uncertainty of the number of emissions was calculated as:

$$\left(\frac{\Delta N_{emitted}}{N_{emitted}}\right)^2 = \left(\frac{\Delta A_0}{A_0}\right)^2 + \left(\frac{\Delta Y}{Y}\right)^2 + \left(\frac{\Delta DF}{DF}\right)^2 \quad (A.9)$$

where the uncertainty of the activity ( $\Delta A_0$ ) was obtained by propagating the manufacturer reported activity uncertainty (at time of calibration) and the isotope half-life uncertainty ( $\Delta T_{1/2}$ ) through the exponential decay formula to the time of scan. The uncertainties of the emission yields ( $\Delta Y$ ) were obtained from the Nuclear Data Sheets (Table 2.1) and the uncertainty of the factor  $DF$  was calculated as:

$$(\Delta DF)^2 = \left( \frac{1}{\ln 2} \left[ 1 - \exp\left(-\frac{\ln 2}{T_{1/2}} T\right) \right] + \frac{1}{T_{1/2}} \left[ T \exp\left(-\frac{\ln 2}{T_{1/2}} T\right) \right] \right)^2 (\Delta T_{1/2})^2. \quad (A.10)$$

The uncertainty of the vial-to-reference geometry (or tube-to-reference) correction factor ( $\Delta \kappa_{VR}$ ) is a combination of the vial (or tube) and reference source transmission factor uncertainties ( $\Delta \langle TF_{vial} \rangle$  and  $\Delta \langle TF_{ref} \rangle$ , respectively):

$$\left(\frac{\Delta \kappa_{VR}}{\kappa_{VR}}\right)^2 = \left(\frac{\Delta \langle TF_{vial} \rangle}{\langle TF_{vial} \rangle}\right)^2 + \left(\frac{\Delta \langle TF_{ref} \rangle}{\langle TF_{ref} \rangle}\right)^2 \quad (A.11)$$

where  $\Delta \langle TF_{vial} \rangle$  and  $\Delta \langle TF_{ref} \rangle$  were calculated by propagating the uncertainties of the source dimensions ( $\Delta R = 0.05$  cm and  $\Delta h_{ref} = 0.05$  cm) through Equation A.3 and Equation A.4:

$$(\Delta\langle TF_{vial}\rangle)^2 = \frac{1}{N^2} \left( \sum_{y_i} \sum_{x_i} \exp \left[ \mu_w \left( \sqrt{R^2 - y_i^2} - x_i \right) \right] \frac{R\mu_w}{\sqrt{R^2 - y_i^2}} \right)^2 \Delta R^2 \quad (\text{A.12})$$

$$(\Delta\langle TF_{ref}\rangle)^2 = \left( \frac{\mu_p}{2} \exp \left[ -\frac{\mu_p h}{2} \right] \right)^2 (\Delta h_{ref})^2. \quad (\text{A.13})$$

Similarly, the uncertainty of the disk-to-reference ( $\Delta\kappa_{DR}$ ) geometry factor was calculated by propagating  $\Delta h_{ref}$  and  $\Delta h_{disk}$  through Equation A.5:

$$(\Delta\kappa_{DR})^2 = \left[ \frac{\mu_p}{2} \exp \left( \frac{\mu_p}{2} [h_{disk} - h_{ref}] \right) \right]^2 (\Delta h_{ref}^2 + \Delta h_{disk}^2). \quad (\text{A.14})$$

The uncertainties of the dead-time and other corrections factors were 0 since these factors were assumed to be equal to 1.

#### Uncertainties of the Sample Activity Determination Using Thyroid Probe

The uncertainties of determination of samples activity were calculated by applying the error propagation formula to Equation 2.7:

$$\left( \frac{\Delta A}{A} \right)^2 = \left( \frac{\Delta N_{photopeak}}{N_{photopeak}} \right)^2 + \left( \frac{\Delta \epsilon'}{\epsilon'} \right)^2 + \left( \frac{\Delta DF}{DF} \right)^2 + \left( \frac{\Delta Y}{Y} \right)^2 + \left( \frac{\Delta \kappa}{\kappa} \right)^2 + \left( \frac{\Delta DT}{DT} \right)^2 + \left( \frac{\Delta f}{f} \right)^2 \quad (\text{A.15})$$

where the uncertainty of the fitted efficiency  $\Delta \epsilon'$  was determined by the uncertainty of the measured efficiency propagated through the logarithmic function in Equation 2.5:

$$(\Delta \log(\epsilon'))^2 = \left( \frac{\Delta \epsilon'}{\epsilon'} \right)^2 = \sum_i \left( \frac{\partial a}{\partial \log(\epsilon_i)} + \frac{E \partial b}{\partial \log(\epsilon_i)} \right)^2 (\Delta \log(\epsilon_i))^2. \quad (\text{A.16})$$

The uncertainty of  $DF$ , and the geometry factors  $\kappa$  were calculated according to Equation A.10 and Equation A.11, respectively. The uncertainty of the photon yields and isotope half-life were obtained from the Nuclear Data Sheets, except for  $^{99m}\text{Tc}$  data which was obtained from the Decay Data Evaluation Project (Table 2.3).

### Uncertainties of the Dose Calibrator Dial Settings

The correct dial setting (DS) was determined from the calibration response curve ( $A'_{app} = c \times DS + d$ ) for the case  $A'_{app} = A_{TP}$  (Section 2.2.1.4):

$$DS = \frac{A_{TP} - d}{c}. \quad (\text{A.17})$$

The uncertainty of the dial setting was obtained by applying the error propagation formula to Equation A.17:

$$(\Delta DS)^2 = \sum_i \left[ \frac{1}{c} \left( \frac{\partial d}{\partial A_{app-i}} \right) + \frac{1-d}{c^2} \left( \frac{\partial c}{\partial A_{app-i}} \right) \right]^2 (\Delta A_{app-i})^2 + \left( \frac{\Delta A_{TP}}{c^2} \right)^2 \quad (\text{A.18})$$

where  $\Delta A_{app-i}$  represents the uncertainty of the dose calibrator measurements of the apparent activity (i.e., repeatability uncertainty).

The uncertainty in the activity measured with the experimentally determined dial setting ( $\Delta A_{DS}$ ) was calculated by propagating the dial setting uncertainty and the uncertainty of  $c$  and  $d$  through the fitting equation of  $A'_{app}$ :

$$(\Delta A_{DS})^2 = (DS \Delta c)^2 + (c \Delta DS)^2 + (\Delta d)^2. \quad (\text{A.19})$$

### A.3 Calculation of the Source Geometry Correction Factor using Monte-Carlo

The efficiency of the thyroid probe depends on the geometry and the density of the material of the radioactive source. In this study, two source geometries were mainly used: a point-like source embedded in a solid acrylic disk and a 25-mL glass vial containing 20-mL liquid solution. Due to photon attenuation within the walls of the vial and the source material, for a same total number of emissions  $N_E$ , the number of photons exiting the vial is lower compared to the disk geometry. This results in fewer detected photons  $N_D$  and therefore a lower efficiency. In order to account for the differences in geometry and to be able to use the disk-source

efficiency curve (reference geometry) to evaluate activity of vial-type sources, a correction for the geometry was required. The vial-to-reference geometry correction factor ( $\kappa_{VR}$ ) was calculated using an analytical method (Section 2.2.1.3). In the following material, the set of Monte-Carlo simulations that were performed to validate the analytical method are described.

### The Monte-Carlo Model of the Thyroid Probe

In the Monte-Carlo method, the vial-to-reference geometry correction factor was defined as:

$$\kappa_{VR-MC} = \frac{N_{D-ref-MC}(E)}{N_{D-vial-MC}(E)} \quad (A.20)$$

where  $N_{D-ref-MC}(E)$  and  $N_{D-vial-MC}(E)$  represent the number of scatter-corrected photopeak photons for the reference and for the vial source, respectively. The factor  $\kappa_{VR-MC}$  represents the change in photopeak counts due to source geometry differences as it includes modelling of attenuation, scatter, more realistic source geometry and efficiency of the thyroid probe. All the simulations in this study were performed using GATE 7.1. A total of 12 sources (6 disk sources, 6 vial sources) of mono-energetic photons corresponding to the photopeak energies of all the isotopes used in this study were simulated. The disk-source geometry was modelled following the manufacturer specifications. The vial source was modelled as a glass hollow cylinder (height = 6.2 cm, internal diameter = 2.5 cm) with 0.15 cm wall thickness, filled with 20 mL of water. The source-to-detector distance was set to 20.5 cm, reproducing the experimental conditions. The thyroid-probe detector was modelled as a 5.08 cm x 5.08 cm (diameter x height) NaI crystal, surrounded by a cylindrical lead collimator of 1 cm thickness. The energy resolution ( $R$ ) of the detector was first measured experimentally using a  $^{99m}\text{Tc}$  source (FWHM  $R_0 = 9.05$  at  $E_0 = 140$  keV) and then it was modelled in the simulations as an inverse square law ( $R(E) =$

$R_0 E_0 / \sqrt{E}$ ) by making use of the digitizer tool in GATE. For each simulation, the energy spectrum of photons detected by the thyroid-probe was recorded and the total number of scatter-corrected photopeak counts ( $N_D$ ) was calculated applying the same method as used in the experiments. A total of  $N = 10^8$  photons were simulated at each energy and source geometry. The relative uncertainty of the geometry factor was calculated using the following expression:

$$\left(\frac{\Delta\kappa_{VR-MC}}{\kappa_{VR-MC}}\right)^2 = \left(\frac{\Delta N_{D-ref-MC}}{N_{D-ref-MC}}\right)^2 + \left(\frac{\Delta N_{D-vial-MC}}{N_{D-vial-MC}}\right)^2 \quad (\text{A.21})$$

where  $\Delta N_{D-ref-MC}$  and  $\Delta N_{D-vial-MC}$  were calculated using the same methodology as in the experiments.

In order to validate the Monte-Carlo model of the thyroid-probe and the geometry correction factors, the efficiency of the simulated thyroid-probe as a function of energy was calculated as:

$$\epsilon_{MC}(E) = \frac{N_{D-ref-MC}}{N}. \quad (\text{A.22})$$

where  $N$  represents the total number of simulated photons for each energy  $E$ . Subsequently, the simulated and experiment efficiency were compared.

### Validation of Monte-Carlo Simulations

The simulated and the experimental efficiency curves are shown in Figure A.2. The measured efficiency agrees (within experimental uncertainty) with the simulations for all measured points. The large difference between simulation and experiments found at the 511 keV  $^{22}\text{Na}$  photopeak. This difference might be explained by the angular correlations of the 511 keV annihilation photons from  $^{22}\text{Na}$ , which were not modelled in the simulation. Overall, the

thyroid-probe simulations modelled the experiments well and served as a validation of the analytical geometry factors used in our experiments.

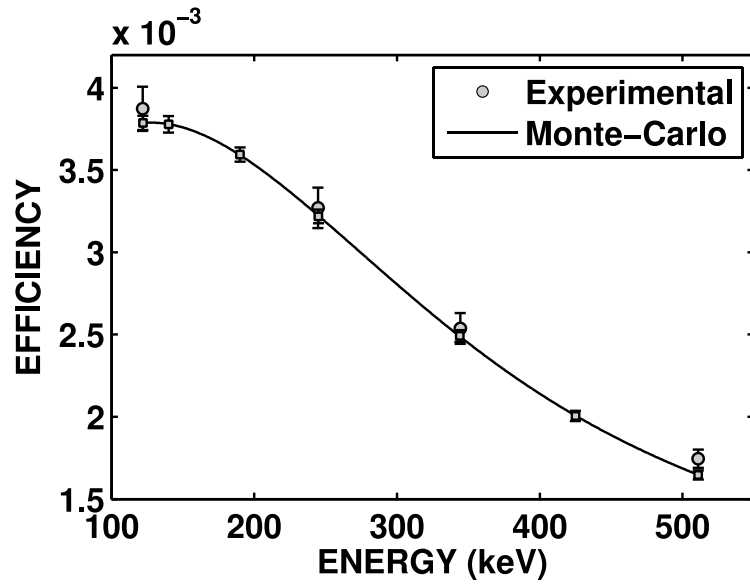


Figure A.7.2 Comparison between experimental and Monte-Carlo simulations of the thyroid probe efficiency.

## Appendix B - Supplementary Material for Chapter 5

### B.1 VECTor/CT Calibration Experiments

In order to obtain 3-D activity distribution, the reconstructed images were re-scaled using a Calibration Factor ( $CF$ ) that converts the voxel values (arbitrary units) into activity concentration (MBq/mL). The  $CF$  was obtained from the reconstructed image of a point source of well-known activity using the following expression:

$$CF = \frac{A}{V \sum R_i} \quad B. 1$$

where  $A$  represents the point source activity (in MBq), measured using a dose calibrator (Atomlab 500, Biodex),  $V$  represents the voxel volume in the reconstructed image (in mL) and  $\sum R_i$  represents the sum of voxel values in a volume of interest (VOI) drawn around the point source. A 1% threshold was applied to segment the point source within the drawn VOI.

The  $CF$  depends on the isotope, collimator and energy window settings. In this study, the  $CF$  was measured for  $^{188}\text{Re}$  (UHRC and HE-UHRC) using a 79 MBq point source scanned during 15 minutes. Similarly, the  $CF$  was also measured for  $^{99\text{m}}\text{Tc}$  (UHRC and HE-UHRC) using a 37 MBq point source scanned during 15 minutes. The point source images were reconstructed using the same window settings and corrections described in the manuscript (Section 4.2.1.2). The measured calibration factors were 3398 MBq/mL, 3100 MBq/mL, 551.8 MBq/mL and 466.9 MBq/mL for  $^{188}\text{Re}$ -UHRC,  $^{188}\text{Re}$ -HE-UHRC,  $^{99\text{m}}\text{Tc}$ -UHRC and  $^{99\text{m}}\text{Tc}$ -HE-UHRC, respectively.

### B.2 Calculation of Image Contrast and Contrast-to-noise Ratio

Image contrast and CNR vs rod diameter were quantified using images of the same Micro-Jaszczak resolution phantom following the method described by Walker *et al.* 2014 [134]. For each image, cylindrical VOIs (5 mm height) were placed on each rod and in the space between

the rods. The diameter of each VOI was 0.9 times the diameter of the analyzed rod. The image contrast was defined as:

$$C_d = \frac{\overline{h_d} - \overline{b_d}}{\overline{h_d}} \quad B. 2$$

where  $\overline{h_d}$  represents the average voxel value of all ROIs drawn on the hot rods within a section of rod diameter  $d$ . Similarly,  $\overline{b_d}$  represents the average voxel value of all ROIs drawn in between the rods (i.e., in the background). The noise  $N_d$  was defined as the variability between ROI mean values, and was calculated as:

$$N_d = \frac{\sqrt{\sigma_{h_d}^2 + \sigma_{b_d}^2}}{\overline{\text{rois}_d}} \quad B. 3$$

where  $\sigma_{h_d}^2$  and  $\sigma_{b_d}^2$  represent the standard deviation of  $h_d$  and  $b_d$  respectively and  $\overline{\text{rois}_d}$  represents the mean value of all ROIs (h and b) within the sector with rods having diameter  $d$ .

The Contrast-to-Noise ratio (CNR) was calculated as  $\frac{C_d}{N_d}$ .

### B.3 Monte-Carlo Model of VECTor/CT

The Monte-Carlo model of the VECTor system included: three 9.5 cm thick NaI detectors covered by a 0.05 cm thick aluminum layer at the front. The back-compartment region of the detector contained a 0.95 cm thick light-guide made of glass followed by 5.65 cm of an uniform material modeling the photomultiplier tubes made of 23% glass, 56% vacuum and 21% air [113]. In addition, three lead panels (3 cm thickness) were added to model the shielding material around the system. Only the UHRC collimator was simulated. For the sake of simplicity, the UHRC was modelled as a Tungsten hollow cylinder with a 9.8 cm bore diameter (van der Have et al. 2009 [127]) and 1.5 cm thickness containing a single ring of pinholes at the center of the tube (15

pinholes in total). The pinhole diameter for this collimator was set to 1 mm, and the opening angle was  $30^\circ$  (Vaissier et al. 2012 [177]).

The  $^{188}\text{Re}$  decay data were built-in in GATE, and it is based on the Evaluated Nuclear Structure Data File (ENSDF) database (Bhat 1992 [115]). The detector energy resolution  $R$  (FWHM) was set at  $R_0=10\%$  for  $E_0=140$  keV photons. The dependence of resolution  $R$  with photon energy was modeled as an inverse square root law ( $R(E) = R_0E_0/\sqrt{E}$ ). Only photons which deposited energies in the range 50 keV to 700 keV in the detector were recorded.

A total of  $10^8$  decays of  $^{188}\text{Re}$  were launched for each of the simulations described in the manuscript, Section 4.2.4.2. The modelling of the system and simulations were performed using Geant4 Application for Tomographic Emissions (GATE), version 6.1 [53,54].